UNIVERSITAT
POLITÈCNICA
DE VALÈNCIA

Departamento de Máquinas y Motores Térmicos

Doctoral Thesis

"Experimental analysis and multidimensional modeling of water condensation due to low-pressure exhaust gas recirculation activation during engine cold starts"

Presented by

Mr. Francisco Moya

Supervised by

Dr. Roberto Navarro

Valencia, July 2022

DOCTORAL THESIS

"Experimental analysis and multidimensional modeling of water condensation due to low-pressure exhaust gas recirculation activation during engine cold starts"

Presented by: Mr. Francisco Moya

Supervised by: Dr. Roberto Navarro

THESIS EXAMINERS

Dr. Gianluca Montenegro

Dr. Xavier Tauzia

Dr. Jesús Vence Fernández

DEFENSE COMMITTEE

Chairman: Dr. José Manuel Luján Martínez

Secretary: Dr. Francisco Vera García

Member: Dr. Xavier Tauzia

Valencia, July 2022

Abstract

The increasing use of the exhaust gas recirculation during the last years due to the impact reduction on the NOx emissions and the high demand on solutions to fulfill the homologation restrictions has revealed the need of studying deeply the system to operate continuously and independently of the boundary conditions. As a consequence of this and knowing that the main drawback of employing the low pressure exhaust gas recirculation is the condensation generation that causes erosion on the compressor impeller, research is required to understand and to predict the condensation during the exhaust gas recirculation activation.

This work has been focused on generating and improving the modelling condensation prediction; and also, the development of experimental techniques that validates the proposed models for calculating the condensation water at cold warm-up homologation cycles.

Concerning the experimental work presented on the thesis, the efforts has been focused on the condensation measurements in two different locations. On one hand, on the low pressure exhaust gas recirculation cooler, changing inlet conditions while simulating warm-up conditions on an engine. On the other hand, the condensation has been measured at the three-way junction outlet where the exhaust gas recirculation is mixed with fresh air coming from the ambient. Also, novel methodologies has been developed for measuring with optical techniques and with indirect measurements the mixing condensation.

In terms of the condensation modeling, this thesis has been based in two main topics. The first topic regarding modeling was a 0D condensation model for calculating the condensation on heat exchangers and in particular, on low pressure exhaust gas recirculation coolers. Following this topic, it has been a quantitative validation of a 3D-CFD condensation submodel by means of experimental measurements. The second topic has been centered on developing new statistical methodologies for reducing the condensation calculation complexity on multi-dimensional simulations and reducing multi-fidelity parameters with the reduction of the computational cost. These methodologies have allowed to calculate the condensation on homologation cycles and to perform sensitivity analysis with different conditions.

Keywords: Condensation; LP-EGR system; Optical techniques; CFD simulations; Multi-fidelity condensation models;

Resumen

El creciente uso de la recirculación de gases de escape durante los últimos años debido a su impacto en la reducción de las emisiones NOx y a la alta demanda de soluciones por parte de los nuevos ciclos de homologación para reducir emisiones, ha provocado la necesidad de estudiar en profundidad el sistema de recirculación de gases de escape para su uso de forma continua y con independencia de las condiciones ambientales. Debido a esta necesidad y sabiendo que el principal problema de su uso en el ciclo de baja presión es la condensación generada que provoca el desgaste del rodete del compresor. Ha hecho necesaria la investigación en profundidad de esta técnica para conocer, entender y predecir la condensación durante el uso de la recirculación de gases de escape de baja presión.

Este trabajo se ha centrado en generar, mejorar y validar los modelos de predicción de condensados, así como de desarrollar técnicas experimentales que validaran y sirivieran para entender mejor el fenómeno de la condensación, con la visión puesta en calcular la condensación en ciclos completos de homologación.

Respecto al trabajo experimental de esta tesis, se han centrado los esfuerzos en medir la condensación generada en el intercambiador de calor de la línea de recirculación de gases de escape de baja presión para diferentes condiciones, simulando un arranque en frío de motor. Otro de los puntos que se ha estudiado, ha sido la condensación a la salida de la unión en la que se mezcla la recirculación de gases de escape de baja presión con el aire del ambiente proveniente de la entrada del motor. Desarrollando nuevas metodologías para la medida experimental mediante técnicas ópticas y medidas indirectas de la condensación por mezcla.

En cuanto al trabajo de modelado de la condensación, se ha investigado sobre dos grandes líneas. La primera ha sido el desarrollo de modelos 0D para el cálculo de la condensación en el intercambiado de calor de la línea de recirculación de gases de escape y la verificación experimental del modelo de condensación 3D-CFD desarrollado previamente a esta tesis. El segundo punto ha consistido en el desarrollo y aproximación de nuevas metodologías

mediante métodos estadísticos de la reducción de la complejidad en el cálculo de la condensación, reduciendo el número de dimensiones necesarias para calcular de forma realista la condensación en un tiempo reducido. Esto ha posibilitado el cálculo de la condensación producida en ciclos de homologación y su posterior estudio mediante análisis de sensibilidad a diferentes condiciones, estimando una duración del rodete del compresor antes de sufrir desgaste debido a la erosión con el agua.

Palabras clave: Condensación; sistema de recirculación de gases de escape de baja presión; Técnicas ópticas; simulaciones CFD; Modelos de condensación multifidelidad;

Resum

El creixent ús de la recirculació de gasos d'escapament durant els últims anys a causa del seu impacte en la reducció de les emissions NOx i a l'alta demanda de solucions per part dels nous cicles d'homologació per a reduir emissions, ha provocat la necessitat d'estudiar en profunditat el sistema per al seu ús de manera contínua i amb independència de les condicions ambientals. A causa d'aquesta necessitat i sabent que el principal problema del seu ús és la condensació generada que provoca el desgast del rodet del compressor, ha fet necessària la seua investigació en profunditat per conéixer, entendre i predir la condensació per l'ús de la recirculació de gasos d'escapament de baixa pressió.

Aquest treball s'ha centrat en generar i millorar els models de predicció de condensats així com de desenvolupar tècniques experimentals que validaren i serviren per entendre millor el fenomen de la condensació, amb l'objectiu d'estimar la condensació en cicles complets d'homologació.

Respecte al treball experimental d'aquesta tesi, s'han centrat els esforços a mesurar la condensació generada a l'intercanviador de calor de la línia de recirculació de gasos d'escapament de baixa pressió per a diferents condicions simulant una arrancada en fred de motor. Un altre dels punts que s'ha estudiat ha sigut la condensació a l'eixida de la unió en la qual es mescla la recirculació de gasos d'escapament de baixa pressió amb l'aire fresc que prové de l'entrada del motor, desenvolupant noves metodologies per a la mesura experimental mitjançant tècniques òptiques i mesures indirectes de la condensació per mescla.

Quant al treball de modelatge de la condensació, s'ha investigat sobre dues grans línies. La primera ha sigut el desenvolupament de models 0D per al càlcul de la condensació a l'intercanviat de calor de la línia de recirculació de gasos d'escapament i la verificació experimental del model de condensació 3D-CFD desenvolupat prèviament a aquesta tesi. El segon punt ha consistit en el desenvolupament i aproximació de noves metodologies mitjançant mètodes estadístics de la reducció de la complexitat en el càlcul de la condensació, reduint les dimensions necessàries per a calcular de manera realista la condensació en

un temps reduït. Això ha possibilitat el càlcul de la condensació produïda en cicles d'homologació i el seu posterior estudi mitjançant anàlisi de sensibilitat a diferents condicions.

Paraules clau: Condensació; sistemes de recirculació de gases de escape de baixa presió; Tècniques òptiques; simulació CFD; Models de condensació multifidelitat;

List of publications

This thesis is based on the work presented in the following papers:

[1] S. Guilain, R. Boubennec, M. Doublet, C. Clement, R. Navarro, D. Tarí, and F. Moya. "Condensation before compressor: a key issue of Low Pressure EGR in Eu7 context". In: *24th Supercharging Conference 2019, Aufladetechnische Konferenz, Dresden*. Sept. 26, 2019

[2] J. Galindo, R. Navarro, D. Tari, and F. Moya. "Development of an experimental test bench and a psychrometric model for assessing condensation on a Low Pressure EGR cooler". *International Journal of Engine Research*, (2020). DOI: 10.1177/1468087420909735

[3] J. Galindo, R. Navarro, D. Tari, and F. Moya. "Analysis of condensation and secondary flows at T-junctions using optical visualization techniques and Computational Fluid Dynamics". *International Journal of Multiphase Flow*, (2021). DOI: 10.1016/j.ijmultiphaseflow.2021.103674

[4] J. Galindo, R. Navarro, D. Tari, and F. Moya. "Quantitative validation of an in-flow water condensation model for 3D-CFD simulations of three-way junctions using indirect condensation measurements". *International Journal of Thermal Sciences*, 172, (2022), pp. 1–11. DOI: 10.1016/j.ijthermalsci.2021.107303

[5] J. Galindo, R. Navarro, F. Moya, and A. Conchado. "Comprehensive method for obtaining multi-fidelity surrogate models for design space approximation: application to multi-dimensional simulations of condensation due to mixing streams". *submitted to Applied Mathematics and Computation*, (2022)

[6] J. Galindo, R. Navarro, L. M. García-Cuevas, and F. Moya. "Engine modeling of heat-exchanger and mixing-streams condensation mechanisms: impact of Exhaust Gas Recirculation strategy on trade-off between emissions and compressor durability during engine cold start". *submitted to Applied Energy*, (2022)

Division of work between authors

The work leading up to this thesis was done in collaboration with other researchers. The respondent is the corresponding author in all of papers on which this thesis is based, author signatures are in order of seniority at the Institute side. The respondent was responsible of the experimental methodology, the post-processing task and to perform the measurements assisted by Alejandro Hernández in the condensation gas stand set up. Also, the respondent was in charge of the CFD simulations and the post-processing performance, however Guillermo García is acknowledged for the help of processing the cases presented in Chapter 5. The respondent was responsible of the development of the reduce order models with multi-fidelity approach with the collaboration and discussion of Prof. Andrea Conchado. Methodology and discussion results were also performed in collaboration with Prof. Roberto Navarro and Prof. José Galindo and the rest of co-authors.

Funding acknowledgements

The respondent wishes to acknowledge the financial support received through contract FPI-GVA-ACIF-2019 grant of the Government of Generalitat Valenciana and the European Social Fund. The equipment used in this work and the international stay has been partially supported through the following project:

- Project grant number GV/2020/008 of the "Conselleria de Innovación, Universidades, Ciencia y Sociedad Digital de la Generalitat Valenciana"
- Grant for the international stay number BEFPI-2020 of the "Conselleria de Innovación, Universidades, Ciencia y Sociedad Digital de la Generalitat Valenciana" and the European Social Fund

Acknowledgments

First of all, I would like to express my sincerely gratitude to Dr. Roberto Navarro for his dedication, support and guidance during my Ph.D studies. Also for his patient and for having, in his busiest agenda, time for off-topic discussions.

Special thanks to Prof. José Galindo for trusting me, allowing me to be part of the Air Management department and for guiding part of this research. I wish also thanks Prof. Héctor Climent for introducing me into the Python knowledge.

I would like also to acknowledge all the technicians for their dedication most of the time with a hidden work, to and specially the ones that help me the most with the experimental set up and measurements, Alejandro Hernández, Rafael Carrascosa and José Gálvez. Also special thanks to Amparo Cutillas for her help with the unpleasant paperwork.

I would thank, Johan Nilsson, Dr. Ulf Aronsson and Dr. Erik Svensson to allow me during these pandemic years the opportunity to do my doctoral stay in Volvo Group and also to all the group at Volvo for a very grateful stay in Malmö.

Extremely thanks to my lab mates Daniel Tarí, Pablo Soler, Chaitanya Patil, Ángel Auñón and Guillermo García, without your support during the hard days I would not have been concluded this thesis and for showing me that always there is reason to smile.

Many thanks to my friends in "Almansa" to teach me that there is always time for a beer or a trip together.

Last but the first ones, I would like to thanks my family: Mamá, Papá and Rubén for teaching me and educating like you do. And thank you, Inma, for being a strong support specially these hard years

Valencia, Mayo 2022

"Nothing in life is to be feared, it is only to be understood. Now is the time to understand more, so that we may fear less."

— Marie Curie

Contents

List of Tables

List of Figures

List of symbols

Latin characters

A	Area	m^2
c	Absolute velocity	$m \cdot s^{-1}$
C_D	discharge coefficient	$-$
c_D	drag coefficient	$-$
c_p	isobaric specific heat capacity	$J \cdot kg^{-1} \cdot K^{-1}$
dt	time variation	s
EGR	Exhaust gas re-circulation	$\%$
F	Force	N
f	additional terms	$-$
f	condensation value	kg/h
f_L	correction factor	$-$
f^*_β	free-shear modification factor	$-$
f_β	vortex-stretching modification factor	$-$
g	surrogate model value	$-$
h	enthalpy	$J \cdot kg^{-1} \cdot K^{-1}$
H	enthalpy	$J \cdot s^{-1}$
I	turbulent intensity	$\%$
k	turbulent kinetic energy	$m^2 \cdot s^{-2}$
L	latent heat	$J \cdot kg^{-1}$
$\bar{Lm}$	normalized luminosity	$-$
MW	molecular weight	$kg \cdot mol^{-1}$
$\dot{m}$	mass flow rate	$kg \cdot s^{-1}$
MFR	Mass flow rate	$kg \cdot h^{-1}$
N	Number of temperature probe	

	locations at junction outlet	$-$
N	Number of photos	$-$
N	number of parameters	$-$
p	pressure	Pa
P	Pressure	bar
P_k	Production term (k)	$kg \cdot m^{-1} \cdot s^{-3}$
P_w	Production term (w)	$kg \cdot m^{-3} \cdot s^{-2}$
$\dot{Q}$	Heat transfer	$J \cdot s^{-1}$
R	specific gas constant	$J \cdot kg^{-1} \cdot K^{-1}$
RH	relative humidity	$\%$
S	source term	$-$
T	temperature	K
$\mathcal{T}$	turbulent time scale	s
t	time	s
u	velocity	$m \cdot s^{-1}$
$\vec{u}$	velocity	$m \cdot s^{-1}$
w	specific humidity	$g_{H_2O} \cdot kg_{air}^{-1}$
x	coordinate in dominant direction	m
x	Parameter value for each points	$-$
y	mass fraction	$-$
y	condensation value	kg/h
z	Intermediate variable	$-$

Greek characters

α	Absolute flow angle
β	Relative flow angle
Δ	Difference between high and low fidelity condensation
Δt	characteristic time

η	T-junction efficiency
ϵ_R	relative error
γ	Specific heat capacities ratio
γ	mass fraction
λ	Eigenvalue
ν	CFL number
μ	dynamic viscosity
μ_t	turbulent eddy viscosity
π	Pressure ratio
ρ	Density
σ	standard deviation
$\sigma_k,\ \sigma_\omega$	SST $k-\omega$ model coefficients
φ	ratio between high and low fidelity condensation
ω	Specific rate of dissipation

Sub- and Superscripts

0	stagnation operating point
$1, 2, 3...$	position in the test rig
$0D$	Low fidelity simulation
$3D$	High fidelity simulation
$a, dis.$	condensate after the discharge
air	air flow
air	intake air branch conditions
$amb.$	ambient conditions
$b, dis.$	condensate before the discharge
$cells$	cells at the mesh
$cond$	condensates
$cool$	coolant conditions

$corr.$	condensates corrected
$corr$	corrected luminosity
dew	dew point
dry	Case with water injection
$dryair$	dry air flow
EGR	egr flow
end	end value of the test
$ener.$	energy
$Exh.$	Engine exhaust gas
$explor$	exploration points
ext	external
$film$	laser sheet
gas	gaseous flow
H_2O	liquid water
i	data for each time step
i	each pixel data
i	number of model parameters
in	intake flow
$init$	initial value of the test
$inlet$	inlet flow
j	number of training data
k	number of space design exploration data
L	Luminosity
$liquid - MFR$	liquid Mass Flow Rate
m	mass
m	multi-fidelity surrogate models
$meas.$	condensates measured
$mom.$	momentum

out	outlet flow
out	outlet branch conditions
outlet	outlet flow
$rate$	ratio between air mass flow and EGR mass flow
s	surrogate model
sat	saturation
$screen$	screening points
t	total including inlet and EGR
t	variable of study
$theo$	theoretical conditions
$train$	training points
$trainparam.$	training parameters
w	Test with water injection
w/o	Test without water injection
vap	water vapor
ver	verification points
water	liquid water
wet	Case with water injection

Acronyms

0D	Zero-dimensional
1D	One-dimensional
ANOVA	analysis of variance
BSFC	Break specific fuel consumption
CFD	Computational fluid dynamics
CFL	Courant-Friedrichs-Lewy condition
CPU	Central processing unit
EGR	Exhaust gas recirculation

FFD	Fraction factorial design
HF	High fidelity
HP-EGR	High-pressure EGR
ICE	Internal combustion engine
LF	Low fidelity
LP-EGR	Low pressure exhaust gas recirculation
MF	Medium fidelity
MFR	Mass flow rate
NOx	Nitrogen oxides
PIV	particle image velocimetry
PRS	Polynomial Response surface
PWM	Pulse-width modulation
RANS	Original image without postprocessing
RAW	Reynolds-Averaged Navier-Stokes
RBF	Radial basis function
RH	Relative humidity
RMSE	Root mean square error
ROI	Region Of Interest
SST	Shear Stress Transport
URANS	Unsteady Reynolds-Averaged Navier-Stokes
WLTC	Worldwide harmonized light vehicles test cycle
WLTP	Worldwide harmonized light vehicles test procedure

Chapter 1

Introduction

Contents

1.1 Motivation

Since time began, humanity has had an urgent need to satisfy its desire to explore the world around us or even the one we are not able to think about yet. This has led us, little by little, to discover and to invent systems to satisfy those needs that come intrinsically in the human being. From the start to satisfy nutritional needs, through the desire to explore the world and discover every inch of it. Until today, the mobility of people in a global world is conceived as a right of the humans in which technologies have advanced to make their use affordable for the average customer. We are not able to imagine how is going to be the future, but what is clear is that the world will be much more global with greater mobility capabilities.

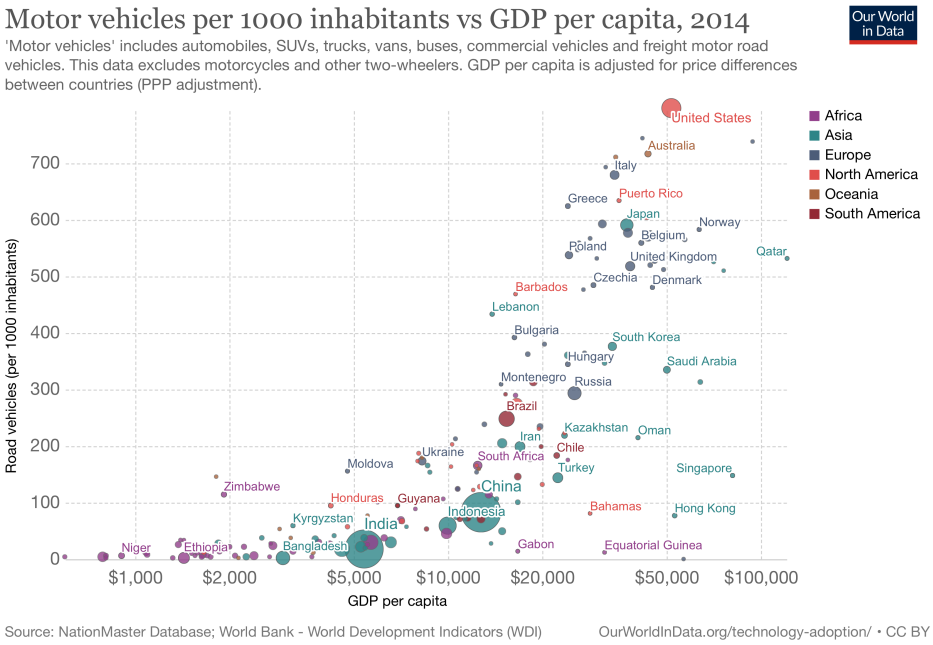

Figure 1.1: *Road vehicles per person comparing with the GDP per capita in different countries* [7]

Regarding the current fleet of vehicles in the world, Figure 1.1 shows how related is the gross domestic product (GDP) per capita of each country with the number of road vehicles per 1000 inhabitants. As it is expected and due to the emerging countries like China or India, the vehicle fleet will increase considerably over the next years once pre-pandemic stability returns. Currently accord-

ing to the European Automobile Manufacturers Association theres is a production of 98.9 million units (2017) per year [8].

Figure 1.2 shows the emissions of CO_2 from the main world's sectors. Transport continues to grow for the last two decades in a second place, only overcame by the electricity and heat production. In response to this, all efforts made in the field of emissions reduction have a clear objective, to reduce greenhouse emissions as much as possible. As a result, in recent years, emissions regulations have become more stringent and stricter to keep up with the growing awareness of the negative health effects of pollutants.

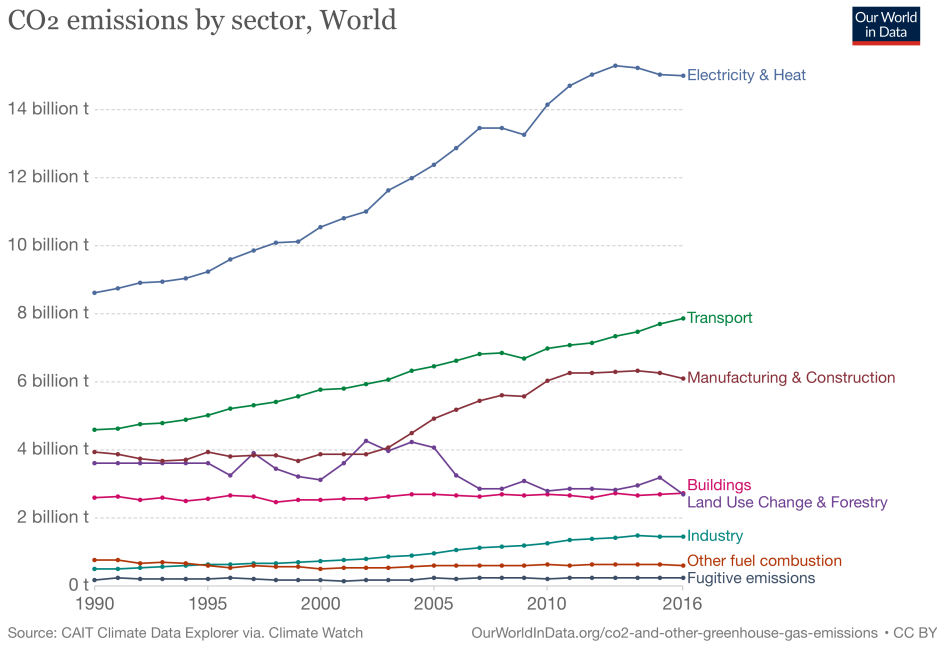

Figure 1.2: *CO_2 emissions by sector over the world* [7]

As mentioned, emissions regulations have started to become more stringent with emissions regulations, even at low temperatures where previous regulations were not focused. In addition, regulations must increasingly take into account actual vehicle operating conditions, such as actual driving emissions.

Figure 1.3 shows the effective dates and transition periods of the European Emission Standards. As can be seen, in 2025 the Euro 7 standard is expected to start, which is going to drastically reduce emission levels and with a higher reduction in NO_x levels, which are expected to be reduced by 3 to 8 times, de-

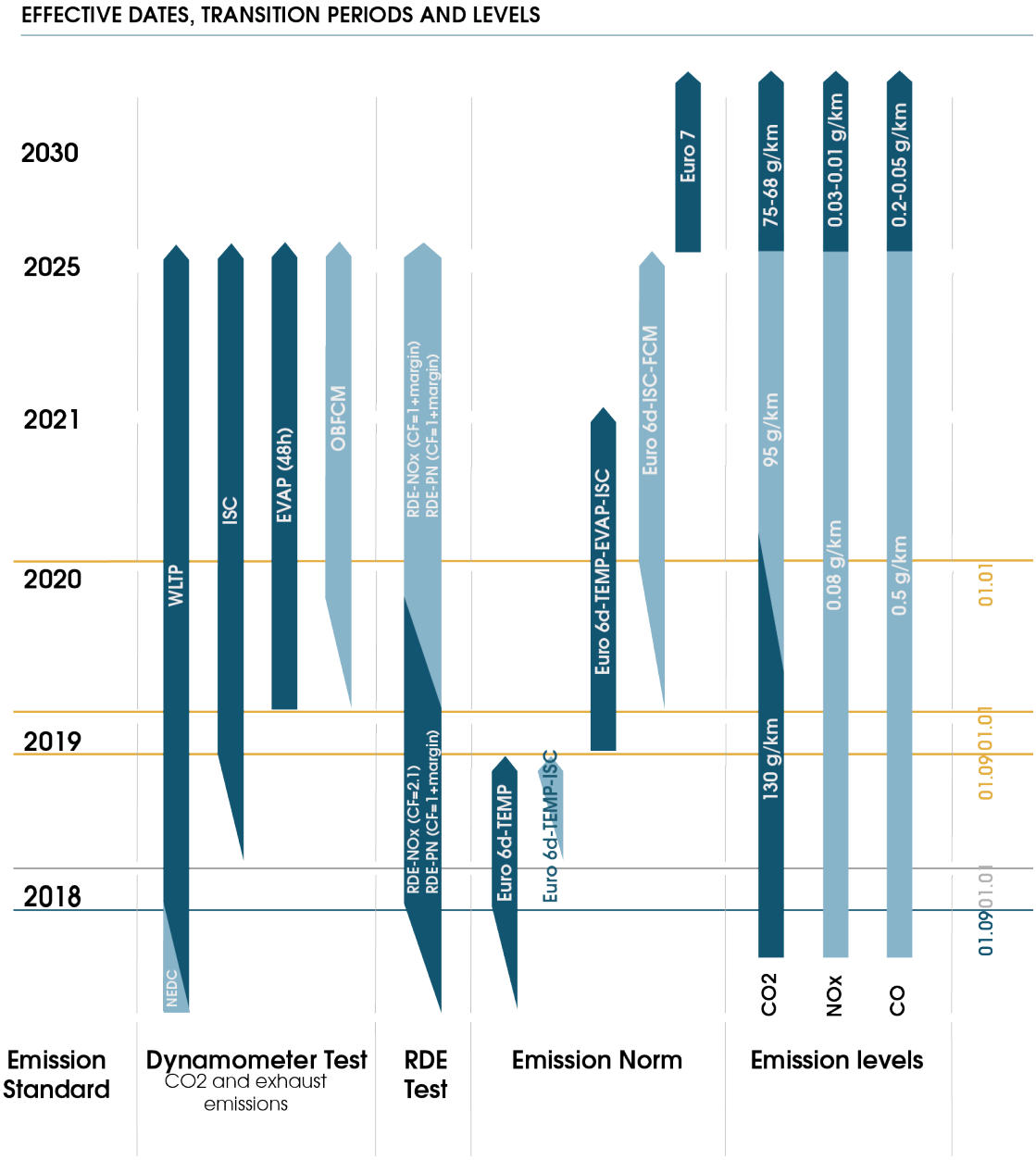

Figure 1.3: *Scheme of the regulations and emission levels* ([9] *Adaptation*)

pending on scenario A or B of the EU/CLOVE consortium proposal in the Vehicle Emission Standards Advisory Group [10]. In addition, 2018 saw the start of cold conditions standards Euro 6d-Temp but, it is known that cold conditions [11] and warm-ups are going to play a key factor for the next few years being a challenge to meet emissions levels in those conditions [12].

The new regulations have led research to focus on finding alternatives to minimize emissions of pollutants such as hydrocarbons (HC), nitrogen oxides (NO_x), carbon dioxide and monoxide (CO and CO_2) and particle matter (PM).

When it comes to reducing pollutant emissions or improving overall efficiency, different paths appear. As far as efficiency improvement is concerned, hybrid engines that allow the internal combustion engine to operate in the maximum efficiency zone or improvements in the mapping at low engine speeds and torques, usually with low efficiency, are the keys to improving engine performance. Conversely, there are also specific techniques to reduce emissions of different pollutants. Such as, for example, the inclusion of diesel or gasoline particulate filters (DPF and GPF) to reduce PM or the reduction of hydrocarbons by working with lean burns. For emissions such as CO_2, attempts have been made to make more efficient engines all over the map, or to use techniques such as "rightsizing" which means, that the car is equipped with an engine adapted to the size of the vehicle or the "downsizing" technique by developing smaller and more efficient IC engines. All these downsizing techniques have been made possible with the advancement of the turbocharger by improving the specific power and efficiency of the vehicle [13]. In terms of reducing NO_x emissions, there are a variety of techniques such as selective catalytic reduction (SCR), the use of lean NO_x trap, the inclusion of adblue and urea and the use of exhaust gas recirculation (EGR) with two different routes, low pressure EGR (LP-EGR) and high pressure EGR (HP-EGR).

EGR is a method to directly reduce the formation of NO_x, this technique consists of recirculating a portion of the exhaust gases back into the engine cylinders mixed with fresh air, which dilutes the concentration of O_2 and brings inert gases into the combustion process. This increases the enthalpy of the reactants and products, which means a reduction of the adiabatic flame temperature in the cylinder and thus a reduction of NO_x emissions produced during the cylinder combustion process due to the Zeldovich mechanism [14, 15]. This technique has been the subject of continuous research since about 1975, when the first reference appeared by Rosen and Erwin using it in a combustion engine [16]. Since then, it has been used in compression ignition (CI) engines, where its use is more widespread, and later for use in spark ignition (SI) engines [17, 18].

There are different routines to use the EGR [19] as can be seen in Fig. 1.4,

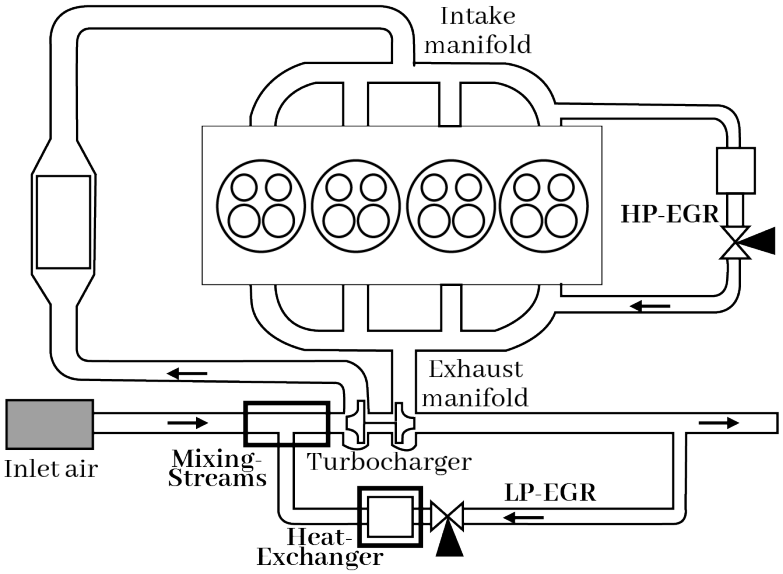

Figure 1.4: *Representative engine diagram with different EGR routes and the places where the condensation appears*

so far the most widespread is called High Pressure EGR (HP-EGR) which connects the exhaust manifolds with the intake manifold. The HP-EGR consists on a connecting duct, a cooler to reduce the temperature of the gases and a valve that regulates the EGR ratio into the cylinders. The system has been used in passenger cars, light, medium and heavy duty due to the simplicity of the system and the ease of incorporation into the engine and its packaging. The gas is extracted before the turbine and is reinserted after the compressor, giving a fast response in transients. It happens that the pressure difference between the EGR inlet and outlet is not sufficient at some working points, being necessary to affect the position of the Variable-geometry turbocharger to achieve the required EGR. On the other hand, the so-called Low Pressure EGR (LP-EGR) has been under increasing study [20, 21, 22]. This technique obtains the EGR after the turbine and the DPF and reintroduces before the compressor. The pressure between the EGR line inlet and outlet is very similar, so an overpressure is generated in the exhaust line by a back pressure valve. This system is also composed with a cooler to reduce the temperature of the gas and a Three-way junction that will be especially important when mixing the EGR with cold air [23].

Regarding both configurations, the differences, advantages and disadvantages of using LP-EGR or HP-EGR respectively [20, 24] are shown. The main differ-

ence, as highlighted, is in the extraction area of the EGR and, consequently, of the air circulating through the turbine and compressor, producing in the case of LP-EGR a higher efficiency value of the turbocharger and with it an improvement in fuel consumption. Both systems generate soot deposition but the HP-EGR generates a higher concentration in the intake line [25].

The LP-EGR is more efficient than the HP-EGR in reducing NO_x emissions, mainly due to the higher recirculation potential that achieves a higher EGR rate and the lower temperature of the recirculated gas due to the use of the LP-EGR cooler and intercooler before the compressor. [19, 26, 27]. The HP-EGR has a quick response for transient operations due to the system closer to the cylinder with a short line compared to the LP-EGR [20, 21, 22] and on cold warm-ups increases the in-cylinder temperature. Another important aspect is the EGR distribution on each cylinder. The mixing of LP-EGR gases and fresh air occurs upstream of the compressor and away from the cylinders, which allows a more homogeneous distribution of exhaust gases inside the cylinders than the HP-EGR [28]. On the other hand, the HP-EGR system may not be able to evenly distribute the exhaust gases into the cylinders due to the closeness of the EGR discharge to the intake pipes. This phenomenon is responsible for non-uniform cylinder charging [29, 30, 31], which increases NO_x or PM emissions.

The main drawback of the LP-EGR line appears in cold operating conditions and in a warm-up. During these phenomena, condensation could appear due to cold temperatures below the dew point, in two different locations; first in the LP-EGR path, especially in the cooler due to low wall and coolant temperature during engine warm-up [2, 11, 32, 33]; second in the LP-EGR path when mixing the EGR gas with fresh air upstream of the compressor. If the condensation generated in the LP-EGR path is understood and mitigated, its use should be prioritized over that of the HP-EGR and even replaced, due to the improved engine performance of the operating map. Water produced due to condensation impacts on the compressor blades producing erosion when a blade rotates with water droplets in the environment. As can be seen in works like Castorrini et al. [34] in which erosion is studied in a wind-turbine while Koka et al. [35] and Serrano et al. [36] present erosion studies in a compressor wheel of a turbocharger when condensation occurs due to the LP-EGR cooler and the LP-EGR junction, obtaining a reduction of the lifetime drastically due to erosion.

This thesis shows special interest in the study of LP-EGR line in both transient and stationary conditions at the two places where the condensation appears: at the EGR junction and at LP-EGR cooler. In both places different techniques are developed and different studies are done to understand the condensation in the LP-EGR line to cope with impeller damage. The methodology and work presented in this thesis could be employed in different areas such as fuel cells where water vapor is produced by mixing oxygen and hydrogen [37, 38, 39], changing the phase to liquid state in turbine expansion or in hydrogen engines that need a large amount of EGR with a considerable percentage of water content in the exhaust gas due to the combustion process [40].

1.2 Background

Considering a complete vision of the phenomena studied in this work, in this section a bibliographic review of the state of the art is made, showing the most relevant works previously studied to initiate this research. The background section is divided into two subsections according to the condensation phenomena performed, condensation in heat exchangers and condensation in mixing junction following the Fig. 1.4. Figure Figure 1.5 presents the psychrometric chart of the two condensation phenomena in which water appears.

1.2.1 Condensation on heat exchangers

In the field of an internal combustion engine with cold coolant, there are different cases in which condensation occurs in the heat exchangers. These conditions are directly related to the gas flow conditions and the coolant conditions, as can be studied theoretically on a psychrometric chart. Figure 1.5 shows the process in which condensation appears in heat exchangers. The starting point being stage 1 under unsaturated conditions, the flow cools down in the heat exchanger until it reaches stage 2 (dew point) without condensing while when the gas cools down below this point, water appears until equilibrium conditions are obtained (stage 3). The difference in specific humidity between stages 1 and 3 is the theoretically condensed water.

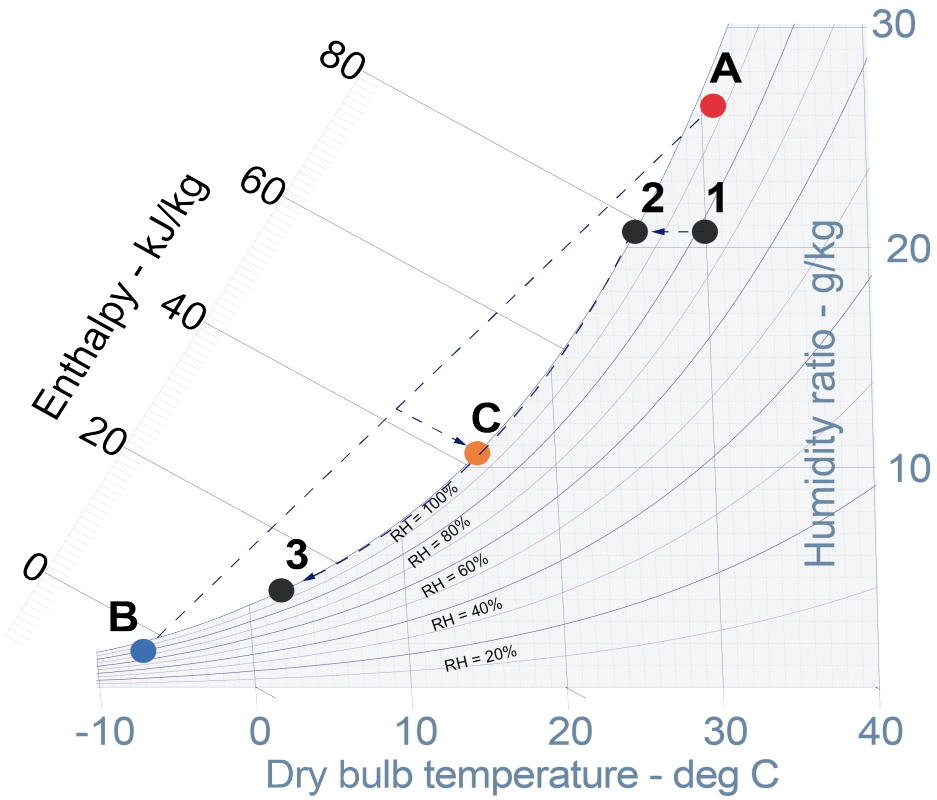

Figure 1.5: *Psychrometric diagram with the ideal evolution on a heat exchanger and on mixing-streams*

Focusing on the work performed in heat exchangers and, in particular, EGR coolers. Hoseini et al. [41] considered three different EGR coolers in terms of experimental and numerical investigation of heat transfer within the exchanger. Condensation in EGR coolers has been studied by Cuevas et al. [42], Abarham et al. [43], Garcia-Cascales et al. and Guao et al. [44] conducted experimental campaigns on heat exchangers of LP-EGR chillers to evaluate condensation at different operating points, but at steady-state conditions with a minimum refrigerant temperature of 20°C. Razmavar et al. [45, 46] studied the thermal performance and influence of secondary flows in EGR coolers. Warey et al. [47] provided a surface condensation model for the EGR cooler including hydrocarbons in the calculations but with a coolant temperature of the experiments higher than 30°C. Paz et al. [48, 49] conducted studies on fouling and hydrocarbon condensation in EGR coolers. In the framework of internal combustion engines, evaporation processes are very relevant. They can be found in the

injection system with the spray [50], in the spray-wall iterations [51]. However, condensation and evaporation appear in some situations, such as in Catalytic converters [52, 53, 54].

Galindo et al. [55] studied the inclusion of a bypass in the cooler under cold conditions to avoid the condensation phenomenon. Regarding the design of the EGR cooler tubes, Ghassembaglou et al. [56] studied different approaches in terms of the condensation produced. Finally, Song et al. [57] investigated the condensation produced in a diesel engine intercooler with 1D simulations by employing HP-EGR and LP-EGR.

1.2.2 Condensation on junctions

In the scope of an internal combustion engine, there is a source of condensation different from that of the heat exchanger. When the outlet temperature of a junction approaches in any area to the dew point, condensation may appear as can be seen in Figure 1.5. The starting points are stage A (hot flow with high humidity) and B (cold flow). The mixing between the two stages/branches of the junction generates saturation conditions and water condensation until stage C is reached.

As for the literature on three-way junctions, many of them studied the flow phenomena for 90° T-junctions but few of them studied condensation. Yang et al. [58], Li et al. [59] or like Lu et al. [60] studied the pressure drop due to the mixing process in a T-junction. Zhou et al. [61, 62] and Evrim et al. [63, 64] studied the thermal mixing in a T-junction by showing the experimental techniques used to characterize the behavior. Simulation studies with T-junctions have been carried out by Georgiou et al. [65] and Sakowitz et al. [66, 67, 68] analyzing turbulent mixing when two flows are mixed. There are works such as Reihani et al. [69, 70] that study the particular case of mixing in the LP-EGR path and identify the main flow parameters that cause significant degradation of compressor performance.

Special interest is given to works that study condensation when two streams are mixed. For example, several authors have determined that condensation is

related to mixing such as Galindo et al. [71, 72]. Also, Serrano et al. [73] proposed and developed a flow water condensation model for a 3D-CFD calculation when two streams are mixed and Galindo et al. [74] performed a comparison between durability tests and water condensation model results. But there was not a complete validation due to the difficulty of obtaining experimentally the water condensation in the flow. The work done by Galindo only compares whether the final impeller erosion was in agreement with the condensation value from the simulations. These works presented in this section by members of CMT Motores Térmicos, and being the group that has mostly worked in the area, are the basis for the current work of this Thesis.

Other works studying condensation due to the mixing process are those presented by Roth et al. [23], Zheng et al. [75] or Walker [76] trying to promote condensation in a mixer, Galindo et al. [71] demonstrate the reduce influence of the compressor on the mixing process by allowing the compressor to be eliminated while calculating the condensation produced at the LP-EGR junction.

Focusing on experimental techniques to characterize condensation in the LP-EGR path, some authors such as Wang et al. [77] proposed a H_2O absorption tomography to quantify the inlet water vapor in a diesel particulate filter. However, this technique provides the H_2O vapor mole fraction rather than the desired liquid water mass flow rate. As for the planar laser visualization (PLV) technique, Pastor et al. [78] and Xue et al. [79] studied the technique to obtain flow patterns for different purposes. As for particle image velocimetry (PIV), many authors such as Torregrosa et al. [80], Brucker et al. [81] and Espinoza et al. [82] performed studies to obtain secondary flows at the exit of the T-junction.

1.3 Main objectives

The study of the LP-EGR line in terms of water condensation involves different parts where water condensation could occur, each location needs to be addressed individually in terms of performance and conditions to properly understand the behavior. The main objectives described in this thesis are summarized as follows:

- Provide experimentally-validated models for the different condensation mechanisms in the LP-EGR line.

- Adapt these models to meet the computational requirements of engine modeling, so as to perform analysis on engine warm-ups.

- Provide guidelines for the trade-off between emissions and compressor damage due to condensation.

1.4 Approach and methodological objectives

To fulfill the promising objectives of the thesis, it is necessary to cover some steps during each chapter to ensure adequate conclusions and lead with the development, validation and experiments of the main objectives.

1.4.1 Condensation on heat exchangers

Following the main objectives, a study of condensation in heat exchangers will be carried out involving experimental and modeling work.

To complete the experimental approach, it will be necessary to develop a new test bench to provide a wide range of comparative cases covering different boundary conditions. Experimental tests will be carried out transiently by varying the coolant temperature and thus bringing the test closer to the actual heating of the engine. Condensation will be measured continuously once it leaves the EGR cooler.

In addition, these data will be the basis for a proper validation of the development 0D model of water condensation in heat exchangers to quantify water generation as a function of different boundary conditions.

1.4.2 Condensation on junctions

Focusing on the condensation generated at the junctions, different novel experimental techniques will be required to study, design and implement in the test bench covering the different issues at the outlet of the Three-way junction (condensation patterns, spatial quantification of water in the outlet section and flow velocity). The novel measurement techniques developed during the thesis to measure mixing condensation will be in line with achieving an in-depth characterization of the phenomenon and the estimation and quantification of patterns and condensation generated. The tests will be stationary to accurately measure each selected operating point.

The experimental test bench data will be the basis to quantitatively validate the 3D-CFD condensation submodel implemented by Serrano et al. [73] at the junctions.

1.4.3 Condensation application to engine modelling

A major challenge of the thesis will be the development of condensation calculation tools capable of being implemented in engine modeling software. To meet this challenge, it will be necessary to develop an order reduction model close to the solution of a 3D-CFD simulation but with reduced computational time. The first step will be to create a 0D perfect mixing condensation model for fast computation and then, correct with a surrogate model to resemble the more accurate solution realized by 3D-CFD. The second step will be to test different surrogate model approaches to obtain the best one for the phenomenon. The last step will be to implement the developed methodology with engine cycles simulations and calculate the condensation solution performing studies with different EGR strategies.

1.5 Thesis outline

Considering this introduction as the Chapter 1, the rest of the thesis is organized as follows:

The complete development of the test bench and validation of the water condensation heat exchanger model is described in chapter 2. First, the test bench development is presented focusing on the heat exchanger water condensation measurements. Then, the development and validation of a 0D condensation model to asses water condensation on heat exchangers is performed, focusing on a wide range of boundary conditions.

A description of the novel experimental techniques to measure different variables like velocity or water condensation on junctions are included in the Chapter 3. Then, it is presented the quantitative validation experimentally of a 3D-CFD submodel to assess junction condensation.

The reduce order model to simulate water condensation in junctions is detailed in chapter 4. First, a novel 0D perfect mixing condensation model including nozzle effects and evaporation process is described in detail. Then, a statistical methodology exploration is detailed, studying different surrogate models and design of experiments. Finishing with a proposed multi-fidelity method and the application of the methodology for the particular case of the Three-way junction water calculation.

Chapter 5 introduces a study applying the reduce order condensation model detailed in the previous chapter. The study is focused on the condensation generation implemented to engine modeling and how affects this condensation on compressor damage. With the methodology developed, a sensitivity analysis on condensation for ambient parameters and with different strategies of LP-EGR and HP-EGR is presented.

Finally, chapter 6 presents a concluding remarks of the thesis. This includes a summary of findings and contributions, the limitations and simplifications carried out and a suggestions for future works.

Chapter 1 References

[2] J. Galindo, R. Navarro, D. Tari, and F. Moya. "Development of an experimental test bench and a psychrometric model for assessing condensation on a Low Pressure EGR cooler". *International Journal of Engine Research*, (2020). DOI: 10.1177/1468087420909735 (cit. on pp. xi, 7, 27, 51).

[7] W. in data. URL: https://ourworldindata.org/ (cit. on pp. 2, 3).

[8] *European Automobile Manufacturers' Association's (ACEA). Brussels. The Automobile industry Pocket Guide*. 2018-2019. URL: https://www.acea.be/uploads/publications/ACEA_Pocket_Guide_2018-2019.pdf (cit. on pp. 3, 24).

[9] Volkswagen. URL: https://www.volkswagenag.com/presence/konzern/group-fleet/dokumente/wltp/GFI_WTLP_Broschuere_EN_WLTP_and_RDE_Insights_WEB.pdf (cit. on p. 4).

[10] *European Automobile Manufacturers Association Position Paper. Views on proposals for Euro 7 emission standard*. 2020. URL: https://www.acea.be/uploads/publications/ACEA_Position_Paper-Views_on_proposals_for_Euro_7_emission_standard.pdf (cit. on p. 4).

[11] M. Weilenmann, J.-Y. Faves, and R. Alvarez. "Cold-start emissions of modern passenger cars at different low ambient temperatures and their evolution over vehicle legislation categories". *Atmospheric Environment*, 43, (15 May 5, 2009), pp. 2419–2429. DOI: 10.1016/j.atmosenv.2009.02.005 (cit. on pp. 4, 7, 25).

[12] T. V. Johnson. "Review of Vehicular Emissions Trends". *SAE Int. J. Engines*, 8, (Apr. 2015), pp. 1152–1167. DOI: 10.4271/2015-01-0993 (cit. on p. 4).

[13] H. Chen and J. Yin. "Turbocharger compressor development for diesel passenger car applications". In: 8^{th} *International Conference on Turbochargers and Turbocharging*. IMechE. 2006 (cit. on p. 5).

[14] Y. B. Zeldovich. *The oxidation of nitrogen in combustion explosions*. 21. URSS: Acta Physicochimica, 1946, pp. 577–628 (cit. on p. 5).

[15] Y. B. Zeldovich. "The Oxidation of Nitrogen in Combustion andExplosions". *Selected Works of Yakov Borisovich Zeldovich, Volume I. Princeton University Press*, (2015). DOI: 10.1515/9781400862979.364 (cit. on p. 5).

[16] Petersen Publishing Company and E. Rosen. *The Petersen Automotive Troubleshooting & Repair Manual*. Grosset & Dunlap, 1975. ISBN: 9780448119465 (cit. on p. 5).

[17] C. Giorgio. Zamboni. Massimo. "Experimental study on the effects of HP and LP EGR in an automotive turbocharged diesel engine". *Applied Energy*, 94, (2012). DOI: 10.1016/j.apenergy.2012.01.046 (cit. on p. 5).

[18] J. M. Luján, H. Climent, R. Novella, and M. E. Rivas-Perea. "Influence of a low pressure EGR loop on a gasoline turbocharged direct injection engine". *Applied Thermal Engineering*, 89, (2015), pp. 432–443. DOI: 10.1016/j.applthermaleng.2015.06.039 (cit. on p. 5).

[19] M. Lapuerta, A. Ramos, D. Fernandez-Rodriguez, and I. Gonzalez-Garcia. "High-pressure versus low-pressure exhaust gas recirculation in a Euro 6 diesel engine with lean-NOx trap: Effectiveness to reduce NOx emission". *International Journal of Engine Research*, -, (Nov. 14, 2018), pp. 0–9. DOI: 10.1177/1468087418817447 (cit. on pp. 5, 7, 24, 151).

[20] J. M. Luján, C. Guardiola, B. Pla, and A. Reig. "Switching strategy between HP (high pressure)-and LPEGR (low pressure exhaust gas recirculation) systems for reduced fuel consumption and emissions". *Energy*, 90, (2015), pp. 1790–1798. DOI: 10.1016/j.energy.2015.06.138 (cit. on pp. 6, 7, 25, 140, 151).

[21] S. Moroz, G. Bourgoin, J. M. Luján, and B. Pla. "Acidic condensation in low pressure EGR systems using diesel and biodiesel fuels". *SAE Int. J. Fuels Lubr*, 2009-01-2805, (2009). DOI: 10.4271/2009-01-2805 (cit. on pp. 6, 7, 25).

[22] D. T. Hountalas, G. C. Mavropoulos, and K. B. Binder. "Effect of exhaust gas recirculation (EGR) temperature for various EGR rates on heavy duty DI diesel engine performance and emissions". *Energy*, 33 (2), (2008), pp. 272–283. DOI: 10.1016/j.energy.2007.07.002 (cit. on pp. 6, 7, 25).

[23] D. Roth, I. G. Tabares, and A. S. Álvarez. "Condensing LPL EGR Mixer with Mid-Pressure Loop". *SAE International Journal of Engines*, 8 (2015-01-1257), (2015), pp. 1544–1552 (cit. on pp. 6, 11).

[24] J. M. Desantes, J. M. Luján, B. Pla, and J. A. Soler. "On the combination of high-pressure and low-pressure exhaust gas recirculation loops for improved fuel economy and reduced emissions in high-speed direct-injection engines". *International Journal of Engine Research*, 14 (1), (2013), pp. 3–11. DOI: 10.1177/1468087412437623 (cit. on p. 6).

[25] L. Cornolti, A. Onorati, T. Cerri, G. Montenegro, and F. Piscaglia. "1D simulation of a turbocharged Diesel engine with comparison of short and long EGR route solutions". *Applied Energy*, 111, (2013), pp. 1–15. DOI: 10.1016/j.apenergy.2013.04.016 (cit. on pp. 7, 140).

[26] P. Michel, A. Charlet, G. Colin, Y. Chamaillard, G. Bloch, and C. Nouillant. "Optimizing fuel consumption and pollutant emissions of gasoline-HEV with catalytic converter". *Control Engineering Practice*, 61, (2017), pp. 198 –205. ISSN: 0967-0661. DOI: 10.1016/j.conengprac.2015.12.010 (cit. on pp. 7, 51).

[27] A. Maiboom, X. Tauzia, and J.-F. Hetet. "Influence of high rates of supplemental cooled EGR on NOx and PM emissions of an automotive HSDI diesel engine using an LP EGR loop". *International Journal of Energy Research*, 32 (15), (2008), pp. 1383–1398. DOI: 10.1002/er.1455 (cit. on p. 7).

[28] Galindo, J. and Serrano, J.R. and Navarro, R. and García Olivas, G. "Numerical modeling of centrifugal compressors with heterogeneous incoming flow due to low pressure exhaust gas recirculation". In: *Proceedings of ASME Turbo Expo 2020: Turbomachinery Technical Conference and Exposition*. GT2020-16030. American Society of Mechanical Engineers. 2020 (cit. on pp. 7, 73).

[29] A. Maiboom, X. Tauzia, and J.-F. Hétet. "Influence of EGR unequal distribution from cylinder to cylinder on NOx-PM trade-off of a HSDI automotive Diesel engine". *Applied Thermal Engineering*, 29 (10), (2009), pp. 2043 – 2050. ISSN: 1359-4311. DOI: 10.1016/j.applthermaleng.2008.10.017 (cit. on p. 7).

[30] A. Sakowitz, M. Mihaescu, and L. Fuchs. "Flow decomposition methods applied to the flow in an IC engine manifold". *Applied Thermal Engineering*, 65 (1–2), (2014), pp. 57–65. ISSN: 1359-4311. DOI: 10.1016/j.applthermaleng.2013.12.082 (cit. on p. 7).

[31] J. Galindo, H. Climent, R. Navarro, G. García-Olivas, S. Guilain, and R. Boubennec. *Effect of Numerical Configuration on Predicted EGR Cylinder-to-Cylinder Dispersion*. Tech. rep. SAE Technical Paper, 2020. DOI: 10.4271/2020-01-1113 (cit. on p. 7).

[32] J. Bishop, M. Stettler, N. Molden, and A. Boies. "Engine maps of fuel use and emissions from transient driving cycles". *Applied Energy*, 183, (Dec. 1, 2016), pp. 202–217. DOI: 10.1016/j.apenergy.2016.08.175 (cit. on pp. 7, 25).

[33] Z. Wei, X. Jinliang, and L. Guohua. "Multi-channel effect of condensation flow in a micro triple-channel condenser". *International Journal of Multiphase Flow*, 34, (12 Dec. 1, 2008), pp. 1175–1184. DOI: 10.1016/j.ijmultiphaseflow.2008.05.004 (cit. on pp. 7, 25).

[34] A. Castorrini, A. Corsini, F. Rispoli, P. Venturini, K. Takizawa, and T. E. Tezduyar. "Computational analysis of wind-turbine blade rain erosion". *Computers & Fluids*, 141 (Supplement C), (2016), pp. 175 –183. ISSN: 0045-7930. DOI: 10.1016/j.compfluid.2016.08.013 (cit. on pp. 7, 51).

[35] P. Z. John, T. Koka, and S. Dayalan. "Water droplet erosion simulation of a turbocharger compressor wheel". In: *ASME Turbo Expo 2014: Turbine Technical Conference and Exposition*. GT2014-26974. American Society of Mechanical Engineers. 2014 (cit. on pp. 7, 51).

[36] J. R. Serrano, P. Piqueras, E. Angiolini, C. Meano, and J. De La Morena. "On Cooler and Mixing Condensation Phenomena in the Long-Route Exhaust Gas Recirculation Line". In: *SAE Technical Paper*. 2015. DOI: 10.4271/2015-24-2521 (cit. on pp. 7, 31, 105, 108, 157, 185).

[37] Y. Zhang, S. Xu, and C. Lin. "Performance improvement of fuel cell systems based on turbine design and supercharging system matching". *Applied Thermal Engineering*, 180, (2020), pp. 1–11. DOI: 10.1016/j.applthermaleng.2020.115806 (cit. on p. 8).

[38] P. Chuang, M. Rahman, F. Mojica, D. Hussey, D. Jacobson, and J. LaManna. "The interactive effect of heat and mass transport on water condensation in the gas diffusion layer of a proton exchange membrane fuel cell". *Journal of Power Sources*, 480, (2020), pp. 1–10. DOI: 10.1016/j.jpowsour.2020.229121 (cit. on p. 8).

[39] T. Wittmann, S. Luck, C. Bode, and J. Friedrichs. "Modelling the Condensation Phenomena within the Radial Turbine of a Fuel Cell Turbocharger". *International Journal of Turbomachinery Propulsion and Power*, (2021). DOI: 10.3390/ijtpp6030023 (cit. on pp. 8, 189).

[40] X. Yu, Z. Guo, L. He, W. Dong, and P. Sun. "Experimental study on lean-burn characteristics of an SI engine with hydrogen/gasoline combined injection and EGR". *International Journal of Hydrogen Energy*, 44, (2019), pp. 1–10. DOI: 10.1016/j.ijhydene.2019.03.236 (cit. on p. 8).

[41] S. S. Hoseini, G. Najafi, and B. Ghobadia. "Experimental and numerical investigation of heat transfer and turbulent characteristics of a novel EGR cooler in diesel engine". *Applied Thermal Engineering*, 108, (2016), pp. 1344–1356. DOI: 10.1016/j.applthermaleng.2016.08.018 (cit. on pp. 9, 26).

[42] C. Cuevas, D. Makaire, and P. Ngendakumana. "Thermo-hydraulic characterization of an automotive intercooler for a low pressure EGR application". *Applied Thermal Engineering*, 31, (14-15 Apr. 19, 2011), pp. 2474–2484. DOI: 10.1016/j.applthermaleng.2011.04.013 (cit. on pp. 9, 25).

[43] M. Abarham, T. Chafekar, J. Hoard, D. Styles, and D. Assanis. "A visualization test setup for investigation of water-deposit interaction in a surrogate rectangular cooler exposed to diesel exhaust flow". *SAE Technical Paper*, 2012-01-0364, (2012). DOI: 10.4271/2012-01-0364 (cit. on pp. 9, 26).

[44] C. Guo, Q. Liu, B. Zheng, Y. You, and Y. Li. "Development of model based on condensation area ratio and effect on heat transfer capacity of indirect evaporative cooling". *Applied Thermal Engineering*, 164, (Jan. 5, 2020). DOI: 10.1016/j.applthermaleng.2019.114557 (cit. on pp. 9, 25).

[45] A. Razmavar, M. Malayeri, and M. Abd-Elhady. "Influence of secondary flow on the thermal performance of exhaust gas recirculation (EGR) coolers". *International Journal of Thermal Sciences*, (2021). DOI: 10.1016/j.ijthermalsci.2020.106720 (cit. on pp. 9, 26).

[46] A. R. Razmavar and M. R. Malayeri. "Thermal performance of a rectangular exhaust gas recirculation cooler subject to hydrocarbon and water vapor condensation". *International Journal of Thermal Sciences*, 143, (Sept. 1, 2019), pp. 1–13. DOI: 10.1016/j.ijthermalsci.2019.05.006 (cit. on pp. 9, 26).

[47] A. Warey, D. Long, S. Balestrino, and P. Szymkowcz. "Visualization and Analysis of Condensation in Exhaust Gas Recirculation Coolers". In: *SAE International Paper*. Aug. 4, 2013. DOI: 10.4271/2013-01-0540 (cit. on pp. 9, 25).

[48] C. Paz, E. Suarez, J. Vence, and A. Cabarcos. "Numerical modelling of fouling process in EGR system: A review". *Environmental Issues and Sustainable Development*, (2020). DOI: 10.5772/intechopen.93062 (cit. on pp. 9, 26).

[49] C. Paz, E. Suarez, J. Vence, and J. Hoard. "Evolution of EGR cooler deposits under hydrocarbon condensation: Analysis of local thickness, roughness, and fouling layer density". *International Journal of Thermal Sciences*, (2021). DOI: 10.1016/j.ijthermalsci.2020.106744 (cit. on pp. 9, 26).

[50] A. Pandal, J. M. Garcia-Oliver, and J. M. Pastor. "Eulerian CFD modeling of nozzle geometry effects on ECN Sprays A and D: Assessment and analysis". *IJER*, 21, (2019), pp. 73–88. DOI: 10.1177/1468087419882500 (cit. on p. 10).

[51] R. Payri, G. Bracho, P. Marti-Aldaravi, and J. Marco-Gimeno. "Analysis of spray/wall impingement using an ECN single-hole injector and a controlled-temperature wall under realistic engine conditions". *Applied Thermal Engineering*, 208, (2022), pp. 118–167. DOI: 10.1016/j.applthermaleng.2022.118167 (cit. on p. 10).

[52] G. Montenegro and A. Onorati. "1D Thermo-Fluid Dynamic Modeling of Reacting Flows inside Three-Way Catalytic Converters". In: 2009, pp. 1444–1459 (cit. on p. 10).

[53] R. J. Clarkson and S. F. Benjamin. "Modelling the Effect of Moisture on Catalyst Warm-up". In: 1995, pp. 555–562 (cit. on p. 10).

[54] R. Payri, G. Bracho, P. Marti-Aldaravi, and J. Marco-Gimeno. "Numerical Analysis of Urea to Ammonia Conversion in Automotive Selective Catalytic Reduction Realistic Conditions". *Ind. Eng. Chem. Res.*, 60, (2021), pp. 14329–14340. DOI: 10.1021/acs.iecr.1c02627 (cit. on p. 10).

[55] J. Galindo, V. Dolz, J. Monsalve-Serrano, M. Maldonado, and L. Odillard. "Advantages of using a cooler bypass in the low-pressurre exhaust gas recirculation line of a compression ignition diesel engine operating at cold conditions". *Internal Journal of Engine Research*, (Apr. 29, 2020). DOI: 10.1177/1468087420914725 (cit. on pp. 10, 25, 51, 140).

[56] N. Ghassembaglou and L. Torkaman. "Efficient design of exhaust gas cooler in cold EGR equipped diesel engine". *Alexandria Engineering Journal*, 55, (2016), pp. 769–778. DOI: 10.1016/j.aej.2016.01.023 (cit. on pp. 10, 25).

[57] H. Song and S. Song. "Numerical investigation on a dual loop EGR optimization of a light duty diesel engine based on water condensation analysis". *Applied Thermal Engineering*, 182, (2021), pp. 1–12. DOI: 10.1016/j.applthermaleng.2020.116064 (cit. on pp. 10, 25, 151).

[58] B. Yang, W. Su, S. Deng, and L. Zhao. "State-of-art of branching T-junction: Experiments, modeling, developing prospects and applications". *Experimental Thermal and Fluid Sciences*, 109, (2019). DOI: 10.1016/j.expthermflusci.2019.109895 (cit. on pp. 10, 51).

[59] H. Li, G. Wei, Y. Wang, D. Yang, B. Sun, and W. Hong. "Investigation on the phase split characteristics of slug and annular flow in a metal foam-filled T-junction". *Experimental Thermal and Fluid Science*, 109 (109878), (Dec. 1, 2019). DOI: 10.1016/j.expthermflusci.2019.109878 (cit. on p. 10).

[60] P. Lu, S. Deng, L. Zhao, Y. Zhao, W. Xu, and Y. Zhang. "Analysis of pressure drop in T-junction and its effect on thermodynamic cycle efficiency". *Applied Energy*, 231, (2018), pp. 1–13. DOI: 10.1016/j.apenergy.2018.09.134 (cit. on p. 10).

[61] M. Zhou, R. Kulenovic, and E. Laurien. "Advanced flow pattern for describing tangential flow oscillation in thermal-mixing pipe flow at a horizontal T-Junction". *International Journal of Thermal Sciences*, 136, (Feb. 1, 2019), pp. 328–336. DOI: 10.1016/j.ijthermalsci.2018.10.045 (cit. on pp. 10, 51).

[62] M. Zhou, R. Kulenovic, and E. Laurien. "T-junction experiments to investigate thermal-mixing pipe flow with combined measurement techniques". *Applied Thermal Engineering*, 150, (Mar. 5, 2019), pp. 237–249. DOI: 10.1016/j.applthermaleng.2018.12.161 (cit. on pp. 10, 51).

[63] C. Evrim, X. Chu, and E. Laurien. "Analysis of thermal mixing characteristics in different T-junction configurations". *International Journal of Heat and Mass Transfer*, 158, (2020), pp. 1–10. DOI: 10.1016/j.ijheatmasstransfer.2020.120019 (cit. on pp. 10, 51).

[64] C. Evrim and E. Laurien. "Numerical study of thermal mixing mechanisms in T-junctions". *Applied Thermal Engineering*, 138, (2021), pp. 1–13. DOI: 10.1016/j.applthermaleng.2020.116155 (cit. on pp. 10, 51).

[65] M. Georgiou and M. V. Papalexandris. "Turbulent mixing in T-junctions: The role of the temperature as an active scalar". *International Journal of Heat and Mass Transfer*, 115, (2017), pp. 793–809. DOI: 10.1016/j.ijheatmasstransfer.2017.08.081 (cit. on pp. 10, 52).

[66] A. Sakowitz, M. Mihaescu, and L. Fuchs. "Turbulent flow mechanisms in mixing T-junctions by Large Eddy Simulations". *International Journal of Heat and Fluid Flow*, 45, (2014), pp. 135–146. DOI: 10.1016/j.ijheatfluidflow.2013.06.014 (cit. on pp. 10, 52, 78, 80).

[67] A. Sakowitz, S. Reifarth, M. Mihaescu, and L. Fuchs. "Modeling of EGR Mixing in an engine intake manifold using LES". *Oil & Gas Science and Technology*, 69 (1), (2014), pp. 167–176. DOI: 10.2516/ogst/2013118 (cit. on p. 10).

[68] A. Sakowitz, M. Mihaescu, and L. Fuchs. "Effects of velocity ratio and inflow pulsations on the flow in a T-junction by Large Eddy Simulation". *Computers & Fluids*, 88, (2013), pp. 374–385. ISSN: 0045-7930. DOI: 10.1016/j.compfluid.2013.10.001 (cit. on p. 10).

[69] A. Reihani, J. Hoard, S. Klinkert, C.-K. Kuan, and D. Styles. "Numerical Evaluation of the Effects of Low Pressure EGR Mixer Configuration on Turbocharger Compressor Performance". In: *ASME 2018 Internal Combustion Engine Division Fall Technical Conference*. American Society of Mechanical Engineers Digital Collection. 2018 (cit. on p. 10).

[70] A. Reihani, J. Hoard, S. Klinkert, C.-K. Kuan, D. Styles, and G. McConville. "Experimental response surface study of the effects of low-pressure exhaust gas recirculation mixing on turbocharger compressor performance". *Applied Energy*, 261, (2020), p. 114349. DOI: 10.1016/j.apenergy.2019.114349 (cit. on pp. 10, 104).

[71] J. Galindo, R. Navarro, D. Tarí, and G. García-Olivas. "Centrifugal compressor influence on condensation due to Long Route-Exhaust Gas Recirculation mixing". *Applied Thermal Engineering*, 144, (2018), pp. 901 –909. ISSN: 1359-4311. DOI: 10.1016/j.applthermaleng.2018.09.005 (cit. on pp. 11, 51, 52, 69, 70, 77, 82, 107).

[72] J. Galindo, A. Gil, R. Navarro, and G. García-Olivas. "Numerical assessment of humid air streams in three-way junctions and impact on volume condensation". *Applied Thermal Engineering*, (2022). DOI: 10.1016/j.applthermaleng.2021.117676 (cit. on pp. 11, 115).

[73] J. Serrano, P. Piqueras, R. Navarro, D. Tarí, and C. Meano. "Development and verification of an in-flow water condensation model for 3D-CFD simulations of humid air streams mixing". *Computers & Fluids*, 167, (2018), pp. 158 –165. ISSN: 0045-7930. DOI: 10.1016/j.compfluid.2018.02.032 (cit. on pp. 11, 13, 25, 51, 53, 66, 95, 105, 107, 153, 183, 184).

[74] J. Galindo, P. Piqueras, R. Navarro, D. Tarí, and C. Meano. "Validation and sensitivity analysis of an in-flow water condensation model for 3D-CFD simulations of humid air streams mixing". *International Journal of Thermal Sciences*, 136, (2019), pp. 410 –419. ISSN: 1290-0729. DOI: 10.1016/j.ijthermalsci.2018.10.043 (cit. on pp. 11, 25, 51, 68, 69, 73, 74, 107, 135, 153, 161, 175, 184).

[75] N. Zheng, L. Zhao, and J. Wei. "Experimental research on liquid-vapor two-phase flow separation of zeotropic mixtures at an impacting T-junction". *Experimental Thermal and Fluid Science*, 89, (2017), pp. 140–152. DOI: 10.1016/j.expthermflusci.2017.08.012 (cit. on p. 11).

[76] C Walker, M Simiano, R. Zboray, and H.-M. Prasser. "Investigations on mixing phenomena in single-phase flow in a T-junction geometry". *Nuclear Engineering and Design*, 239 (1), (2009), pp. 116–126. DOI: 10.1016/j.nucengdes.2008.09.003 (cit. on p. 11).

[77] Z. Wang, S. Sanders, J. A. Backhaus, A. Munnannur, and N. M. Schmidt. "H2O absorption tomography in a diesel aftertreatment system using a polymer film for optical access". *Applied Physic B*, 127, (286 2017). DOI: 10.1007/s00340-017-6867-8 (cit. on pp. 11, 52).

[78] J. V. Pastor, J. J. Lopez, J. E. Julia, and J. V. Benajes. "Planar Laser-Induced Fluorescence fuel concentration measurements in isothermal Diesel sparys". *Optical Society of America*, 10, (7 2002). DOI: 10.1364/OE.10.000309 (cit. on pp. 11, 60).

[79] T. Xue and S. Zhang. "Investigation on heat transfer characteristics of falling liquid film by planar laser-induced fluorescence". *International Journal of Heat and Mass Transfer*, 126, (2018), pp. 715–724. DOI: 10.1016/j.ijheatmasstransfer.2018.05.039 (cit. on pp. 11, 52).

[80] A.J.Torregrosa, A.Broatch, J.V.Pastor, and J.García-Tíscar. "Measuring turbocharger compressor inlet backflow through particle image velocimetry". *Experimental Thermal and Fluid Science*, 99, (2018), pp. 420–432. DOI: 10.1016/j.expthermflusci.2018.08.015 (cit. on pp. 11, 55, 56).

[81] C. Brucker. "Study of the three-dimensional flow in a T-junction using a dual-scanning method for three-dimensional scanning-particle-image velocimetry (3-D SPIV)". *Experimental Thermal and Fluid Science*, 14 (1), (1997), pp. 35–44. DOI: 10.1016/S0894-1777(96)00110-0 (cit. on pp. 11, 52).

[82] C. Espinoza, M. Simmons, F. Alberini, O. Mihailova, D. Rothman, and A. Kowalski. "Flow studies in an in-line Silverson 150/250 high shear mixer using PIV". *Chemical Engineering Research and Design*, (2018). ISSN: 0263-8762. DOI: 10.1016/j.cherd.2018.01.028 (cit. on pp. 11, 52).

Chapter 2

Condensation on a Low-Pressure EGR cooler

Contents

2.1 Introduction

Light-duty vehicles play an important role in modern societies [83], improving the mobility of people and goods [84]. As a result, the vehicle fleet has increased significantly during the last decades, generating or increasing issues which were not a concern some time ago, including the pollution produced by the manufacturing process and usage of internal combustion engines (ICE) [85]. With a production of 98.9 million units (European Automobile Manufacturers Association (ACEA) [8]) only in 2017, any improvement in the reduction of ICE emissions would became a positive contribution to the world.

Pollution regulations are steadily becoming more restrictive, as already said in Chapter 1. It is widely known that the Worldwide harmonized Light vehicles Test Cycle (WLTC) [86] will consider low and realistic winter temperatures as boundary conditions [87]. Under these conditions, pollutant emissions are mainly emitted during the warm-up of the engine [88, 89].

Emissions reduction technologies are divided into active (in-cylinder) or passive (aftertreatment control measurements) [90]. In-cylinder control systems functioning is based in the reduction of pollutants within the source. This chapter is focused on using EGR as an emission reduction technique [19]. As it was discussed previously, the EGR technique consists in recirculating a portion of the exhaust gases back to the engine cylinders mixed with fresh air, which dilutes the concentration of O_2 and provides inert gases to the combustion process.

As presented in Chapter 1, considering a turbocharged engine, two possible paths of EGR are available, depending on location of extraction and reintegration of the exhaust gases. The most commonly used technique (as in 2020) is the so-called High-Pressure EGR (HP-EGR) which connects the exhaust and the intake manifolds. The other path available is the Low-Pressure EGR (LP-EGR), which consists in taking the exhaust gases downstream the aftertreatment and reintroducing them before the compressor.

LP-EGR presents several advantages over HP-EGR and it is the reason to focus this thesis on a deeply study the impact of the LP-EGR. Some authors like Lapuerta et al. [19] concluded that LP-EGR is more efficient than HP-EGR to re-

duce NOx emissions, mainly due to the higher recirculation potential and the lower temperature of the recirculated gas; for this reason, the LP-EGR has attracted much research in the last years [20, 21, 22].

To cope with the pollution issue, an early activation of the LP-EGR system during the engine warm-up could be a solution in order to fulfill the emission regulations at those boundary conditions. However, a drawback appears when using a LP-EGR at low engine temperatures. Water condensation may be produced in two different localizations; first in the LP-EGR path, specially in the cooler due to the low temperature of the walls and the coolant during the warm-up of the engine [11, 32, 33]. In addition, it can be found in the mixing region between fresh air and EGR gas, due to its high water content [73, 74]. Water droplets can produce an important damage to the compressor impeller, severely reducing its durability. In other research fields such as steam jets [91, 92] or nozzles [93], water condensation is also a problem.

Authors such as (Noori [94], Murphy [95] or Vasyliv [96]) have studied the phenomena of in-flow condensation, but with another gases (propane or steam) instead of most air. Regarding the condensation in EGR coolers, Warey et al. [47] proposed a surface condensation model to evaluate how affects the different hydrocarbons in the water condensation generation without considering low temperatures, the lowest coolant temperature of the experiments is higher than 30°C. Whereas Cuevas et al. [42] conducted an experimental campaign on LP-EGR cooler to assess condensation, but in steady conditions. In terms of condensation models, Guo et al. [44] developed a mathematical approach to obtain a condensation area ratio on the heat exchanger area walls or Ghassembaglou at al. [56] that studied different approaches in terms of the condensation produced and developed a comparison between different EGR cooler technologies. Also, Song et al. [57] investigated the condensation produced in a diesel engine intercooler with 1D simulations by employing HP-EGR and LP-EGR and only obtaining the condensation generation on the charge-air-cooler.

While employing LP-EGR and also reducing water condensation on the line, Galindo et al. [55] studied the possibility of bypassing the LP-EGR cooler during engine cold starts. The results show that the activation of the bypass led to a reduction in the warm-up time and thus a decrease of CO emissions compared to the case without cooler bypass. Besides, the period where condensation is

produced is greatly reduced, so the issue discussed in this chapter could be diminished at the expense of an increase of production cost, control complexity and packaging constraints. Focusing on the parameters that affects directly the condensation on EGR coolers are the wall temperature distribution and the heat transfer efficiency. As for example Hoseini et al. [41] considered three different EGR coolers technologies and assessed by experiments and simulations a comparison between designs.

Due to the employment of LP-EGR cooler, fouling appears as an important issue as it is shown by Paz et al. [48, 49] proposed numerical models in order to estimate and predict the deposit formation and growth, obtaining that the thickness of the fouling layer decreased in regions near the outlet section. Also, Abarham et al. [43] and Razmavar [45, 46] studied the effect of water condensation on the fouling deposition formation and how affects into the EGR cooler efficiency

The aim of this chapter is to assess the implications of using the LP-EGR system during the warm-up of an automotive cycle, in terms of condensation in the LP-EGR cooler. The first novelty of this chapter is the development of an experimental test bench to quantify the condensation on a heat exchanger, while other authors such as Luján et al. [97] only were able to study the condensation in a qualitative way. The advantages and the limitations of the test rig will be addressed as well. The analysis of water generation covers the operating range of a C-segment passenger car into the future taking into account regulations, in which, an early activation of the LP-EGR will be required. Finally, a development of a simple mean value condensation model is shown based on a psychrometric analysis. During the development of this chapter, the LP-EGR cooler performance was evaluated under transient conditions to emulate the thermal inertia and the warm-up of the engine coolant of the engine. In sequence, a weighing scale was added after the LP-EGR cooler to quantify the evolution of the water generation. At last, a detailed analysis of the tests and the comparison with the model was performed to assess the impact of using a LP-EGR system during the cold conditions of an early activation.

This chapter is organized as follows. First, the experimental apparatus and an explanation of the developed experimental test bench is showed in Section 2.2. After, in Section 2.3 it is proceeded with the development and validation for the

0D condensation model with experimental data. This validation is made with an approximation of a real WLTC cycle for different working points and for a given LP-EGR cooler. Finally, some concluding remarks will be provided in Section 2.4.

2.2 Experimental apparatus

In order to assess the condensation produced in the LP-EGR cooler, a continuous flow test rig has been used to replicate engine exhaust conditions, reducing, thus, the complexity of an actual Internal Combustion Engine (ICE) test bench. In this way, humid air will be used instead of exhaust gases with unburned hydrocarbons, particles matter. The difference related with the condensation produced between using an ICE or a flow test rig is low, as assessed in [2] with a deviation between 1-4% in terms of accumulated water. The flow test rig layout is depicted in Fig. 2.1.

As will be presented in Section 2.3.2, with this arrangement it is possible to reproduce the transient operating range of a LP-EGR cooler during an engine warm-up and also to arrive to any operative point of a wide range of common steady operating points from both medium and light duty ICEs.

At the core of the rig, there is an Atlas Copco ZE 3C-300-5E VSD volumetric screw compressor (between stations 1 to 2 of Fig 2.1), which is able to provide up to 720 kg/h of mass flow and a maximum pressure of 4 bars. This compressor is connected to five heaters (Watlow, 9 kW each) (between stations 2 to 3) to increase the flow temperature to 400 °C, in order to guarantee a complete evaporation of the water injected downstream. A counter-pressure valve controls the mass flow rate circulating through the flow test rig.

Because of the high flow temperature and the water content, it is complex to measure the mass flow rate. For this reason, it was decided to employ a calibrated orifice (Fig. 2.2). The mass flow meter described in Table 3.1 was previously employed to characterize the relation between pressure drop and MFR of the orifice. Equation 2.2 shows how the target EGR humid MFR is calculated to be imposed in the calibrated orifice. This target depends on the desired MFR, the

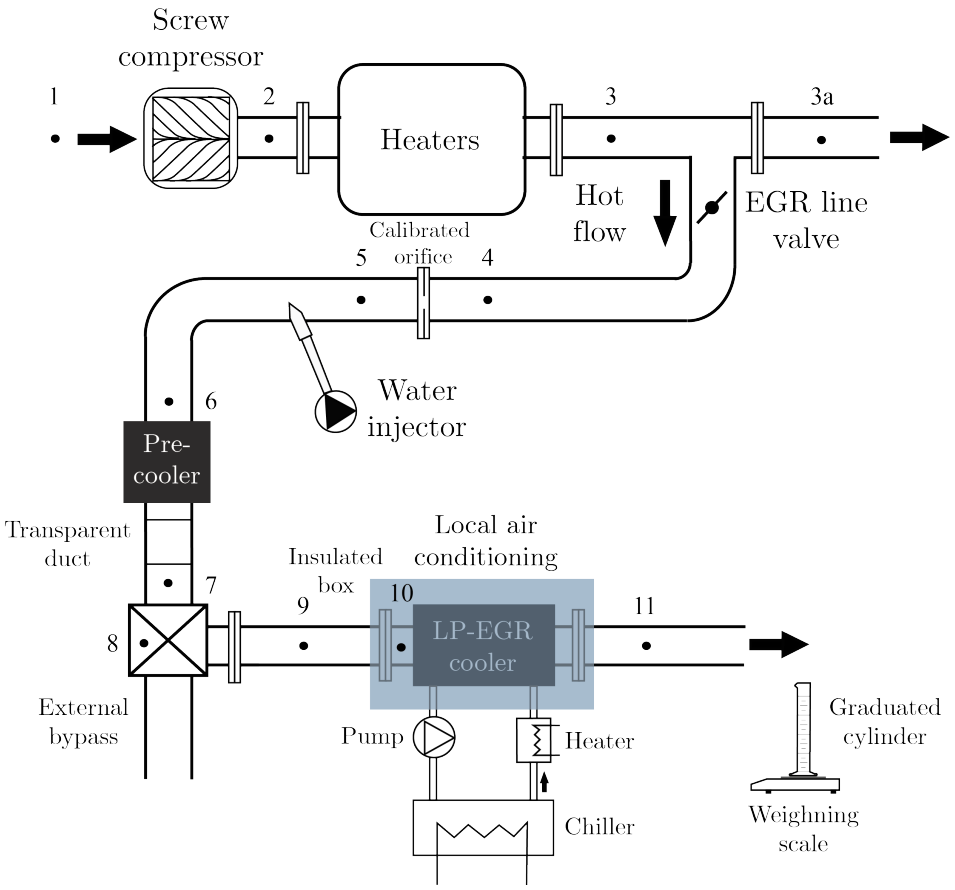

Figure 2.1: *Scheme of the LP-EGR cooler condensation test rig with the stations.*

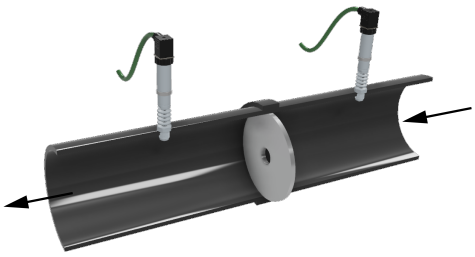

Figure 2.2: *Calibrated orifice.*

ambient conditions, and the specific humidity (w) of the EGR gas.

$$\dot{m}_{orif} = \dot{m}_{EGR} \cdot \frac{1 - w_{EGR}}{1 - w_{amb}} \tag{2.1}$$

$$\dot{m}_{inj} = \dot{m}_{EGR} \cdot \frac{w_{EGR} - w_{amb}}{1 - w_{amb}} \tag{2.2}$$

After the orifice, a *Bosch AdBlue dosing module denoxtronic 2.1 injector* is placed, which adds the desired water content. An arduino board [98] controls the injection rate using a pulse-width modulation (PWM) signal. The operating range of the injector is between 0 and 3 l/h, which limits the maximum specific humidity that can be set. A further constraint over EGR humidity is the maximum quantity of water that the flow is able to evaporate (dependent of the MFR). In order to make sure the evaporation of the water content occurs, 3 extra meters of pipe are installed between the injector and the next element. A calibration of the injector is performed which correlates the water injection rate with the duration pulse lengths of the PWM signal in order to be able to set the exact water quantity at the tests. Then, a weighing scale is set in the water reservoir to measure and double-check the water injection. Next, a pre-cooler is installed to control the temperature of the flow required for each specific test. In order to check that the flow is not condensing in the pre-cooler, a transparent duct is installed on its outlet to visualize the presence of liquid water. Between points 7 and 9 of Fig. 2.1, a bypass is mounted in order to allow a proper settling of the flow temperature when the target cooler is placed in the insulated box, prior to start measuring.

Table 2.1: *Instrumentation accuracy*[1]

Sensor	Model	Accuracy [%]	Range
Thermocouples	Thermocouple K-type	1	-260–1260 °C
Pressure sensor	Piezoresistive KISTLER	0.3	0–6 bar
Flow meter	ABB SENSYCON	1	0–50 kg/h
Weighting scale inject.	Balance AND GX-20K	0.1	0–20 kg
Weighting scale cond.	Balance AND EK-300i	0.001	0–0.3 kg

[1] According to datasheets

This insulated box features a local air conditioning as shown in Fig. 2.3. Inside the box, there are the following elements: a radiator with a fan in order to set a cold ambient in the box and the target LP-EGR cooler, both connected through the coolant line. This coolant line is connected to a heater, a chiller and a pump.

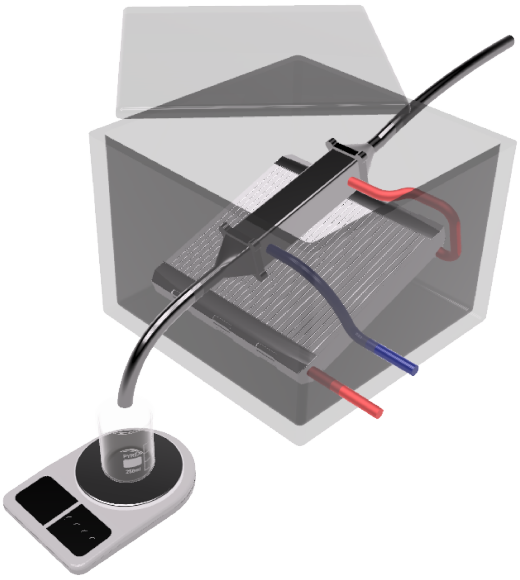

Figure 2.3: *Local air conditioning.*

The chiller is an Euroklimat M10 MICRO with 3.75 kW of nominal cooling capacity. Inside the chiller, there is a pump that moves coolant (ethylene glycol 30 % - water 70 %) in the coolant circuit through the LP-EGR cooler, the radiator, the heater and the chiller. Finally, in order to simulate warm-up conditions, a 5 kW heater is set in the coolant line to obtain an approximation of the WLTC coolant temperature profile, which will control the condensation produced in the LP-EGR line. At the beginning of the test, once all parameters are stabilized, the bypass valve is closed and the flow is redirected towards the cooler in the insulated box. Then, the chiller is switched off and the heater switched on. The outlet of the LP-EGR discharges on a reservoir which collects the fraction of condensed water travelling as large droplets, not being able to collect the tiny droplets existing as fog inside the stream. In any case, the fog generates less damage if arriving to the compressor. The condensed water is measured using a weighing scale connected with a data acquisition system, as can be seen in Fig. 2.3.

Piezoresistive pressure sensors are mounted along the different ducts of the rig. Their specifications are noted in Table 3.1. For the temperature sensors, K-type thermocouples are used. The two different weighing scales employed in the test rig, one for obtain the condensation produce in the cooler and the other to check the correct functioning of the injector, are shown as well in Table 3.1.

Table 2.2 shows the operating range of the flow test rig with the current setup, being mainly constrained by the ability of the EGR stream to fully evaporate the spray of injected water.

Table 2.2: Flow test rig - operating range

EGR Temperature[1]	40–180 °C
EGR flow	10–50 kg/h
Specific Humidity	0–65 g/kg
Coolant temperature	-15–60 °C
Local air conditioning	-15–60 °C

[1] Temperature at the pos. 8 of the test rig.

2.3 Development and validation of 0D model to assess cooler condensation

2.3.1 0D Condensation model in LP-EGR cooler

The simple condensation model proposed in this work does not take into account the local wall temperature in the LP-EGR cooler, the cooler capacity to retain water inside, which delays condensation appearance at the cooler outlet, the partial evaporation and the possible icing generation.

Condensation in the LP-EGR cooler is an undesired phenomenon. Water droplets appear whenever the local gas temperature is below dew temperature. If these droplets are dragged by the EGR flow, the compressor impeller may be damaged [36]. Condensation depends on the gas temperature at the cooler outlet, the heat exchange across the cooler and the dew point of the LP-EGR flow. More in detail, the dew temperature depends on the specific humidity and, to a lesser degree, on the gas pressure. In Eq. 2.3, Serrano et al. [36] defined a correlation of the dew temperature with the RH and the temperature.

$$T_{dew} = \sqrt[8]{\frac{RH}{100}} \cdot (112 + 0.9 \cdot T) + (0.1 \cdot T) - 112 \tag{2.3}$$

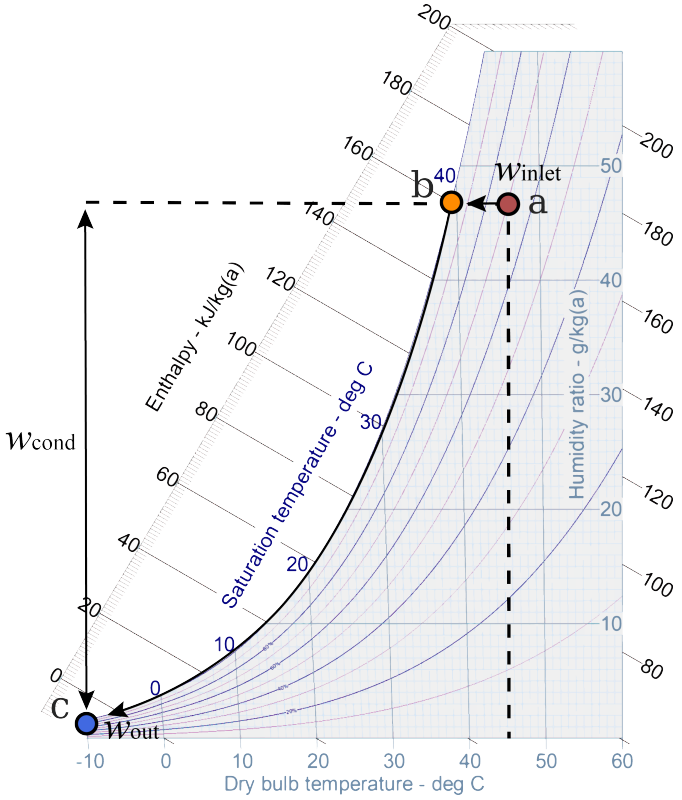

Figure 2.4: *Psychrometric diagram with the ideal evolution between points a to c.*

Figure 2.4 shows a particular moisture air psychometric diagram of the Fig. 1.5 focused on the condensation on EGR coolers, in which the inlet and outlet conditions for a given point (T_{inlet}=45 °C, T_{out}=-10 °C, w_{inlet}=46 g/kg) have been represented. Point (a) is cooled down until saturated conditions (b). Then, cooling continues and the point follows the curve RH=100% defined by Eqs. 2.4, 2.5, 2.6 until it achieves the outlet temperature (c).

$$p_{vap} = \frac{p_{gas}}{1 + 1000 \dfrac{MW_{H2O}}{w_i \cdot MW_{dryair}}} \tag{2.4}$$

$$p_{sat} = 10^{4.6543 - \dfrac{1435.264}{T_{gas} + 273.15 - 64.848}} \tag{2.5}$$

$$RH = \frac{p_{vap}}{p_{sat}} \cdot 100 \tag{2.6}$$

The model only considers the cooler outlet temperature of each time step for the water condensation prediction. The estimation of the humidity that has condensed (Eq. 5.1) at each time step (same as sampling time), being w_i the saturation specific humidity at each time step, is given by:

$$w_{cond}(t) = \frac{w_{EGR}(t) - w_i(t)}{1 + \frac{w_{EGR}(t)}{1000}} \tag{2.7}$$

$$\dot{m}_{cond} = w_{cond} \cdot \dot{m}_{dryair} \tag{2.8}$$

$$m_{cond}(warm - up//test) = \int_0^{T_{test}} \dot{m}_{cond} \cdot dt \tag{2.9}$$

The Equations 5.2 and 2.9 are used to calculate the accumulation of condensed water since the beginning of the test. As aforementioned, the wall temperature in the LP-EGR cooler which could be locally below the gas outlet temperature, is not taken into account due to the 0D approximation. The cooler capacity to retain water inside is not considered due to the geometrical complexity of each specific design, then neglecting the delays produced by the soak capacity of the cooler that presents some of the condensates to come out of the cooler. Other phase change phenomena are not considered either, such as evaporation and icing.

2.3.2 Operating conditions

As it is mentioned in the introduction, the purpose of the work performed is to assess the impact of the condensation generation during the warm-up, considering the WLTC cycle as a reference to obtain the boundary conditions.

Figure 2.5 shows the specific humidity during the first 10 minutes of a WLTC cycle comparing with the EGR mass flow rate that is being introduced on a diesel

engine for a C-segment passenger car (1.6 L) and the speed of the WLTC cycle. The specific humidity is calculated with the Air-Fuel ratio knowing surrogate C_8H_{15}. Knowing these values and considering the operating range capabilities of the test rig showed in the Table 2.2, a test matrix is able to be defined in a way that covers a wide range of common operating conditions for a low and medium loads, being specified in Table 2.3. In Section 5.3, the proposed test matrix will be processed to assess the produced condensation. Only the initial stage of a WLTC cycle was analyzed since the coolant temperature being under the dew point. For the current test, a specific humidity of 46 g/kg is selected as a characteristic and conservative value (dashed black line at Fig. 2.5).

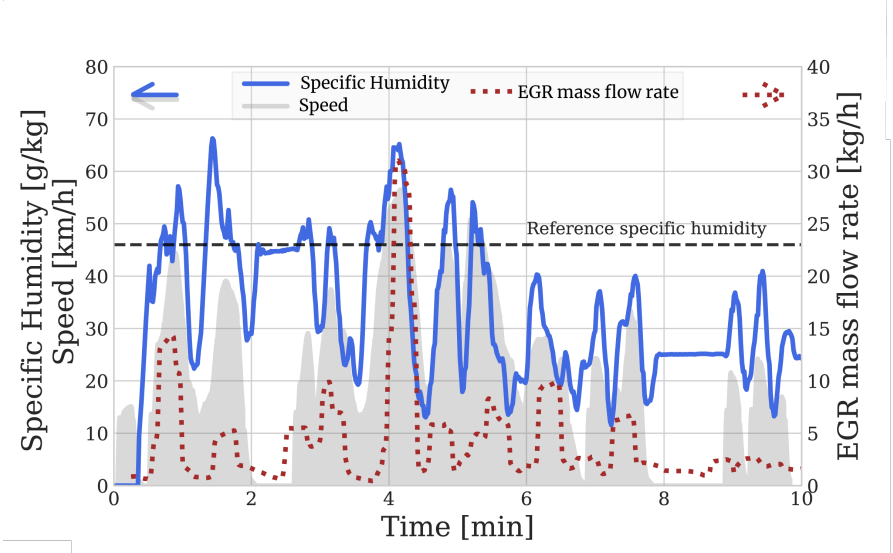

Figure 2.5: *The evolution in time during the WLTC cycle of the specific humidity vs EGR mass flow rate compared with speed.*

Concerning the initial coolant temperature, three values are selected: -10, -2.5 and 5 °C (Table 2.3). Figure 2.6 shows the coolant temperature evolution of the warm-up tests with a 5kW heater, compared with the coolant temperature evolution of a WLTC cycle. The test with the coldest initial temperature (-10 °C) takes near 10 minutes to reach the dew temperature (≈ 40 °C) like in the engine WLTC cycle. Condensation in the LP-EGR cooler is only produced during this period.

Taking into account the results observed at Fig. 2.5, three different mass flow rates are selected: 10, 20 and 40 kg/h (Table 2.3). A higher value than the one

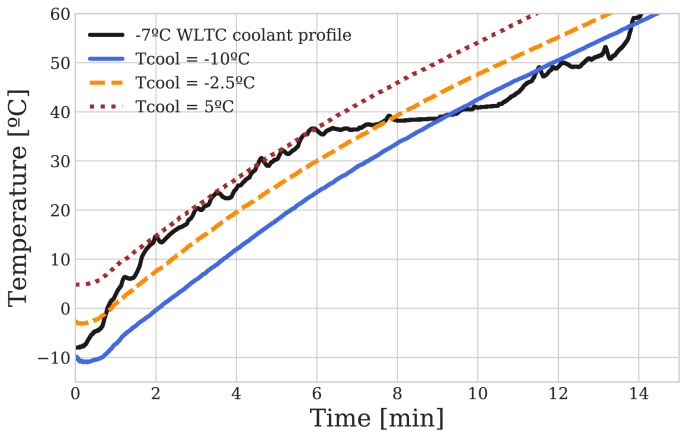

Figure 2.6: *Different coolant temperature evolution during the WLTC cycle using a 5 kW heater compared with an engine coolant evolution.*

shown in Fig.2.5 (40 kg/h) has been selected considering a future increase of EGR rate, to be able to anticipate futures tightening of the emission requirements.

Finally, in order to cover different EGR temperatures at the inlet of the LP-EGR cooler, four different values are selected (Table 2.3): 45, 70, 90 and 150 °C. These EGR temperature values have been measured during the tests (Position 7 in Fig. 2.1).

Table 2.3: *Operating points*

EGR Temperature[1]	45, 70, 90 and 150 °C
EGR flow	10, 20 and 40 kg/h
Specific Humidity	46 g/kg
Initial coolant temperature	-10, -2.5 and 5 °C
Initial local air conditioning	-10, -2.5 and 5 °C

[1] Temperature at the pos. 8 of the test rig.

2.3.3 Results and discussion

The results are divided into three subsections. The first subsection (2.3.3.1) shows the pressure and temperature evolution during the beginning of the test. In the second subsection (2.3.3.2), the condensation rate produced during the warm-up test is compared with the model results developed in section 2.3.1. Finally, the last subsection (2.3.3.3) presents the total amount of condensates for the proposed test matrix and the time in which the test takes to finish the production of condensates.

2.3.3.1 Pressure and Temperature evolution

In order to evaluate the changes in the boundary conditions due to the start of the test and related with the methodology employed, a test is carried out and the evolution of pressure and temperature are assessed. Figure 2.7a shows the pressure evolution before and after the starting of the test; when the test starts, the pressure downstream the orifice rises due to the higher pressure drop that causes the LP-EGR cooler compared to the external bypass valve is activated. Consequently, and following the nozzle equation (Eq.2.10), Figure 2.7b shows a reduction in the theoretical mass flow rate close to the 2 % for the cases with the higher amount of MFR, which agrees with a value of $C_D \simeq 1$ in Eq.2.10 for the calibrated orifice as was obtained by a 3D-CFD simulation.

$$\dot{m}_{theo} = A_{orif} \cdot C_D \cdot \frac{p_{04}}{\sqrt{R \cdot T_{04}}} \cdot \sqrt{\frac{2 \cdot \gamma_{air}}{\gamma_{air} - 1} \cdot \left(\frac{p_5}{p_{04}}\right)^{\frac{2}{\gamma_{air}}} - \left(\frac{p_5}{p_{04}}\right)^{\frac{\gamma_{air}+1}{\gamma_{air}}}} \tag{2.10}$$

The temperature evolution for the working point with an initial coolant temperature of -10 °C, mass flow rate of 20 kg/h and EGR temperature of 70 °C is shown in the Fig. 2.8. The evolution temperature is represented in two instants: at $t < 0$ and at time t_{dew}, when the cooler outlet exceeds the dew temperature (Eq. 2.11). The EGR mass flow temperature is being considered as the position 8 in the test rig (see Fig. 2.1) in order to procedure with the setup of the installation

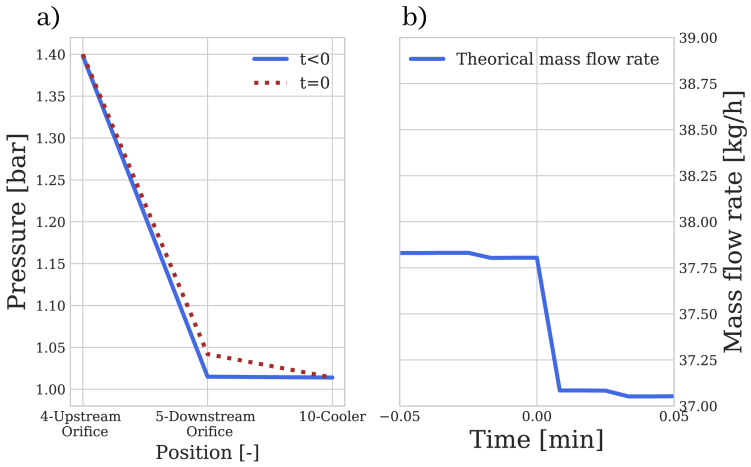

Figure 2.7: Evolution of pressure and MFR in the flow test rig for $t < 0$ and $t > 0$.

previously on the test.

$$T_{11}(t = t_{dew}) = T_{dew,10}; \quad T_{dew,10} = T_{dew,10}(w_{init}, P_{11}) \tag{2.11}$$

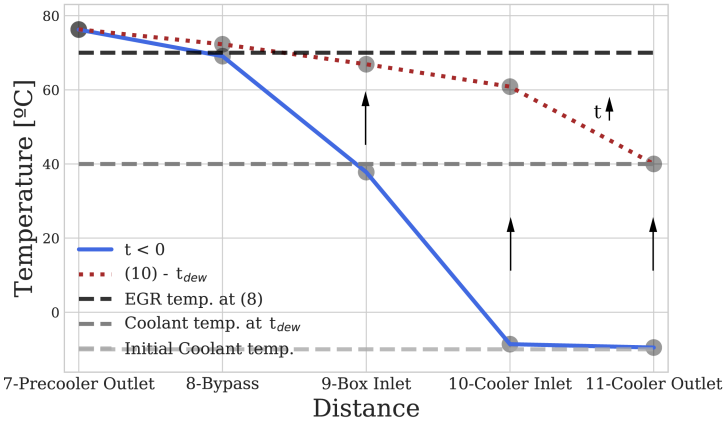

Figure 2.8: Temperature evolution at different points of the test rig for $t < 0$ and $t > 0$ at T_{cool}= -10 °C $\dot{m}$=20 kg/h and T_{EGR} = 70 °C.

Notice that the test starts with ($T_{10} = T_{11} = T_{cool,init}$) and, after that, the temperatures 9 (Box inlet), 10 (Cooler inlet) and 11 (Cooler outlet) begin to increase (Fig. 2.8). Looking at the difference between cooler inlet and outlet temperature, the time-dependent EGR cooler efficiency can be calculated.

2.3.3.2 Condensation rate

Some comparisons of the condensation rate produced during the warm-up tests with the estimation of the model developed in section 2.3.1 are shown in Figures 2.9, 2.10 and 2.11. In order to process the measurements obtained by the weighing scale, one has to take into account the extra weight measured due to the discharge flow momentum. Moreover, a partial derivative of the measured condensation weight trace is performed to obtain the condensation rate and a running mean average is used.

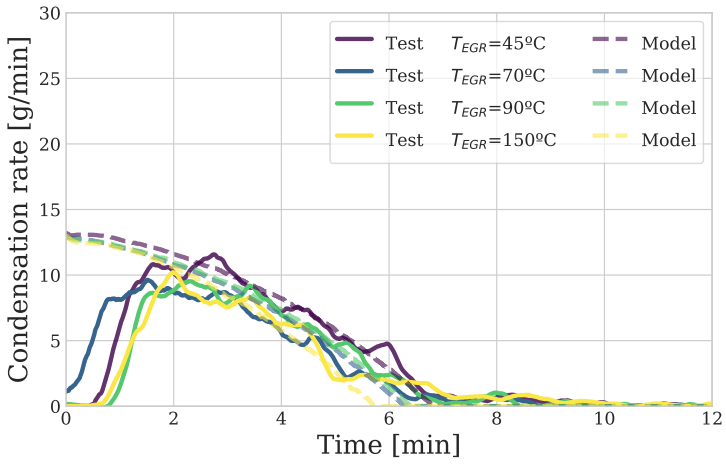

Figure 2.9: *Condensation rate evolution during time for $\dot{m}$=20 kg/h, T_{cool}=5 °C and modifying T_{EGR}.*

In first place, Fig. 2.9 shows the tests with different EGR temperature at a mass flow rate of 20 kg/h and at an initial coolant temperature of 5 °C. As can be seen, three noticeable stages are outstanding in the figure. On one hand, the first stage (Stage I) where the condensates starts and where the difference between the test and the model prediction is maximum. In the second stage (Stage II), the measured and modeled condensation rate are similar, decreasing due to the increasing coolant temperature, and ends when the theoretical condensation stops (t_{dew} from Eq. 2.11). On the other hand, the third stage (Stage III) ends when the actual condensation is stopped.

Compared with the previous figure, Fig. 2.10 shows the tests with a mass flow

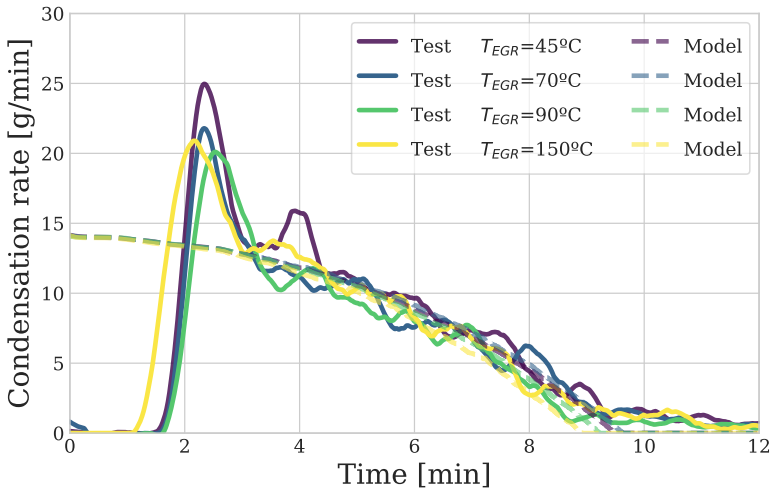

Figure 2.10: *Condensation rate evolution during time for $\dot{m}$=20 kg/h, T_{cool}=-10 °C and modifying T_{EGR}.*

rate of 20 kg/h and a coolant temperature of -10 °C. The most noticeable difference in Stage I is the possibility of distinguish two parts. Stage Ia considers the period until the condensation is detected at the cooler outlet. Then, in the Stage Ib some condensation rate peaks appear caused by the formation of ice inside the cooler during the first minutes of the test (temperatures below 0 °C) followed by its melting and a sudden release through the cooler outlet to the weighing scale.

Finally, Fig. 2.11 shows, for the same mass flow rate ($\dot{m}$=20 kg/h) and EGR temperature (T_{EGR}=150 °C), some tests modifying the initial coolant temperature (T_{cool}) between values of -10 to 5 °C. As can be seen, when comparing with the previous figures, the difference appears between the length of the Stages II and III. For each test, the time t_{dew} in which the cooler outlet exceeds the dew temperature is different because of the initial coolant temperature of each test. Thus, Stage II increases its length with the reduction of T_{cool}.

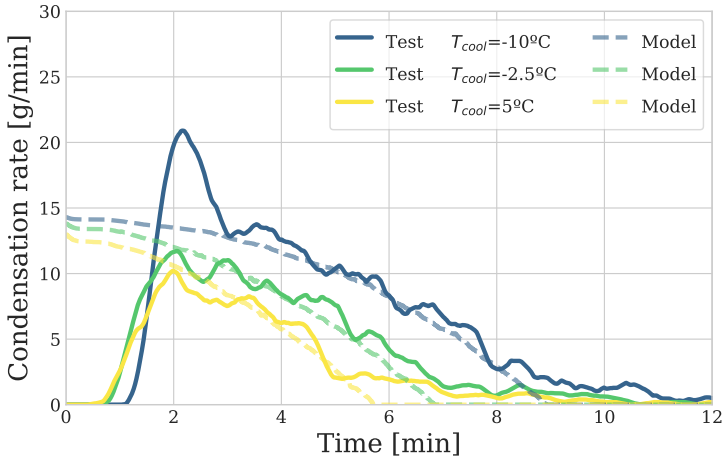

Figure 2.11: Condensation rate evolution during time for $\dot{m}$=20 kg/h, T_{EGR}=150 °C and modifying T_{cool}.

2.3.3.3 Accumulated condensation map

The accumulated condensates produced during the warm-up approximations for the cases of 20 kg/h are presented in Figs. 2.12 and 2.13, which represent the experimental results and the predictions of the model, respectively.

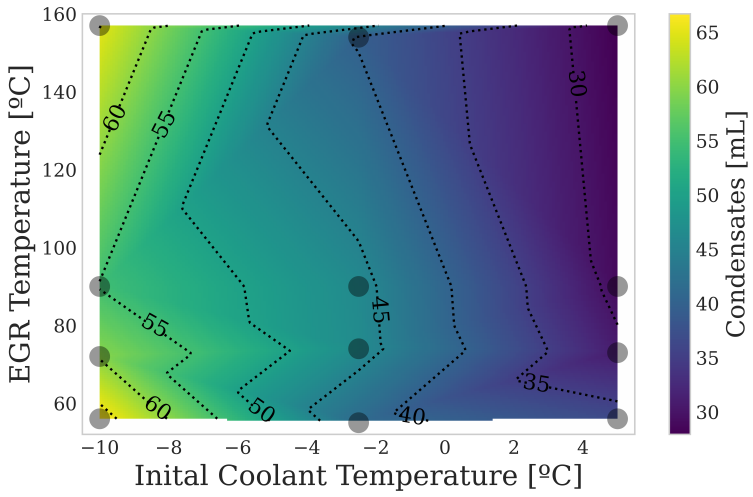

Figure 2.12: Final condensates at 20 kg/h, experimentally measured.

Starting with the experimental results, Fig. 2.12 shows the accumulated condensates depending on the EGR temperature (position 8 in Fig. 2.1) (for $t < 0$) and the initial coolant temperature. As aforementioned, the key parameter that controls the generated condensation is the coolant temperature, which produces higher condensates as it decreases. In fact, due to the high efficiency of the LP-EGR cooler, the impact of the EGR temperature is quite low, as can be seen in the figure.

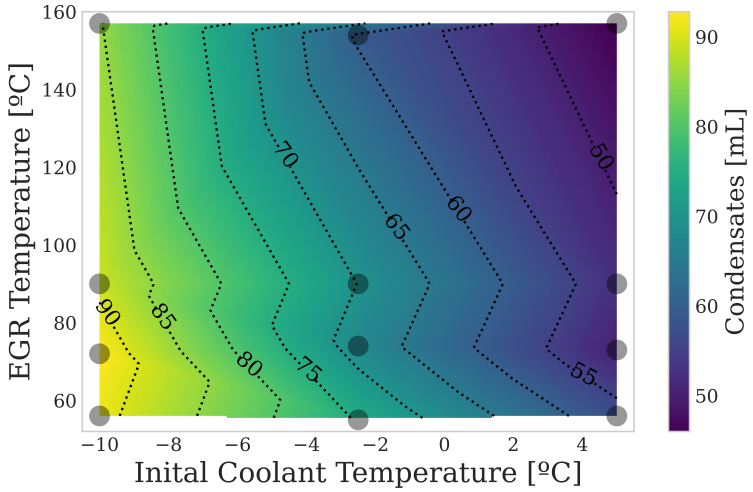

Figure 2.13: *Final condensates at 20 kg/h obtained by the model.*

Concerning the model prediction, Fig. 2.13 shows a result analogous to the previous figure but with an overprediction of the condensates of around 20-40 %. The trends found in the experimental figure are captured by the model. As exposed in Section 2.3.1, the model only considers the cooler outlet temperature of each time step for the water condensation prediction. Thus, differences appear due to the simplified thermal modelling of the cooler which implies an underestimation of the condensates due to neglecting some phenomena such as the presence of cold spots inside the cooler below dew conditions.

Regarding t_{dew} in which the production of condensates stops, as it is mentioned in Eq. 2.11, notable differences are observed between mass flow rates, coolant temperatures and EGR temperatures. In Fig. 2.14, the time until the condensation stops is shown for all mass flow rates and initial coolant temperature at a EGR temperature of 90 °C. There are not significant differences between

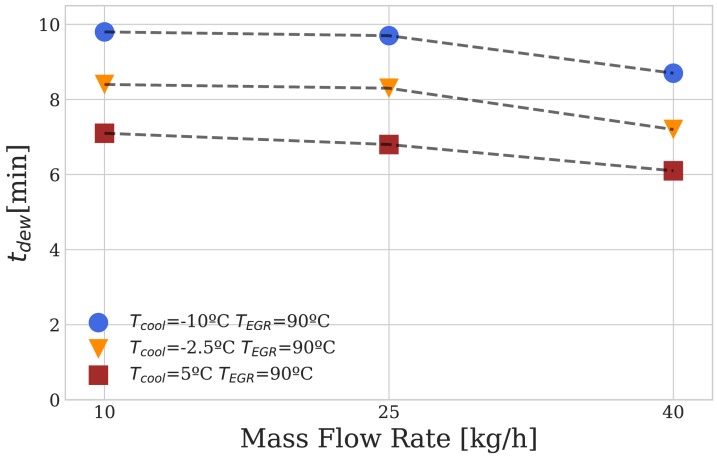

Figure 2.14: *Time to finish the condensates compared with the mass flow rates for a T_{EGR} = 90 °C and different coolant temperatures.*

EGR temperatures, but discrepancies appear between different initial coolant temperatures and, in a smaller scale, between mass flow rates. The greater the reduction on the initial coolant temperature, the longer the time to finish the condensation produced in the LP-EGR cooler. Comparing by mass flow rates, some differences appear due to the aforementioned effect of the cooler efficiency, with a higher amount of MFR, and an increase of thermal load occurs, being able to reduce the t_{dew}.

2.4 Conclusions

The effects of low ambient temperature on condensation formation inside the LP-EGR cooler are analysed in this chapter, thanks to the experimental setup proposed for this task. Experimental tests were carried out on simulating the warm-up transient evolution of a WLTC cycle in a flow test rig.

Regarding the condensation produced, different behaviors were observed. On the one hand, the coolant temperature takes the key role in the condensation production, a lower initial coolant temperature produces a higher condensation rate and accumulated water at the end of the test. On the other hand,

the gas inlet temperature and the MFR gas have a noticeable but lower influence on the condensation production due to the modification of the cooler efficiency, i.e., as the MFR increases, a non-ideal cooler is not able to cool down the gas until the coolant temperature, thus reducing the condensed water. Moreover, a relevant tendency appears in the cases of a coolant temperature of -10 °C. Ice forms inside the cooler at the beginning of the warm-up and is later rapidly melted and expelled through the outlet.

Concerning the condensation model presented in this article, the predicted results are consistent with the experimental tests, except at the very beginning of the test. This error is produced due to not considering the local wall temperature in the LP-EGR cooler, the cooler capacity to retain water inside, the partial evaporation and the icing produced in the cases of coolant temperature below 0 °C.

Finally, regarding the time until the condensation stops (t_{dew}), a strongly dependence of the coolant temperature has been found as well. The inlet gas temperature and the mass flow rate, which lower the efficiency as they rise, also reduce the time to stop the condensation.

The experimental setup has some limitations regarding the maximum gas mass flow rate and water injection rate that can be achieved. Nevertheless, the requirements for simulating a C-segment passenger car diesel engine are covered. In order to simulate heavy duty engine conditions, an upgrade should be applied to the test rig including more water injectors.

Chapter 2 References

[2] J. Galindo, R. Navarro, D. Tari, and F. Moya. "Development of an experimental test bench and a psychrometric model for assessing condensation on a Low Pressure EGR cooler". *International Journal of Engine Research*, (2020). DOI: 10.1177/1468087420909735 (cit. on pp. xi, 7, 27, 51).

[8] *European Automobile Manufacturers' Association's* (*ACEA*). *Brussels*. *The Automobile industry Pocket Guide*. 2018-2019. URL: https://www.acea.be/uploads/publications/ACEA_Pocket_Guide_2018-2019.pdf (cit. on pp. 3, 24).

[11] M. Weilenmann, J.-Y. Faves, and R. Alvarez. "Cold-start emissions of modern passenger cars at different low ambient temperatures and their evolution over vehicle legislation categories". *Atmospheric Environment*, 43, (15 May 5, 2009), pp. 2419–2429. DOI: 10.1016/j.atmosenv.2009.02.005 (cit. on pp. 4, 7, 25).

[19] M. Lapuerta, A. Ramos, D. Fernandez-Rodriguez, and I. Gonzalez-Garcia. "High-pressure versus low-pressure exhaust gas recirculation in a Euro 6 diesel engine with lean-NOx trap: Effectiveness to reduce NOx emission". *International Journal of Engine Research*, -, (Nov. 14, 2018), pp. 0–9. DOI: 10.1177/1468087418817447 (cit. on pp. 5, 7, 24, 151).

[20] J. M. Luján, C. Guardiola, B. Pla, and A. Reig. "Switching strategy between HP (high pressure)-and LPEGR (low pressure exhaust gas recirculation) systems for reduced fuel consumption and emissions". *Energy*, 90, (2015), pp. 1790–1798. DOI: 10.1016/j.energy.2015.06.138 (cit. on pp. 6, 7, 25, 140, 151).

[21] S. Moroz, G. Bourgoin, J. M. Luján, and B. Pla. "Acidic condensation in low pressure EGR systems using diesel and biodiesel fuels". *SAE Int. J. Fuels Lubr*, 2009-01-2805, (2009). DOI: 10.4271/2009-01-2805 (cit. on pp. 6, 7, 25).

[22] D. T. Hountalas, G. C. Mavropoulos, and K. B. Binder. "Effect of exhaust gas recirculation (EGR) temperature for various EGR rates on heavy duty DI diesel engine performance and emissions". *Energy*, 33 (2), (2008), pp. 272–283. DOI: 10.1016/j.energy.2007.07.002 (cit. on pp. 6, 7, 25).

[32] J. Bishop, M. Stettler, N. Molden, and A. Boies. "Engine maps of fuel use and emissions from transient driving cycles". *Applied Energy*, 183, (Dec. 1, 2016), pp. 202–217. DOI: 10.1016/j.apenergy.2016.08.175 (cit. on pp. 7, 25).

[33] Z. Wei, X. Jinliang, and L. Guohua. "Multi-channel effect of condensation flow in a micro triple-channel condenser". *International Journal of Multiphase Flow*, 34, (12 Dec. 1, 2008), pp. 1175–1184. DOI: 10.1016/j.ijmultiphaseflow.2008.05.004 (cit. on pp. 7, 25).

[36] J. R. Serrano, P. Piqueras, E. Angiolini, C. Meano, and J. De La Morena. "On Cooler and Mixing Condensation Phenomena in the Long-Route Exhaust Gas Recirculation Line". In: *SAE Technical Paper*. 2015. DOI: 10.4271/2015-24-2521 (cit. on pp. 7, 31, 105, 108, 157, 185).

[41] S. S. Hoseini, G. Najafi, and B. Ghobadia. "Experimental and numerical investigation of heat transfer and turbulent characteristics of a novel EGR cooler in diesel engine". *Applied Thermal Engineering*, 108, (2016), pp. 1344–1356. DOI: 10.1016/j.applthermaleng.2016.08.018 (cit. on pp. 9, 26).

[42] C. Cuevas, D. Makaire, and P. Ngendakumana. "Thermo-hydraulic characterization of an automotive intercooler for a low pressure EGR application". *Applied Thermal Engineering*, 31, (14-15 Apr. 19, 2011), pp. 2474–2484. DOI: 10.1016/j.applthermaleng.2011.04.013 (cit. on pp. 9, 25).

[43] M. Abarham, T. Chafekar, J. Hoard, D. Styles, and D. Assanis. "A visualization test setup for investigation of water-deposit interaction in a surrogate rectangular cooler exposed to diesel exhaust flow". *SAE Technical Paper*, 2012-01-0364, (2012). DOI: 10.4271/2012-01-0364 (cit. on pp. 9, 26).

[44] C. Guo, Q. Liu, B. Zheng, Y. You, and Y. Li. "Development of model based on condensation area ratio and effect on heat transfer capacity of indirect evaporative cooling". *Applied Thermal Engineering*, 164, (Jan. 5, 2020). DOI: 10.1016/j.applthermaleng.2019.114557 (cit. on pp. 9, 25).

[45] A. Razmavar, M. Malayeri, and M. Abd-Elhady. "Influence of secondary flow on the thermal performance of exhaust gas recirculation (EGR) coolers". *International Journal of Thermal Sciences*, (2021). DOI: 10.1016/j.ijthermalsci.2020.106720 (cit. on pp. 9, 26).

[46] A. R. Razmavar and M. R. Malayeri. "Thermal performance of a rectangular exhaust gas recirculation cooler subject to hydrocarbon and water vapor condensation". *International Journal of Thermal Sciences*, 143, (Sept. 1, 2019), pp. 1–13. DOI: 10.1016/j.ijthermalsci.2019.05.006 (cit. on pp. 9, 26).

[47] A. Warey, D. Long, S. Balestrino, and P. Szymkowcz. "Visualization and Analysis of Condensation in Exhaust Gas Recirculation Coolers". In: *SAE International Paper*. Aug. 4, 2013. DOI: 10.4271/2013-01-0540 (cit. on pp. 9, 25).

[48] C. Paz, E. Suarez, J. Vence, and A. Cabarcos. "Numerical modelling of fouling process in EGR system: A review". *Environmental Issues and Sustainable Development*, (2020). DOI: 10.5772/intechopen.93062 (cit. on pp. 9, 26).

[49] C. Paz, E. Suarez, J. Vence, and J. Hoard. "Evolution of EGR cooler deposits under hydrocarbon condensation: Analysis of local thickness, roughness, and fouling layer density". *International Journal of Thermal Sciences*, (2021). DOI: 10.1016/j.ijthermalsci.2020.106744 (cit. on pp. 9, 26).

[55] J. Galindo, V. Dolz, J. Monsalve-Serrano, M. Maldonado, and L. Odillard. "Advantages of using a cooler bypass in the low-pressurre exhaust gas recirculation line of a compression ignition diesel engine operating at cold conditions". *Internal Journal of Engine Research*, (Apr. 29, 2020). DOI: 10.1177/1468087420914725 (cit. on pp. 10, 25, 51, 140).

[56] N. Ghassembaglou and L. Torkaman. "Efficient design of exhaust gas cooler in cold EGR equipped diesel engine". *Alexandria Engineering Journal*, 55, (2016), pp. 769–778. DOI: 10.1016/j.aej.2016.01.023 (cit. on pp. 10, 25).

[57] H. Song and S. Song. "Numerical investigation on a dual loop EGR optimization of a light duty diesel engine based on water condensation analysis". *Applied Thermal Engineering*, 182, (2021), pp. 1–12. DOI: 10.1016/j.applthermaleng.2020.116064 (cit. on pp. 10, 25, 151).

[73] J. Serrano, P. Piqueras, R. Navarro, D. Tarí, and C. Meano. "Development and verification of an in-flow water condensation model for 3D-CFD simulations of humid air streams mixing". *Computers & Fluids*, 167, (2018), pp. 158 –165. ISSN: 0045-7930. DOI: 10.1016/j.compfluid.2018.02.032 (cit. on pp. 11, 13, 25, 51, 53, 66, 95, 105, 107, 153, 183, 184).

[74] J. Galindo, P. Piqueras, R. Navarro, D. Tarí, and C. Meano. "Validation and sensitivity analysis of an in-flow water condensation model for 3D-CFD simulations of humid air streams mixing". *International Journal of Thermal Sciences*, 136, (2019), pp. 410 –419. ISSN: 1290-0729. DOI: 10.1016/j.ijthermalsci.2018.10.043 (cit. on pp. 11, 25, 51, 68, 69, 73, 74, 107, 135, 153, 161, 175, 184).

[83] R. D. Reitz, H. Ogawa, R. Payri, T. Fansler, and S. Kokjohn. "IJER editorial: The future of the internal combustion engine". *International Journal of engine Research*, 21, (1 2020), pp. 0–8. DOI: 10.1177/1468087419877990 (cit. on p. 24).

[84] M. Dalla Chiara B. Pellicelli. "Sustainable road transport from the energy and modern society points of view: Perspectives for the automotive industry and production". *Journal of cleaner production*, 133, (2016), pp. 1283–1301. DOI: 10.1016/j.jclepro.2016.06.015 (cit. on p. 24).

[85] P. Prevedouros and L. Mitropoulos. "Life Cycle Emissions and Cost Study of Light Duty Vehicles". *Transportation Research Procedia*, 15, (2016), pp. 749–760. DOI: 10.1016/j.trpro.2016.06.062 (cit. on p. 24).

[86] M. Andre. "The ARTEMIS European driving cycles for measuring car pollutant emissions". *Science of The Total Environment*, 334-335, (Dec. 1, 2004), pp. 73–84. DOI: 10.1016/j.scitotenv.2004.04.070 (cit. on p. 24).

[87] P. Olmeda, J. Martín, F. Arnau, and S. Artham. "Analysis of the energy balance during World harmonized Light vehicles Test Cycle in warmed and cold conditions using a Virtual Engine". *International Journal of Engine Research*, -, (Oct. 3, 2019), pp. 0–18. DOI: 10.1177/1468087419878593 (cit. on p. 24).

[88] J. M. Luján, H. Climent, L. M. García-Cuevas, and A. Moratal. "Pollutant emissions and diesel oxidation catalyst performance at low ambient temperatures in transient load conditions". *Applied Thermal Engineering*, 129, (2018), pp. 1527 –1537. ISSN: 1359-4311. DOI: 10.1016/j.applthermaleng.2017.10.138 (cit. on p. 24).

[89] K. Jinyoung, S. Jeonghun, M. Cha-Lee, and P. Simsoo. "Comparative study on low ambient temperature regulated/unregulated emissions characteristics of idling light-duty diesel vehicles at cold start and hot restart". *Fuel.*, 233, (2018), pp. 620–631. DOI: 10.1016/j.fuel.2018.05.144 (cit. on p. 24).

[90] K. Fotis, S. Kim, S. Shobhana, and C. Thomas. "Modeling and optimization of integrated exhaust gas recirculation and multi-stage waste heat recovery in marine engines". *Energy Conversion and Management*, 151, (Nov. 1, 2017), pp. 286–295. DOI: 10.1016/j.enconman.2017.09.004 (cit. on p. 24).

[91] X. Yang, J. Liu, P. Fu, N. Chen, and J. Wei. "Experimental and theoretical study of pressure oscillation of unstable steam-air jet condensation in water in a rectangular channel". *International Journal of Multiphase Flow*, 119, (Oct. 1, 2019), pp. 14–27. DOI: 10.1016/j.ijmultiphaseflow.2019.07.009 (cit. on p. 25).

[92] L. Seungho, C. Jinho, L. Haneol, K. Taejoon, and S. Weon. "Understanding the condensation process of turbulent steam jet using the PDPA system". *International Journal of Multiphase Flow*, 98, (Jan. 1, 2018), pp. 168–181. DOI: 10.1016/j.ijmultiphaseflow.2017.09.007 (cit. on p. 25).

[93] D. Hongbing, W. Chao, and C. Chao. "Experimental and numerical studies on self-excited periodic oscillation of vapor condensation in a sonic nozzle". *Experimental Thermal and Fluid Science*, 68, (November 2015), pp. 288–299. DOI: 10.1016/j.expthermflusci.2015.05.002 (cit. on p. 25).

[94] N. Rahim, W. Davies, P. Hrnjakbc, and J. Meyera. "Numerical study of steam condensation inside a long inclined flattened channel". *International Journal of Heat and Mass Transfer*, 134, (May 1, 2019), pp. 450–467. DOI: 10.1016/j.ijheatmasstransfer.2019.01.063 (cit. on p. 25).

[95] D. Murphy, M. Macdonald, A. Mahvi, and S. Garimella. "Condensation of propane in vertical minichannels". *International Journal of Heat and Mass Transfer*, 137, (July 1, 2019), pp. 1154–1166. DOI: 10.1016/j.ijheatmasstransfer.2019.04.023 (cit. on p. 25).

[96] Y. Vasyliv, D. Lee, R. Tower Ted. Ng, V. Polashock, and A. Alexeed. "Modeling condensation on structured surfaces using lattice Boltzmann method". *International Journal of Heat and Mass Transfer*, 136, (June 1, 2019), pp. 196–212. DOI: 10.1016/j.ijheatmasstransfer.2019.02.090 (cit. on p. 25).

[97] J. M. Luján, V. Dolz, J. Monsalve-Serrano, and M. A. Bernal. "High-pressure exhaust gas recirculation line condensation model of an internal combustion diesel engine operating at cold conditions". *International Journal of Engine Research*, -, (July 4, 2019), pp. 0–10. DOI: 10.1177/1468087419868026 (cit. on p. 26).

[98] Z. Akram Ali. Zachary. "Open Source Building Science Sensors (OSBSS): A low-cost Arduino-based platform for long-term indoor environmental data collection". *Building and Environmental*, 100, (May 1, 2016), pp. 114–126. DOI: 10.1016/j.buildenv.2016.02.010 (cit. on p. 29).

Chapter 3

Condensation on a Low-Pressure EGR junction

Contents

3.1 Introduction

In the previous Chapter 2, the approach to deal with the condensation on heat exchangers and in particular on EGR coolers has been shown. But as it was presented at the Chapter 1, it is also important to study the condensation on junctions and when two flows are mixed, as it is one of the two places where condensation appears at the LP-EGR line affecting to the integrity of the compressor impeller.

This chapter investigates experimentally and with 3D CFD simulations the mixing of humid streams in a junction at situations that lead to condensation. As already discussed, the produced condensation is particularly harmful for the case of exhaust gases mixing with cold ambient air in a turbocharged internal combustion engine working with Low-Pressure Exhaust Gas Recirculation (LP-EGR) [71]. In this case, water droplets may reach the compressor impeller and cause wear on the surface [1, 34, 35]. LP-EGR is a promising technology due to its high potential on reducing NO_x, CO_2 and particulate matter emissions [26]. However, the critical drawback of the generation of condensates not only in the LP-EGR junction but also at the LP-EGR cooler [55, 2, 99] has challenged researchers to address this issue, as it was presented at the chapter 2 when the condensation at the LP-EGR cooler has been studied.

To study the condensation generation at mixing processes, Serrano et al. [73] proposed an in-flow water condensation model to be embedded in 3D-CFD codes. Galindo et al. [74] compared the experimental results of impeller durability tests with 3D-CFD simulations in a qualitative manner, showing that the condensation mass flow rate predicted by the CFD model was a good estimator of the observed compressor damage, i.e., higher condensation rates corresponded to stronger impeller erosion. Therefore, it seems convenient to assess how junction design and operating conditions dictate the generated condensation mass flow rate.

Numerous authors have studied flow characteristics in junctions, like Brune et al. [100] or Yang et al. [58]. There are researchers that have investigated thermal mixing phenomena appearing inside a junction, such as Evrim et al. [63, 64] or Zhou et al. [61, 62]. Other authors have focused on the modeling issues of

turbulent flow mixing in T-junctions [65, 66].

However, when addressing the experimental quantification of in-flow condensation mass flow rate without affecting the flow, several issues arise. Some authors like Wang et al. [77] proposed an H_2O absorption tomography to quantify the in-flow water vapor on a Diesel Particle Filter. However, this technique provides H_2O vapor mole fraction instead of the desired liquid water mass flow rate. A method to collect liquid water (after humid air has been externally cooled in a heat exchanger) and measure its mass flow rate is the usage of separators ([101, 102]). This technique is not valid in the framework of junction condensation, as the vortical flow established in such devices promote flow mixing ([103, 104]) and thus will spuriously increase the generated condensation [71]. Therefore, no adequate experimental quantification of junction condensation mass flow rate has been found in the literature, and in turn 3D CFD models designed to predict condensation cannot be validated.

A novel flow test rig able to assess condensation in three way junctions is developed at this thesis in order to study with different techniques the condensation flow at the outlet of a junction. This flow test rig provides hot humid air to one junction inlet and cold air to the other. Regarding the techniques employed, laser particle image velocimetry (PIV) measurement [81, 82] is conducted to obtain secondary flows at the junction outlet cross-section, these secondary flows are related with condensation quantity. Secondly, a Planar laser-induced visualization, which is used in the scope of multiphase problems in other works [79], is employed for the first time on the condensation behavior, to experimentally characterize condensation patterns in three-way junction. And finally, an innovative technique is developed in this work to conduct an indirect measurement of the bulk flow water condensation rate, based on an enthalpy balance on the cross section of study. This technique takes advantage of the energy released (latent heat) of the condensation process in order to infer the condensation rate, through finely-resolved campaigns of temperature measurements with and without formation of condensation. The main novelty of this technique is therefore the non-intrusive experimental quantification of the condensation produced by mixing streams.

Concerning the numerical simulations performed in this section, the commercial code STAR-CCM+ [105] is used to conduct the CFD campaign, including the

previously mentioned condensation model [73].

3.2 Experimental techniques to assess junction condensation

3.2.1 Experimental facility

In order to assess the condensation produced in the LP-EGR junction, a novel test bench has been developed, which provides hot humid air through one branch (representing EGR) and conditioned air through the other (to simulate ambient intake from cold climates). The pair of inlets of the three-way junction are fed by their corresponding branch, while the outlet directly blows into the test rig (free discharge configuration), at this place it is going to set the different technique presented in the Sections 3.2.2.1, 3.2.3 and 3.2.4. A free discharge is more convenient for the sake of outlet visualization and to be able to work with the different techniques, and section 3.3 will show that the impact of removing the outlet duct is small. For LP-EGR applications, a compressor would be installed in that outlet duct. However, Galindo et al. [106] concluded that the presence of the compressor has a low influence on the formation of condensation; the error being 4% or lower for representative LP-EGR boundary conditions.

Figure 3.1 depicts the scheme of the test rig employed, being an upgrade from the test bench presented in Fig. 2.1 at the Chapter 2. At the previous chapter, the flow test rig was prepared for measuring water condensation on a LP-EGR cooler while warm-up temperature conditions were applied. In this case, a test rig enhancement is performed in terms of including a new cold flow branch keeping the rest of the test bench equipment. The upgraded test rig is prepared to provide to the three-way junction geometry hot humid flow (station 7) and cold flow (station8).

Regarding the hot humid flow stream (EGR) and following the test bench approach presented in Chapter 2, the same equipment and path is described here for the sake of completeness. Again, this branch is employed as in previous chapter, only considering that the LP-EGR cooler is kept at constant temperature

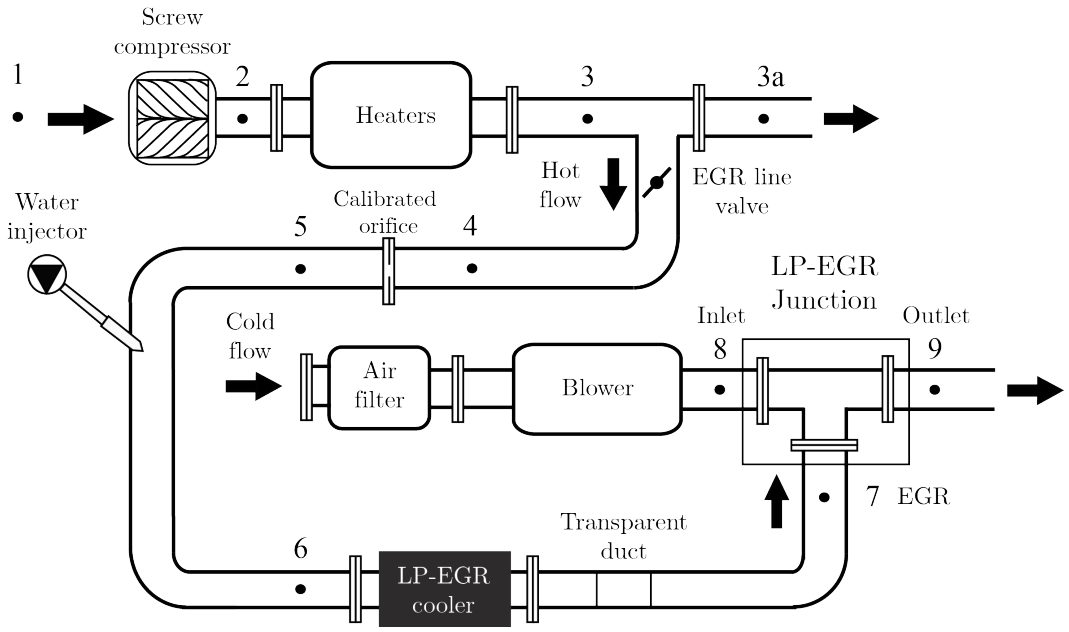

Figure 3.1: *Scheme of the flow test rig*

instead of employing a transient temperature profile.

At the core of the rig (between station 1 and 3), there is a volumetric screw compressor that supplies compressed air and five heaters (9kW each) that increase the flow temperature up to 400°C. A counter-pressure valve controls the mass flow rate (MFR) that goes through the three-way junction EGR inlet. A calibrated orifice was used to set the desired MFR in the EGR line (between stations 4 and 5). To simulate humid LP-EGR flow conditions, water is injected between stations 5 and 6 to increase the specific humidity. The high flow temperature helps to vaporize the injected water. Once the water is vaporized, the flow temperature is reduced in the LP-EGR cooler down to the target value.

As it is mentioned, the upgraded of the previous test bench was on the cold flow branch to provide the inlet fresh air gas for the three-way junction. To produce this stream of cold flow, air is cooled and dried in a climatic chamber that could reduce the temperature below to -20°C. Then, using a blower, it is pushed through the cold branch to be mixed with the humid stream in the LP-EGR junction (stations 7-9). At this position, different LP-EGR junctions are going to test during this thesis.

Table 3.1: Instrumentation range and accuracy[1]

Sensor	Variable	Range	Accuracy [%]
Thermocouples K-type	Temperature	-260 – 1260 °C	1
Pressure sensor	Pressure	0 – 6 bar	0.3
Flow meter	Air mass flow	0 – 720 kg/h	1
Weighing scale	Water injected mass	0 – 20 kg	0.1

[1] According to datasheets

The operating range and accuracy of the instrumentation used to establish the working point is shown in Table 3.1. K-type thermocouples are used for measuring temperature at all flow test rig stations (1-9), as well as, on the different techniques employed to measured the condensation patterns and flows. Piezoresistive pressure sensors are mounted along the different ducts. A flow meter is installed in the cold flow branch downstream of the blower, together with a frequency controller to set the desired air mass flow rate. A weighing scale is used in the water injector to check that the system is injecting the desired amount of water mass flow in the EGR line.

3.2.2 Laser PIV measurements

3.2.2.1 Apparatus and methods

In order to characterize the flow distribution with condensation in a cross-section just downstream the junction discharge a PIV technique is employed. Fig. 3.2 shows a schematic representation of the laser PIV system. In this study, a standard 2D PIV system by TSI has been selected to measure 2D instantaneous velocity fields following the validated methodology presented by Torregrosa et al. [80] and Pastor et al. [107]. This involves a 15 Hz flashlamp pumped Nd:YAG laser with 135 mJ/pulse at 532 nm. A redirecting optical system with a set of lenses and mirrors is used to set the measurement plane a 4 Mpixel, 12-bit straddle CCD camera (PowerView Plus 4MP) and a synchronization device is used to capture the images. Tests were carried out with both fresh air and EGR inlets seeded with

particles to allow the processing of the velocimetry. For this purpose, oil droplets of 1 μm of diameter are supplied to the flow using an atomizer. A commercial synthetic oil based on liquid paraffin and isopropyl palmitate is employed, in accordance with the work of Torregrosa et al. [80].

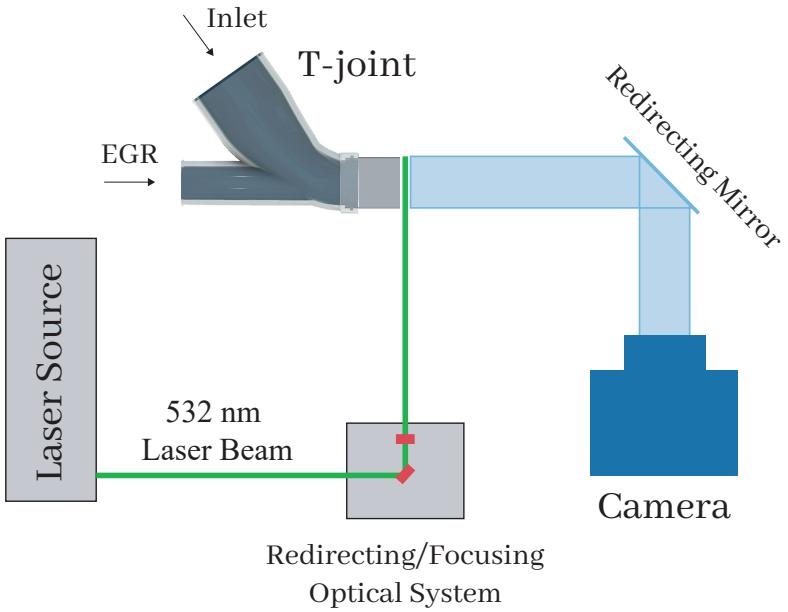

Figure 3.2: *Schematic representation of the employed laser PIV apparatus.*

Images were processed with the software TSI Insight 3G in order to obtain the components of the velocity vectors and the in-plane velocity modules. The software is configured to obtain the maximum available spatial resolution of velocity vectors. Additional custom routines are developed in Python to crop the outlet section of the raw snapshot (Fig.3.3a) and for representing velocity vectors and contours previously calculated by the software TSI Insight 3G.

The magnification of the images was 860 pixel/mm, whereas the visualization resolution and the size of the cross correlation were set to 16x16 pixels so as to prevent an excessive interpolation during data processing. The time elapsed between the two laser shots was established as 15 μs, since it provided the flow velocity field in the greatest detail. This is the maximum time difference with which the particles at the two snapshots are confined within the laser sheet. Velocity vector field is averaged by considering 200 images for each case, which extend

over a time period of 3 ms. If the uncertainty of time-averaged in-plane velocity [108] is spatially averaged for the cross section of interest and normalized with the mean in-plane velocity (temporally and spatially averaged) in accordance with Eq. 3.1.

$$\widetilde{U_u}(\%) = \frac{\widehat{\sigma_{\overline{u}}}/\sqrt{N}}{\hat{\overline{u}}} 100 \tag{3.1}$$

3.2.2.2 Example of proposed method

Figure 3.3a depicts a raw cross section at junction outlet, detailing the available region of interest (ROI) of the cross section where the impeller should be place. As can be seen, extremely small seeding particles are inside the flow which allows to obtain the radial velocity. Figure 3.3b shows an example of the postprocessing performed in the measurement ROI plane, allowing to obtain the radial velocity and the flow movement trends at the outlet which is directly related to the condensation generation.

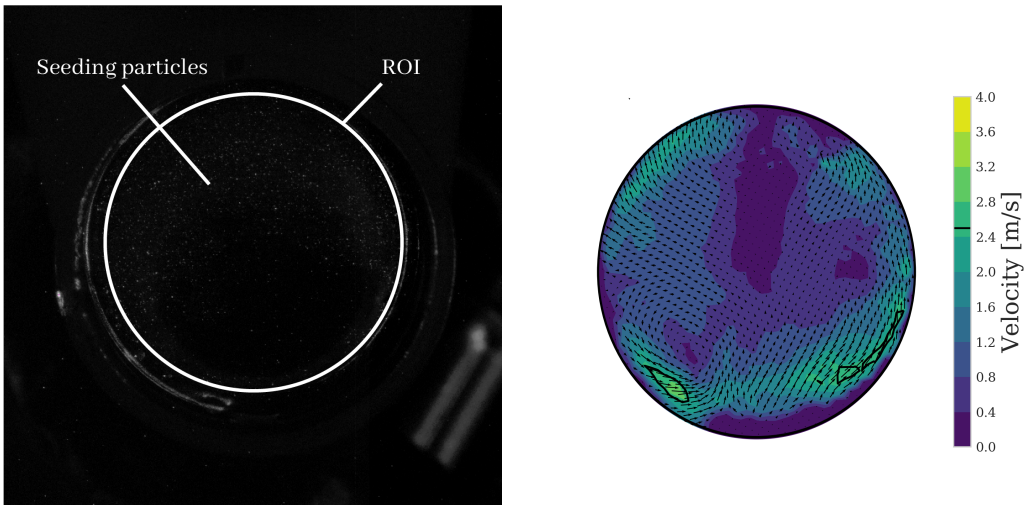

(a) *Raw snapshot.* (b) *Postprocessed velocity field.*

Figure 3.3: *Example of laser PIV process to measure velocity field at the three-way junction outlet.*

3.2.3 Planar Laser-induced Visualization

3.2.3.1 Apparatus and methods

Considering the impossibility of providing an accurate quantitative measurement of the liquid phase distribution in a foggy environment, the condensation pattern is assessed by means of planar laser-induced visualization in this work. Given the difficulty of quantifying the uncertainty of liquid sprays visualization [109], the main objective is therefore to characterize experimentally the locus at which condensation is produced. To allow a proper comparison of the qualitative changes in condensation distribution, the same luminosity conditions have been kept for all cases. In any case, the differences in the local amount of condensed water should produce a corresponding variation in the luminosity distribution. This effect will be used in Section 3.3.2 in order to compare the condensates predicted by CFD simulations with the laser-induced visualization of the condensation pattern.

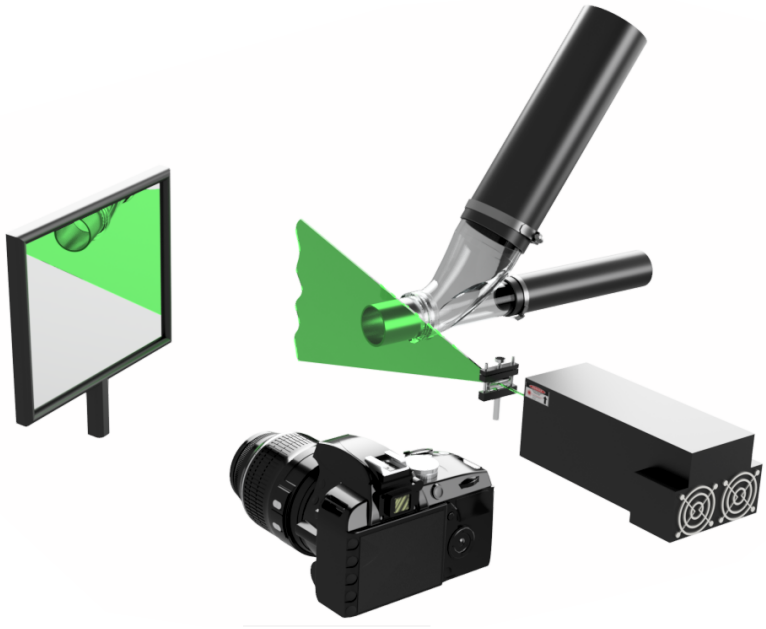

Figure 3.4: *Schematic representation of the employed planar laser-induced visualization apparatus.*

The layout for the laser-induced visualization (Fig. 3.4) seems similar to that of the PIV measurements depicted by Fig.3.2, but the laser and camera are different. The measurements conducted with the planar laser-induced visualization involve a 3kW laser with a wavelength of 532nm (MGL-N-532B 3kW) provided by a power supply (PSU-H-LED) and a plano-concave lens for the laser beam expansion to cover the diameter of the circular outlet section with around 1mm thickness at the measurement section. A 24 Mpixel, DSLR camera (Nikon D3400) and a redirecting mirror to protect the equipment from the condensed water are used to take the pictures. A long exposition of 3 seconds is employed to average the temporal fluctuations of the condensation pattern.

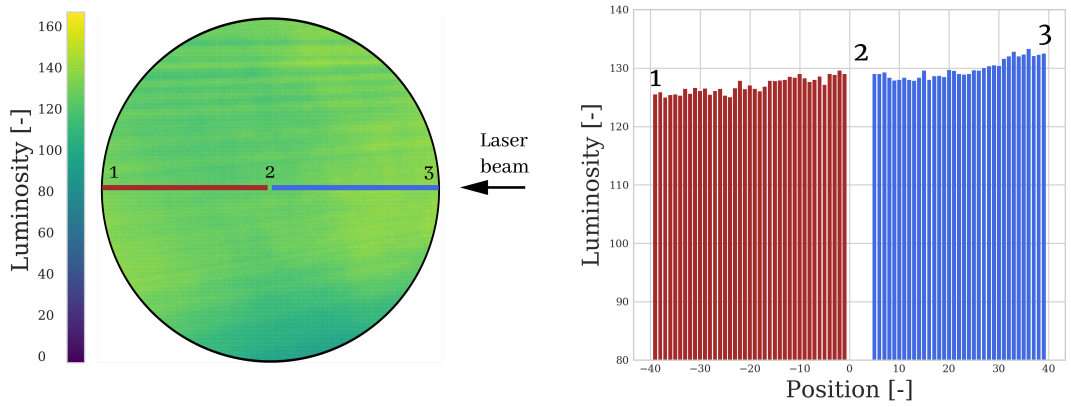

(a) *Luminosity distribution for a homogeneous cloud of dopant.* **(b)** *Luminosity profile at lines 1–2 and 2–3.*

Figure 3.5: *Laser sheet characterization.*

Due to the plano-concave lens, a correction of the measured luminosity data is required. Figure 3.5 shows a picture of the measured luminosity for a still ambient with a cloud of droplets of 1 μm diameter obtained by means of an oil atomizer. An ideal laser beam would produce a homogeneous sheet in these conditions. However, Fig. 3.5a presents a luminosity loss due to the beam expansion, quantified at two lines in Fig. 3.5b. Therefore, the uneven distribution shown in Fig. 3.5a is characterized and employed to correct the raw pictures that will be obtained in the experimental campaign discussed in section 3.3.2. The correction procedure is done by virtue of equations 3.2 and 3.3, in accordance with

the works of Pastor et al. [78] and Charogianni [110]:

$$f_L(i) = \frac{L_{max}}{L_i} \tag{3.2}$$

$$L_{corr}(i) = f_L(i) \mathring{u} L_{raw}(i) \tag{3.3}$$

3.2.3.2 Example of proposed method

Figure 3.6 shows, at the top left side, a sample of the raw data extracted directly from the tests, together with the reference laser sheet characterization (bottom left) within the region of interest (ROI). The two pictures are then processed to depict the measured luminosity. The laser sheet reference luminosity (bottom center) is employed to calculate the distribution of the correction factor (Eqn. 3.2), by dividing the maximum luminosity of the reference sheet by the luminosity of each pixel of the reference sheet. Finally, the luminosity of the considered test (top center) is corrected by means of equation 3.3 to obtain the processed image on the right side of Fig. 3.6.

3.2.4 Indirect condensation measurements

3.2.4.1 Apparatus and methods

As it is mentioned, it is extremely difficult to measure the in-flow water condensation experimentally. Thus, a novel technique entirely developed on this thesis is presented being able to obtain the condensation as a smog inside the flow. This techniques is employed at the outlet of a LP-EGR junction, but could be use in any other area in which condensation or evaporation takes place.

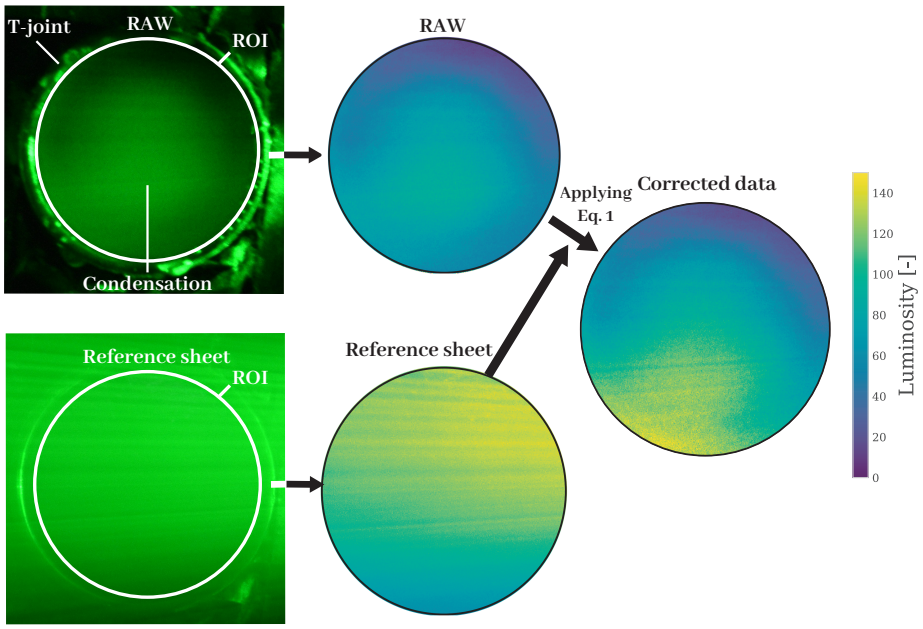

Figure 3.6: Method to correct the raw data measured with the planar laser-induced visualization.

3.2.5 Temperature array measurement

Figure 3.7 depicts the array of thermocouples set in the three-way junction outlet (station 9 in Fig. 3.1), in order to characterize the temperature distribution in the cross section of study. Table 3.2 shows the reference locations of the 5 thermocouples, which are set at different radial and circumferential positions. The ability of the array to be rotated azimuthally along the 360° allows the thermocouples to characterize the whole cross-section. Measurements were taken at 24 different angular positions of the thermocouple array, each of them shifted by 15°, resulting in a total of 97 temperature measurements evenly distributed in the cross section as depicted in Fig. 3.8. Test repeatability was ensured by checking that the temperatures were consistent with the initial readings after a whole rotation (360°). For easier processing and visualization of the results shown in sections 3.3.2, a linear interpolation of the temperature will be performed between the points. The annulus consisting in the outer area between the thermocouple "e" (see Fig. 3.7 and Table 3.2) and the wall is not being extrapolated or displayed

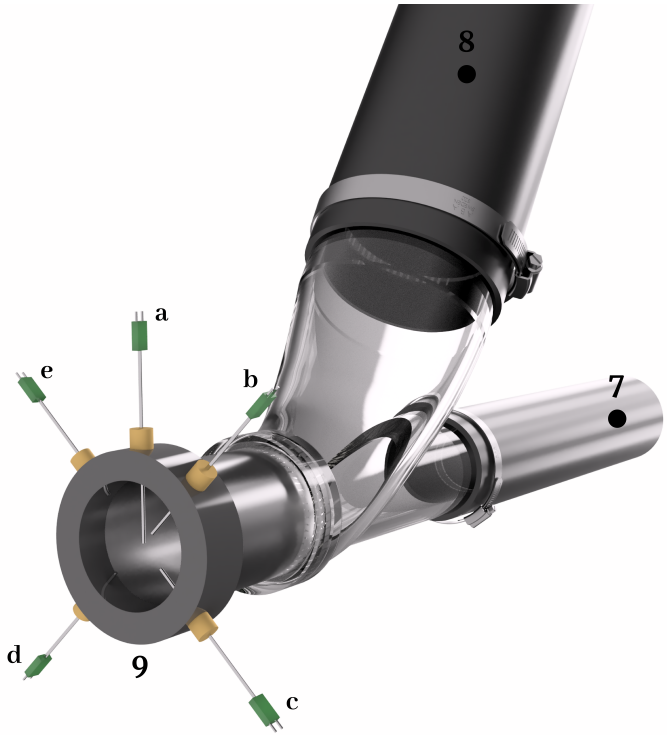

Figure 3.7: *Representation of the thermocouple array located at the junction outlet section.*

in the images, but it will be considered for the calculation of condensation mass flow rate in order to compare with the 3D CFD simulations across the whole cross section.

Table 3.2: *Thermocouple array protrusion and angle*

	a	b	c	d	e
Protrusion	R	0.75R	0.5R	0.25R	1 mm
θ (angle)	0°	45°	135°	225°	315°

3.2.5.1 Derivation of method

The underlying idea of the proposed method is that the condensation due to the mixing of humid streams releases its latent heat, thus increasing the temperature of the flow. If the streams to be mixed were dry instead, condensation

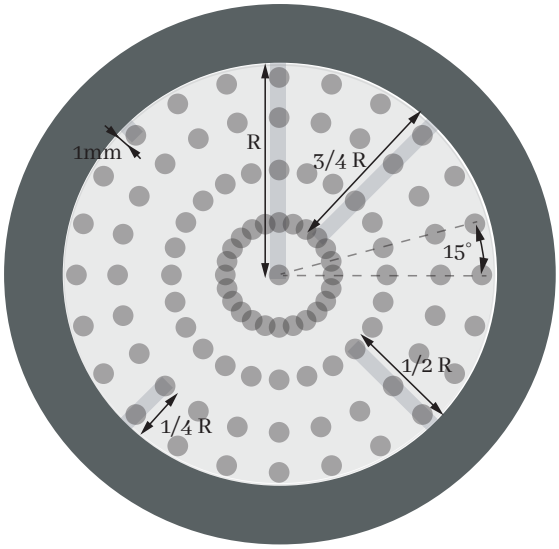

Figure 3.8: *Location of 97 temperature measurements performed at the juntion outlet section.*

will not appear. Therefore, by comparing the temperature when condensation appears against that of the case without condensation with the same inlet conditions, one is able to quantify the condensation mass flow rate. In this way, the temperature is experimentally characterized at the section of interest (see Fig. 3.8) twice for the same working point: once injecting the desired water and again with no water injected. By casting the corresponding energy balances for the two configurations and assuming certain simplifications, it will be shown that the difference in temperature of the dry and humid cases is proportional to the released energy of the condensation process and, in turn, to the condensation mass flow rate.

Figure 5.1 shows a scheme of the volume control for the three-way junction, where the factors to take into account for the energy balance are presented. Equation 3.4 presents the energy balance in steady state, being $\dot{H}_0$ the flow rate of stagnation enthalpy associated to each stream, considering perfect gas assumption and averaging over the cross section (Eq. 3.5).

$$\dot{H}_{0\_in,air} + \dot{H}_{0\_in,EGR} + \dot{Q}_{cond} = \dot{H}_{0\_outlet} + \dot{Q}_{ext} \quad , where \tag{3.4}$$

$$\dot{H}_0 = \int_{SC} \rho \cdot \left(h + \frac{c^2}{2} \right) \cdot \overrightarrow{u} \cdot \overrightarrow{dA} = \dot{m} \cdot \overline{h_0} \overset{Assuming}{\underset{perfect,gas}{=}} \dot{m} \cdot \overline{C_p} \cdot \overline{T_0} \tag{3.5}$$

Left hand side of equation 3.4 shows the enthalpies of the two inlet streams flowing into the three-way junction, being the (fresh air) inlet $\dot{H}_{0\_in,air}$ and the stream coming from the LP-EGR $\dot{H}_{0\_in,EGR}$. Another term on equation 3.4 is the heat released due to condensation, which only appears in the test in which the water injection exists (Q_{cond}). In the right hand side of equation 3.4, the enthalpy of the outlet flow (characterized by the thermocouple array) is $\dot{H}_{0\_outlet}$, and, finally, the term related to the heat exchanged with the surroundings is Q_{ext}.

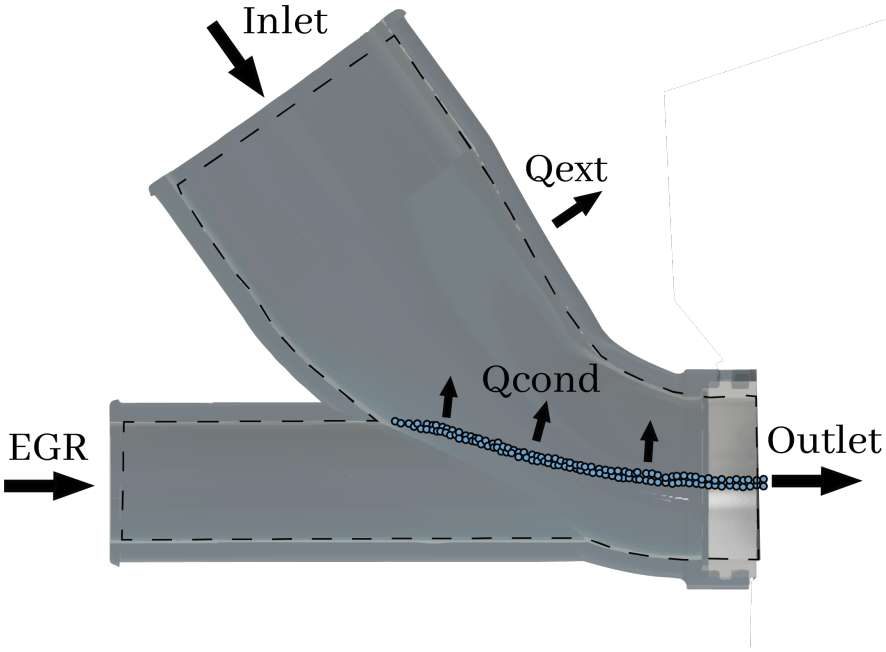

Figure 3.9: *Scheme of control volume with energy transfers for a three-way junction with in-flow condensation.*

Eq. 3.6 and Eq. 3.7 present the enthalpy balance for the cases with (w) and without (w/o) injection, respectively. In these, Eq. 3.4 is written for the considered case, isolating the stagnation outlet enthalpy. Equation 3.5 is used as well and Q_{cond} is expressed in terms of the latent heat L and the condensed mass flow rate of water $\dot{m}_{H_2O}$.

$$\left[\dot{m}_t \cdot \overline{C_p} \cdot \overline{T}_{0,out}\right]_w = \dot{m}_{H_2O} \cdot L - \dot{Q}_{ext,w} + \left[\dot{m}_{in} \cdot \overline{C_{p_{in}}} \cdot T_{0,in}\right]_w + \left[\dot{m}_{EGR} \cdot \overline{C_{p_{EGR}}} \cdot T_{0,EGR}\right]_w \tag{3.6}$$

$$\left[\dot{m}_t \cdot \overline{C_p} \cdot \overline{T}_{0,out}\right]_{w/o} = 0 - \dot{Q}_{ext,w/o} + \left[\dot{m}_{in} \cdot \overline{C_{p_{in}}} \cdot T_{0,in}\right]_{w/o} + \left[\dot{m}_{EGR} \cdot \overline{C_{p_{EGR}}} \cdot T_{0,EGR}\right]_{w/o} \tag{3.7}$$

Equation 3.8 considers the subtraction between Eq. 3.7 and 3.6, assuming that the heat transfer with the surroundings is the same for both cases $\left(Q_{ext,w} = Q_{ext,w/o}\right)$:

$$\dot{m}_t \cdot \overline{C_p} \cdot \overline{T_{0,out,w/o}} = \dot{m}_t \cdot \overline{C_p} \cdot \overline{T_{0,out,w}} - \dot{m}_{H_2O} \cdot L \tag{3.8}$$

Equation 3.9 then presents the calculation of the water mass flow rate condensed by the mixing of two streams for each area division (see section 3.2.5), considering that mass flow rate is evenly distributed. The $\overline{C_p}$ that is really employed is calculated locally (cell to cell). In there, it is considered the temperature of the cell and a mass weighted average of both gases (dry air and water vapor). Finally, Equation 3.10 provides the total condensation mass flow rate going through the junction outlet.

$$\dot{m}_{H_2O}(i) = \frac{\frac{\dot{m}_t}{n_{cells}} \cdot \overline{C_p}(i) \cdot \left(\overline{T_{0,out,w}}(i) - \overline{T_{0,out,w/o}}(i)\right)}{L} \tag{3.9}$$

$$\dot{m}_{H_2O} = \sum_{i=1}^{97} \dot{m}_{H_2O}(i) \tag{3.10}$$

A non-comprehensive list of the explicit and implicit hypotheses assumed for the indirect measurement of condensation flow rates would include: considering that introducing humidity on EGR stream and condensation does not affect neither the velocity flow field nor heat transfer with the surroundings, neglecting the effect of gravity over the condensed droplets, so that they are convected by

the flow in the same way as the released heat, and assuming a homogeneous distribution of mass flow rate at the target cross-section.

3.2.5.2 Example of proposed method

Figure 3.10 shows the different steps required to obtain the indirect measurement of condensation as proposed in Section 3.2.3.1, with an example of application. A custom postprocessing script is programmed in Python. A 500x500 grid is employed to linearly interpolate the scattered data coming from the 97 temperature samples (grey dots in Fig. 3.10). In this way, a continuous temperature field can be depicted at the junction outlet section, allowing to also calculate and display iso-contours as can be seen in Fig. 3.10.

Firstly, Figure 3.10a shows the temperature measurement for P1wet (with injection; see Table 3.4) at the cross section of study when the low-mixing junction Fig. 3.14b is used. In parallel, Figure 3.10b shows the temperature P1dry, where no injection is employed. Then, the difference of the temperature scalar field in the cross section between Fig. 3.10a and Fig. 3.10b is shown in Fig. 3.10c. In this picture, there is a region with no difference in temperature (hence, without condensation) and another region (the interface where the streams are mixed) where a positive temperature difference appears due to the local heat released due to condensation. Finally, Fig. 3.10d shows the water condensation at the outlet section when applying Eq. 3.9 to the difference in temperature shown in Fig. 3.10c.

3.3 Description and validation of a 3D-CFD model to assess junction condensation

The condensation submodel implemented in STAR-CCM+ for assessing junction condensation is based on the work presented by Serrano et al. [73], which estimates the quantity of condensates that a given cell of the simulation geometry should produce in order to reach an equilibrium state at saturated conditions, following an isenthalpic process. The estimation of the vapor that condenses is

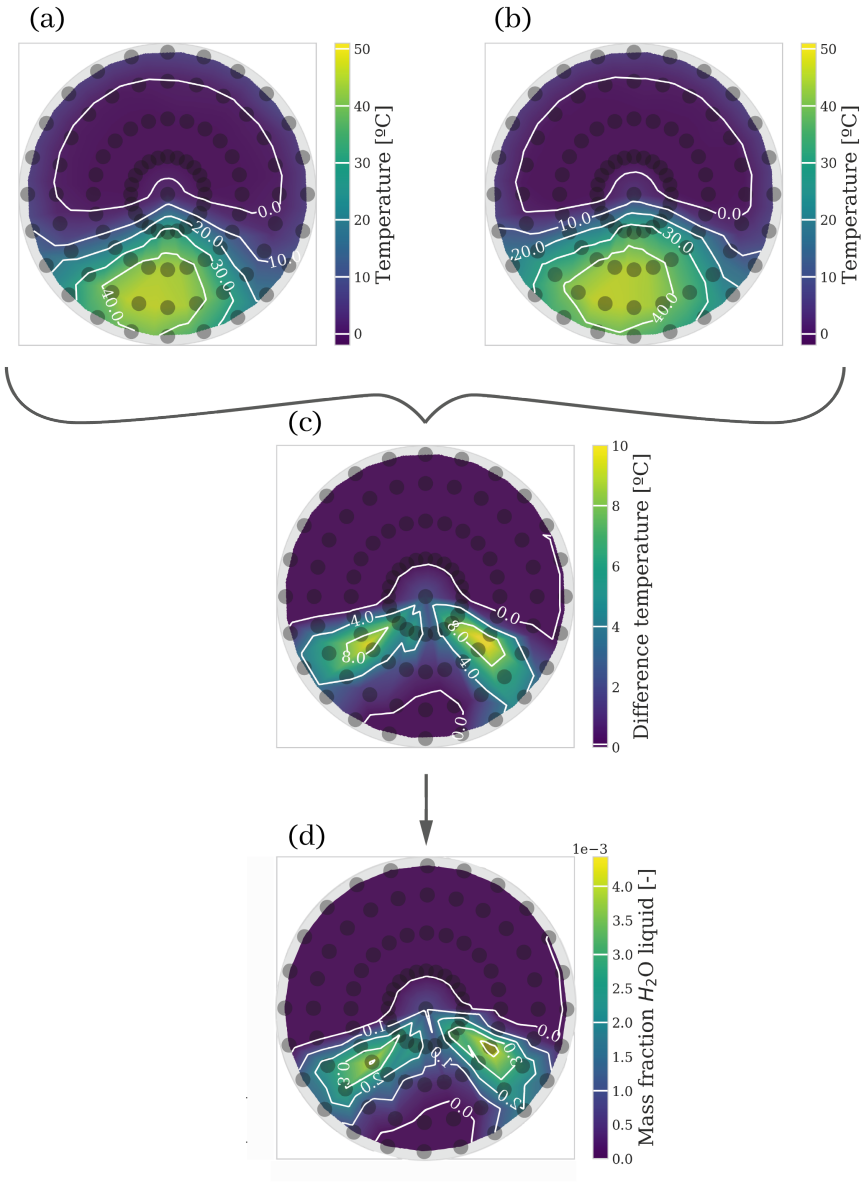

Figure 3.10: Temperature cross section at working points P1wet (a) and P1dry (b) with the temperature difference (c) between figure (a) and (b) and the water mass fraction obtained by the temperatures (d), corresponding to the low-mixing three-way junction.

calculated with the psychrometric variables of the gas, (temperature, pressure and specific humidity), which are in turn calculated employing Dalton's Law and an Antoine equation for the saturation curve. Then, the model interacts with the numerical solver through the transport equation source terms, replicat-

ing the actual condensation process. Notice that droplet nucleation and subsequent Lagrangian particle tracking, as employed by Schuster et al. [111, 112] or Wittmann et al. [113] in the framework of condensation in radial turbines, are not considered in this work due to the significant increase in computational effort when shifting to a Eulerian-Lagrangian approach [114]. It is possible that these phenomena (droplet distribution, fluid film) affect the compressor impeller damage, but it is true that the work presented by Galindo et al. [74] shows that the predicted condensation mass flow rate correlates very well with the impeller damage, regardless of the liquid water morphology.

Many simplifications and hypotheses were assumed for the model implementation due to the hard task to simulate the condensation phenomenon:

- Instantaneous condensation. Since low velocities appear at the LP-EGR junction, it is acceptable to assume that condensation occurs instantaneously whenever a cell presents over-saturation.
- Adiabatic walls. The walls are considered adiabatic as this model it is prepared for in-flow condensation.
- Evaporation process is not modeled. The evaporation would be minimal due to the conditions close to the saturation ones if the condensation has been employed.
- Condensed liquid water is not modeled. Liquid water mass fraction is low, even with highly condensing boundary conditions which not affect the mixing process. Therefore, the impact of this simplification on the conservation of the transport variables is negligible, close to a 0.5%.

A general transport equation is presented in Eq. 3.11. The solved transport equations governing the flow field (save for k and ω turbulent transport equations) are yielded when the terms in Table 3.3 are particularized in Eq. 3.11, considering that diffusion coefficients are *effective* (RANS). Besides, the custom source terms of mass, energy and momentum due to the condensation submodel are presented in Eqs. 3.12, 3.13 and 3.14 respectively.

$$\frac{\partial(\rho\varphi)}{\partial t} + \nabla\left(\rho\varphi u_i\right) = \nabla\left(\rho\Gamma_\varphi\nabla(\varphi)\right) + S_\varphi \tag{3.11}$$

Table 3.3: Convective, diffusive and source terms of solved transport equations (excluding turbulence).

Equation	φ	Γ_φ	S_φ
Mass	1	–	S_{vap}
Species	y	D	S_{vap}
Momentum	u_i	ν	$-\partial p/\partial x_i + f_m + f_v + S_{mom}$
Energy	h	α	$-Dp/Dt + f_t + f_v + S_{\text{ener}}$

$$S_{vap} = \frac{\rho\gamma_{air}(w_f - w_1)}{\Delta t} \tag{3.12}$$

$$S_{ener.} = -S_{vap}(L - c_pT) \tag{3.13}$$

$$S_{mom..} = S_{vap}\overrightarrow{u} \tag{3.14}$$

3.3.1 Numerical configuration

In this section, a description of the CFD model domain, mesh, setup and condensation submodel is provided. The numerical configuration is based on the works of Galindo et al. [71, 74].

3.3.1.1 Geometry and mesh

The element studied in this work is a three-way junction, such as the one shown in Fig. 3.11. In particular, the junction has two entries, one for the cold fresh air (inlet) and one for the humid and warm flow (EGR). The lengths of the inlet and the EGR lines in the numerical domain are extended three additional diameters upstream from the actual junction entries. Downstream the original outlet cross-section, five diameters are extruded. These extrusions are employed to limit the impact of the boundary conditions in the region of interest. Notice how the

compressor that should be in the outlet duct of a LP-EGR junction is not considered for the reasons discussed by Galindo et al. [71].

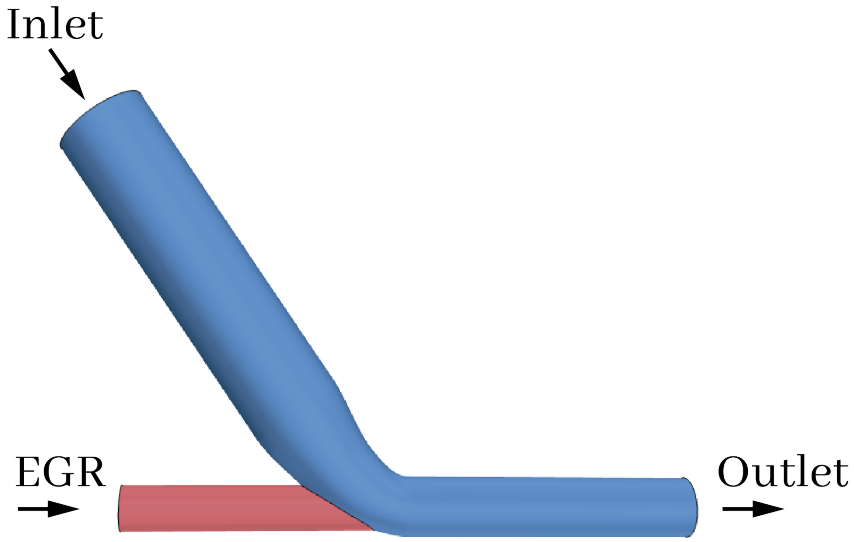

Figure 3.11: *Complete geometry of the LP-EGR junction*

To assess the impact of neglecting the actual experimental configuration in terms of outlet discharge, a more representative domain is considered in Fig. 3.12b. In this case, there is free flow discharge from the junction outlet into a cylindrical volume of 5 outlet diameters. The difference in condensation between the free-discharge domain (Fig. 3.12b) and the extruded-duct configuration 3.12a at the reference cross section is below 3%, considering that the target surface is 2 mm away from the duct outlet, since there is where visualization techniques are conducted. This difference in condensation is due to the expansion of the discharge stream after being released from the duct over these 2 mm. Figure 3.13 shows a comparison between the lower part of the target cross section with both domains. For the free-discharge domain (bottom side of Fig. 3.13), a small fraction of condensation region exists outside the target surface (depicted as a white line), which accounts for this missing 3% of condensation compared to the extruded-outlet domain (top side of Fig. 3.13) with the same cross-section area. Since the computational effort of the case representing the free discharge was 2 times higher than that of the extruded outlet duct, it was decided to proceed with the latter for the rest of the work.

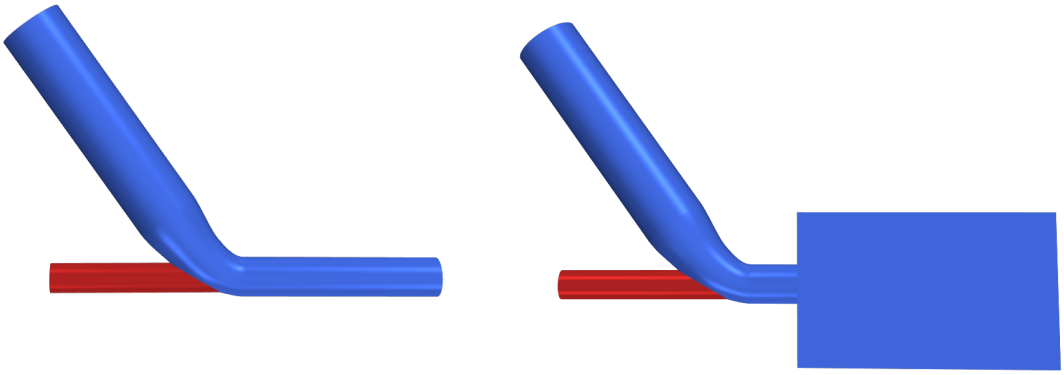

(*a*) *Extruded-outlet domain.* (*b*) *Free-discharge domain.*

Figure 3.12: *Comparison between the domains simulated, (a) the selected domain with the extruded outlet and (b) the free-discharge domain*

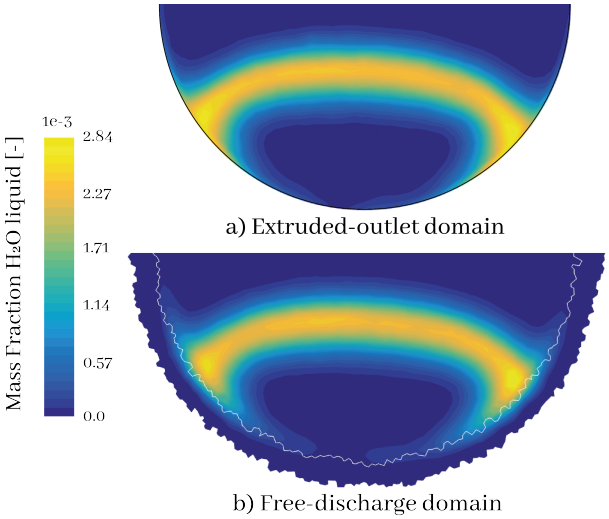

Figure 3.13: *Contours of condensed mass fraction at the bottom part of target cross-section with same area for (a) the extruded outlet domain and (b) the free-discharged domain.*

The meshes are composed of polyhedral cells with a base size of 0.6 mm as can be seen in Fig. 3.14. In the extruded regions, the corresponding cross section mesh is swept longitudinally. Eight prism layers are created in the vicinity of the walls in order to improve the prediction of the boundary layer. A grid independence study is performed with three different cell accounts at one operating point P1wet (see Table 3.4) and the low-mixing junction (Fig. 3.14): 300

thousand, 3 and 11 million elements. Figures 3.15 and 3.16 show respectively the profiles of temperature and condensed water mass fraction at the vertical diameter of the junction outlet, which is represented as a solid line in Fig. 3.14. The distributions plotted in Figs. 3.15 and 3.16 are in great agreement for the grids of 3M and 11M cells, whereas the mesh of 300k elements provides dissimilar profiles. In this way, the refinement from 300k to 3M cells changed condensation predicted by 13%, but a difference of only 1% was observed for the increase between 3 to 11 million cells. To limit the computational effort, the mesh of 3 million elements was therefore selected for the whole numerical campaign. The employed grid features a base size of 0.6 mm, with 99% of its wall cells presenting a y^+ value below 1.

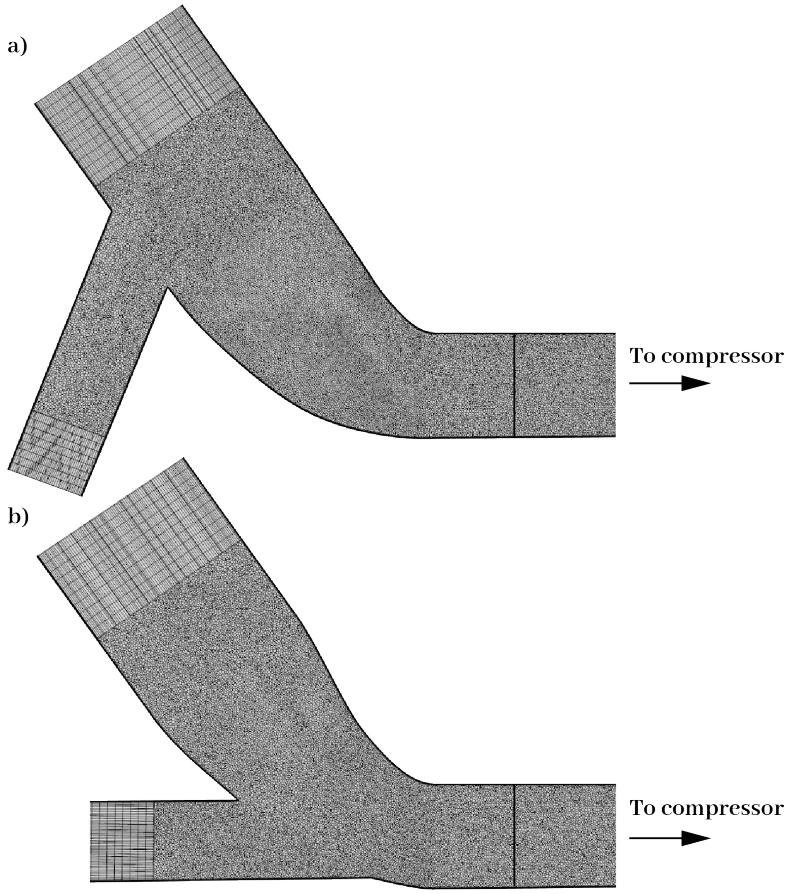

Figure 3.14: *High-mixing (above) and low-mixing (below) three-way junctions studied, with longitudinal section of mesh.*

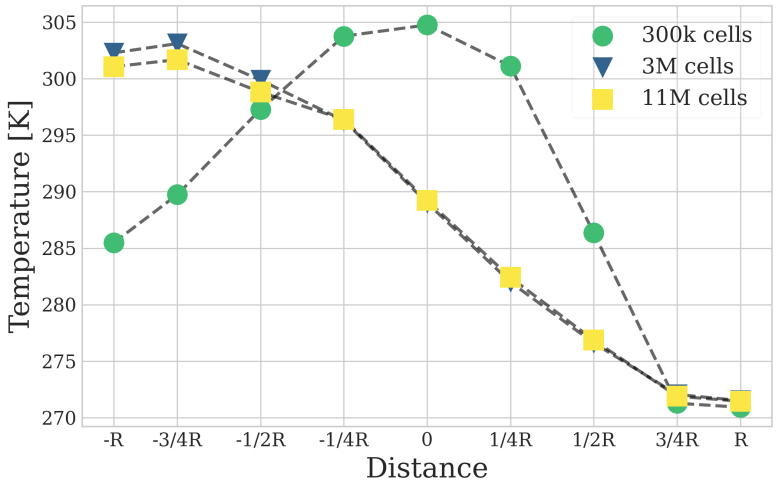

Figure 3.15: Temperature profiles for different grid densities at vertical diameter of high-mixing junction outlet at the operating point P1wet.

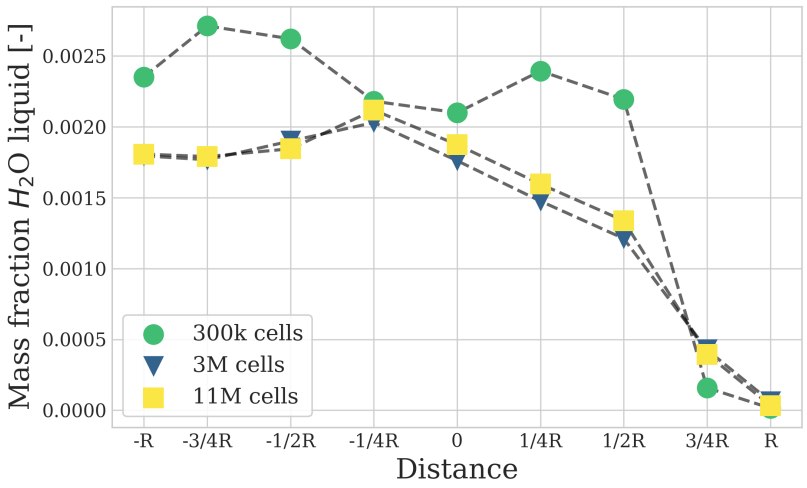

Figure 3.16: Profiles of condensed water mass fraction for different grid densities at vertical diameter of high-mixing junction outlet at the operating point P1wet.

3.3.1.2 Setup and boundary conditions

The numerical configuration of the simulations is set up following in accordance with the work of Galindo et al. [74, 28]. The segregated solver is selected in the

3D-CFD Finite Volume Method code STAR-CCM+ [105], employing second-order upwind schemes for the discretization of convective terms. Even though the maximum Mach number does not go above 0.2 for the considered simulations, the flow is not regarded as incompressible and the ideal gas equation of state is employed for air and vapor water.

For modeling turbulence(which is required as Reynolds numbers based on inlet and EGR diameters range between $18 \cdot 10^3$ and $51 \cdot 10^3$), RANS and unsteady RANS (URANS) approaches were used, both employing the *k*-ω SST submodel [115]. Steady RANS simulations have been used for the geometry shown in Fig. 3.14b, whose reduced mixing produced a fluctuation of condensation MFR (once converged) of less than 1%. However, URANS was required with the geometry depicted in Fig. 3.14a due to the strong condensation instability produced by the detachments that will be discussed in Section 3.3.2. The effect of such secondary flows on the transient behavior of the flow field has been analyzed by Galindo et al. [74]. The sensitivity of condensation prediction to time-step size has been assessed also at point P1wet (see Table 3.4) with the high-mixing junction (Fig. 3.14a), considering three different time-step sizes: $\Delta t = 10^{-4}$ s, $\Delta t = 5 \cdot 10^{-5}$ s and $\Delta t = 10^{-5}$ s. Condensation mass flow rate changes only by 0.01 % when comparing simulations with $\Delta t = 10^{-5}$ s and $\Delta t = 5 \cdot 10^{-5}$ s. A further coarsening on the time-step size from $\Delta t = 5 \cdot 10^{-5}$ to $\Delta t = 10^{-4}$ still provides a small variation of 0.09 % on condensed water. With these results, a time-step size of $\Delta t = 10^{-4}$ s is selected for the unsteady cases with a second-order implicit unsteady solver, which is similar to the one employed in the work of Galindo et al. [74] ($\Delta t = 2 \cdot 10^{-4}$ s). When unsteady simulations are employed, the solution is averaged for at least 40 ms, starting when condensation achieves a periodic state.

Concerning the boundary conditions, mass flow rate is established in both fresh air and EGR inlet boundaries, together with the total temperature and the mass fraction of each component (dry air and water vapor). The corresponding values for the two studied working conditions will be presented in Table 3.4. Turbulence intensity of 0.01 was set in both inlet boundaries. Regarding the outlet specifications, the test rig ambient pressure is established as the outlet boundary condition, whereas the compressor intake in an internal combustion engine would operate slightly below atmospheric pressure. In any case, Tarí

[116] showed a low impact of the junction pressure on the generated condensation rate.

3.3.2 Results and discussion

3.3.2.1 Test campaign

In order to proceed with the study of the secondary flows, condensation pattern, quantification of the in-flow water condensation in a LP-EGR junction while a validation of the 3D-CFD condensation model is obtained, different working points and geometries are selected to represent the operating range of a C-segment passenger car.

As can be seen in Table 3.4, the operating conditions considered in the test matrix present a 50% difference in the EGR rate, which is obtained by modifying the inlet MFR. These operating points share the same EGR temperature, EGR mass flow rate, specific humidity when water is injected (wet cases) and 0 when it is not (dry cases), keeping a similar inlet temperature. A higher EGR temperature than the dew conditions was set, in order to prevent condensation at the cooler and therefore study the condensation generated only on the three-way junction. Finally, a low temperature (near 0°C) was set at the inlet, to represent intake from a cold weather.

Table 3.4: *Test Matrix*

Operating points	P1wet	P1dry	P2wet	P2dry
EGR Temperature [°C]	50	50	50	50
EGR mass flow rate [kg/h]	40	40	40	40
EGR Rate [%]	21	21	32	32
Specific Humidity [g/kg]	60	0	60	0
Inlet Temperature [°C]	-2	-2	0	0
Inlet mass flow [kg/h]	150	150	85	85

Additionally, two three-way junction geometries (Fig. 3.14) are used to study

their influence on the condensation produced, with the objective of producing a completely different flow pattern and condensation. As can be seen, Fig. 3.14b shows a geometry where the EGR duct is aligned with the outlet duct. On the contrary, Fig. 3.14a depicts a geometry with the EGR branch oriented towards the fresh air inlet.

3.3.2.2 Longitudinal evolution of the flow

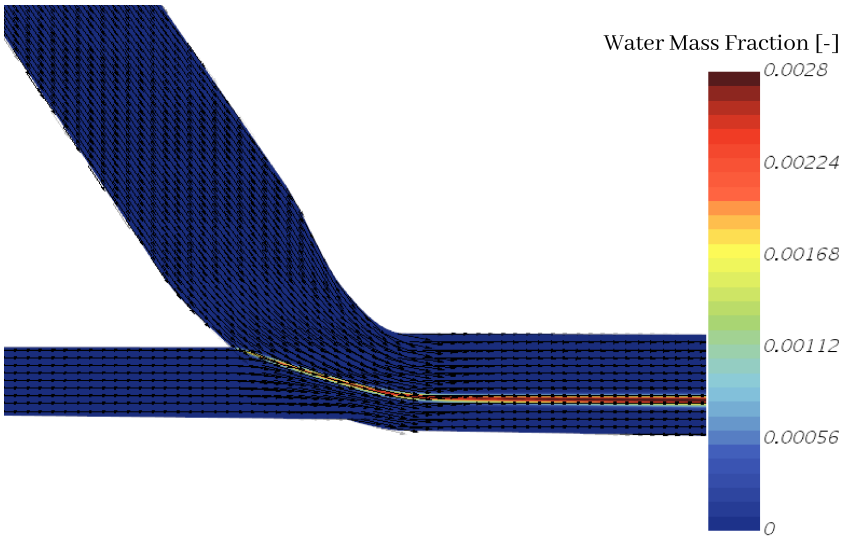

Figure 3.17: *Condensation water mass fraction together with in-plane velocity vectors in the longitudinal section for the junction A at the operating point P1*

In Figures 3.17 and 3.18, a longitudinal cross-section of the CFD simulation results is provided for the working point P1 (see Table 3.4) with both geometries of study. In the case of Fig. 3.18, the variables of the unsteady simulation are time-averaged. In these figures, the liquid condensation water produced by the CFD simulation at the junction due to the mixing process is shown. The three-way junction of Fig. 3.17 displays a reduced air-EGR mixing in the longitudinal section, due to the alignment between the EGR duct and the main duct. On the contrary, Fig. 3.18 shows a strong separation when the EGR stream is discharged into the air mass flow due to the geometry of junction B, which presents the EGR duct oriented slightly opposed to the main stream. The enhanced mixing at the longitudinal cross-section of junction B (Fig. 3.18) compared to junction A

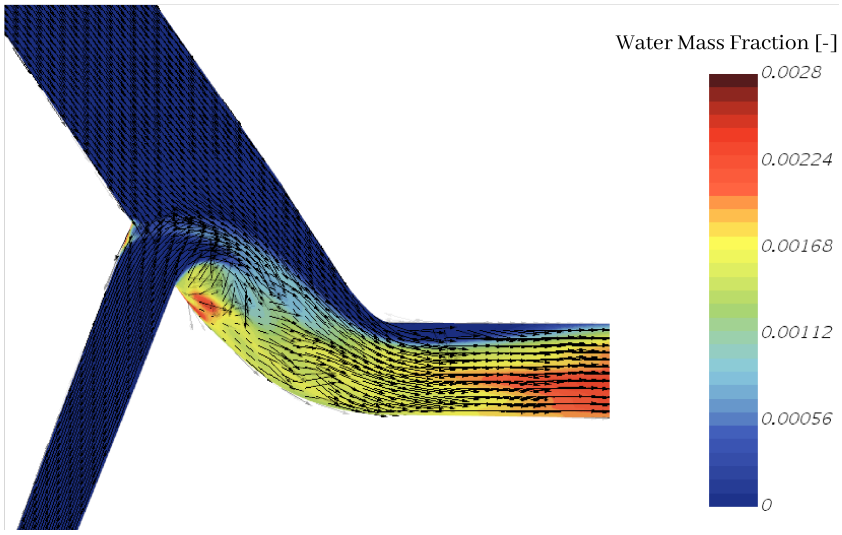

Figure 3.18: *Time-averaged condensation water mass fraction together with in-plane velocity vectors in the longitudinal section for the junction B at the operating point P1*

(Fig. 3.17) entails an increase in condensation.

3.3.2.3 Transversal secondary flows: PIV vs CFD

According to Galindo et al. [71], the condensation produced in the junction depends on the intensity of the air-EGR mixing. Therefore, the first comparison to be conducted between experimental PIV measurements (as described in Section 3.2.2.1) and CFD simulations is in terms of secondary flows at the cross section of study (see Fig. 3.11). With this purpose, in-plane velocity contours of both techniques are shown in the Figs. 3.19, 3.20, 3.21 and 3.22 along with velocity vectors.

For all the figures, the iso-velocity of 2 m/s is represented at each figure, including as well dashed curved arrows to represent the main vortices that can be identified. In first place, Figures 3.19 and 3.20 show the velocity at operating points P1 and P2 while the three-way junction A is set. The flow at these working points is alike. There is a pair of large counter-rotating vortices in the upper part of the cross-section generated by the cold stream that comes from the upper duct, since this branch behaves as an elbow (see Fig. 3.17), thus creating the

so-called Dean vortices [66, 117]. Such Dean vortices appear at curved pipes due to the inertia of the core stream, that tends to flow towards the outer part of the bend. This centripetal motion in the elbow plane is balanced by the fluid returning close to the walls [118]. Hence, a pattern of secondary flows is established as a pair of counter-rotating vortices [119]. These Dean vortices induce in turn a second pair of counter-rotating vortices in the lower part of the transversal section, because the EGR stream is aligned with the outlet pipe in three-way junction A (Fig. 3.17) and therefore is not suitable to create secondary flows by itself.

For the low mass flow rate case (P1), two small counter-rotating swirling structures are indeed created at the low part of the cross section in the CFD case (Fig. 3.19b), while the experimental case shows only one of the two swirl structures (Fig. 3.19a), probably due to their low intensity. Concerning the working point P2 with a higher mass flow rate than P1, Figure 3.20 shows the two pairs of counter-rotating swirling structures, both measured by PIV and predicted by CFD simulations.

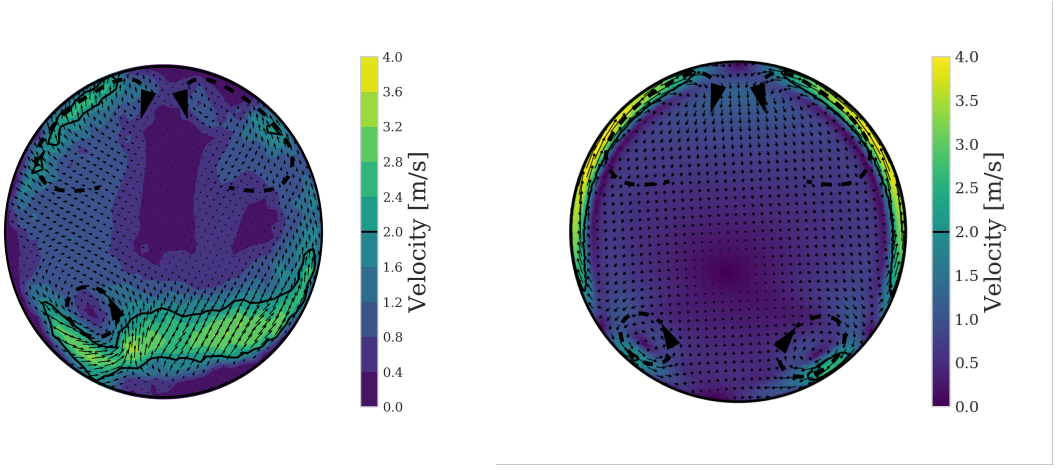

(a) *PIV technique* (b) *CFD simulation*

Figure 3.19: *Comparison between the in-plane velocity field at P1 and junction A for the PIV technique (a) and the CFD RANS simulations (b). Large dashed arrows are manually added to highlight main vortical patterns.*

Finally, Figures 3.21 and 3.22 show the results with the junction B, in which a higher penetration of the EGR stream exists due to the geometry. As a consequence, the presented vortical patterns and secondary flows are of greater

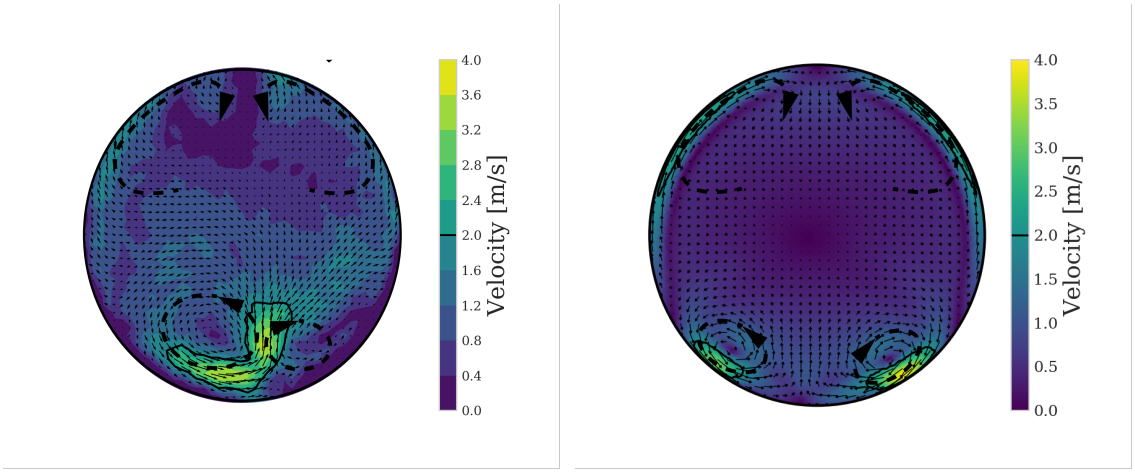

(*a*) *PIV technique* (*b*) *CFD simulation*

Figure 3.20: *Comparison between the in-plane velocity field at P2 and junction A for the PIV technique (a) and the CFD RANS simulations (b). Large dashed arrows are manually added to highlight main vortical patterns.*

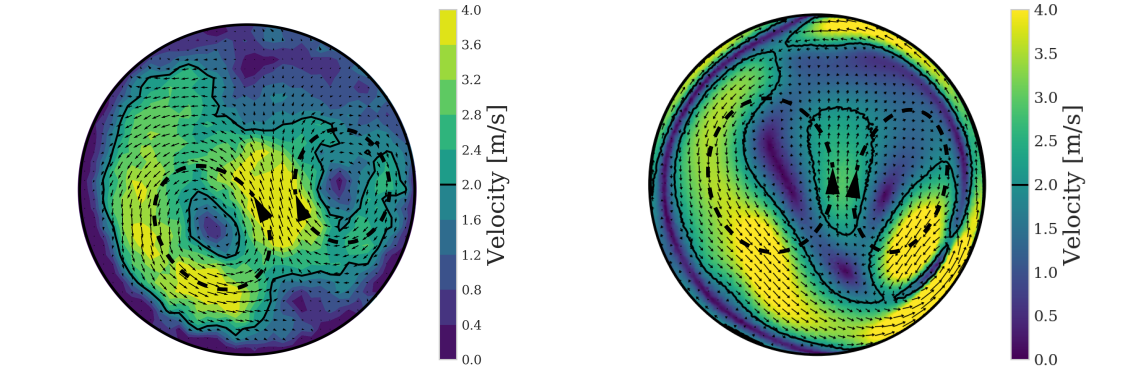

(*a*) *PIV technique* (*b*) *CFD simulation*

Figure 3.21: *Comparison between the time-averaged in-plane velocity field at P1 and junction B for the PIV technique (a) and the CFD URANS simulations (b). Large dashed arrows are manually added to highlight main vortical patterns.*

intensity when compared to junction A (Figures 3.19 and 3.20). The impact of junction geometry is well predicted by CFD simulations.

The significant detachment of the EGR stream at junction B due its high penetration into the core stream and the sharp bend between its duct and the main

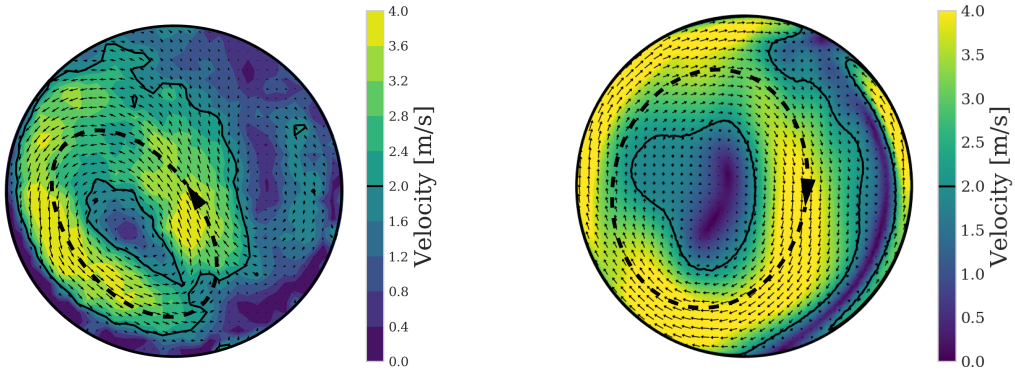

(a) *PIV technique* (b) *CFD simulation*

Figure 3.22: *Comparison between the time-averaged in-plane velocity field at P2 and junction B for the PIV technique (a) and the CFD URANS simulations (b). Large dashed arrows are manually added to highlight main vortical patterns.*

duct (see Fig. 3.18), causes the flow of junction B to be inherently unsteady and thus require URANS instead of RANS, unlike junction A. These transient oscillations in junctions were also experienced by Lu et al. [120], in the form of low-frequency temperature fluctuations due to the mixing of hot and cold streams. Lyne [121] first discovered that the elbow centrifugal pattern (and therefore the direction of the Dean vortex pair) can be reversed when shifting from steady to unsteady flow. Tunstall et al. [117] analyzed the complex vortical pattern at T-junctions, showing how the Dean vortices present an unsteady switch between different modes. Sakowitz et al. [66] found that Dean-like vortices were predicted with opposite directions depending on whether LES or k-ϵ URANS were considered.

The literature shows that flow separation makes the case to be more sensitive to variations of geometry and working points, and therefore it is more difficult to accurately predict its transversal secondary flows. One may have expected the Dean-like vortical pattern of the upper part of junction A (Figs. 3.19 and 3.20) to appear in junction B again, as the main duct bend angle is the same for both junctions. Aside from the reported complexity of the unsteady vortical phenomena, the greater intensity of secondary flows at junction B would mask any lesser pattern, such as the Dean vortices of junction A. The comparison of secondary flows strength can be assessed through the area determined by the iso-velocity

of 2 m/s, being much greater at junction B (Figs. 3.21 and 3.22) than at junction A (Figs. 3.19 and 3.20).

All in all, there is an agreement between CFD simulations and the PIV technique at the Fig. 3.21, when observing the velocity pattern produced by the two counter-rotating swirling structures at the center of the cross section. These larger and more intense vortices increase the mixing of air and EGR streams compared to that of junction A. Working point P2 presents an EGR rate 50% greater than that of P1 (see Table 3.4), so the penetration of the EGR stream into the fresh air is even more intense than the one depicted in Fig. 3.18. This severe flow detachment at P2 for junction B generates a clearly asymmetrical in-plane velocity field in Fig. 3.22, in which both PIV and CFD depict a single large vortex, but with different rotating direction. As aforementioned, this unstable flow field is more challenging to be modeled by CFD due to its greater sensitivity to slight variations on geometry or upstream boundary conditions.

3.3.2.4 Analysis of condensation patterns: PLV vs CFD

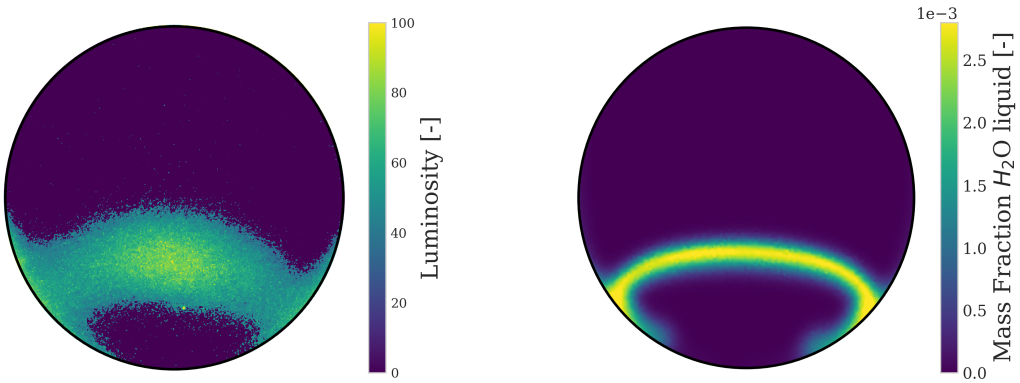

(a) *Laser visualization* **(b)** *CFD simulation*

Figure 3.23: *Comparison between the luminosity on the Laser visualization (a) and the mass fraction of condensed water predicted by the CFD RANS simulation (b) at the outlet cross section of junction A for working point P1.*

Section 3.3.2.3 has shown an overall good agreement between CFD simulations and experimental tests in terms of secondary flow patterns, which is critical

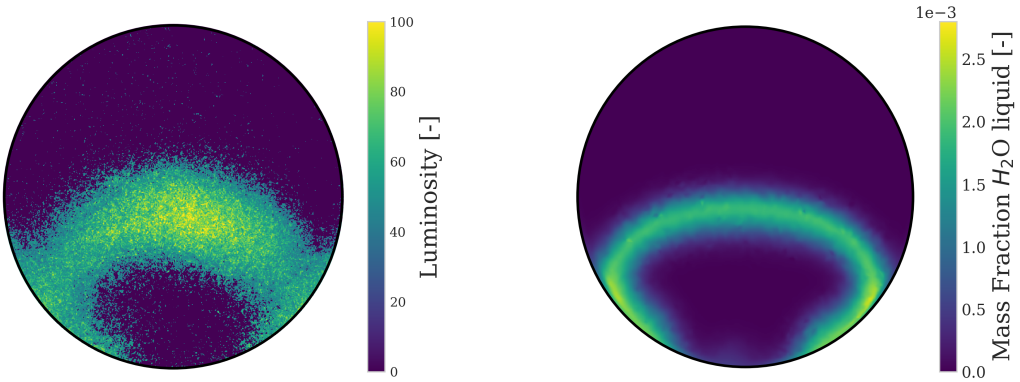

(*a*) *Laser visualization* (*b*) *CFD simulation*

Figure 3.24: *Comparison between the luminosity on the Laser visualization (a) and the mass fraction of condensed water predicted by the CFD RANS simulation (b) at the outlet cross section of junction A for working point P2.*

for condensation [71]. In any case, the prediction of the condensation distribution at the target cross section is assessed by comparing the water mass fraction calculated by CFD simulations with the luminosity obtained by the planar laser-induced visualization described in Section 3.2.3.1. The underlying idea is that the condensation produced experimentally at the section is correlated with the measured luminosity, i.e, a greater quantity of condensed water would reflect light in a more intense way when a laser sheet is projected onto the cross section.

Figures 3.23, 3.24, 3.25 and 3.26 show the luminosity with a range between 0-255 for the case of the experimental laser visualization and the mass fraction of condensed water for the CFD simulations, depending on the working point and the geometry employed. The mass fraction of condensed water at CFD simulations as shown in these figures is obtained by calculating the condensed mass flow rate at the cross section and dividing by the total mass flow rate

Figures 3.23 and 3.24 show that the condensation is produced at the thin interface of the two streams (EGR and fresh air). As it is shown in Figures 3.19 and 3.20, the mixing occurs at the bottom part of the cross section due to vertices that add fresh air from the core to the lower side, which is dominated by the EGR stream. If junction A is kept but the EGR rate is increased (P2), Fig. 3.24 presents a higher penetration due to the higher EGR rate than Fig. 3.23. This dif-

ference causes a larger condensation interface due to the increase of air-EGR of mixing.

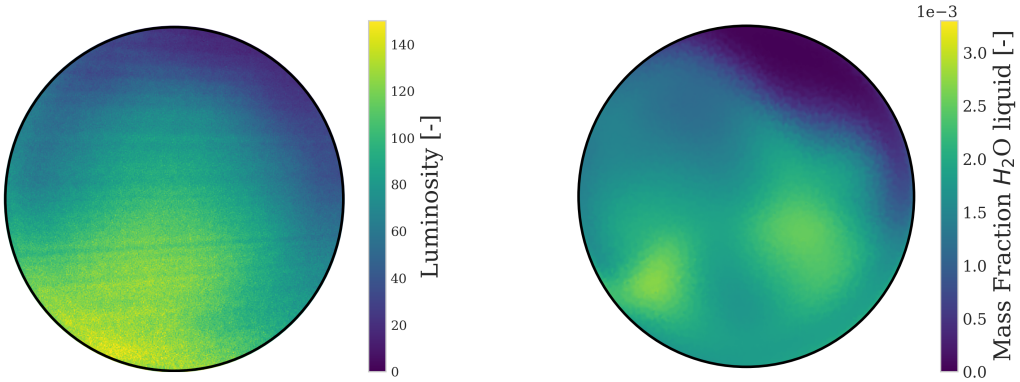

(*a*) *Laser visualization* (*b*) *CFD simulation*

Figure 3.25: *Comparison between the luminosity on the Laser visualization (a) and the time-averaged mass fraction of condensed water predicted by the CFD URANS simulation (b) at the outlet cross section of junction B for working point P1.*

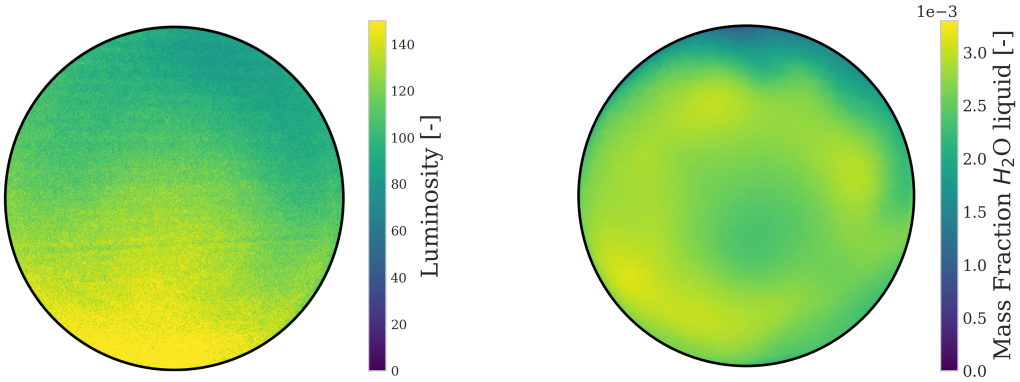

(*a*) *Laser visualization* (*b*) *CFD simulation*

Figure 3.26: *Comparison between the luminosity on the Laser visualization (a) and the time-averaged mass fraction of condensed water predicted by the CFD URANS simulation (b) at the outlet cross section of junction B for working point P2.*

When three-way junction B is considered, Figures 3.25 and 3.26 show condensation at the whole perpendicular cross-section for both working points. This happens due to the stronger secondary flows and mixing existing for junction B,

as seen previously in Figs. 3.21 and 3.22.

Finally, a quantitative comparison is conducted to assess the capability of the CFD model to predict the influence of junction geometry and working point on condensation. To do so, values of luminosity (experimental) and condensed mass fraction (numerical) depicted at Figs. 3.23-3.26 are averaged at the outlet cross section. The results for junction J and working point P for each technique are normalized with those of the case with higher condensation, i.e., the working point P2 with the junction B. Equations 3.15 and 3.16 show how this average and normalization are conducted:

$$\widetilde{L}_{\text{J,P}} = \frac{\sum L_{\text{J,P}}/N}{\sum L_{\text{JB,P2}}/N} \tag{3.15}$$

$$\widetilde{y}_{\text{cond. J,P}} = \frac{1/A \sum y_{\text{cond. J,P}} \cdot dA}{1/A \sum y_{\text{cond. JB,P2}} \cdot dA} \tag{3.16}$$

As a sample of the method employed for obtaining the data that will be reported in table 3.5, the calculations for junction B at working point P1 are described. First, luminosity is summed over all pixels and divided by this number of pixels, providing an average luminosity of $L_{\text{JB,P1}} = 62.84$ (see Fig. 3.25a). For that point, the area-weighted average of condensed mass fraction is directly provided by StarCCM+, with a value of $y_{\text{cond. JB,P1}} = 1.58 \cdot 10^{-3}$ (see Fig. 3.25b). To normalize, the same method is applied for junction B at working point P2 (maximum condensation), yielding an average luminosity of $L_{\text{JB,P2}} = 91.70$ (see Fig. 3.26a) and an area-weighted average of liquid water mass fraction of $y_{\text{cond. JB,P2}} = 1.90 \cdot 10^{-3}$ (see Fig. 3.26b). Dividing the corresponding values in accordance with Eqs. 3.15 and 3.16, one obtains the normalized values for the experiments ($\widetilde{L}_{\text{JB,P1}} = 0.69$) and for the CFD simulations ($\widetilde{y}_{\text{cond. JB,P1}} = 0.83$).

Table 3.5 shows the normalized luminosity for the laser visualization technique and the normalized condensation at the CFD simulations. As can be seen, the tendencies discussed in previous sections are in agreement with the quantification presented at table 3.5. Both junctions provide less condensation at working point P1 than at P2. Also, three-way junction A produces less condensation than junction B for both operating conditions. Even though the relationship between condensation mass fraction and luminosity is not necessarily linear, the

Table 3.5: *Normalized luminosity (exp) and predicted condensation (CFD) for all the test matrix.*

	Operating point	$\widetilde{L}_{\text{J,P}}$ (exp)	$\widetilde{y}_{\text{cond. J,P}}$ (CFD)
Junction A	P1	0.14	0.18
Junction A	P2	0.19	0.19
Junction B	P1	0.69	0.83
Junction B	P2	1.0	1.0

agreement between the normalized luminosity and normalized condensation is satisfactory for the 3 remaining cases (excluding obviously the one used to normalize).

3.3.2.5 Analysis of temperature distribution: Temperature array measurements vs CFD

Temperature contours at the junction outlet cross section shown in Fig. 3.14, obtained by 3D-CFD simulations as well as measured experimentally,are shown in Fig. 3.27 (for the low-mixing junction) and Fig. 3.28 (for the high-mixing junction). Experimental data is gathered with the strategy described at Section 3.2.5 for the two operating points with water injection activated ("wet", in Table 3.4), so that there is condensation due to mixing. CFD results are obtained at the cross section mesh but then resampled at the 97 locations displayed in Fig. 3.8, for the sake of consistency with the experimental data.

Figures 3.27a and 3.27b show the temperature distribution at the working point P1wet when the low-mixing three-way junction is employed, for the experimental test and for the 3D-CFD simulation. As can be seen, a similar pattern is found with both methods: a higher temperature at the bottom of the section, representing the core of the EGR stream; a lower temperature at the upper part, corresponding to the cold fresh air and a strong temperature gradient located in the interface of both regions. The temperature field is consistent with the ob-

jective of the design of keeping the streams separated, i.e., with low mixing. The temperature gradient in the interface is steeper for the CFD case (Fig. 3.27b) than for the experiments (Fig. 3.27a).

Figures 3.27c and 3.27d depict temperature contours at the working point P2wet, again for the three-way junction that is designed to reduce the mixing between streams. Temperature distributions follow the same pattern as already described for Figs. 3.27a and 3.27b. In the case of point P2wet, the higher EGR rate compared to point P1wet (see Table 3.4) increases the hot area for both experimental and numerical results.

It is worth noting that CFD predictions of temperature (Fig. 3.27b and 3.27d) depict a maximum of 50 °C, corresponding to the inlet EGR temperature (see table 3.4). However, experimental measurements do not achieve the same temperature of 50 °C (see Fig. 3.27a and 3.27c) due to the heat transfer with the surroundings. Indeed, the minimum temperature of the experiments is about 0 °C (air inlet temperature in table 3.4), but it is achieved only at the core of the fresh air stream. Heat transfer is again responsible for this observed tendency of the fluid at the vicinity of the walls to present temperatures closer to the cross-section average in the experiments than what is predicted by CFD. In any case, the method developed in section 3.2.4.1 does not employ directly the values of the temperature at the humid working points P1wet and P2wet (Fig. 3.27a and 3.27c) but the temperature differences with their dry counterparts P1dry and P2dry. Therefore, the effect of neglecting the heat transfer in CFD should not be a major concern for the experimental indirect determination of the condensation mass fractions, provided that heat transfer remains the same with and without condensation, as assumed by Eq. 3.8.

Regarding the cases with the high-mixing three-way junction, Figures 3.28a and 3.28b show the temperature contours for operating conditions P1wet. The change in pattern compared to Fig. 3.27 is significant: while CFD simulations (Fig. 3.28b) predict the EGR stream to be still located at the bottom of the section but with a much gradual transition towards the cold region, the experiments (Fig. 3.28a) show that the EGR core with the high-mixing junction is able to penetrate the cold stream and be located at the middle of the cross section. In any case, both methods suggest at P1wet higher mixing in terms of lower temperature gradients than that of their counterparts with the low-mixing junction:

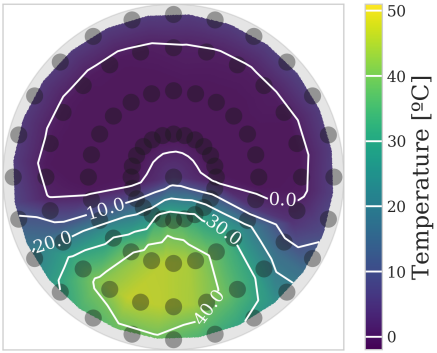

(a) Experimental results at P1wet

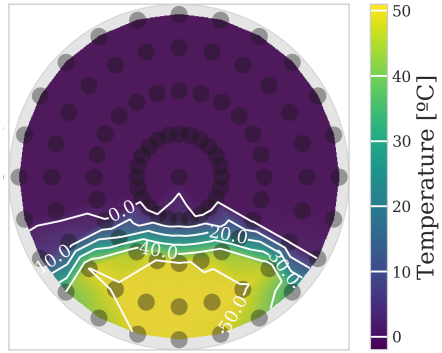

(b) CFD results at P1wet

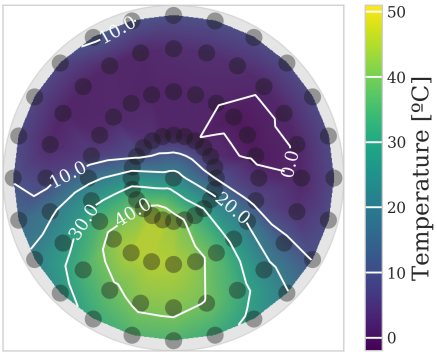

(c) Experimental results at P2wet

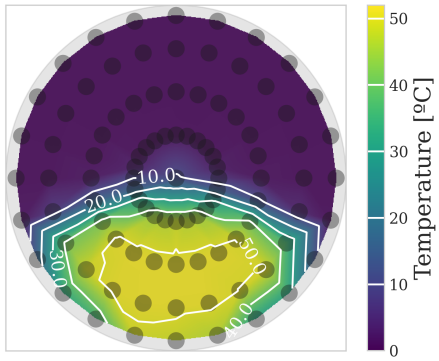

(d) CFD results at P2wet

Figure 3.27: *Temperature contours at low-mixing three-way junction outlet for two operating conditions, obtained by experiments and CFD simulations.*

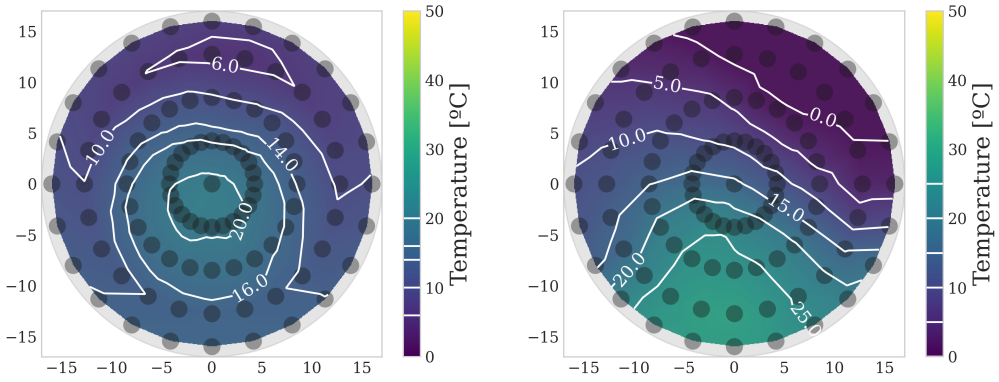

(a) Experimental results at P1wet

(b) CFD results at P1wet

(c) Experimental results at P2wet

(d) CFD results at P2wet

Figure 3.28: *Temperature contours at high-mixing three-way junction outlet for two operating conditions, obtained by experiments and CFD simulations.*

Fig. 3.27a and Fig. 3.27b. When shifting to point P2wet, CFD (Fig. 3.28d) predicts a higher penetration of the EGR stream, whereas experiments (Fig. 3.28c) show the greatest flow homogeneity of all the cases, with a temperature range at the cross-section of only 6 °C. Fig. 3.28c and Fig. 3.28d show also at P2wet reduced temperature differences due to the enhanced mixing of the junction displayed in Fig. 3.14a when compared with the results provided by the low-mixing junction (Fig. 3.27c and Fig. 3.27d).

In order to quantify the difference between temperature distributions obtained experimentally and numerically (as displayed in Fig. 3.27 and Fig. 3.28), the root mean square error (RMSE) is defined as follows:

$$RMSE = \sqrt{\frac{\sum_{i=1}^{N=97} \left(T_{exp,i} - T_{CFD,i}\right)^2}{n}} \ . \tag{3.17}$$

Since the maximum temperature difference that could be observed is

$$\Delta T_{max} = T_{EGR} - T_{inlet} \ , \tag{3.18}$$

which can be calculated for each working point using the information from Table 3.4, it will be used to normalize $RMSE$ (Eq. 3.17) by means of the following expression:

$$\widetilde{RMSE} = \frac{RMSE}{\Delta T_{max}} \cdot 100 \ . \tag{3.19}$$

Table 3.6 presents the results of $\widetilde{RMSE}$ for all the studied cases. As can be seen, the error between techniques is small, with $\widetilde{RMSE}$ of temperature distributions ranging between 2.8 % and 4.4 %. In this way, the CFD model is regarded as appropriate to predict the experimental temperature distributions. It is worth mentioning that the experiment may present some features that are not modeled and would have an impact on junction outlet temperature distribution, including: non-homogeneous velocity and temperature distribution at the junction inlets (despite the long, straight ducts), three-way junction manufacturing imperfections, junction conductive heat transfer and external convective heat transfer (despite material low conductivity).

Table 3.6: *Normalized RMSE for each working point and junction geometry.*

Operating point	Junction	$\widetilde{RMSE}$ [%]
P1wet	Low-mixing	2.81
P1wet	High-mixing	2.76
P2wet	Low-mixing	4.39
P2wet	High-mixing	3.72

3.3.2.6 Analysis of condensation mass flow: Indirect condensation measurements vs CFD

Contours of condensed liquid water mass fraction at the outlet cross section are displayed in Fig. 3.29 and Fig. 3.30, considering the low-mixing and high-mixing junctions, respectively. Experimental results have been obtained with the method developed in this work, explained in section 3.2.2.1. The condensation submodel described in section 3.3.1.2 and embedded in the 3D CFD cases is the one responsible for providing the numerical results. Again, CFD results have been resampled at the experimental thermocouple locations (see Fig. 3.8).

Figure 3.29 shows how the low-mixing junction prevents condensation from happening outside the air-EGR interface discussed in Fig. 3.27, which means that both the cold and hot streams present an unmixed core and only interact through that interface. Besides, it also confirms the shift of the interface towards the upper part of the cross section when increasing the EGR rate from P1wet to P2wet operating conditions, both for the experimental (Figs. 3.29a and 3.29c) and numerical (Figs. 3.29b and 3.29d) methods. The existence of condensation only at the air-EGR interface for the low-mixing junction and the modification of the location of such interface with the working point was also observed experimentally with the planar laser-induced visualization of droplet patterns. In this way, Fig. 3.29 shows that there is a strong agreement between the CFD predictions and the indirect measurements of condensation for the low-mixing junction.

The much wider regions with non-zero condensation mass fraction displayed in Fig. 3.30 for the high-mixing junction, compared to those of the low-mixing

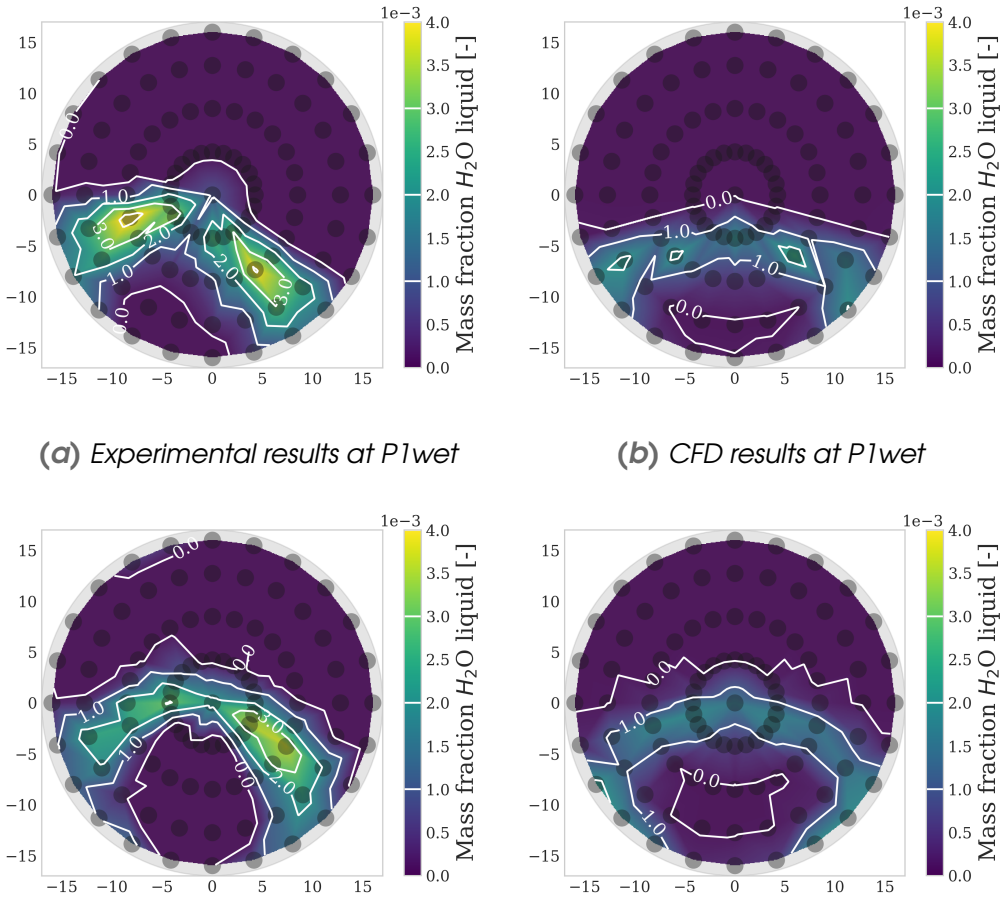

(a) Experimental results at P1wet

(b) CFD results at P1wet

(c) Experimental results at P2wet

(d) CFD results at P2wet

Figure 3.29: *Condensation mass fraction contours at low-mixing three-way junction outlet for two operating conditions, obtained by experiments and CFD simulations.*

junction (Fig. 3.29), establish a clear relation between junction design, mixing between streams and subsequent formation of condensation. Only the measurements for P1wet (Fig. 3.30a) suggest that the EGR stream has penetrated into the cold stream and there is an outer area surrounding that jet (see Fig. 3.28a), almost free from condensation. The rest of cases of Fig. 3.30 show generalized mixing and condensation. Planar laser-induced visualization of condensation for the high-mixing junction also provide patterns with fog across the whole section, showing less intensity at the upper part as depicted in Fig. 3.30.

In order to conduct a quantitative comparison of the condensed mass flow rate through the junction outlet cross section between experiments and CFD simulations, it is normalized with the total mass flow rate leaving the junction. Equation 3.20 shows the average mass fraction of liquid water obtained in this way:

$$\overline{\gamma_{cond}} = \frac{\dot{m}_{H_2O}}{\dot{m}_{tot,out}} \tag{3.20}$$

Besides, Eq. 3.21 computes a relative difference between average mass fractions of condensed water, considering the corresponding experimental and CFD results for each case:

$$\varepsilon = \frac{\left|\overline{\gamma_{cond}}_{,CFD} - \overline{\gamma_{cond}}_{,exp}\right|}{\overline{\gamma_{cond}}_{,exp}} \cdot 100 \tag{3.21}$$

Figure 3.31 shows the comparison between the average mass fraction of condensed water calculated with Eq. 3.20, at the high-mixing and low-mixing junctions (see Fig. 3.14) for the operating conditions P1wet and P2wet (see table 3.4). The average mass fractions are obtained experimentally and numerically, and the relative difference between them (Eq. 3.21) is displayed. Figure 3.31 shows the great increase of condensation when replacing the low-mixing with the high-mixing junction, as was anticipated when Fig. 3.29 and Fig. 3.30 were compared. Besides, while shifting from P1wet to P2wet (and thus increasing the EGR rate) with the low-mixing junction does not change significantly the condensation mass flow rate, it does magnify the average mass fraction of liquid water for the high-mixing junction.

Finally, the relative differences depicted in Fig. 3.31 range between 2 and

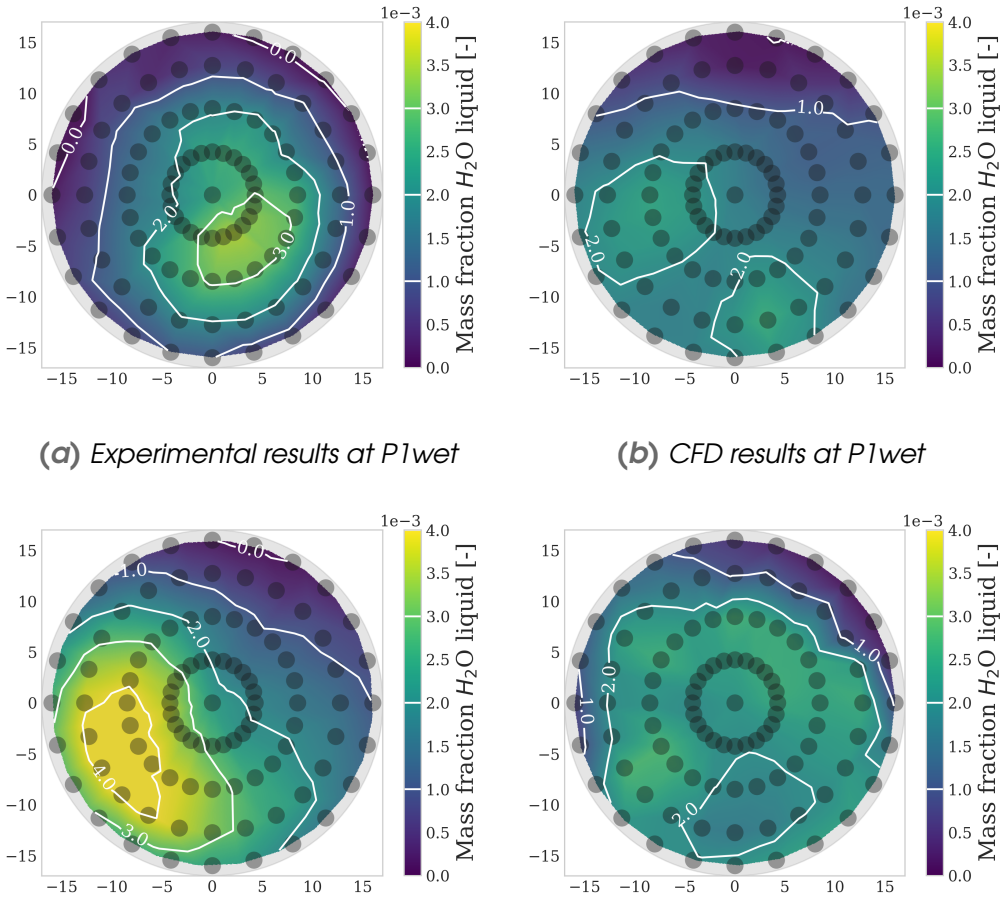

(a) Experimental results at P1wet

(b) CFD results at P1wet

(c) Experimental results at P2wet

(d) CFD results at P2wet

Figure 3.30: *Condensation mass fraction contours at high-mixing three-way junction outlet for two operating conditions, obtained by experiments and CFD simulations.*

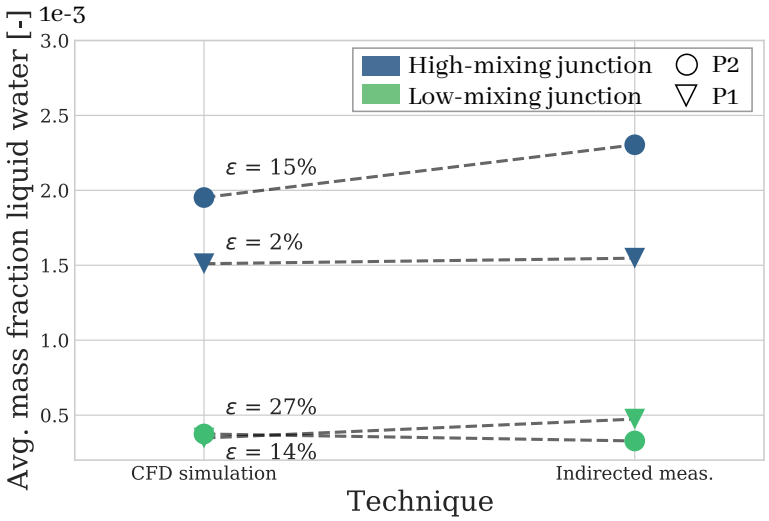

Figure 3.31: *Average mass fraction of liquid water for two junctions at two operating conditions, with relative differences between measurements and simulations.*

27%. A weighted-average error of $\bar{\varepsilon} = 11\%$ is calculated using Eq. 3.22. The fair agreement between CFD simulations and experimental measurements allow the trends to be consistent for each operating point and geometry regardless of the method, as shown in Fig. 3.31.

$$\bar{\varepsilon} = \frac{\sum_i |\dot{m}_{H_2O,CFD} - \dot{m}_{H_2O,exp}|}{\sum_i \dot{m}_{tot,out}} \cdot 100 \tag{3.22}$$

3.4 Conclusions

In this Chapter, the mixing between two streams with different psychrometric conditions in a three-way junction has been addressed by means of experiments and simulations. Firstly, the secondary flows presented at the outlet cross-section and the condensation pattern generated in the junction have been analyzed. Secondly, a novel technique to experimentally characterize the in-flow water condensation patterns and mass fraction has been developed, being measured for the first time.

Regarding the experimental measurements, a humid gas stand to reproduce

EGR and a climatic chamber to obtain cold flow are originally combined to reproduce the flow in a LP-EGR junction. A free-discharge configuration is selected for the junction, whose impact is found to be below 3%. This configuration allows the employment of different experimental techniques to characterize the outlet of the T-junction.

The laser PIV measurements have been used to characterize the in-plane velocity of the cross section and to obtain the pattern of the secondary flows. The condensation generated due to the mixing process is studied for the first time with planar laser-induced visualization. Finally, the experimental condensation patterns are obtained by comparing temperature distributions with or without humidity and combining the corresponding enthalpy balances to perform the indirect condensation measurements.

The proposed CFD configuration obtains a flow distribution which is generally in agreement with the experimental PIV measurements. The CFD model predicts the main flow features and how they change when considering different junctions or operating points. Considering planar laser-induced visualization and CFD condensation simulations, they both agree in showing a greater condensation for those cases with stronger secondary flows and air-EGR mixing.

Regarding the indirect condensation measurements, modeling heat transfer with the surroundings may improve the accuracy of the thermal flow field and subsequent condensation. Nevertheless, all CFD cases presented normalized RMSE for the temperature distributions below 5%. With this, the 3D CFD models is known to predict accurately not only temperature distributions but also secondary flows and qualitative condensation patterns. Indirect condensation measurements and CFD predictions are in good agreement in terms of condensation mass flow rates and trends, with an average difference of 11%. In this case, condensation measurements cannot be considered as a reference of accuracy by themselves, since they have been obtained indirectly with a developed method that employs certain hypotheses. Concluding that the developed experimental method is useful to measure indirectly condensation flow rate patterns, and the in-flow condensation submodel developed by Serrano et al. [73] is quantitatively validated.

Chapter 3 References

[1] S. Guilain, R. Boubennec, M. Doublet, C. Clement, R. Navarro, D. Tarí, and F. Moya. "Condensation before compressor: a key issue of Low Pressure EGR in Eu7 context". In: *24th Supercharging Conference 2019, Aufladetechnische Konferenz, Dresden*. Sept. 26, 2019 (cit. on pp. xi, 51, 128).

[2] J. Galindo, R. Navarro, D. Tari, and F. Moya. "Development of an experimental test bench and a psychrometric model for assessing condensation on a Low Pressure EGR cooler". *International Journal of Engine Research*, (2020). DOI: 10.1177/1468087420909735 (cit. on pp. xi, 7, 27, 51).

[26] P. Michel, A. Charlet, G. Colin, Y. Chamaillard, G. Bloch, and C. Nouillant. "Optimizing fuel consumption and pollutant emissions of gasoline-HEV with catalytic converter". *Control Engineering Practice*, 61, (2017), pp. 198 –205. ISSN: 0967-0661. DOI: 10.1016/j.conengprac.2015.12.010 (cit. on pp. 7, 51).

[28] Galindo, J. and Serrano, J.R. and Navarro, R. and García Olivas, G. "Numerical modeling of centrifugal compressors with heterogeneous incoming flow due to low pressure exhaust gas recirculation". In: *Proceedings of ASME Turbo Expo 2020: Turbomachinery Technical Conference and Exposition*. GT2020-16030. American Society of Mechanical Engineers. 2020 (cit. on pp. 7, 73).

[34] A. Castorrini, A. Corsini, F. Rispoli, P. Venturini, K. Takizawa, and T. E. Tezduyar. "Computational analysis of wind-turbine blade rain erosion". *Computers & Fluids*, 141 (Supplement C), (2016), pp. 175 –183. ISSN: 0045-7930. DOI: 10.1016/j.compfluid.2016.08.013 (cit. on pp. 7, 51).

[35] P. Z. John, T. Koka, and S. Dayalan. "Water droplet erosion simulation of a turbocharger compressor wheel". In: *ASME Turbo Expo 2014: Turbine Technical Conference and Exposition*. GT2014-26974. American Society of Mechanical Engineers. 2014 (cit. on pp. 7, 51).

[55] J. Galindo, V. Dolz, J. Monsalve-Serrano, M. Maldonado, and L. Odillard. "Advantages of using a cooler bypass in the low-pressurre exhaust gas recirculation line of a compression ignition diesel engine operating at cold conditions". *Internal Journal of Engine Research*, (Apr. 29, 2020). DOI: 10.1177/1468087420914725 (cit. on pp. 10, 25, 51, 140).

[58] B. Yang, W. Su, S. Deng, and L. Zhao. "State-of-art of branching T-junction: Experiments, modeling, developing prospects and applications". *Experimental Thermal and Fluid Sciences*, 109, (2019). DOI: 10.1016/j.expthermflusci.2019.109895 (cit. on pp. 10, 51).

[61] M. Zhou, R. Kulenovic, and E. Laurien. "Advanced flow pattern for describing tangential flow oscillation in thermal-mixing pipe flow at a horizontal T-Junction". *International Journal of Thermal Sciences*, 136, (Feb. 1, 2019), pp. 328–336. DOI: 10.1016/j.ijthermalsci.2018.10.045 (cit. on pp. 10, 51).

[62] M. Zhou, R. Kulenovic, and E. Laurien. "T-junction experiments to investigate thermal-mixing pipe flow with combined measurement techniques". *Applied Thermal Engineering*, 150, (Mar. 5, 2019), pp. 237–249. DOI: 10.1016/j.applthermaleng.2018.12.161 (cit. on pp. 10, 51).

[63] C. Evrim, X. Chu, and E. Laurien. "Analysis of thermal mixing characteristics in different T-junction configurations". *International Journal of Heat and Mass Transfer*, 158, (2020), pp. 1–10. DOI: 10.1016/j.ijheatmasstransfer.2020.120019 (cit. on pp. 10, 51).

[64] C. Evrim and E. Laurien. "Numerical study of thermal mixing mechanisms in T-junctions". *Applied Thermal Engineering*, 138, (2021), pp. 1–13. DOI: 10.1016/j.applthermaleng.2020.116155 (cit. on pp. 10, 51).

[65] M. Georgiou and M. V. Papalexandris. "Turbulent mixing in T-junctions: The role of the temperature as an active scalar". *International Journal of Heat and Mass Transfer*, 115, (2017), pp. 793–809. DOI: 10.1016/j.ijheatmasstransfer.2017.08.081 (cit. on pp. 10, 52).

[66] A. Sakowitz, M. Mihaescu, and L. Fuchs. "Turbulent flow mechanisms in mixing T-junctions by Large Eddy Simulations". *International Journal of Heat and Fluid Flow*, 45, (2014), pp. 135–146. DOI: 10.1016/j.ijheatfluidflow.2013.06.014 (cit. on pp. 10, 52, 78, 80).

[71] J. Galindo, R. Navarro, D. Tarí, and G. García-Olivas. "Centrifugal compressor influence on condensation due to Long Route-Exhaust Gas Recirculation mixing". *Applied Thermal Engineering*, 144, (2018), pp. 901 –909. ISSN: 1359-4311. DOI: 10.1016/j.applthermaleng.2018.09.005 (cit. on pp. 11, 51, 52, 69, 70, 77, 82, 107).

[73] J. Serrano, P. Piqueras, R. Navarro, D. Tarí, and C. Meano. "Development and verification of an in-flow water condensation model for 3D-CFD simulations of humid air streams mixing". *Computers & Fluids*, 167, (2018), pp. 158 –165. ISSN: 0045-7930. DOI: 10.1016/j.compfluid.2018.02.032 (cit. on pp. 11, 13, 25, 51, 53, 66, 95, 105, 107, 153, 183, 184).

[74] J. Galindo, P. Piqueras, R. Navarro, D. Tarí, and C. Meano. "Validation and sensitivity analysis of an in-flow water condensation model for 3D-CFD simulations of humid air streams mixing". *International Journal of Thermal Sciences*, 136, (2019), pp. 410 –419. ISSN: 1290-0729. DOI: 10.1016/j.ijthermalsci.2018.10.043 (cit. on pp. 11, 25, 51, 68, 69, 73, 74, 107, 135, 153, 161, 175, 184).

[77] Z. Wang, S. Sanders, J. A. Backhaus, A. Munnannur, and N. M. Schmidt. "H2O absorption tomography in a diesel aftertreatment system using a polymer film for optical access". *Applied Physic B*, 127, (286 2017). DOI: 10.1007/s00340-017-6867-8 (cit. on pp. 11, 52).

[78] J. V. Pastor, J. J. Lopez, J. E. Julia, and J. V. Benajes. "Planar Laser-Induced Fluorescence fuel concentration measurements in isothermal Diesel sparys". *Optical Society of America*, 10, (7 2002). DOI: 10.1364/OE.10.000309 (cit. on pp. 11, 60).

[79] T. Xue and S. Zhang. "Investigation on heat transfer characteristics of falling liquid film by planar laser-induced fluorescence". *International Journal of Heat and Mass Transfer*, 126, (2018), pp. 715–724. DOI: 10.1016/j.ijheatmasstransfer.2018.05.039 (cit. on pp. 11, 52).

[80] A.J.Torregrosa, A.Broatch, J.V.Pastor, and J.García-Tíscar. "Measuring turbocharger compressor inlet backflow through particle image velocimetry". *Experimental Thermal and Fluid Science*, 99, (2018), pp. 420–432. DOI: 10.1016/j.expthermflusci.2018.08.015 (cit. on pp. 11, 55, 56).

[81] C. Brucker. "Study of the three-dimensional flow in a T-junction using a dual-scanning method for three-dimensional scanning-particle-image velocimetry (3-D SPIV)". *Experimental Thermal and Fluid Science*, 14 (1), (1997), pp. 35–44. DOI: 10.1016/S0894-1777(96)00110-0 (cit. on pp. 11, 52).

[82] C. Espinoza, M. Simmons, F. Alberini, O. Mihailova, D. Rothman, and A. Kowalski. "Flow studies in an in-line Silverson 150/250 high shear mixer using PIV". *Chemical Engineering Research and Design*, (2018). ISSN: 0263-8762. DOI: 10.1016/j.cherd.2018.01.028 (cit. on pp. 11, 52).

[99] K. L. Wang, D. Li, N. Husnain, and S. Fareed. "Numerical and experimental investigation on water vapor condensation in turbulent flue gas". *Applied Thermal Engineering*, 160, (Sept. 1, 2019). DOI: 10.1016/j.applthermaleng.2019.114009 (cit. on p. 51).

[100] K.-H. Brune, H.-P. Schiffer, R Christmann, and M Gnewikow. "Experimental investigations of the disturbed inlet-flow structure caused by mixing geometries and its influence on the performance of a turbocharger centrifugal compressor". In: *ASME Turbo Expo 2009: Power for Land, Sea, and Air*. American Society of Mechanical Engineers Digital Collection. 2009, pp. 1295–1304 (cit. on p. 51).

[101] J. Choi, S. Satpathy, J. Hoard, D. Styles, and C. Kuan. "An Experimental and Computational Analysis of Water Condensation Separator Within a Charge Air Cooler". *International Combustion Engine Division Fall Technical Conference*, (2017), pp. 1–11. DOI: 10.1115/ICEF2017-3609 (cit. on pp. 52, 140).

[102] E. Randolph, F. Bocher, S. Kroll, and N. Wright. "Visual, Thermodynamic, and Electrochemical Analysis of Condensate in a Stoichiometric Spark-Ignited EGR Engine". *SAE Technical Paper*, (2017), pp. 1–12. DOI: 10.4271/2018-01-1406 (cit. on p. 52).

[103] L. Chen, X. Zhang, C. Wang, and C. Yang. "Analysis on High-Pressure Water Separator". *Procedia Engineering*, 121, (Aug. 10, 2015), pp. 558–566. DOI: 10.1016/j.proeng.2015.08.1034 (cit. on p. 52).

[104] E. Randolph, F. Bocher, S. Kroll, and N. Wright. "Research and development of Self-contained Water Injection Systems". *International Journal of Environmental Research and Public Health*, 18, (2017), pp. 1–10. DOI: 10.3390/ijerph18105392 (cit. on p. 52).

[105] *STAR-CCM+*. Release version 12.06.010. CD-adapco. 2018. URL: http://ww.cd-adapco.com (cit. on pp. 52, 74).

[106] J. Galindo, A. Gil, R. Navarro, and D. Tarí. "Analysis of the impact of the geometry on the performance of an automotive centrifugal compressor using CFD simulations". *Applied Thermal Engineering*, 148, (2019), pp. 1324–1333. ISSN: 1359-4311. DOI: 10.1016/j.applthermaleng.2018.12.018 (cit. on p. 53).

[107] J. V. Pastor, J. M. García-Oliver, A. García, and M. Pinotti. "Effect of laser induced plasma ignition timing and location on Diesel spray combustion". *Energy Conversion and Management*, 133, (2017), pp. 41–55. DOI: 10.1016/j.enconman.2016.11.054 (cit. on p. 55).

[108] A. Sciacchitano and B. Wieneke. "PIV uncertainty propagation". *Measurement Science and Technology*, 27, (2016), pp. 1–16. DOI: 10.1088/0957-0233/27/8/084006 (cit. on p. 57).

[109] L. Pickett, C. Genzale, J. Manin, and L.-M. Malbec. "Measurement Uncertainty of Liquid Penetration in Evaporating Diesel Sprays". In: 23^{rd} *Annual Conference on Liquid Atomization and Spray Systems*. ILASS Americas. 2011 (cit. on p. 58).

[110] A. Charogiannis, J. Sik, V. Voulgaropoulos, and C. Markides. "Structured planar laser-induced fluorescence (S-PLIF) for the accurate identification of interfaces in multiphase flows". *International Journal of Multiphase Flow*, 118, (2019), pp. 193–204. DOI: 10.1016/j.ijmultiphaseflow.2019.06.002 (cit. on p. 60).

[111] S. Schuster, D. Brillert, and F. Benra. "Condensation in Radial Turbines-Part I: Mathematical Modeling". *Journal of Turbomachinery*, 140, (2018), pp. 1–9. DOI: 10.1115/1.4040934 (cit. on p. 68).

[112] S. Schuster, D. Brillert, and F. Benra. "Condensation in Radial Turbines-Part II: Application of the Mathematical Model to a Radial Turbine Series". *Journal of Turbomachinary*, 140, (2018), pp. 1–7. DOI: 10.1115/1.4040935 (cit. on p. 68).

[113] T. Wittmann, C. Bode, and J. Friedrichs. "The Feasibility of an Euler-Lagrange Approach for the Modeling of Wet Steam". *Journal of Engineering for gas turbines and power*, 143, (2021), pp. 1–8. DOI: 10.1115/1.4049859 (cit. on p. 68).

[114] T. Wittman, S. Luck, C. Bode, and J. Friedrichs. "Numerical Simulation of Nucleation and Condensation and Radial Turbines". In: *CAD-FEM ANSYS Simulation Conference, Dusseldorf, Germany*. 2019 (cit. on p. 68).

[115] D. C. Wilcox. "Reassessment of the scale-determining equation for advanced turbulence models". *AIAA journal*, 26 (11), (1988), pp. 1299–1310. DOI: 10.2514/3.10041 (cit. on p. 74).

[116] D. Tarí. "Effect of inlet configuration on the performance and durability of an automotive turbocharger compressor". PhD thesis. Universitat Politècnica de València. Departamento de Máquinas y Motores Térmicos, 2018. DOI: 10.4995/Thesis/10251/104410. URL: http://hdl.handle.net/10251/104410 (cit. on pp. 75, 106).

[117] R. Tunstall, D. Laurence, R. Prosser, and A. Skillen. "Large eddy simulation of a T-Junction with upstream elbow: The role of Dean vortices in thermal fatigue". *Applied Thermal Engineering*, 107, (Aug. 25, 2017), pp. 672–680. DOI: 10.1016/j.applthermaleng.2016.07.011 (cit. on pp. 78, 80).

[118] E. Idelchik and E. Fried. *Handbook of hydraulic resistance*. Jaico Publishing House, 1986. ISBN: 9788179921180 (cit. on p. 78).

[119] Y. Xue, R. Hhellmuth, and D. Shin. "Formation of Vortices in Idealised Branching Vessels: A CFD Benchmark Study". *Cardiovascular Engineering and Technology*, 11, (2020), pp. 544–559. DOI: 10.1007/s13239-020-00477-9 (cit. on p. 78).

[120] T. Lu, D. Attinger, and S. M. Liu. "Large-eddy simulations of velocity and temperature fluctuations in hot and cold fluids mixing in a tee junction with an upstream straicht or elbow main pipe". *Nuclear Engineering and Design*, 263, (Apr. 2, 2013), pp. 32–41. DOI: 10.1016/j.nucengdes.2013.04.002 (cit. on p. 80).

[121] W. H. Lyne. "Unsteady viscous flow in a curved pipe". *Journal of Fluid Mechanics*, 45 (1), (1971), pp. 13–31. DOI: 10.1017/S0022112071002970 (cit. on p. 80).

Chapter 4

Multi-fidelity surrogate models for Low-Pressure EGR junction Condensation

Contents

4.1 Introduction

In the previous Chapter 3, new experimental tools to measure condensation at the junction outlet and a validation of a 3D-CFD condensation model have been presented obtaining a good agreement between experiments and simulations. These CFD simulations are therefore accurate but computationally demanding. This poses an issue if a large quantity of cases are required, for instance to evaluate junction condensation in transient warm-up engine calculations. In this Chapter, the concept of surrogate model is about to be introduced. Then, a strategy to characterize condensation in LP-EGR junctions will be developed by combining a campaign of expensive 3D CFD simulations (such as those conducted in Chapter 3) with much cheaper 0D simulations of junction condensation in order to produce a multi-fidelity surrogate model.

A typical engineering problem is found when trying to simplify the behavior of a complex system. Ideally, one would like to be able to predict the performance of the system on the basis of a combination of inputs that define its characteristics and particular operating conditions. To do so, a set of (training) data is generated by means of experimental measurements or numerical simulations and a so-called surrogate model of the system is built. Such experiments and simulations are usually expensive [122], so the number of evaluations should be kept as low as possible. Surrogate models (also known as black-box models or metamodels) therefore aim at predicting the outcome of the system with *adequate* accuracy at different points to those that were employed to construct the model. In the framework of Industry 4.0 and the paradigm shift to the Digital Twin concept [123], surrogate models are believed to play a key role [124, 125].

Surrogate models can be used for many different purposes [122], including sensitivity analyses [126, 127, 128], optimization [129, 130, 131] and design space approximation. The latter is employed when the surrogate is required to represent the global behavior of the complex system over the whole design space. For instance, surrogates can be employed to create turbocompressor [132, 133, 134] and turbine [135] characteristic maps, which provide the performance of the devices in terms of pressure ratio and isentropic efficiency. Heat transfer in heat exchangers [136] and in other applications [137], aerothermoelastic performance of hypersonic vehicles [138] and piston engine volumetric efficiency

[139] are problems of design space exploration that have been addressed by means of surrogate modeling.

Most of the research available in the literature is devoted to the usage of surrogates for optimization [140, 141]. Unfortunately, the surrogate methods that are useful for optimization may not be the right choices for design space approximation [142]. This chapter is therefore committed to investigate the methodology that should be followed in the scope of surrogate modeling for design space approximation for applying ino condensation modeling.

There is a wide variety of surrogate models that can be employed. Yondo et al. [140] conducted a comprehensive review about different surrogate-based methods regarding aircraft aerodynamic studies. Radial Basis Function model (RBF), Polynomial Response Surface Model (PRS), and kriging model are amongst the most common types of surrogates found in the literature. Reihani et al. [70] used PRS to assess the sensitivity of low-pressure exhaust gas recirculation characteristics on turbocharger compressor performance. Simpson et al. [143] found that kriging surrogates were more accurate than PRS ones in the scope of aerospike nozzle design, whereas Fang et al. [144] concluded that RBF models presented a higher quality to predict non-linear effects than PRS models in several test problems. Nevertheless, the accuracy of surrogate models is case-dependent [142], so methods that seek to obtain adequate surrogate models for a certain application should compare between different alternatives [145].

For problems with numerous parameters and computationally-demanding simulations, it may be unaffordable to conduct a numerical campaign with the required design space sampling to develop an accurate surrogate. For these cases, the possibility of multi-fidelity surrogates arises as a means to alleviate the computational effort. In this way, the surrogate employs not only the outcome from the high-fidelity expensive simulations, but also involves the prediction of a much cheaper low-fidelity model. Again, the existing literature reviews [140, 141, 146] show that multi-fidelity surrogates have been applied essentially to optimization [147, 130, 148] and uncertainty quantification [149, 150], with few works in which there is some degree of application to design space exploration [151, 152]. Besides, the performance of such surrogates is often assessed by means of synthetic and benchmark problems, which leaves unanswered the question of how to adequately employ multifidelity surrogates for original problems.

In this chapter, a comprehensive method is defined in order to obtain multi-fidelity surrogate models for design space approximation in the framework of "real life" engineering problems. In this way, the method is able to cope with situations in which it is not affordable to explore many parameters of a space design by means of expensive 3D CFD simulations. Therefore, an original procedure is developed so that different multi-fidelity surrogate models are assessed in a systematic way by means of well-established error metrics. Different designs of experiments are employed to obtain multi-purpose numerical campaigns that only consider the relevant parameters in accordance with the objective of each campaign. Therefore, the computational effort of the multi-fidelity strategy proposed in this chapter is limited.

The developed method is presented by means of a step-by-step recipe employing a thorough mathematical notation so that the interested researchers are able to obtain a multi-fidelity surrogate model useful for their problem. Besides, the strategy is applied to the prediction of condensation when two humid air streams are mixed on a three-way junction with a twofold objective: prove the validity of the method in a real problem and set an example on how to apply the method.

Determining the condensation mass flow rate generated by the mixing of two streams of moist air is relevant for air conditioning [153] and internal combustion engines [36]. Such condensation can be roughly estimated by means of 0D models [36] or more accurately predicted using 3D CFD simulations [73]. In this chapter, the former will be used as a low-fidelity model of condensation mass flow rate and the latter as its high-fidelity counterpart.

4.2 Methods

4.2.1 High Fidelity: 3D CFD condensation model

The 3D-CFD simulations process is described with the geometry, the mesh and the setup for the whole range of simulations carried out at this chapter following the work presented at the Chapter 3.

Mass flow rates, total temperatures and the mass fraction of the gas components at both inlets (EGR and Fresh air) are selected to represent characteristic conditions in a C-passenger car engine. At the outlet section, and in order to simulate the compressor influence at the cross section, a relative pressure is established as the boundary condition as it is mentioned in the study done by Tarí [116].

4.2.1.1 *Numerical configuration*

The geometry of study is a LP-EGR T-junction where inlet fresh air and EGR is mixed before the compressor. As can be seen in Fig. 4.1, there is two inlet branches and one outlet. Some differences appeared at the geometry compared with the one presented at the Section 3.3.1, one difference is that at this case a 90◦ junction is selected. Another difference is the nozzle area, at this geometry starts once the EGR duct is connected to the main branch. This small nozzle is set at the mixing area to study in parallel with the perfect mixing model this phenomenon and how affects on the condensation.

Regarding the inlet air diameter is 50 mm and the EGR diameter keeps a ratio with the inlet of 0.2, the outlet diameter is 34 mm. In order to proceed with the CFD simulations and following the methodology described in Section 3.3.1, an extrusion of three additional diameters at both inlets and two more at the outlet are set assuring the stability of the boundary conditions without affecting the solution.

Regarding the meshing methodology, the same methodology proposed by the Chapter 3 is followed. At this case, a mesh composed with polyhedral cells with a base size of 1.5 mm is employed adding at the walls eight prism layers with a total thickness of 30 % of the base to help with the solution near the walls obtaining a mesh of 3M cells. The final mesh has been selected according to a grid mesh independence. Reducing the mesh 10 times and obtaining 300 thousand cells appears a difference of 10.4 % in condensation at the outlet section compare to the one selected. Increasing the mesh to a 11M cells made a difference of 3 % in condensation. Considering the computational cost and the higher number of simulations (more than 180 simulations) the mesh of 3M cells

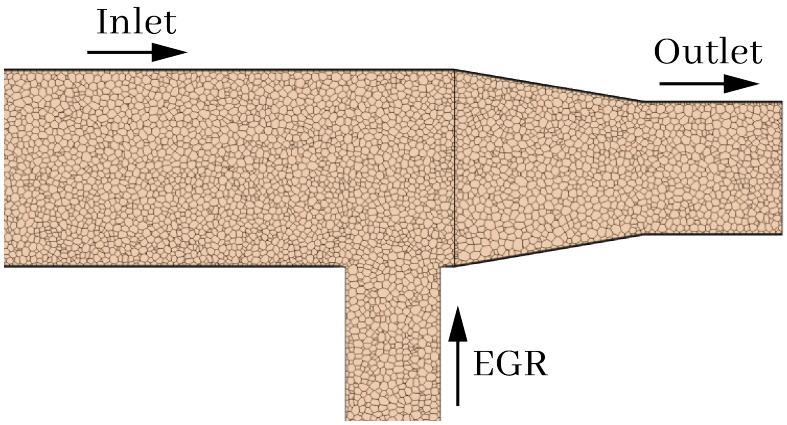

Figure 4.1: *LP-EGR T-joint with cross section of the mesh employed*

was selected providing a $y^+ < 1.5$ for the 99 % of wall cells.

4.2.1.2 *Setup conditions*

Concerning the setup conditions of the CFD simulations and following the work done by Galindo et al. [71, 74] and presented at the Chapter 3. Segregated solver is selected for the simulations. Regarding the turbulence approach, a Reynolds-Average Navier-Stokes (RANS) was employed for the iterations with low under-relation factors to converge the solution and to reduce the fluctuations at the solution and to achieve the final water mixing condensation. The turbulence intensity at both flows is set depending on the working point between values of 1–10 %.

The boundary conditions are presented in the subsection 4.5.1.1, each case of the analysis has different values of, mass fractions, temperatures, specific humidity..., these values are set at the simulation for each working point.

The embedded condensation model at the 3D-CFD simulation is based on the work done by Serrano et al. [73] and presented in this thesis at Section 3.3, which the in-flow water condensation model was deeply studied.

4.2.2 Low fidelity: 0D (perfect mixing) condensation model

A 0D perfect mixing model (low-fidelity simulations) based in the psychrometric process and including effects like nozzle reduction or evaporation has been developed to estimate the condensation flow in the mixing process of two streams on T-junctions, in this particular case with the intake air and the LP-EGR streams. The model considers perfect mixing between branches with ideal gases, Figure 4.2 shows ,schematically, the inputs of the model described. This model is based in the research of Serrano et al. [36] but including nozzle effects and evaporation processes which makes a more completely model, a flow chart is presented in the Fig. 4.3 with the calculation process.

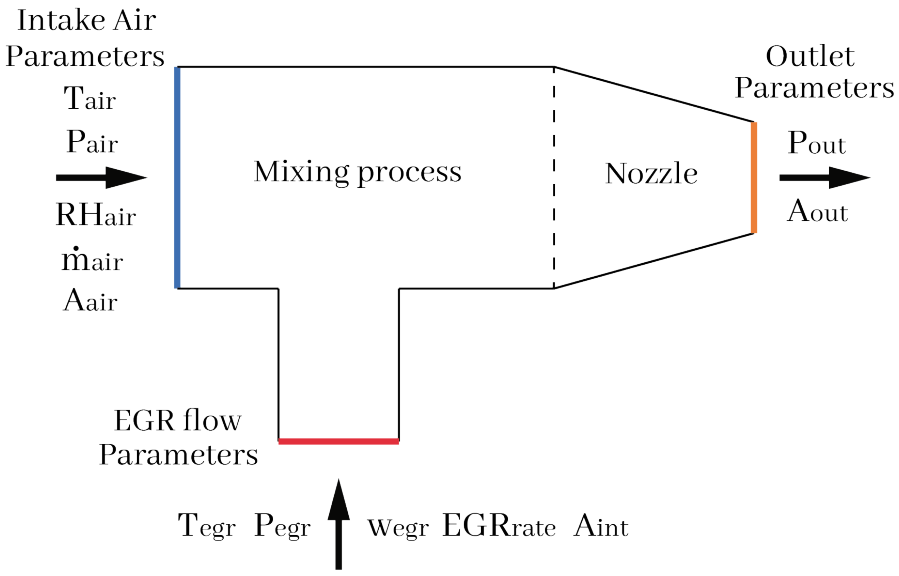

Figure 4.2: Scheme of the input parameters on the perfect mixing model

The intake conditions are managed by the pressure, relative humidity and dry bulb ambient temperature. In order to convert the relative humidity into specific humidity, the saturation pressure is obtained with the Antoine like correlation (Eq. 4.1) for temperatures below 373 K:

$$p_{sat_{int}} = 10^{4.6543 - \frac{1435.265}{T_{int}+64.848}} \tag{4.1}$$

Applying the law of Dalton (Eq. 4.2) can obtain the dry gas partial pressure,

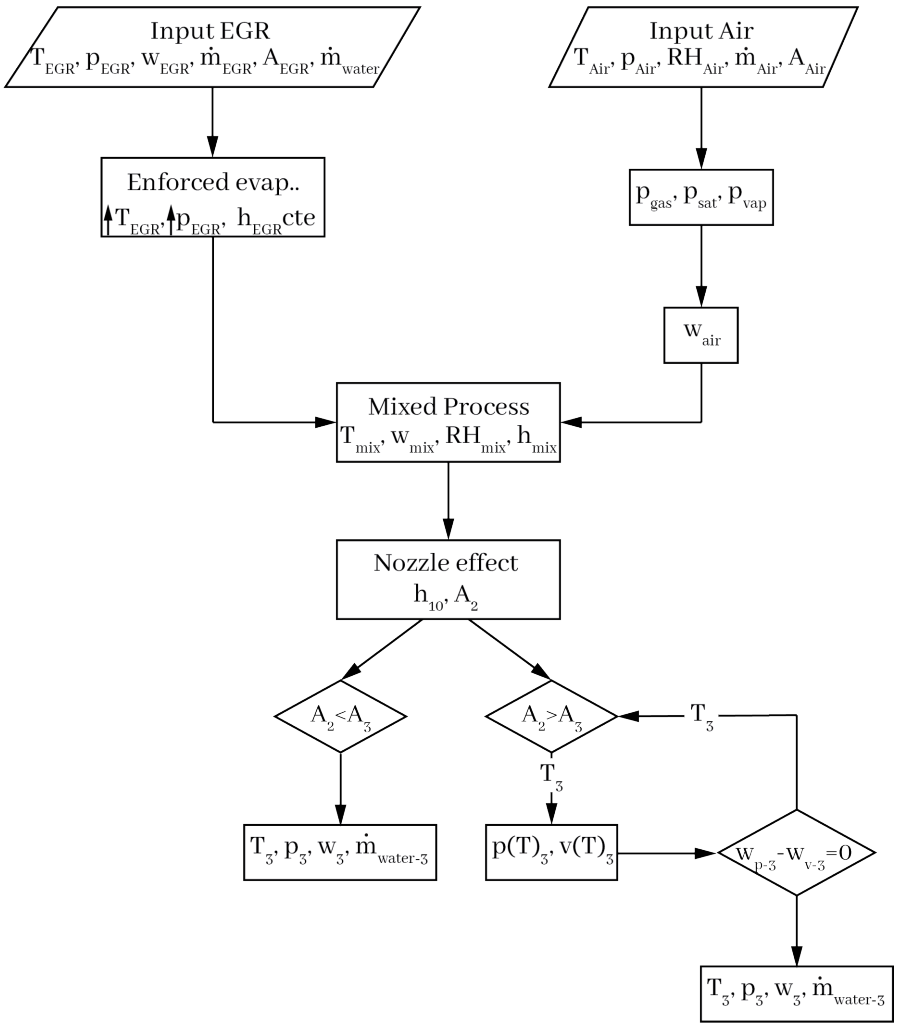

Figure 4.3: *Flow chart of the T-junction calculation model*

while the vapor partial pressure is obtained by the equation 4.3.

$$p_{gas_{int}} = p_{int} - p_{vap_{int}} \tag{4.2}$$

$$p_{vap_{int}} = p_{sat_{int}} \frac{RH}{100} \tag{4.3}$$

Once obtained the partial pressures, the specific humidity can be calculated with the molecular weight of the dry air (28.9g) and the water vapor (18.01g),

as can be shown in Eq. 4.4

$$w_{int} = 1000 \frac{p_{vap_{int}} MW_{vap_{int}}}{p_{gas_{int}} MW_{dryair_{int}}} \tag{4.4}$$

The evaporation process takes an important role at this stage. The model considers that water is completely evaporated at the EGR and it is mixed with the intake air. With this new conditions of the EGR, the mixing process is done obtaining the maximum condensation with a perfect mixing between branches. If the value of condensation at the mixing process has a minor value than the previous condensation at the EGR, there is evaporation. If the value of condensation due to the mixing is higher than the condensation coming from the EGR, then condensation is taking place due to the mixing.

The evaporation process modifies the specific humidity increasingly with the water it was condensed. Consequently, the EGR temperature is modified following the Eq.4.5 and keeping constant the enthalpy.

$$T_{egr} = \frac{h_{egr} - \frac{w_{egr} h_{egr}}{1000}}{cp_{egr}} \tag{4.5}$$

The partial saturation pressure is modified by changes in temperature (Eq. 4.1) and the relative humidity changes (Eq. 4.3).

In the perfect mixing process, both streams are mixed completely in an homogenous flow, obtaining the maximum amount of water that can be condense in perfect conditions. Parameters such as, specific humidity and the enthalpy can be calculated with a weighing of mass flow rates.

$$w_{mix} = \frac{\dot{m}_{dry\ gas_{int}} w_{int} + \dot{m}_{dry\ gas_{EGR}} w_{EGR}}{\dot{m}_{dry\ gas_{int}} + \dot{m}_{dry\ gas_{EGR}}} \tag{4.6}$$

$$h_{mix} = \frac{\dot{m}_{dry\ gas_{int}} h_{int} + \dot{m}_{dry\ gas_{EGR}} h_{EGR}}{\dot{m}_{dry\ gas_{int}} + \dot{m}_{dry\ gas_{EGR}}} \tag{4.7}$$

where the mixing temperature is obtained by the definition of the mixing en-

thalpy Eq. 4.8 and the saturated vapor enthalpy is obtained by correlated tables, dependent on the mixing temperature by the Eq. 4.9.

$$T_{mix} = \frac{h_{mix} - \frac{w_{mix} h_{vap}}{1000}}{cp_{mix}} \tag{4.8}$$

$$h_{vap} = 0.4368 T_{mix} + 2501.4 \tag{4.9}$$

The partial pressures can be calculated with the mixing specific humidity and the mixing temperature obtained previously, directly calculating the relative humidity of the mixing process (Eq. 4.10).

$$RH_{mix} = \frac{p_{vap_{mix}}}{p_{sat_{mix}}} 100 \tag{4.10}$$

$$\dot{m}_{water_{mix}} = \frac{w_{EGR} \dot{m}_{EGR} + w_{Air} \dot{m}_{Air} - w_{mix} (\dot{m}_{EGR} \dot{m}_{Air})}{1000} \tag{4.11}$$

If the relative humidity is below 100 % there is no saturation, thus, no condensation occurs at the mixing process and starts the nozzle calculations with these parameters. If the relative humidity is above the saturation limit (100 %) the process is solved iteratively keeping the mixing enthalpy as constant to obtain the water condensation and the parameters are updated with this new conditions. As can be seen in Fig. 1.5, the solution of the stages A (EGR) and B (Inlet) is the stage C (mix solution) with the constant enthalpy (Eq. 4.11).

The nozzle effect is considered in this perfect mixing model due to the significant modifications of the conditions that managed the condensation. When a section reduction occurs (convergent nozzle) during the space, the velocity is increased and the pressure and temperature are reduced modifying the thermal conditions and increasing the relative humidity, which could be cross the saturation limits.

Figure 4.4 shows a diagram with the options and stages when calculating the nozzle effect. The stage 1 starts with a relative humidity below 100 % it is

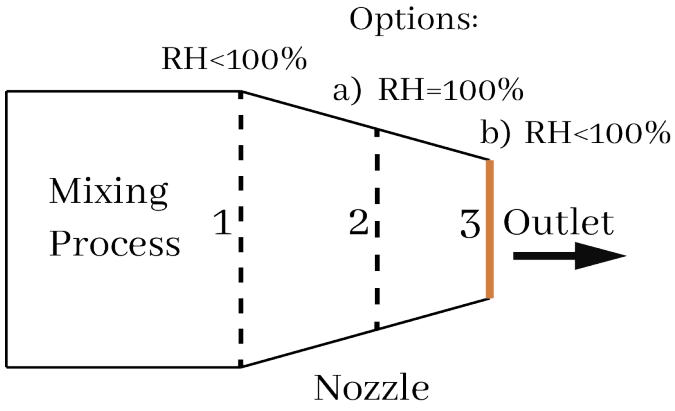

Figure 4.4: *Scheme of the nozzle calculation process*

guarantee by the previously mixing calculations. As it is a calculation of a convergent nozzle, the stagnation enthalpy keeps constant during the nozzle (Eq. 4.13) where h1 is the enthalpy at the stage 1 and it can be calculated by the Eq. 4.12.

$$h_1 = T_1(cp_{air}\dot{m}_{air} + cp_{vapor}\dot{m}_{vapor} + cp_{water}\dot{m}_{water}) \tag{4.12}$$

$$h_{10} = h_1 + \frac{{v_1}^2}{2}(\dot{m}_{air} + \dot{m}_{vapor} + \dot{m}_{water}) \tag{4.13}$$

Once the conditions at the stage 1 are obtained, the next step is to calculate the position in which the relative humidity achieves 100 % (At the scheme of the Fig. 4.4 stage 2). This stage could be find inside the nozzle or outside. If it is inside, condensation appears while if it is outside, there is not any increment of condensation due to the nozzle.

In order to calculate the next steps, three equations manage the nozzle process. The equation 4.13 in which the stagnation enthalpy is calculated and which keeps constant $h_{10} = h_{20} = h_{30}$. The equation 4.14, as it is a nozzle calculation the pressure is related with the temperature by the heat capacity ratio.

Finally, the relations of mass flow rates which keeps constant $\dot{m}_1 = \dot{m}_2 = \dot{m}_3$.

$$\frac{p_3}{p_1} = \left(\frac{T_3}{T_1}\right)^{\frac{\gamma}{\gamma-1}} \tag{4.14}$$

Saturated conditions are imposed to obtain the partial pressures and relative humidity Eq. 4.1, 4.3 and 4.2. The temperature at the stage 2 can be consider with a linear pressure reduction from stage 1 that takes place at the nozzle. Once the temperature and the pressure is obtained, the enthalpy can be calculated with Eq. 4.12 and the area in which the relative humidity achieves 100 % is obtained by Eq. 4.16, calculating the velocity at the stage 2 with the Eq. 4.15.

$$v_2 = \sqrt{\frac{2}{\dot{m}_{air} + \dot{m}_{vapor} + \dot{m}_{water}} (h_{10} - h_2)} \tag{4.15}$$

$$A_2 = \frac{\dot{m}_{air} + \dot{m}_{vapor}}{v_2} \cdot \frac{RT_2}{p_2} \tag{4.16}$$

Once the area of the stage 2 in which the relative humidity achieve 100 % is obtained. The area of the stage 3 is compared with the one in the stage 2 to check if it is bigger or smaller. If the area of the outlet (stage 3) is bigger, there is not an increased of condensation and the outlet parameters can be obtain following the Eq. 4.17 to obtain the temperature with a lineal interpolation between temperatures and areas, and with the Eq. 4.14 to obtain the outlet pressure. Having the temperature and the pressure at the outlet, the specific humidity and the partial pressures can be obtain following the Eqs. 4.4, 4.1 and 4.3.

$$T_3 = T_1 + \left(\frac{T_2 - T_1}{A_2 - A_1}\right)(A_3 - A_1) \tag{4.17}$$

If the condensation appears at the nozzle, because of the bigger area of the stage 2 rather than area of the stage 3. An iterative process is used to solve the psychrometric diagram. A new condition at this stage is employ together with the three previous equations that was managing the nozzle process, the momentum conservation Eq. 4.18, which compares the momentum at the stage 3

with the momentum at the stage 3 with the consideration of the pressure losses at the walls due to the nozzle shape.

$$\dot{m}_2 v_2 + p_2 A_2 = \dot{m}_3 v_3 + p_3 A_3 + \int_{A2}^{A3} p(A) dA \tag{4.18}$$

Once the iterative process is solved at the stage 3, the temperature, pressure, velocity and specific humidity are known and with this parameters, the condensation generated at the nozzle is calculated by follows in the Eq. 4.19.

$$\dot{m}_{water-3} = \dot{m}_{water_{mix}} + (w_{mix} - w_3) \frac{\dot{m}_{EGR} \dot{m}_{Air}}{1000} \tag{4.19}$$

4.2.3 T-junction flow analysis

To assess the difference in performance between the 0D PM model (LF) and the 3D-CFD condensation model (HF), two cases are selected from the numerical campaign that will be described in Section 4.5.2.1: one delivering low condensation (Fig. 4.6) and another providing a greater condensation (Fig. 4.5). The results predicted by these models are included in Table 4.1.

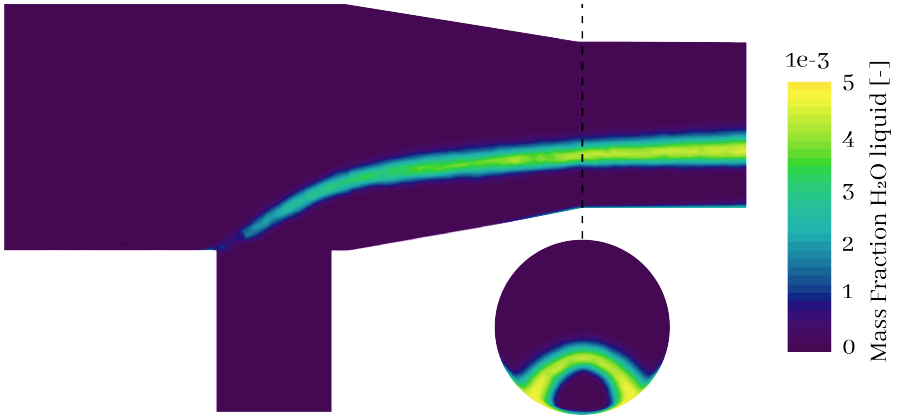

Figure 4.5: Example of low T-junction condensation cases

Working points of Table 4.1 present the same air mass flow rate, but point B features a much greater EGR (humid stream) mass flow rate than point A, which is the main responsible for the increase of 0D condensation mass flow rate by

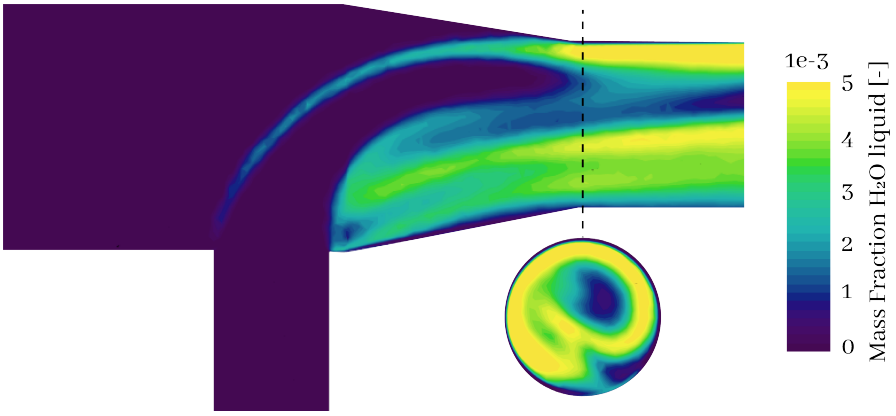

Figure 4.6: *Example of high T-junction condensation cases*

Table 4.1: *Condensation mass flow rates predicted by the LF (0D) and HF (3D) model for two working points.*

Working point	$\dot{m}_{0D}$ [kg/h]	$\dot{m}_{3D}$ [kg/h]
A (Low condensation)	1.182	0.2406
B (High condensation)	2.673	1.651

130%. The high-fidelity model also predicts an increase in condensation mass flow rate when shifting from case A to case B, but a much greater one (590%; see Table 4.1). Whereas the LF only considers the global psychrometric information, the HF also takes into account the local flow features.

The different prediction of the LF and HF models can be therefore explained on the basis of the flow patterns depicted by Fig. 4.5 and 4.6. Case A presents a low EGR mass flow rate, which results in a wall-jet flow configuration (see Kimura et al. [154]), while case B with a greater EGR rate displays a flow pattern in the threshold between a deflecting-jet and an impinging-jet. The 0D model provides an upper bound for the condensation mass flow rate, as it considers a perfect mixture between the streams. The different deviation between the 3D and the 0D models depends on the flow mixing as predicted by the 3D CFD model, as condensation is strongly correlated with mixing [72]. The mixing intensity (and thus condensation) is much greater for working point B (Fig. 4.5) due to the high penetration of the EGR stream than for case A (Fig. 4.6). In the framework of multi-fidelity modeling [155], the 0D case could be useful to provide the psychrometric information of the operating conditions, being a LF model with

negligible computational effort. However, a comprehensive set of expensive 3D CFD simulations will still be required, as the examples analyzed in this section show how the deviation between the LF and HF models can be quite different when shifting the working point.

4.3 Proposed multi-fidelity method

Table 4.2 enumerates all the steps included in the comprehensive method designed in this chapter, which provides multi-fidelity surrogate models for design space approximation. The table distinguishes between the actions required in the HF and MF frameworks. The mathematical notation featured in Table 4.2 avoids particularities from the problem used as example (condensation in mixing streams) and thus, allows researchers from other fields to use the proposed method.

The first stage of Table 4.2 is the *Conceptual modeling*, in which one defines the complete dataset $X_N = \{x_i^l\}$ by identifying the model parameters i and determining the particular values for each parameter at level l. Section 4.5.1.1 shows an example of such steps. The conceptual modeling ends by selecting a set of intermediate variables (z_m) that will be assessed for their use as surrogates, together with the target variable, which is the one that is required to be mapped (z_t). In this work, these variables are defined in Section 4.5.1.2.

The next section of the Table 4.2 is the *Identification of significant parameters* which aims to reduce the computational effort of the surrogate construction. In this way, a subset of X_{scr} points can be determined by means of a certain design of experiments and then run High-Fidelity models Y_{scr}^{HF} and Low-Fidelity models Y_{scr}^{LF} at these working points to obtain a multi-fidelity evaluation. After the screening analysis over all metamodeled variables z (using for instance ANOVA, as described in Section 4.4.2), the non-significant parameters can be removed, leaving only N' significant parameters for the subsequent steps.

The last stage of the proposed method (see Table 4.2) is the *Surrogate modeling* (*for space design exploration*), devoted to the surrogate modeling itself. Firstly, s surrogate candidates are selected (see Section 4.4.3) and a set of train-

Table 4.2: List of method steps and actions to be conducted depending on the fidelity level.

Stage and included steps	High-Fidelity model[1]	Multi-Fidelity framework
1. Conceptual modeling		
1.1 Definition of N model parameters and l number of levels	$X_N = \left\{ x_i^l \right\},\ i = 1, \cdots, N;\ \ell = 1, \cdots, L$	-
1.2 Definition of target and intermediate variables	z_t=$y\left(x\right)$ $z_m\left(y, x\right):\ y = f_m\left(z_m, x\right)$	$z_m^{MF}\left(y^{HF}, y^{LF}\right):$ $y^{HF} = f_m^{MF}\left(z_m^{MF}, y^{LF}\right)$
2. Identification of significant parameters		
2.1 Determination of screening subset	$X_{scr} \subseteq X_N$	-
2.2 Running the models at screening points	$Y_{scr} = y\left(X_{scr}\right)$ $Z_{m,scr} = z_m\left(Y_{scr}, X_{scr}\right)$	$Y_{scr}^{LF} = y^{LF}\left(X_{scr}\right)$ $Z_{m,scr}^{MF} = z_m^{MF}\left(Y_{scr}^{HF}, Y_{scr}^{LF}\right)$
2.3 Identification of N' significant parameters (x_j)	$\forall j, \exists z:\ F_N\left(x_j, z\right) > F_{(L-1),residual}\left(x_j, z\right)$	
2.4 Removal of $N - N'$ non-significant parameters	$X_{N'} = \left\{ x_j^l \right\},\ j = 1, \cdots, N';\ \ell = 1, \cdots, L$ $N' \leqslant N$	-
3. Surrogate modeling (for space design exploration)		
3.1 Selection of surrogate candidates	$g_s:\ \hat{z}_s = g_s\left(x\right)$	
3.2 Determination of training subset	$X_{tra} \subseteq X'_N$	-
3.3 Running the models at training points	$Y_{tra} = y\left(X_{tra}\right)$ $Z_{m,tra} = z_m\left(Y_{tra}, X_{tra}\right)$	$Y_{tra}^{LF} = y^{LF}\left(X_{tra}\right)$ $Z_{m,tra}^{MF} = z_m^{MF}\left(Y_{tra}^{HF}, Y_{tra}^{LF}\right)$
3.4 Construction of surrogate models	$g_{s,t}:\ min\, \varepsilon_{s,t}\left(\hat{Y}_{tra}, Y_{tra}\right)$ $g_{s,m}:$ $min\, \varepsilon_{s,m}\left(\hat{Z}_{m,tra}, Z_{m,tra}\right)$	$g_{s,m}^{MF}:$ $min\, \varepsilon_{s,m}^{MF}\left(\hat{Z}_{m,tra}^{MF}, Z_{m,tra}^{MF}\right)$
3.5 Determination of verification subset	$X_{ver} \equiv X_{scr}$	-
3.6 Prediction of target variable at verification subset	$\hat{Y}_{s,t,ver} = g_{s,t}\left(X_{ver}\right)$ $\hat{Y}_{s,m,ver} = f_m\left(g_{s,m}\left(X_{ver}\right), X_{ver}\right)$	$\hat{Y}_{s,m,ver}^{MF} = f_m^{MF}\left(g_{s,m}^{MF}\left(X_{ver}\right), y^{LF}\left(X_{ver}\right)\right)$
3.7 Calculation of error metrics and selection of best surrogate variable and model	$z, s:\ min\, \varepsilon\left(\hat{Y}_{s,z,ver}, Y_{ver}\right)$	
3.8 Usage of surrogate for space design exploration	$\forall X_{exp},\ Y_{exp} \simeq g_{s,t}\left(X_{exp}\right)\ \mid\ Y_{exp} \simeq f_m^{HF}\left(g_{s,m}^{HF}\left(X_{exp}\right), X_{ver}\right)\ \mid$ $Y_{exp} \simeq f_m^{MF}\left(g_{s,m}^{MF}\left(X_{exp}\right), y^{LF}\left(X_{exp}\right)\right)$	

[1] For the sake of simplicity, HF superscript is omitted from the notation in this column, as it affects to all variables and functions.

ing points X_{tra} is determined using another design of experiments. Here, Box-Behnken design is employed, as justified in Section 4.4.1.2. Next, High-Fidelity $\left(g_{s,t}, g_{s,m}^{HF}\right)$ and Multi-Fidelity $\left(g_{s,m}^{MF}\right)$ surrogate models are constructed using the evaluation of High-Fidelity Y_{tra}^{HF} and Low-Fidelity models Y_{tra}^{HF} at the training points. These surrogate models are then used to predict values of target variable at the verification points $\hat{Y}_{s,t,ver}$, $\hat{Y}_{s,m,ver}^{HF}$ and $\hat{Y}_{s,m,ver}^{MF}$. Notice that these Section suggests to consider the screening subset X_{scr} to be used as verification subset X_{ver} to reduce the computational cost. Since the exact results are already available from stage 2.2 of Table 4.2, the error metrics (as defined in Section 4.4.4) are evaluated, allowing to qualify the different combinations of HF or MF surrogate models with target or intermediate variables as adequate or not in terms of accuracy. Finally, the best couple of surrogate s and variable z is selected so as to be used for space design exploration at any working point within the assessed range X_{exp}.

4.4 Statistical methodology

4.4.1 Design of experiments

The proposed multi-fidelity method requires several sets of working points for screening, training and verification purposes, correspondingly. Different designs of experiments are considered, depending on the required characteristics of each set of point. In this way, a fractional factorial design is employed to obtain the screening points and a Box-Behnken design is used to provide the training points. For the sake of computational effort, the same set of points employed for screening will be used as well for verifying the accuracy of the surrogate models.

4.4.1.1 Fractional factorial design

A subset of points X_{scr} is required by the proposed method to conduct the screening stage. Full factorial design would be a candidate for this purpose, as it allows to explore a wide variety of combinations between the parameters

at different levels, entailing a high level of resolution in the estimation effects. However, it may produce a verification subset with a prohibitive computational cost, depending on the number of parameters of the model and the cost of each simulation. Besides, at the screening stage it is not necessary to present great accuracy in the estimation of high-level interaction terms.

Thus, for the sake of keeping a limited computational effort, it is decided in this chapter to perform instead a fractional factorial design. The objective of the factorial fractions is to identify the characteristic parameters with the greatest effects on the high and multi-fidelity variables. One-half fraction designs reduce the number of simulations by half, but researchers can further reduce the number of simulations by selecting a quarter, an eighth or even a sixteenth of a fraction. Increasing the denominator of the fraction reduces the number of simulations required, but also the resolution in estimating higher order interaction effects. Factor fractions of order p for factors with 2 levels and N characteristic parameters, with the possible inclusion of an intermediate level for center points, are represented by 2^{N-p}.

The resolution of the fraction design influences the number of high-order interaction effects that are confounded, to estimate main effects and low-order interactions based on a reduced number of simulations. Since the characteristics of this fraction design meet the requirements of the screening stage as well as the verification stage, the verification subset will coincide with the screening subset ($X_{ver} \equiv X_{scr}$), so that the effort of this extensive numerical campaign is exploited twice.

4.4.1.2 Box-behnken design

When fitting a polynomial response surface (PRS) model, quadratic surfaces are estimated in order to represent the curved shape of continuous factors. Box-Benkhen designs [156] are incomplete second-order designs based on three levels, which make them appropriate to obtain training subsets X_{tra} to construct surrogates. The number of simulations required by this design is calculated by $2N(N-1)$. Center points can be added to this set of simulations to improve the statistical power of analysis. This design is more efficient than other response sur-

face designs such as the composite center design, or three–level full factorial design [157]. In addition, this design does not include combinations of levels where all characteristic parameters are at the same time at high or low levels. Therefore, it does not force the execution of simulations under extreme conditions that may provide meaningless results in the scope of design space exploration.

4.4.2 Screening stage

The proposed method (see Table 4.2) conducts a screening phase to identify the characteristic parameters that generate significant differences in either high fidelity variables or multi-fidelity variables. In this phase of the analysis, the focus is on main and linear effects, rather than on possible quadratic or nonlinear effects. Analysis of variance (ANOVA) is a versatile method for this screening phase as it allows the exclusion of nonlinear terms from the model, thus increasing the power of the model. Thus, non-significant terms that usually correspond to interaction effects can be specifically eliminated in order to improve the significance of the model by including only main effects. ANOVA has been proved to be a useful technique to screen input parameters and thus reduce the extension of subsequent numerical [158] or experimental campaigns [159] for optimization.

This analysis of variance (ANOVA) is based on the multiple comparison of the means of the high and multi-fidelity variables at different levels of the characteristic input parameters. In the ANOVA model, the F-statistic and its corresponding p-value are critical in identifying the characteristic parameters that cause significant differences in the high fidelity and multi-fidelity variables. This F-statistic is calculated for the main effect of each characteristic parameter as well as for the residual variability of the model. The F-statistic follows a Fisher - Snedecor distribution, assuming the null hypothesis (H_0) that different levels of the characteristic parameters do not produce significant differences in the high and multi-fidelity variables. The F statistic represents a ratio between two measures of variability weighted by degrees of freedom (mean squares): the variability explained by each characteristic parameter relative to the residual variability of the model. Thus, the F statistic represents the variability explained by each characteristic parameter, relative to the variability not explained (residual) by the model.

The variability explained by different levels of characteristic parameters can be calculated as the Explained Sum of Squares (ESS):

$$ESS = \sum n_i \frac{(\bar{Y}_i - \bar{Y})^2}{l-1} \tag{4.20}$$

where $\bar{Y}_i$ represents the sample mean of the high or multi-fidelity variable at each level of the characteristic parameter, $\bar{Y}$ represents the overall mean of this variable and l denotes the number of levels of the parameter.

The residual (intra-level) variability (Residual Sum of Squares) is calculated as follows:

$$RSS = \sum_{ij} \frac{(Y_{ij} - \bar{Y}_i)^2}{N-l} \tag{4.21}$$

where Y_{ij} represents the j-th simulation at each of the i-th level of the high or multi-fidelity variable, and $\bar{Y}$ represents the mean value of that variable at each level of the characteristic parameter, N represents the total sample size and l represents the number of levels.

Using both terms, the F statistic of each parameter characteristic can be computed as the ratio between the variability explained by different levels and the (unexplained) residual variability, within levels of characteristic parameters.

$$F = \frac{ESS}{RSS} \tag{4.22}$$

Along with this F-statistic, p-values can be obtained for identifying significant effects (p-value $< \alpha$). These p-values are based on the comparison between calculated F-statistics and critical values of Fisher - Snedecor distribution. Degrees of freedom for the numerator and denominator of this distribution are calculated combining the number of levels and the screening sample size. A 95% confidence level is usually considered for assessing the significance of p-values, although more restrictive approaches (99% confidence level). In this screening stage, some low-level interaction (double or even triple) may show significant

effects. The retention of these interaction terms is at the discretion of the researcher, although in most cases it is not interesting for research.

4.4.3 Surrogate models

A key stage in the developed method (see Table 4.2) is the construction of surrogate models. In this chapter, three widely-employed surrogate models have been considered: Polynomial Response Surface (PRS), Radial Basis Function (RBF) and Ordinary Kriging. All of them will be used to obtain metamodels of each and every variable z assessed, on the basis of the training subset X_{tra}. Notice that the MF surrogates developed in this chapter are based in scaling functions z_m^{MF} [122].

4.4.3.1 *Polynomial Response Surface Models (PRS)*

Polynomial response surface models (PRS) have been extensively used for data-fitting and regression analysis in order to examine the relationship between variables and outputs [160, 161, 162]. A second-order polynomial surrogate can be written as:

$$g_s = \beta_0 + \sum_{i=1}^{N'} \beta_i x_i + \sum_{i=1}^{N'} \sum_{j=1}^{N'} \beta_{ij} x_i x_j \tag{4.23}$$

Calibration of coefficients β of Eq. 4.23 for the polynomial response surface have been set by means of a R software library [163].

4.4.3.2 *Radial Basis Function Models (RBF)*

A so-called radial function employs the euclidean distance between the input parameter and a fixed point, known as center. A Radial Basis Function (RBF)

model is constructed by means of a linear superposition of different radial basis functions, which is presented in Eq. 4.24:

$$g_s = \sum_{t=1}^{N_{tra}} w_t \psi \left(\| x - x_t \| \right) \tag{4.24}$$

In order to use the combination of N_{tra} radial functions as a RBF surrogate, each point x_t corresponding to the training subset ($X_{tra} = \{x_t\}$) is employed as center, w_t are weights associated with each center x_t and ψ is a basis function that acts over the aforementioned euclidean distance. In this section, a library called PySMO [164] developed by the Institute for the Design of Advanced Energy Systems based on the work of Forrester and Rippa et al. [130] is employed on Python to construct RBF surrogates. Depending on the variable to be metamodeled, the best function ψ amongst those available in the library [164] (linear, cubic, thin-plane spline, gaussian and multi-quadratic) is selected to obtain the greatest fitting.

4.4.3.3 *Ordinary Kriging Model*

A surrogate model combining a known function $f(x)$ (regression) with a function $Z(x)$ as Eq. 4.25 shows:

$$g_s = \sum_{t=1}^{N_{tra}} \beta_t f(x) + Z(x) \tag{4.25}$$

is referred as a Kriging model, due to its first use in the field of geostatistics [165]. The so-called kernel $Z(x)$ considers the deviation between the metamodeled variable and the prediction of the deterministic function $f(x)$ (here considered as constant) by means of a stochastic Gaussian process, so Kriging models are also known as Gaussian process regressions. In Eq. 4.25, β_t are the regression coefficients, N_{tra} the number of training points and $Z(x)$ presents zero mean and a co-variance of $\sigma^2\psi$, where the correlation function ψ employed in this work is the squared exponential (see [166, 167]).

For this chapter, Kriging surrogates have been built by means of a Toolbox on Python environment [166] developed by Bouhlel et al. [167]. According to Xiao

et al. [168], Kriging models better describe the local features of the data to be metamodeled than PRS. Comparing Eq. 4.25 with Eq. 4.24, the functions ψ play a similar role as either radial basis functions in RBF model or kernel in Kriging model [169]. In this way, Chandrashekarappa and Duvigneau [170] noted that the normal distribution considered in the Kriging kernel functions is more adequate for experimental measurements than for computational simulations, which is the application example considered in this chapter (section 5.3).

4.4.4 Error metrics

Several steps of the proposed strategy to develop multi-fidelity surrogates (see section 4.3) require a quantitative assessment of the obtained models, to evaluate and compare their performance so as to select the best combination of metamodeled variable and surrogate type. Generically, these metrics check the error committed between the observed values and the predicted values, but the roles of observed and predicted data at the corresponding stage will determine which is the error indicator best suited for the task.

The first indicator employed in this section is the coefficient of determination R^2. It quantifies the proportion of the total variability of the data that the model is able to explain. To do so, this error metric employs the co-variance of the predicted and observed cases as well as the variance of each case, as can be seen in Eq. 4.26:

$$R^2 = \frac{\sigma_{z\hat{z}}^2}{\sigma_z^2 \sigma_{\hat{z}}^2} = \frac{\left(\frac{\sum_{i=1}^{n} (z_i - \bar{z})\left(\hat{z}_i - \bar{\hat{z}}\right)}{n} \right)^2}{\frac{\sum_{i=1}^{n} (z_i - \bar{z})^2}{n} \frac{\sum_{i=1}^{n} \left(\hat{z}_i - \bar{\hat{z}}\right)^2}{n}} \tag{4.26}$$

Notice that R^2 in this chapter is only employed to assess the fitting capability of each model outcome (y_i) to the training data (x_i). Indeed, the coefficient is known to be inadequate when attempting to evaluate the predicting capability of the models in the verification stage [171]. To the latter purpose, the Mean Absolute Error (MAE) is preferred [171, 172]. MAE directly calculates the average magnitude of the error between the values predicted by a surrogate ($\hat{y}_i$) and

the values actually observed at the verification stage (y_i), as Eq. 4.27 shows.

$$MAE = \frac{\sum_{i=1}^{n} |y_i - \hat{y}_i|}{n} \tag{4.27}$$

Following the work performed by Roy et al. [173], MAE can be employed as a means of qualitative assessment to determine whether a surrogate model can be considered to provide a good prediction or not. To do so, the 5% of data with the highest residual values is firstly removed and then MAE is normalized considering the training dataset range R_{tra} and the dispersion of the errors. Equations 4.28 and 4.29 show the conditions required to grant a good evaluation to the surrogate. When the two conditions are fulfilled at the same time, a good agreement is obtained. If only one of these conditions is satisfied, a moderate agreement is set. If no condition is met, a bad agreement is therefore considered.

$$\widetilde{MAE} = \frac{MAE(95\%)}{R_{tra}} \leq 0.1 \tag{4.28}$$

$$\widetilde{MAE}_{\sigma} = \frac{MAE(95\%) + 3 \cdot \sigma}{R_{tra}} \leq 0.2 \tag{4.29}$$

4.5 Application of the proposed method to the problem of volume condensation due to mixing: results and discussion

4.5.1 Conceptual modeling

4.5.1.1 Operating conditions: definition of model parameters and their range

The developed method starts the conceptual modeling stage by identifying the model parameters, as stated by Table 4.2. In this case, one only needs to identify the boundary conditions employed in the 3D CFD model (x_{HF}), as described in section 5.2.3.2, and the inputs of the 0D model (x_{LF}), as depicted by Fig. 4.2. By doing so, Table 4.3 is obtained, providing a total of $N = 9$ parameters. Notice that $N_{LF} = 7$, as the parameters for the LF model are the same as the HF one save for the turbulent intensities at both inlet and EGR ducts. Then, 3 levels are selected for each parameter, with values covering a typical range of working points in a piston engine featuring LP-EGR that may produce condensation. The rightmost column of Table 4.3 includes the matrix of elegible parameter values x_i^ℓ that will be employed for conducting the different designs of experiments. Notice that in this case the geometry of the junction has been kept as constant, so that the exploration is performed in terms of operating conditions.

4.5.1.2 Definition of target and intermediate variables

The method developed in this chapter is applied to obtain a surrogate for the condensation mass flow rate that 3D CFD simulations (HF model) would predict. Therefore, this is the target variable z_t sought:

$$z_t = \dot{m}_{cond.,3D} \tag{4.30}$$

Table 4.3: Characteristic parameters of operating range conditions for the applied design of experiments

Parameters	Variables	Units	Low, medium and High values
Inlet air mass flow	$\dot{m}_{air}$	[kg/h]	50, 175, 300
Inlet temperature	T_{air}	[°C]	-10, 0, 10
Relative Humidity	RH_{air}	[%]	50, 75, 100
Inlet turbulent intensity	I_{air}	[%]	1, 5.5, 10
EGR temperature	T_{egr}	[°C]	40, 50, 60
EGR rate	EGR_{rate}	[%]	10, 25, 40
EGR specific humidity	w_{EGR}	[g/kg]	30, 50, 70
EGR turbulent intensity	I_{EGR}	[%]	1, 5.5, 10
Outlet pressure	P_{out}	[bar]	0.8, 0.9, 1

Besides, the method suggests (see Table 4.2) to define additional intermediate variables that could be in turn modeled through surrogates. The underlying idea is that the distribution of such variables across the design space could be more adequate to build surrogate models than that of the target variable. Table 4.4 presents the target and intermediate variables that will be metamodeled in this chapter.

Table 4.4: Target and intermediate variables studied.

Name	Variable	Type
3D condensation	$\dot{m}_{cond.,3D}$	HF Target var.
Condensation humidity	$w_{cond.,3D}$	HF Intermediate var.
Condensation ratio	φ	MF Multiplicative scaling var.
Condensation difference	Δ	MF Additive scaling var.
Junction efficiency	η	MF Hybrid scaling var.

An intermediate variable can be defined within the domain of the HF model (z_m), as long as it involves the target variable and other input parameters. This is the case of the condensation humidity, which normalizes the target condensation mass flow rate by the inlet mass flow rate of ambient dry air:

$$\left(z_{m=w_{cond.,3D}}\right) : w_{cond.,3D} = \frac{\dot{m}_{cond.,3D} \cdot (1 + w_{air})}{\dot{m}_{air}} \cdot 1000 \tag{4.31}$$

$$\left(f_{m=w_{cond.,3D}}\right) : \dot{m}_{cond.,3D} = \frac{\dot{m}_{air}}{1 + w_{air}} \cdot \frac{w_{cond.,3D}}{1000} \tag{4.32}$$

Notice that the equation for the function f_m is also included before, as it

will be required to later obtain $\dot{m}_{cond.,3D}$ on the basis of the surrogate model for $w_{cond.,3D}$ and the parameters w_{air} and $\dot{m}_{air}$ corresponding to the working point studied.

But aside from the HF intermediate variables, the objective of this section is to show hot to build and assess multi-fidelity surrogate models for space design exploration. In this way, Jiang et al. [122] identify three types of variables for MF models based on scaling functions: multiplicative, additive and hybrid variables. For instance, a multiplicative variable can be defined as just the ratio between the HF and LF prediction for condensation mass flow rate:

$$(z^{MF}_{m=\varphi}) : \varphi = \frac{\dot{m}_{cond.,3D}}{\dot{m}_{cond.,0D}} \tag{4.33}$$

$$(f^{MF}_{m=\varphi}) : \dot{m}_{cond.,3D} = \dot{m}_{cond.,0D} \cdot \varphi \tag{4.34}$$

A MF additive variable is also built by calculating the difference between the condensation mass flow rates obtained by the 0D (LF) and 3D CFD (HF) models:

$$(z^{MF}_{m=\Delta}) : \Delta = \dot{m}_{cond.,0D} - \dot{m}_{cond.,3D} \tag{4.35}$$

$$(f^{MF}_{m=\Delta}) : \dot{m}_{cond.,3D} = \dot{m}_{cond.,0D} - \Delta \tag{4.36}$$

Finally, a hybrid variable may combine multiplications and additions of the LF and HF variables in its definition. In this chapter, a so-called junction efficiency η is defined:

$$(z^{MF}_{m=\eta}) : \eta = \frac{\dot{m}_{cond.,0D} - \dot{m}_{cond.,3D}}{\dot{m}_{cond.,0D}} \cdot 100 \tag{4.37}$$

$$(f^{MF}_{m=\eta}) : \dot{m}_{cond.,3D} = \dot{m}_{cond.,0D} \cdot (1 - \eta/100) \ , \tag{4.38}$$

so that it is useful not only as a MF intermediate variable for design space exploration but also as a figure of merit to assess the junction design [1, 174]. Indeed, since $\dot{m}_{cond.,0D}$ is an upper bound for $\dot{m}_{cond.,3D}$, the junction efficiency defined in 4.37 ranges from 0% (maximum condensation) to 100% (avoids all condensation).

To conclude this section, the working points already discussed in Section 4.2.3 are again employed to obtain the values of the intermediate variables stated in Table 4.4, on the basis of the LF and HF results featured in Table 4.1. In this way,

Table 4.5 shows an example of the values that these different variables may take. For instance, the lower mixing of case A compared to case B (see Fig. 4.5 and 4.6) results in a greater junction efficiency in terms of avoiding condensation (79.65% vs 38.24%), in accordance with Table 4.5.

Table 4.5: *Values of target and intermediate variables for two working points.*

Working point	$\dot{m}_{cond,3D}$ [kg/h]	$w_{cond,3D}$ [g/kg]	η [%]	Δ [kg/h]	φ [-]
A (Low condensation)	0.2406	0.8023	79.65	0.9417	0.2035
B (High condensation)	1.651	5.505	38.24	1.022	0.6176

4.5.2 Determination of significant parameters

4.5.2.1 Selection of screening points and results of the HF and LF

In order to produce a subset of points for the screening stage, a one-quarter fraction factorial design 2^{9-2} was applied to obtain a collection of 128 simulations, instead of the $2^9 = 512$ simulations that would have been required by the full factorial design. This (fractional) design of experiments is characterized by a high resolution (VI) and confounded effects over fifth or higher - order interaction. Simulations were executed for the 3D Model and the 0D Model. Target and intermediate variables were computed on the basis of these simulated values.

High and low levels of characteristic parameters were complemented with a number of center points, to improve the accuracy of the standard error of estimation. When the phenomena of condensation was not physically feasible due to the influence of local irregular flows or negligible amounts of condensed water, values of condensation mass flow were considered missing. Some other experiments were slightly modified in order to make sure condensation was produced, for a more profitable data analysis. Based on this screening design, the variability in the five metamodeled variables was assessed for different combinations in the initial set of characteristic parameters.

4.5.2.2 ANOVA and removal of non-significant parameters

The analysis of variance described in section 4.4.2 compares the variability of each metamodeled variables z regarding the main effects produced by each model parameter. Table 4.6 presents these values in terms of the F-statistic defined in Eq. 4.22.

Comparing the results shown in Table 4.6 with the corresponding critical value, three non significant parameters (inlet turbulent intensity, EGR turbulent intensity and outlet pressure) were identified and excluded from subsequent analysis. It is worth noting that there are model parameters that are deemed as significant (usually with the highest confidence level of 99.9%) for every variable z, namely, inlet mass flow, EGR temperature, EGR humidity and EGR rate. The remaining parameters (inlet temperature and inlet relative humidity) are significant or not depending on the variable considered, so they will not be dismissed, as the best variable to construct a surrogate is not known yet.

Table 4.6: *Identification of significant main effects according to ANOVA F-statistics for different HF model parameters and metamodeled variables.*

Parameter	$F\left(\dot{m}_{cond.,3D}\right)$	$F\left(w_{cond.,3D}\right)$	$F\left(\varphi\right)$	$F\left(\Delta\right)$	$F\left(\eta\right)$
Inlet air mass flow	59.6***	31.1***	38.8***	87.9***	38.7***
Inlet temperature	4.4*	16.1***	35.8***	0.2	52.5***
Inlet relative humidity	0.5	0.9	27.2***	0.5	15.4***
Inlet turbulent intensity	0.1	0.0	0.0	0.1	0.0
EGR temperature	11.8***	27.1***	24.7***	18.7***	25.2***
EGR rate	53.4***	103.1***	143.1***	22.0***	128.9***
EGR specific humidity	38.8**	85.8***	61.3***	53.0***	77.7***
EGR turbulent intensity	0.2	0.4	0.0	0.3	0.1
Outlet pressure	0.03	0.3	1.00	0.6	1.8

Significant effects with 99.9% (***), 99.0% (**) or 95.0% (*) of confidence level.

4.5.3 Surrogate modeling for space design exploration

4.5.3.1 Selection of surrogate candidates

All surrogate models defined in section 4.4.3 are assessed for this problem, so $s = PRS, RBF, Krig$.

4.5.3.2 Selection of training points and subsequent obtention of HF and LF results

To calibrate the surrogate models corresponding to each of the five metamodeled variables, a numerical campaign of 54 simulations was produced by means of a Box–Behnken design (see section 4.4.1.2), considering the remaining six significant parameters. Two replicates of this design were added as well as center points to deal with some missing data and also to improve the accuracy of the standard error of estimation. These replicates were obtained through the inclusion of random modifications to previously discarded (non-significant) factors. Thanks to these enhancements, the percentage of missing data was reduced to 13% due to the increase of the sample size. The collection of HF and LF simulations run at the 54 determined working points was used as training data set in next stage to obtain the surrogate models.

4.5.3.3 Construction of surrogate models and prediction of target variable at verification points

In this chapter, three surrogated models have been selected: Polynomial Response Surface (PRS), Radial Basis Function (RBF) and Kriging model. All of them have been already described in section 4.4.3. These three different surrogate models s were constructed for each of the variables defined in section 4.5.1.2, seeking to minimize the error between the metamodeled variable $\hat{Z}_{m,tra} = g_{s,m}\left(X_{tra}\right)$

and the actual values $Z_{m,tra}$ at the training dataset X_{tra}.

An example is presented employing the surrogate Polynomial Response Surface model ($s = PRS$) for the multi-fidelity intermediate variable "condensation difference" ($m = \Delta$) defined in Eq. 4.35. For the sake of brevity, only the first 5 terms out of 28 are presented of the surrogate featured in Eq. 4.39. This model determines the coefficients β of Eq. 4.23 that minimize the error of comparing $\hat{\Delta}$ (the metamodel of Δ) against Δ itself at the set of training points .

$$g^{MF}_{s=PRS,m=\Delta} = -7.5 \cdot 10^{-2} + 1.2 \cdot 10^{-2} * EGR_{rate} - 7.2 \cdot 10^{-3} * \dot{m}_{air} + 6.1 \cdot 10^{-3} * RH_{air} - 2.8 \cdot 10^{-3} * T_{air} + \dots \quad (4.39)$$

To provide an example, a $\hat{\Delta}$ value of 0.89 kg/h is predicted for case 24 amongst the training data when applying Eq. 4.39. Comparing this value with the actual Δ for such working point (0.96 kg/h), an error of 7% appears between the observed and predicted values.

4.5.3.4 Calculation of error metrics and assessment of surrogate models

The error metrics described in section 4.4.4 were finally calculated for the 15 combinations of surrogated models and variables aforementioned, being shown in Table 4.7. Coefficients of determination R^2 (see Eq. 4.26) were obtained to assess the fitting of each surrogate model to the corresponding variable at the training dataset. This adjustment is also evaluated for intermediate variables when the corresponding surrogate is employed to represent the target variable z_t

Generally speaking, satisfactory values in terms of R^2 were obtained for the majority of combinations, as Table 4.7 displays. The analysis showed perfect goodness of fit for the estimations employing radial basis function models and kriging models. However, when such surrogates employ the ratio of condensations φ between HF and LF models, their fitting to the training dataset is deterio-

rated when the results are translated into values of HF condensation mass flow rate $\dot{m}_{cond.,3D}$, which is the target variable. Polynomial Response Surface models provide excellent (but not perfect) calibrations as well, except for the ratio of condensations φ.

In any case, the ultimate test for the surrogate models is their ability to predict results in points not employed for their training, i.e., the verification stage. To do so, several metrics based on the Mean Square Error (MAE) of Eq. 4.27 were identified in section 4.4.4, such as the MAE retaining 95% of data with smallest residuals and the normalized $\widetilde{MAE}$ (Eq. 4.28) and $\widetilde{MAE}_\sigma$ (Eq. 4.29). Finally, Table 4.7 includes a qualitative assessment of the predictive capability of each metamodel based on the last two indicators, in accordance with the work of Roy et al. [173].

Table 4.7 shows that 12 combinations of surrogate models and variables provide good predictive capability, 2 obtain a moderate one and only 1 delivers a bad performance. Kriging model is the only surrogate that provides evaluation deemed as "good" for all metamodeled variables. Interestingly, there is at least one MF variable that performs better than the target variable for each surrogate model, but not all MF variables necessarily provide better agreement than the HF target variable (such as φ for PRS and Δ and η for Kriging model). This idea was already noted by Fernández-Godino et al. [175], which identify that MF models "may be less accurate than a surrogate built using only HF training data points".

The results included in Table 4.7 support the idea of the current chapter of assessing not only MF but also HF intermediate variables. Indeed, the HF intermediate variable $w_{cond.,3D}$ performs better than the HF target variable $\dot{m}_{cond.,3D}$ for all surrogate models when applied to the problem of volume condensation due to mixing. Furthermore, $w_{cond.,3D}$ is the best intermediate variable to be surrogated by means of a Radial Basis Function, since it presents the lowest $\widetilde{MAE}$ and $\widetilde{MAE}_\sigma$ amongst all assessed variables, including the MF ones. For the Kriging model there is not a MF variable that presents lower values of both $\widetilde{MAE}$ and $\widetilde{MAE}_\sigma$ than those of $w_{cond.,3D}$, so the best intermediate variable to be metamodeled using a Kriging model will depend on the weighting of such error metrics. Finally, the best overall combination of surrogate and variable is the Polynomial Response Surface of the MF variable Δ, in accordance with the values of $\widetilde{MAE}$

Table 4.7: *Evaluation of the surrogate models to predict water condensation for different metamodeled variables.*

Surrogate models		Training		Verification				Evaluation
		$R^2\,(z_m)$	$R^2\,(z_t)$	MAE	MAE 95%	$\widetilde{MAE}$	$\widetilde{MAE}_\sigma$	
PRS	$\dot{m}_{cond.,3D}$	0.94		0.1596	0.139	0.0601	0.1851	Good
	$w_{cond.,3D}$	0.95	0.98	0.1376	0.096	0.0415	0.1425	Good
	φ	0.56	0.39	0.4587	0.2428	0.1044	0.4605	Bad
	Δ	0.95	0.98	0.0969	0.0793	0.0341	0.1001	Good
	η	0.97	1.0	0.1274	0.0829	0.0356	0.1726	Good
RBF	$\dot{m}_{cond.,3D}$ (Gauss.)*	1.0		0.1824	0.1553	0.0688	0.1988	Good
	$w_{cond.,3D}$ (Gauss.)*	1.0	1.0	0.1078	0.0826	0.0355	0.1252	Good
	φ (Multi-quad.)*	1.0	0.74	0.1413	0.1061	0.0457	0.1867	Good
	Δ (Cubic)*	1.0	1.0	0.2348	0.2052	0.0883	0.2566	Moderate
	η (Multi-quad.)*	1.0	1.0	0.1601	0.0925	0.0398	0.2313	Moderate
Kriging	$\dot{m}_{cond.,3D}$	1.0		0.2391	0.2176	0.0936	0.1964	Good
	$w_{cond.,3D}$	1.0	1.0	0.1409	0.1128	0.0473	0.1603	Good
	φ	1.0	0.85	0.1467	0.1066	0.0459	0.1916	Good
	Δ	1.0	1.0	0.1616	0.1409	0.0606	0.1486	Good
	η	1.0	1.0	0.1171	0.0681	0.0293	0.1767	Good

* On each case is selected the best transformation type to obtain the greatest R^2 evaluating the variable of study.

and $\widetilde{MAE}_\sigma$ shown in Table 4.7.

In order to visualize the results underlying Table 4.7 and exemplify the implications of the multi-fidelity proposal, an analysis on the surrogate model based on polynomial response surface acting over condensation difference (Eq. 4.35) is conducted, since this combination is the one providing lowest error, as aforementioned. Figure 4.7 shows the calibration plots for the observed and predicted (metamodeled) values of the intermediate variable Δ and Fig. 4.8 the equivalent plot in terms of the target variable $\dot{m}_{cond.,3D}$, which has been obtained on the basis of the surrogate of Δ and the LF model $\dot{m}_{cond.,0D}$ by means of Eq. 4.36. Considering the training dataset (green triangles), the surrogate is constructed for the intermediate variable (see Fig. 4.7) with a $R^2\,(z_m)$=0.95, increasing the correlation up to $R^2\,(z_t)$=0.98 when representing the target variable (Fig. 4.8). For the verification dataset (blue circles), the error displayed at Fig. 4.7 is much greater than that of Fig. 4.8, in which few points lay outside the depicted 10% dispersion band. A close-up of Fig. 4.8 shows that the performance of the surrogate is less adequate close to the origin. However, this region corresponds to low

mass flow rates, so their contribution to the absolute error is low (notice that the normalized $\widetilde{MAE}$ for this combination is below 3.5%). Indeed, for the application of this MF surrogate model it is worth reminding that higher impeller damage is produced with greater condensation mass flow rates [74].

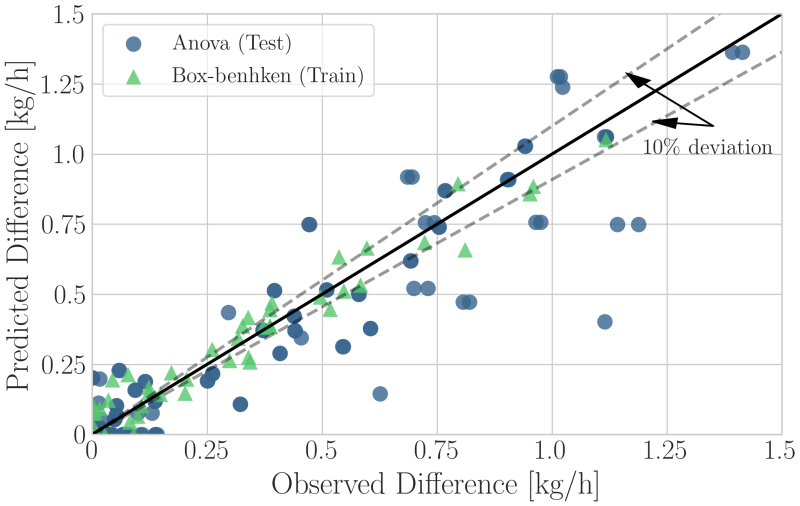

Figure 4.7: Observed vs predicted values for the difference parameter

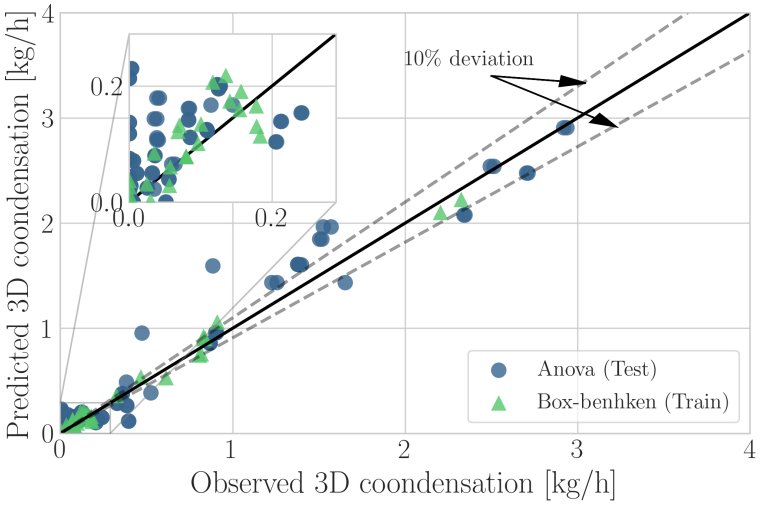

Figure 4.8: Observed vs predicted values for 3D condensation

Finally, a graphical representation of the relation between the MF variables and the six significant input parameters regarded by ANOVA (see section 4.5.2.2)

is provided. Figures 4.9, 4.10 and 4.11 show such 3D plots by considering pairs of parameters and leaving the omitted ones in their medium level (see table 4.3). The same structure is considered at Figs. 4.9, 4.10 and 4.11, in which the low fidelity (a), intermediate variable (b) and high fidelity (c) are represented. Due to the negligible computational effort of the LF model employed in this section (see section 5.2.3.1), the surface representation of Figs. 4.9a, 4.10a and 4.11a is obtained by means of an ad-hoc 100x100 simulation campaign followed by a linear interpolation. Figs. 4.9b, 4.10b and 4.11b are the graphical depiction of the corresponding polynomial response surface, whose first terms were included in Eq. 4.39. Then, Eq. 4.36 allows to obtain the metamodel of $\dot{m}_{cond.,3D}$ using the proposed MF strategy, represented in Figs. 4.9c, 4.10c and 4.11c. To provide further assessment of the method, the actual condensation mass flow rate as calculated by the HF 3D CFD simulation is depicted as a small blue sphere in the rightmost subplots of Figs. 4.9, 4.10 and 4.11. Comparing this value with the one predicted by means of the MF PRS surrogate based on Δ, a relative error of 0.23% is obtained for this specific point.

Considering Figs. 4.9, 4.10 and 4.11, the similarities between the LF prediction ((a) subplots) and the prediction of the target variable ((c) subplots) is likely to be one of the root causes of this combination providing the overall best goodness-of-fit. Indeed, Fernández-Godino et al. [175] considered that a strong correlation between LF and HF data is an indicator of a good performance of the subsequent MF surrogate model. In this case, the metamodeled MF intermediate variable Δ acts as a moderator of this relationship by correcting the *differences* in magnitude.

4.6 Conclusions

The present chapter provides a methodological proposal for obtaining and assessing surrogate models for design space approximation. Apart from straightforward metamodels of the target variable, the usage of intermediate HF variables as well as MF scaling functions to provide surrogates is addressed in a systematic and quantitative way for the first time, to the author's knowledge. Considering the steadily increasing production of new metamodels in the framework of digital twins and machine learning, the proposed method could be use-

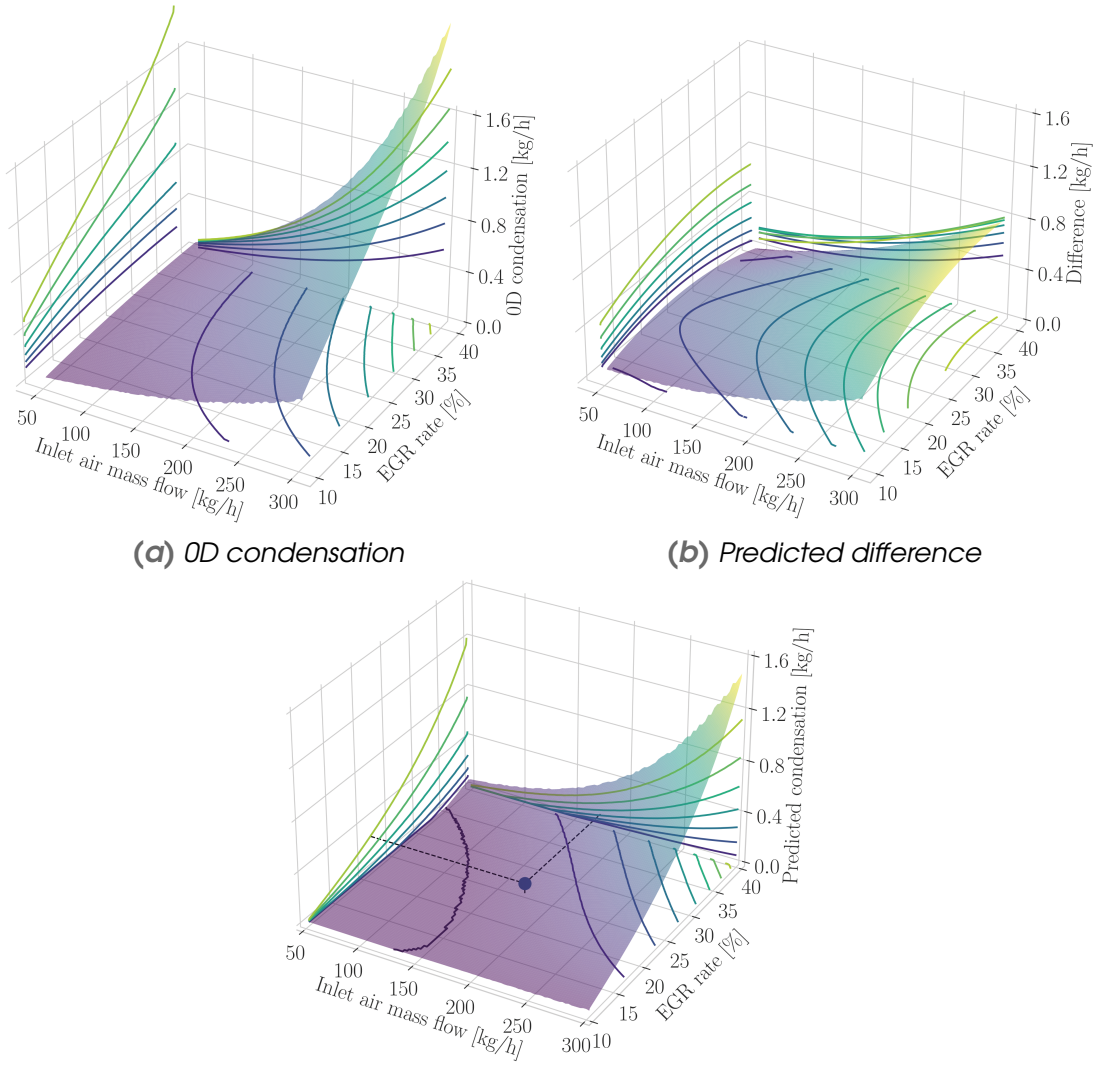

(a) 0D condensation

(b) Predicted difference

(c) Predicted 3D condensation

Figure 4.9: *Sweep of the inlet MFR and the EGR rate obtaining the 0D condensation, the predicted difference and the predicted 3D condensation*

ful to discern which combinations of surrogate models and intermediate variables should provide the best results for design space exploration. The developed method is founded upon a strategy of screening, training and verification; reusing the screening dataset for the verification stage for the sake of computational effort reduction. After describing the comprehensive method, it is then applied to the complex engineering problem of condensation prediction in three-way junctions. The usage of this original example validates the proposed

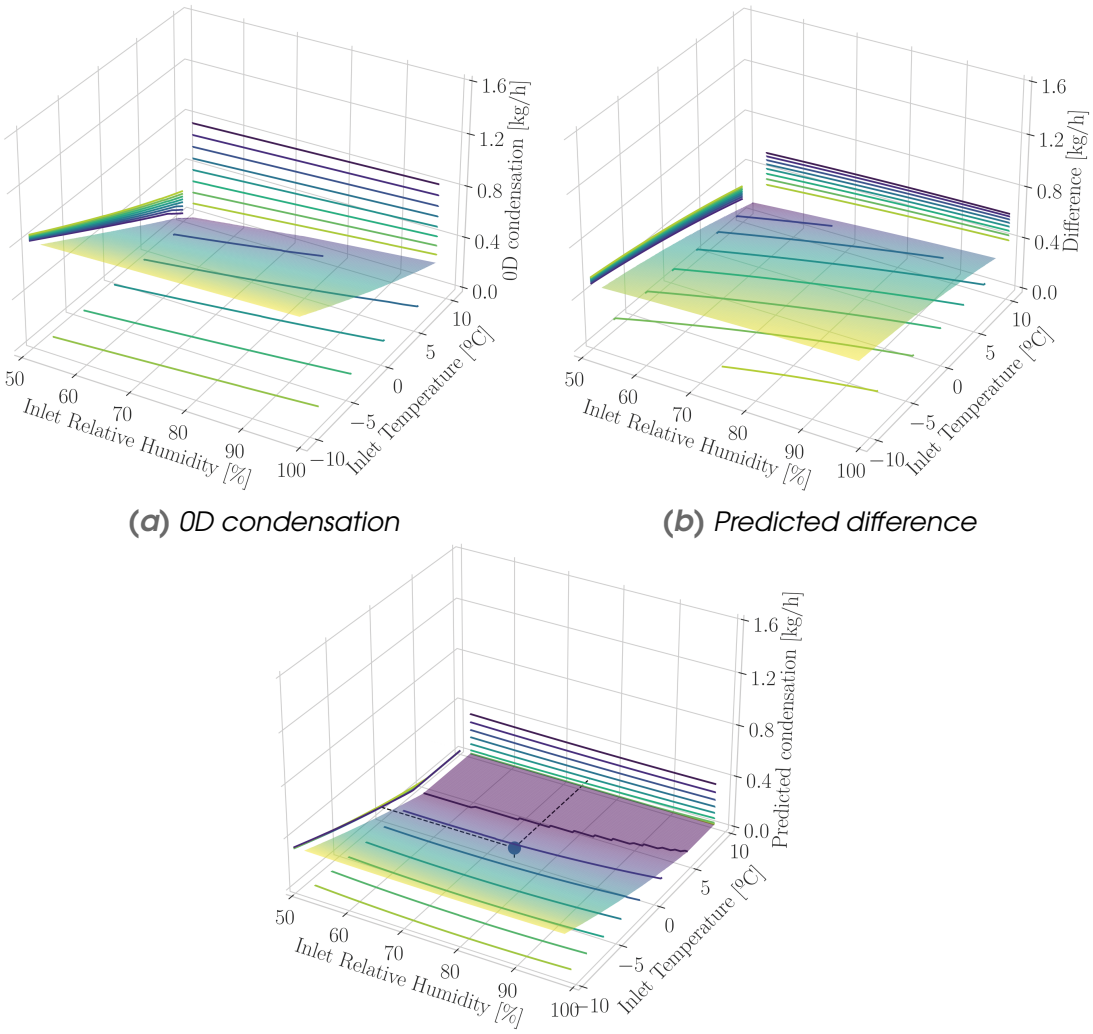

(a) 0D condensation

(b) Predicted difference

(c) Predicted 3D condensation

Figure 4.10: *Sweep of the inlet RH and the Inlet temperature obtaining the 0D condensation, the predicted difference and the predicted 3D condensation*

methodology for the case of "real-life" problems, compared to the synthetic and benchmark problems often found in the literature.

In the studied particular case, the best abatement of the normalized MAEs has been found by constructing a polynomial response surface of a multi-fidelity additive scaling variable that computes the difference between the low-fidelity and high-fidelity predictions of condensation mass flow rate. This results confirm the utility of low-fidelity models in combination with selected campaigns

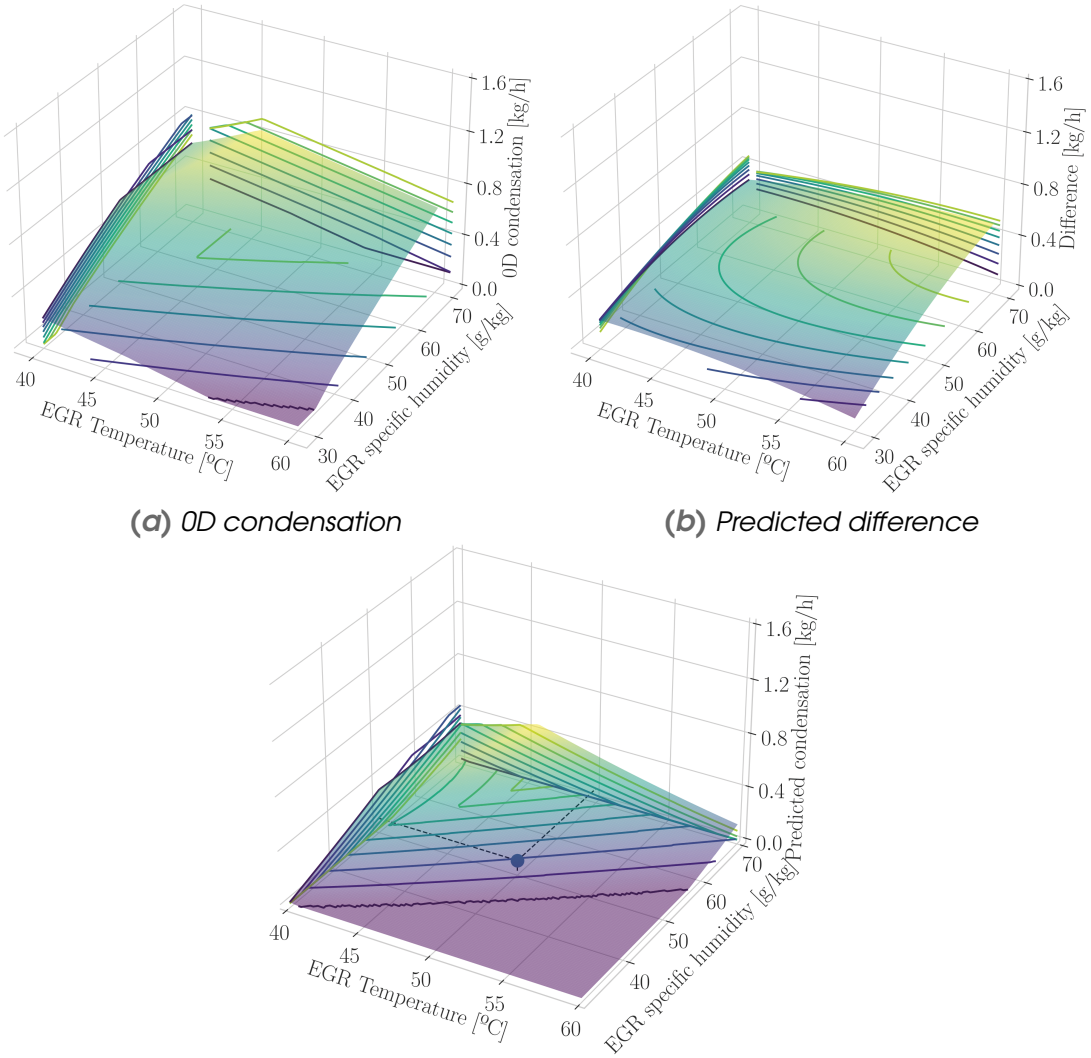

(a) 0D condensation

(b) Predicted difference

(c) Predicted 3D condensation

Figure 4.11: *Sweep of the EGR temperature and the EGR humidity obtaining the 0D condensation, the predicted difference and 3D condensation*

of HF simulations to evaluate the performance of systems with otherwise highly computational demanding models. In spite of the overall victory of a PRS combination, radial-basis function and Kriging models obtained the best agreement for the training datasets, with the later model providing "good" surrogates for all variables assessed in terms of normalized MAEs. Besides, HF intermediate variables (that are derived from the combination of target variables and model parameters) have been found to improve the accuracy of the surrogates built

directly from the target variable, which is a benefit without the need to resort to MF models.

However, these findings are case-specific and cannot be generalized for the application to other problems. Indeed, this chapter proposes a strategy to explore all combinations of surrogate models and intermediate variables (both HF and MF) evaluating them in terms of the metamodeling error after the verification stage. For instance, in this section there are two explored variables ($\frac{\eta}{100}$ and φ) whose summation yields one, yet they behave in a really different way. Therefore, we recommend to assess this double-entry matrix for each studied problem, as the computational effort of conducting the simulation campaigns in complex engineering problems is much greater than that of constructing and evaluating surrogates. As future work, the specific algorithms to construct the surrogates for intermediate variables at the training datasets could be modified to minimize not the error of this intermediate variable but the error in terms of the target variable, which may further improve their results in the verification stage.

Regarding the application of the developed method to the characterization of condensation produced in a LP-EGR junction, the proposed strategy has provided different findings. Both inlet and EGR turbulence intensities as well as outlet pressure were found to have a non-significant effect on condensation for all metamodeled variables assessed. Considering the best combination of surrogate (PRS) and multi-fidelity variable (condensation difference) found in this chapter, there are even less significant parameters (effect of inlet temperature and relative humidity can be neglected). Therefore, the campaign of 54 HF simulations required to build the surrogate and thus characterize the condensation produced by a certain junction geometry could be further reduced. With such affordable computational effort, several challenges could be now addressed in the framework of internal combustion engine cold start, such as determining the adequate moment to switch between HP and LP EGR modes [20, 25] or introducing devices to limit the production or the impact of condensation, which could be correspondingly a cooler bypass [55] and a water separator [101].

Chapter 4 References

[1] S. Guilain, R. Boubennec, M. Doublet, C. Clement, R. Navarro, D. Tarí, and F. Moya. "Condensation before compressor: a key issue of Low Pressure EGR in Eu7 context". In: *24th Supercharging Conference 2019, Aufladetechnische Konferenz, Dresden*. Sept. 26, 2019 (cit. on pp. xi, 51, 128).

[20] J. M. Luján, C. Guardiola, B. Pla, and A. Reig. "Switching strategy between HP (high pressure)-and LPEGR (low pressure exhaust gas recirculation) systems for reduced fuel consumption and emissions". *Energy*, 90, (2015), pp. 1790–1798. DOI: 10.1016/j.energy.2015.06.138 (cit. on pp. 6, 7, 25, 140, 151).

[25] L. Cornolti, A. Onorati, T. Cerri, G. Montenegro, and F. Piscaglia. "1D simulation of a turbocharged Diesel engine with comparison of short and long EGR route solutions". *Applied Energy*, 111, (2013), pp. 1–15. DOI: 10.1016/j.apenergy.2013.04.016 (cit. on pp. 7, 140).

[36] J. R. Serrano, P. Piqueras, E. Angiolini, C. Meano, and J. De La Morena. "On Cooler and Mixing Condensation Phenomena in the Long-Route Exhaust Gas Recirculation Line". In: *SAE Technical Paper*. 2015. DOI: 10.4271/2015-24-2521 (cit. on pp. 7, 31, 105, 108, 157, 185).

[55] J. Galindo, V. Dolz, J. Monsalve-Serrano, M. Maldonado, and L. Odillard. "Advantages of using a cooler bypass in the low-pressurre exhaust gas recirculation line of a compression ignition diesel engine operating at cold conditions". *Internal Journal of Engine Research*, (Apr. 29, 2020). DOI: 10.1177/1468087420914725 (cit. on pp. 10, 25, 51, 140).

[70] A. Reihani, J. Hoard, S. Klinkert, C.-K. Kuan, D. Styles, and G. McConville. "Experimental response surface study of the effects of low-pressure exhaust gas recirculation mixing on turbocharger compressor performance". *Applied Energy*, 261, (2020), p. 114349. DOI: 10.1016/j.apenergy.2019.114349 (cit. on pp. 10, 104).

[71] J. Galindo, R. Navarro, D. Tarí, and G. García-Olivas. "Centrifugal compressor influence on condensation due to Long Route-Exhaust Gas Recirculation mixing". *Applied Thermal Engineering*, 144, (2018), pp. 901 –909. ISSN: 1359-4311. DOI: 10.1016/j.applthermaleng.2018.09.005 (cit. on pp. 11, 51, 52, 69, 70, 77, 82, 107).

[72] J. Galindo, A. Gil, R. Navarro, and G. García-Olivas. "Numerical assessment of humid air streams in three-way junctions and impact on volume condensation". *Applied Thermal Engineering*, (2022). DOI: 10.1016/j.applthermaleng.2021.117676 (cit. on pp. 11, 115).

[73] J. Serrano, P. Piqueras, R. Navarro, D. Tarí, and C. Meano. "Development and verification of an in-flow water condensation model for 3D-CFD simulations of humid air streams mixing". *Computers & Fluids*, 167, (2018), pp. 158 –165. ISSN: 0045-7930. DOI: 10.1016/j.compfluid.2018.02.032 (cit. on pp. 11, 13, 25, 51, 53, 66, 95, 105, 107, 153, 183, 184).

[74] J. Galindo, P. Piqueras, R. Navarro, D. Tarí, and C. Meano. "Validation and sensitivity analysis of an in-flow water condensation model for 3D-CFD simulations of humid air streams mixing". *International Journal of Thermal Sciences*, 136, (2019), pp. 410 –419. ISSN: 1290-0729. DOI: 10.1016/j.ijthermalsci.2018.10.043 (cit. on pp. 11, 25, 51, 68, 69, 73, 74, 107, 135, 153, 161, 175, 184).

[101] J. Choi, S. Satpathy, J. Hoard, D. Styles, and C. Kuan. "An Experimental and Computational Analysis of Water Condensation Separator Within a Charge Air Cooler". *International Combustion Engine Division Fall Technical Conference*, (2017), pp. 1–11. DOI: 10.1115/ICEF2017-3609 (cit. on pp. 52, 140).

[116] D. Tarí. "Effect of inlet configuration on the performance and durability of an automotive turbocharger compressor". PhD thesis. Universitat Politècnica de València. Departamento de Máquinas y Motores Térmicos, 2018. DOI: 10.4995/Thesis/10251/104410. URL: http://hdl.handle.net/10251/104410 (cit. on pp. 75, 106).

[122] P. Jiang, Q. Zhou, and X. Shao. *Surrogate Model-Based Engineering Design and Optimization*. Springer Tracts in Mechanical Engineering, 2020. ISBN: 978-981-15-0730-4. DOI: 10.1007/978-981-15-0731-1 (cit. on pp. 103, 122, 128).

[123] B. Rodic. "Industry 4.0 and the New Simulation Modelling Paradigm". *Organizacija*, 50, (2017), pp. 193–207. DOI: 10.1515/orga-2017-0017 (cit. on p. 103).

[124] A. Barkanyi, T. Chovan, S. Nemeth, and J. Abonyi. "Modelling for Digital Twins-Potential Role of Surrogate Models". *Processes*, 9, (2021), p. 476. DOI: 10.3390/pr9030476 (cit. on p. 103).

[125] L. Wright and S. Davidson. "How to tell the difference between a model and a digital twin". *Advanced Modeling and Simulation in Engineering Sciences*, 7, (2020), pp. 1–10. DOI: 10.1186/s40323-020-00147-4 (cit. on p. 103).

[126] K. Cheng and C. Ling. "Surrogate-assisted global sensitivity analysis: an overview". *Structural and Multidisciplinary Optimization*, 61, (2020), pp. 1187–1213. DOI: 10.1007/s00158-019-02413-5 (cit. on p. 103).

[127] J. Galindo, H. Climent, R. Navarro, and G. Garcia-Olivas. "Assessment of the numerical and experimental methodology to predict EGR cylinder-to-cylinder dispersion and pollutant emissions". *International Journal of Engine Research*, 1, (2020), pp. 1–10. DOI: 10.1177/1468087420972544 (cit. on p. 103).

[128] P. Piqueras, M. J. Ruiz, J. Martin, and A. Tsolakis. "Sensitivity of pollutants abatement in oxidation catalysts to the use of alternative fuels". *Fuel*, 297, (2021), pp. 1–10. DOI: 10.1016/j.fuel.2021.120686 (cit. on p. 103).

[129] Z. Li and X. Zheng. "Review of design optimization methods for turbomachinery aerodynamics". *Progress in aerospace science*, 93, (2017), pp. 1–23. DOI: 10.1016/j.paerosci.2017.05.003 (cit. on p. 103).

[130] A. Forrester, A. Sobester, and A. Keane. "Engineering Design via Surrogate Modelling". *Proceedings of the royal society A*, 463, (2007), pp. 3251–3269. DOI: 10.1098/rspa.2007.1900 (cit. on pp. 103, 104, 123).

[131] S. Shan and G. Wang. "Survey of modeling and optimization strategies to solve high-dimensional design problems with computationally-expensive black-box functions". *Structural and Multidisciplinary Optimization*, 41, (2010), pp. 219–241. DOI: 10.1007/s00158-009-0420-2 (cit. on p. 103).

[132] J. Galindo, R. Navarro, L. M. García-Cuevas, D. Tarí, H. Tartoussi, and S. Guilain. "A zonal approach for estimating pressure ratio at compressor extreme off-design conditions". *International Journal of Engine Research*, 20 (4), (2019), pp. 393–404. DOI: 10.1177/1468087418754899 (cit. on p. 103).

[133] J. Galindo, A. Tiseira, R. Navarro, D. Tarí, H. Tartoussi, and S. Guilain. "Compressor Efficiency Extrapolation for 0D-1D Engine Simulations". In: *SAE Technical Paper*. SAE International, Apr. 2016. DOI: 10.4271/2016-01-0554 (cit. on p. 103).

[134] R.Tirnovan, S.Giurgea, A.Miraoui, and M.Cirrincione. "Surrogate modelling of compressor characteristics for fuel-cell applications". *Applied Energy*, 85, (2008), pp. 394–403. DOI: 10.1016/j.apenergy.2007.07.003 (cit. on p. 103).

[135] Z. Leylek and A. J. Neely. "Global Three-Dimensional Surrogate Modeling of Gas Turbine Aerodynamic Performance". In: *Proceedings of ASME Turbo Expo 2017: Power for Land, Sea and Air*. ASME, 2017, pp. 1–12. DOI: 10.1115/GT2017-63920 (cit. on p. 103).

[136] Z. Qian, C. Seepersad, V. Roshan, and J. Allen. "Building Surrogate Models Based on Detailed and Approximate Simulations". *Journal of mechanical design*, 128, (2006), pp. 668–677. DOI: 10.1115/1.2179459 (cit. on p. 103).

[137] F. Sanchez, M. Budinger, and I. Hazyuk. "Dimensional analysis and surrogate models for the thermal modeling of Multiphysics systems". *Applied Thermal Engineering*, 110, (2017), pp. 758–771. DOI: 10.1016/j.applthermaleng.2016.08.117 (cit. on p. 103).

[138] C. Xin, L. Li, L. Teng, and Y. Zhenjiang. "A reduced order aerothermodynamic modeling framework for hypersonic vehicles based on surrogate and POD". *Chinese Journal of Aeronautics*, 28, (2015), pp. 1328–1342. DOI: 10.1016/j.cja.2015.06.024 (cit. on p. 103).

[139] J. M. Luján, H. Climent, L. M. García-Cuevas, and A. Moratal. "Volumetric efficiency modelling of internal combustion engines based on a novel adaptive learning algorithm of artificial neural networks". *Applied Thermal Engineering*, 123, (2017), pp. 625–634. DOI: 10.1016/j.applthermaleng.2017.05.087 (cit. on p. 104).

[140] R. Yondo, E. Andres, and E. Valero. "A review on design of experiments and surrogate models in aircraft real-time and many-query aerodynamic analyses". *Progress in Aerospace Sciences*, 96, (2018), pp. 23–61. DOI: 10.1016/j.paerosci.2017.11.003 (cit. on p. 104).

[141] G. Fernandez, C. Park, N. Kim, and R. Haftka. "Issues in Deciding Whether to Use Multifidelity Surrogates". *AIAA Journal*, 57, (2019), pp. 1–16. DOI: 10.2514/1.J057750 (cit. on p. 104).

[142] B. Williams and S. Cremaschi. "Selection of surrogate modeling techniques for surface approximation and surrogate-based optimization". *Chemical Engineering Research and Design*, 170, (2021), pp. 76–89. DOI: 10.1016/j.cherd.2021.03.028 (cit. on p. 104).

[143] T. Simpson, T. Mauery, J. Norte, and F. Mistree. "Kriging models for global approximation in simulation-based multidisciplinary design optimization". *AIAA Journal*, 39, (2001), pp. 2233–2241. DOI: 10.2514/3.15017 (cit. on p. 104).

[144] H. Fang and M. Horstemeyer. "Global response approximation with radial basis functions". *Engineering Optimization*, 38, (2006), pp. 407–424. DOI: 10.1080/03052150500422294 (cit. on p. 104).

[145] L. Jia, R. Alizadeh, J. Hao, G. Wang, J. Allen, and F. Mistree. "A rule-based method for automated surrogate model selection". *Advanced Engineering Informatics*, 45, (2020), pp. 1–16. DOI: 10.1016/j.aei.2020.101123 (cit. on p. 104).

[146] B. Peherstorfer, K. Willcox, and M. Gunzburger. "Survey of Multifidelity Methods in Uncertainty Propagation, Inference, and Optimization". *Society for Industrial and Applied Mathematics*, 60, (2018), pp. 1–42. DOI: 10.1137/16M1082469 (cit. on p. 104).

[147] N. Razaaly, G. Persico, and P. Congedo. "Multi-fidelity surrogate-based optimization of transonic and supersonic axial turbine profiles". In: *Proceedings of ASME Turbo Expo 2020*. 2020 (cit. on p. 104).

[148] K. Yoo, O. Bacarreza, and M. Ferri. "Multi-fidelity robust design optimisation for composite structures based on low-fidelity models using successive high-fidelity corrections". *Composite structures*, 259, (2021), pp. 1–12. DOI: 10.1016/j.compstruct.2020.113477 (cit. on p. 104).

[149] C. Bastidasa, M. DeFilippo, C. Chryssostomidis, and G. E. Karniadakis. "A Multifidelity Framework and Uncertainty Quantification for Sea Surface Temperature in the Massachusetts and Cape Cod Bays". *Earth and Space science*, 7, (2020), pp. 1–10. DOI: 10.1029/2019EA000954 (cit. on p. 104).

[150] K. Vishal and R. Ganguli. "Multi-fidelity analysis and uncertainty quantification of beam vibration using co-kriging interpolation method". *Applied Mathematics and Computation*, 398, (2021), pp. 1–10. DOI: 10.1016/j.amc.2021.125987 (cit. on p. 104).

[151] A. Hebbal, L. Brevault, M. Balesdent, E. Talbi, and N. Melab. "Multi-fidelity modeling with different input domain definitions using Deep Gaussian processes". *Structural and Multidisciplinary Optimization*, (2021). DOI: 10.1007/s00158-020-02802-1 (cit. on p. 104).

[152] M. Xiao, G. Zhang, P. Breitkopf, and P. Villon. "Extended Co-Kriging interpolation method based on multi-fidelity data". *Applied Mathematics and Computation*, 323, (2018), pp. 120–131. DOI: 10.1016/j.amc.2017.10.055 (cit. on p. 104).

[153] P. Vojkuvkova, O. Sikula, and J. Weyr. "Assessment of condensation of water vapor in the mixing chamber by CFD method". In: *EPJ Web of Conferences*. Vol. 92. 2015. DOI: 10.1051/epjconf/20159202112 (cit. on p. 105).

[154] N. Kimura, H. Ogawa, and H. Kamide. "Experimental study on fluid mixing phenomena in T-pipe junction with upstream elbow". *Nuclear Engineering and Design*, 240 (10), (2010), pp. 3055–3066. DOI: 10.1016/j.nucengdes.2010.05.019 (cit. on p. 115).

[155] S. Rezaeiravesh, R. Vinuesa, and P. Schlatter. "Towards multifidelity models with calibration for turbulent flows". In: *14th WCCM-ECCOMAS Congress*. 2020 (cit. on p. 115).

[156] G. Box and D. Benhken. "How to tell the difference between a model and a digital twin". *Technometrics*, 2, (1960), pp. 455–475. DOI: 10.1080/00401706.1960.10489912 (cit. on p. 119).

[157] S. Ferreira, R. Bruns, H. Ferreira, and G. Matos. "Box-Behnken design: An alternative for the optimization of analytical methods". *Analytica Chimica Acta*, 597 (2), (2007), pp. 179–186. DOI: 10.1016/j.aca.2007.07.011 (cit. on p. 120).

[158] W. Song and A. Keane. "Parameter screening using impact factors and surrogate-based ANOVA techniques". In: *11th AIAA/ISSMO Multidisciplinary Analysis and Optimization Conference*. AIAA, 2006, pp. 188–196 (cit. on p. 120).

[159] V. B. Silva and A. Rouboa. "Optimizing the DMFC operating conditions using a response surface method". *Applied Mathematics and Computation*, 218 (12), (2012), pp. 6733–6743. ISSN: 0096-3003. DOI: 10.1016/j.amc.2011.12.039 (cit. on p. 120).

[160] J. D. C. Díaz, P. G. Nieto, D. Castro-Fresno, and P. M. Rodríguez. "Steady state numerical simulation of the particle collection efficiency of a new urban sustainable gravity settler using design of experiments by FVM". *Applied Mathematics and Computation*, 217 (21), (2011), pp. 8166–8178. ISSN: 0096-3003. DOI: 10.1016/j.amc.2011.03.044 (cit. on p. 122).

[161] L. Chen, Y. Ma, Y. Guo, C. Zhang, Z. Liang, and X. Zhang. "Quantifying the effects of operational parameters on the counting efficiency of a condensation particle counter using responde surface Design of Experiments (DOE)". *Journal of Aerosol Science*, 106, (2017), pp. 11–23. DOI: 10.1016/j.jaerosci.2016.12.005 (cit. on p. 122).

[162] S. Subramani, R. Govindasamy, G. Lakshmi, and N. Rao. "Predictive correlations for NOx and smoke emission of DI CI engine fuelled with diesel-biodiesel-higher alcohol blends-response surface methodology approach". *Fuell*, 269, (Feb. 1, 2020). DOI: 10.1016/j.fuel.2020.117304 (cit. on p. 122).

[163] R. V. Lenth. "Response-Surface Methods in R, Using rsm". *Journal of Statistical Software*, 32 (7), (2009), pp. 1–17. DOI: 10.18637/jss.v032.i07 (cit. on p. 122).

[164] I. for the Design of Advanced Energy Systems. URL: https://idaes-pse.readthedocs.io/en/1.5.1/surrogate/pysmo/pysmo_radialbasisfunctions.html (cit. on p. 123).

[165] D. G. Krige. "A statistical approach to some mine valuation and allied problems on the Witwatersrand: By DG Krige". PhD thesis. University of the Witwatersrand, 1951 (cit. on p. 123).

[166] U. o. M. Department of Aerospace Engineering. URL: https://smt.readthedocs.io/en/latest/_src_docs/surrogate_models/krg.html (cit. on p. 123).

[167] M. A. Bouhlel, J. T. Hwang, N. Bartoli, R. Lafage, J. Morlier, and J. R. R. A. Martins. "A Python surrogate modeling framework with derivatives". *Advances in Engineering Software*, (2019), p. 102662. ISSN: 0965-9978. DOI: https://doi.org/10.1016/j.advengsoft.2019.03.005 (cit. on p. 123).

[168] M. Xiao, P. Breitkopf, R. Filomeno, and C. Knopf-Lenoir. "Model reduction by CPOD and Kriging-application to the shape optimization of an intake port". *Structural and Multidisciplinary Optimization*, 41, (2010), pp. 555–574. DOI: 10.1007/s00158-009-0434-9 (cit. on p. 124).

[169] S. Bagheri, W. Konen, and T. Bäck. "Comparing kriging and radial basis function surrogates". In: *Proc. 27. Workshop Computational Intelligence*. Universitätsverlag Karlsruhe. 2017, pp. 243–259 (cit. on p. 124).

[170] P. Chandrashekarappa and R. Duvigneau. "Radial basis functions and kriging metamodels for aerodynamic optimization". *INRIA Document*, (2007), p. 44 (cit. on p. 124).

[171] D. Legates and G. Mccabe. "Evaluating the Use Of Goodness-of-Fit Measures in Hydrologic and Hydroclimatic Model Validation". *Water Resources Research*, 35, (1999), pp. 233–241. DOI: 10.1029/1998WR900018 (cit. on p. 124).

[172] A. Davydenko and R. Fildes. "Measuring Forecasting Accuracy: Problems and Recommendations (by the example of SKU-level judgmental adjustments)". *Intelligent Fashion Forecasting Systems: Models and Applications*, 43, (2013), pp. 43–70. DOI: 10.1007/978-3-642-39869-8_4 (cit. on p. 124).

[173] K. Roy, R. Nayaran, P. Ambure, and R. Aher. "Be aware of error measures. Further studies on validation of predictive QSAR models". *Chemometrics and Intelligent Laboratory Systems*, 152, (2016), pp. 18–33. DOI: 10.1016/j.chemolab.2016.01.008 (cit. on pp. 125, 133).

[174] Galindo, José and Climent, Héctor and Navarro, Roberto. "Modeling of EGR Systems". In: *1D and Multi-D Modeling Techniques for IC Engine Simulation*. Ed. by A. Onorati and G. Montenegro. SAE International, 2020. Chap. 7, pp. 257–278. DOI: 10.4271/9780768099522 (cit. on p. 128).

[175] M. Fernandez, S. Dubreuil, N. Bartoli, and C. Gogu. "Linear regression-based multifidelity surrogate for disturbance amplification in multiphase explosion". *Structural and Multidisciplinary Optimization*, 60, (2019), pp. 2205–2220. DOI: 10.1007/s00158-019-02387-4 (cit. on pp. 133, 136).

Chapter 5

Impact of Exhaust Gas Recirculation strategy on emissions and compressor durability during engine cold start

Contents

5.1 Introduction

In the previous chapter 4, a methodology has been developed to obtain a reduced order model with multifidelity conditions to resemble 0D simulations to 3D-CFD simulations. With this development, a reduction on the computational cost in the condensation calculation is obtained. In this chapter and to finalize the content of the thesis, the methodology previously developed in the rest of the chapters is used to apply it into the engine warm-up cycles to quantify water condensation. The quantification of compressor damage and the study of different strategies in LP-EGR and HP-EGR under real cycles conditions are also presented.

As described in Chapter 1, the EGR system has two different types depending on the location of the exhaust gas extraction and mixing, as can be seen in Fig. 5.1. The most widespread circuit is the high-pressure EGR (HP-EGR) which extracts the exhaust gases in the exhaust manifold and feeds them into the intake manifold. The second path is the low-pressure EGR (LP-EGR) which connects the exhaust line downstream of the aftertreatment and reintroduces before the compressor.

Some engines feature both LP-EGR and HP-EGR circuits due to the advantages of each system depending on operating conditions [176]. Commonly, LP-EGR presents several advantages over HP-EGR due to the emission reduction capabilities, the higher EGR rates capable of achieving and the more efficient system [20, 177], but as a drawback it has a slower response and the generation of water condensation in two locations, in the LP-EGR cooler (heat exchanger) and in the junction where the LP-EGR is mixed with the fresh air.

Different authors have studied dual-loop EGR and how to optimize the changes between LP-EGR and HP-EGR, Lapuerta et al. [19] studied the differences between LP-EGR and HP-EGR in NEDC cycles but limiting LP-EGR only when the coolant temperature and intake air temperature were above a threshold, limiting condensation production. Park et al. [178] attempted to optimize the LP-EGR and HP-EGR strategies obtaining an improvement in fuel consumption with LP-EGR compared to HP-EGR. Song et al. [57] investigated the optimization of double-loop EGR by focusing on the condensation generated in the water

charge air cooler when LP-EGR was activated, which is not correct since the main condensation occurs in the LP-EGR path and being the worst for the engine integrity. Appearing in the LP-EGR cooler and in the mixing process at the T-junction.

Special interest appears on the early activation of the LP-EGR due to the stringent regulation, being a key factor to fulfill the homologation limits under cold conditions [179, 180], where pollutant emissions are mainly emitted during the warm-up of the engine. To cope with the early activation of the LP-EGR, a "realistic" study of the condensation production on LP-EGR path with different strategies, a compressor damage quantification and the trade-off between different emissions is performed in this work.

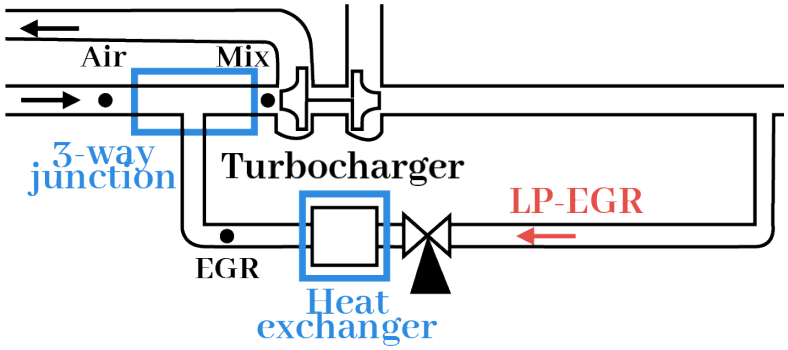

Figure 5.1: Close-up of the LP-EGR on the Fig. 1.4

As can be seen in Fig. 5.1, the LP-EGR system has two places to generate condensing water. First, the heat exchanger where the EGR temperature is reduced below the dew point, a 0D condensation model presented in chapter 2 is used in this chapter to model the condensation of the LP-EGR cooler. Secondly, condensation appears at the location where the streams mix in the LP-EGR loop, at this position (3-way junction) the wet EGR stream is in contact with the cold fresh air.

As for condensation at the junctions, it cannot be addressed with a simple 0D model as it is a phenomenon that strongly depends on local flow features, so 3D-CFD condensation model should be involved with a surrogate model that could be employed. Chapter 4 explores the possibility of not only doing a standard metamodel based only in the 3D-CFD simulations but also to involve somehow a 0D model to alleviate the extension of the numerical campaign. To do so,

Chapter 4 presented a novel multifidelity methodology to obtain the condensation by two different models, a two-branch 0D (low-fidelity) perfect mixing condensation model presented in section 4.2.2 and a validated 3D-CFD condensation model of high computational cost (high fidelity) developed by Serrano et al. [73] and validated with experiments in Chapter 3.

Once the condensation in the LP-EGR system is properly calculated, a quantification of the compressor damage is performed by qualitatively obtaining the damage threshold, based on the durability test performed by Galindo et al. [74]. Also, condensation and emissions are studied as a function of environmental parameters such as ambient temperature and different LP-EGR and HP-EGR strategies as a function of refrigerant temperature and how it affects emissions and condensation.

5.2 Methods

5.2.1 Engine simulations and measurements

5.2.1.1 Engine modeling

The engine modeling simulations have been carried out using VEMOD [181], developed at CMT-Motores Térmicos. VEMOD is able to solve compressible thermo-fluid dynamic processes in zero-dimensional and one-dimensional domains, as well as other phenomena such as simple electric systems, incompressible flow and control systems. The computations are vectorized using Eigen C++ template library for linear algebra [182].

Compressible flow in one-dimensional elements, such as engine ducts, is solved by a finite-volume method, in which Euler's equations are calculated using a MUSCL scheme [183]: second order spatial accuracy is achieved wherever the solution is smooth enough, gracefully transitioning to first order as the ratio of successive gradients increases in magnitude. The HLLC approximate Riemann solver by Toro [184] is used, coupled with the monotonies central limiter function

by van Leer [185] to limit the extrapolation of the solution towards the cell interfaces, as well as Heun's method for time integration. Source terms are added to take into account effects such as area variation, heat transfer and friction, the latter being computed using the phenomenological Colebrook-White equation to compute the friction factor. The ideal gas equation of state is used, while the thermodynamic properties such as the specific heat capacities, viscosities or conductivities are functions of the fluid composition and temperature.

Zero-dimensional elements, such as the cylinders or stagnation plenums, are computed solving mass, energy and species accumulation equations with a semi-implicit method. Heat transfer through the cylinder walls takes into account also swirl effects.

Heat transfer through any solid element, such as the duct or the cylinder walls, is computed using a finite-element approach, coupled with the heat fluxes calculated in the flow elements in contact with it.

Incompressible fluid circuits, such as those for the engine coolant and lubricant, are solved using quasi-steady methods, as well as electric circuits. Heat transfer effects are also included, as described in [186].

Boundary conditions are applied between different zero- dimensional and one-dimensional elements, using ghost cells in which their state vectors are related to the ones inside the computational cells connected to them.

Turbochargers are computed by imposing their performance parameters, extrapolated from that present in manufacturer maps as described in [187, 188], as source terms in both the compressor and the turbine. Other effects are also included, such as heat transfer and mechanical losses [189, 190, 191].

Each time-integration iteration, the time-step is computed taking into account restrictions due to the Courant-Friedrichs-Levvy stability criterion in one-dimensional ducts and a maximum relative change in mass and species concentration inside the zero-dimensional elements.

In these simulations, the heat released inside the combustion chamber is computed by means of a predictive model. Pollutant emissions, such as NO_x and soot, are computed by a feedforward neural network.

5.2.1.2 Engine experiental apparatus and engine maps

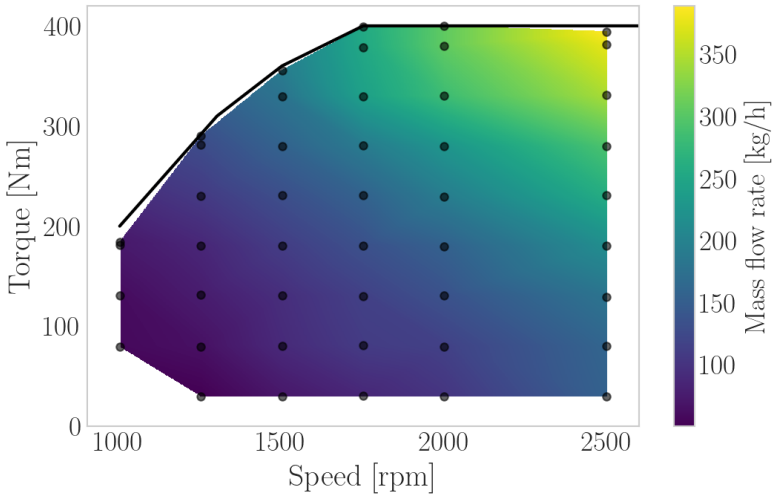

Figure 5.2: Mass flow rate for an engine operating map.

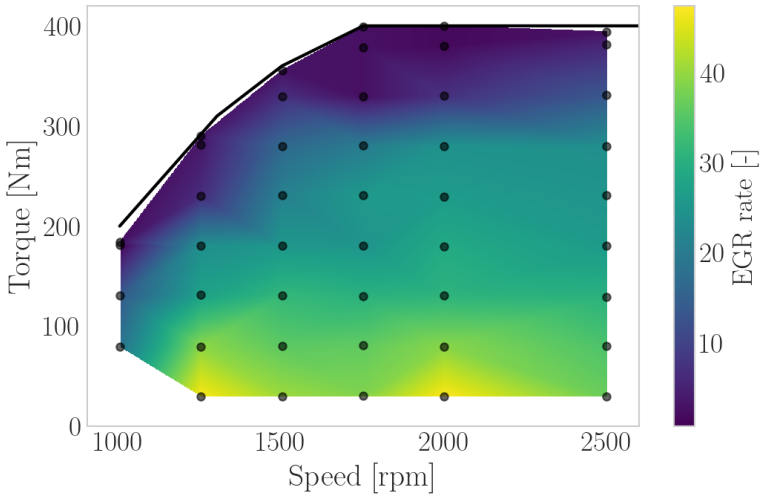

Figure 5.3: EGR mass flow rate for an engine operating map.

The experimental setup of the engine is presented in order to obtain the operating limitations in steady state conditions in a real engine and thus, to obtain the ranges of the variables that affect the condensation in the LP-EGR system. The engine used to extract the information is a 4-cylinder diesel engine with 2 L

of displacement, turbocharged and with direct injection. This engine integrates the water charge air cooler in the intake manifold and employs the LP-EGR and HP-EGR systems. The engine was mounted on an engine dynamometer maintaining a constant speed using a braking strategy. Engine sensors are recorded by an acquisition system while the ECU controls the fuel injected and actuators such as the exhaust throttle and the LP-EGR and HP-EGR valves. A hot wire anemometer is used to measure intake air mass flow and pressure sensors and thermocouples are installed to measure flow characteristics in the engine. Finally, fuel consumption is measured using an external fuel balance.

The engine just described has been modeled and calibrated with VEMOD (presented at Section 5.2.1.1) and for that, it is presented the most representative variables at the LP-EGR line, like the inlet Air Mass Flow at the Fig. 5.2, the EGR mass flow rate (Fig. 5.3) and the EGR specific humidity at the Fig. 5.4. This parameter depends mainly on the combustion process in which water vapor is produced as a product of the in-cylinder reaction.

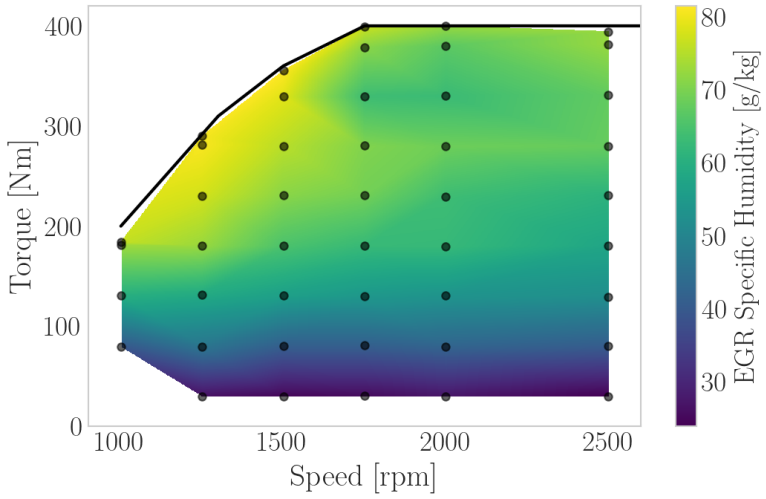

Figure 5.4: *EGR mass specific humidity for an engine operating map.*

5.2.2 Cooler condensation model

The 0D condensation model of the cooler used in this chapter to calculate the condensation water generated with engine cycles at different conditions was presented in Section 2, based on the specific humidity difference between the inlet and outlet conditions of the heat exchanger. For the reader's convenience, the equations employed on the 0D condensation model in Section 2 are mentioned again. Employing Eq. 5.1 between stages 2 and 3 as seen in Fig 1.5 of the background section (Section 1.2), the condensation obtained is the difference between stages being the maximum water content that, at saturated conditions, the flow could hold as vapor in stage 2 and 3. Then, the transformation of the specific humidity difference into the mass flow rate of water is shown in Eq. 5.2.

$$w_{\text{cond}}\,(t) = \frac{w_{EGR}(t) - w_i(t)}{1 + \frac{w_{EGR}(t)}{1000}} \tag{5.1}$$

$$\dot{m}_{\text{cond}} = w_{\text{cond}} \cdot \dot{m}_{\text{dryair}} \tag{5.2}$$

5.2.3 Junction condensation models

5.2.3.1 0D Perfect mixing condensation model

A 0D perfect mixing model based on the psychrometric process and including effects such as nozzle reduction or evaporation has been used to estimate the condensation flux in the two-stream mixing process, in this particular case, with the intake air and LP-EGR streams. The model has been presented in chapter 4.2 based on the literature but adding effects that directly affect the condensation produced. The model considers perfect interbranch mixing with ideal gases. Figure 4.2 shows, schematically, the inputs to the model described. This model is based on the research of Serrano et al. [36] but including the effects of nozzle and evaporation processes which makes a more complete model. If

there was condensation previously at the junction in the EGR line, the mixture condensation is not affected as it maintains the same EGR temperature.

In the perfect mixing process, both streams are mixed completely in an homogeneous flow, obtaining the maximum amount of water that can be condensed in perfect conditions.

5.2.3.2 Multifidelity model: 0D Perfect mixing condensation model and 3D-CFD condensation model

As for the 3D-CFD condensation simulations (high fidelity simulations) performed in this chapter, they are based on the previous chapter 3 in which the 3D-CFD condensation model and simulations have been presented and validated with experiments. The boundary conditions used in the simulations are defined in the Section 4.5.1.1 which are based on a cycle described at Section 2.3.2 based on the characteristic operating ranges.

The studied geometry was presented at Section 4.2.3, a T-junction where two flows are mixed (Inlet and EGR) with one outlet and a nozzle with an area reduction.

As for the meshing methodology, the same methodology proposed by Chapter 3 is followed. In this case, a mesh composed of polyhedral cells with a base size of 1.5 mm is used by adding on the walls eight layers of prisms with a total thickness of 30 % from the base to assist the solution near the walls.

A multi-fidelity approximation is performed with the 0D PM and 3D-CFD junction mixing models using a variable that employs both results, the Three-way junction difference . The methodology employed was defined at the Chapter 4 where the Three-way junction difference was selected as the one of the approaches to have the closest results to the reality when the RSM was trained (as can be seen in Figs. 4.9,4.10,4.11). The difference was defined as the difference between the 0D PM model and the 3D-CFD (Eq. 4.35). Then, a statistical method is developed to obtain a response surface to predict water condensation.

Finally, a comparison between the models and an application of the response surface on engine maps and cycles is performed.

5.2.3.3 0D PM model with an efficiency

Another alternative to approach in a simple way the 0D PM model to the 3D-CFD model is to employ a constant value of the efficiency at the whole range of points, reducing the computational cost that was required to train an RSM but increasing the discrepancies with the "real" condensation values. This alternative is considered to compare with a more realistic approach which is the RSM, employing an efficiency of a 50 % [1].

The Three-way junction efficiency, defined previously at section 4.5.1.2, is the parameter that compares the condensation obtained in the mixing currents at the junction by the 0D PM model and the 3D-CFD condensation model. Once it is imposed the 50 % constant efficiency, the correlation between models are followed by Eq. 5.3.

$$\dot{m}_{cond.,0D,\eta=50\%} = \dot{m}_{cond.,0D} \cdot 0.5, \tag{5.3}$$

5.2.3.4 Comparison between T-junction prediction condensation approaches

As mentioned above, the 0D PM model predicts the maximum condensation that the junction is able to condense, as opposed to the 3D-CFD condensation simulation which calculates more accurately the condensation due to the mixing phenomenon. There are large differences between the 0D PM model and the 3D-CFD condensation simulations depending on each case and, in addition, on the calculation of the Three-way junction difference which is not constant.

[1] This value is taken and not another one because there are not yet characterized several unions that allow to know what is the typical range of values of this parameter.

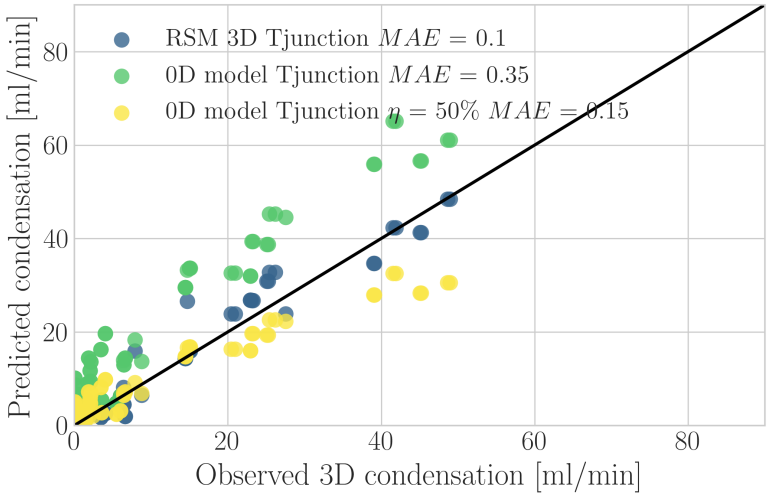

Figure 5.5: Predicted 3D condensation dispersion

In order to compare the different Three-way junction condensation approaches presented in this chapter as the 0D PM model, the polynomial RSM and the constant efficiency, Figure 5.5 shows the comparison between the models on the predicted condensation with the 128 DoE cases, including a 0D PM model affected by a constant efficiency of 0.5. As can be seen, employing the polynomial response surface model, more accurate values on condensation predictions are obtained with $MAE = 0.1$, once employing the constant efficiency obtains a MAE of 0.15 and without affecting the 0D model gets a MAE of 0.35. For the 0D PM model and as mentioned, it overpredicts condensation due to the model definition that obtains the maximum water condensation capable of condensing at a junction as a perfect mixing between branches. Setting a constant efficiency of 0.5 gives better results than with the 0D PM model and good agreement at low values of condensation but at higher values it differs from the observed condensation.

5.2.4 Estimation of compressor durability

With the models to predict different condensation sources presented in Sections 5.2.2 and 5.2.3, the temporal trace of the condensation produced during a

warm-up cycle can be obtained. With this, the erosion caused on the compressor impeller could be calculated in terms of kinetic energy, as an estimation of the impeller durability is represented considering each day a WLTC warm-up cycle under cold conditions. It should be mentioned that condensation within the flow is considered, but as shown in the work of Galindo et al. [74], the predicted flow rate correlates with the impeller damage.

A work philosophy methodology is presented to estimate a quantitative *toy-model* study of the compressor impeller performed by setting a time threshold at which the impeller blades start to erode with a WLTC cycle under cold conditions. An experimental durability test was performed by Galindo et al. [74] comparing the blade damage after 50h with constant condensation and turbocharger speed. Considering this study, the parameters of the threshold conditions for the case where a slightly experimental observation of erosion appears were obtained by setting as reference for this chapter in Eq. 5.4 (condensation, turbocharger speed and durability test duration) to obtain the energy threshold.

Considering a WLTC warm-up cycle under cold conditions, the equation 5.5 presents the energy calculation for the whole cycle including condensation in the LP-EGR cooler and in the Three-way junction and the turbocharger speed for each time step. This term calculates the energy damage on the blades.

Equation 5.6 presents the correlation between the threshold Energy (Eq. 5.4) and the warm-up cycle Energy (Eq. 5.5), being $n_{cold,warm-up}$ the number of cycles during a year, considering for this study 365 cycles/year.

$$E_{threshold} = \dot{m}_{cond-ref.} \cdot {N_{ref.}}^2 \cdot t_{ref.} \tag{5.4}$$

$$E_{warm-up} = \sum_{i=1}^{cycle} \dot{m}_{cond}(i) \cdot N(i)^2 \cdot \Delta t \tag{5.5}$$

$$Durab. = \frac{E_{threshold}}{E_{warm-up}} \cdot \frac{1}{n_{cold,warm-up}} \tag{5.6}$$

5.3 Results and discussion

Most of the parameters that manage the condensation at the LP-EGR system on the engines are imposed by the engine operating conditions: EGR rate EGR_{rate}, EGR specific humidity w_{EGR} and inlet air mass flow $\dot{m}_{air}$. But there are other parameters that are not imposed by the working point on the engine. Those that are driven by the environment, the weather, the time....

In this group are the ambient variables: ambient temperature T_{air}, the ambient Relative Humidity RH_{air} and outlet pressure p_{out} which is the compressor inlet pressure and mainly depends on the ambient pressure. An special case is the EGR temperature T_{EGR} which starts the cycle with the ambient temperature undergoing a change that impacts the condensation until it reaches the nominal value, main reason to study the warm-up cycles.

The results section is divided depending on the ambient parameters employed in each case, studying in depth the effect on the condensation.

5.3.1 Reference study for constant ambient conditions

In this section, a constant ambient temperature of -7 ºC, Relative humidity of 85 % and an EGR temperature of 30 ºC is selected to perform a reference study basing on engine maps and engine cycles.

5.3.1.1 Condensation on engine maps

The model obtained to predict water condensation in a T-junction, employing an RSM with the condensation difference as a combination of the 3D-CFD model and the 0D PM model, and the 0D cooler model presented in Sect. 5.2.2 are employed to predict condensation in the LP-EGR loop (EGR cooler and T-junction) on stable engine maps and WLTC homologation cycles at -7 °C.

As for the engine steady maps, Figure 5.6 shows the combination of the water

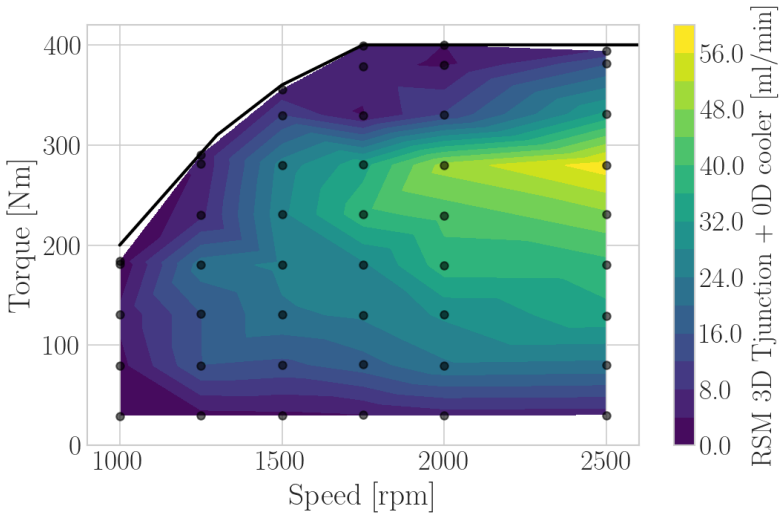

Figure 5.6: Predicted condensation total condensation (T-junction + cooler) on an engine map for Inlet temperature of -7 °C, RH of 85 % and EGR temperature of 30 °C

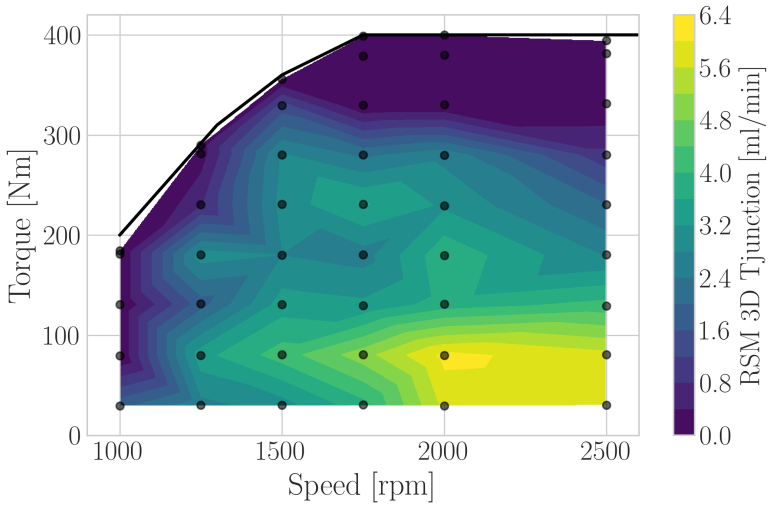

Figure 5.7: Predicted condensation on the T-junction employing a RSM on an engine map for Inlet temperature of -7 °C, RH of 85 % and EGR temperature of 30 °C

condensation models, an RSM for the Three-way junction water and the 0D PM model for the cooler for given environmental parameters. As the inlet temperature has been set to -7 °C, a Relative Humidity of 85 % and an EGR temperature of 30 °C. This EGR temperature has been selected as a reference, the value is

below T_{dew} to have both condensation phenomena (cooler and T-junction) as can be seen in Fig. 5.10. The rest of the engine parameters were presented in Sect. 5.2.1. As can be seen, at high speed values a maximum condensation of 64 ml/min appears, while at low torques and speed there is almost no condensation.

Focusing on the water produced at the Three-way junction, Figure 5.7 presents the condensation map of the engine using the RSM. As can be seen, there is no condensation in the maximum torque curve while in the rest of the map it appears with a maximum value of 7 ml/min.

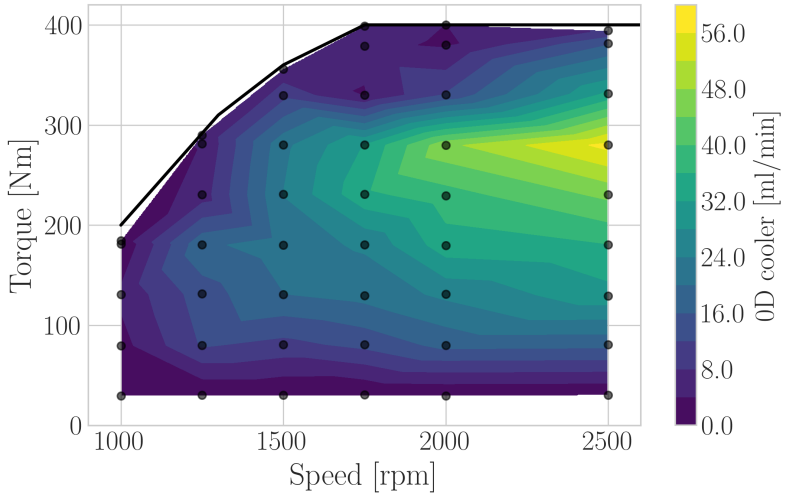

Figure 5.8: *Predicted condensation on the EGR cooler employing a 0D PM model on an engine map for Inlet temperature of -7 °C, RH of 85 % and EGR temperature of 30 °C*

As for the water condensation in the EGR cooler, figure 5.8 presents the water condensation in the EGR heat exchanger. As can be seen, there is a maximum value of 56 ml/min which is higher than that obtained at the Three-way junction and with lower condensation at low torque and close to the maximum torque and speed curve.

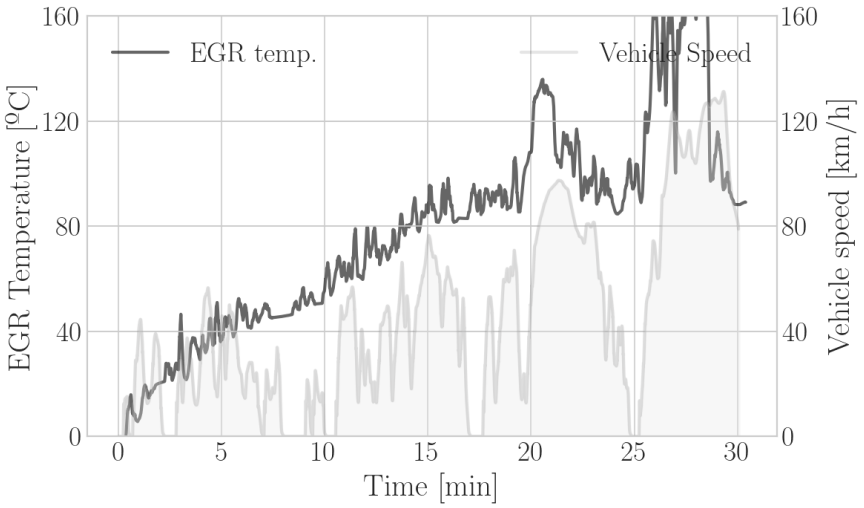

Figure 5.9: *WLTC condensation evolution on different approaches and EGR temperature evolution*

5.3.1.2 Condensation on engine cycles

As for the water condensation generated with the homologation cycles, a WLTC warm-up cycle has been performed under cold conditions (Ambient temperature of -7 °C) with the calibrated Vemod (Virtual Engine) model and with a relative humidity of 85 %. During warm-up, the engine coolant temperature increases from the ambient temperature, as can be seen in Fig. 5.9, increasing the EGR temperature with the thermal load of the engine. As an example, when the vehicle speed goes down as the 17 min the EGR temperature keeps constant.

Focusing on the "realistic" approach used by RSM in the Three-way junction water calculation, Figure 5.10 presents separately the condensation caused by the junction and by the EGR cooler. As can be seen, the condensation due to the EGR cooler decreases with time starting at 5 minutes, which almost disappears due to the increase in EGR temperature as shown in the Fig. 5.9. The condensation generated due to Three-way junction mixing remains permanent due to the whole cycle as it is affected by the cold inlet temperature.

Table 5.1 presents the estimation damage threshold for the condensation approaches following the Section 5.2.4. Employing the 0D PM model for the

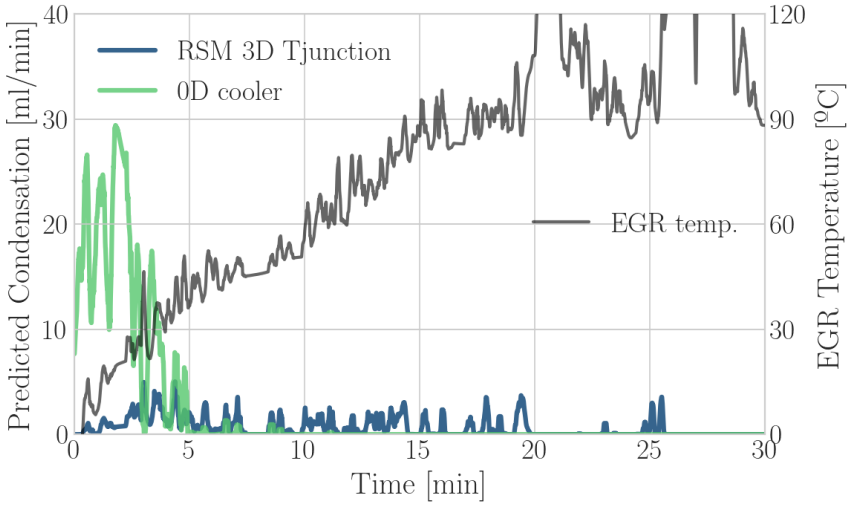

Figure 5.10: *WLTC condensation evolution comparing the water produced at the T-junction and the EGR cooler*

Three-way junction and for the EGR cooler, it results in a period of 4.3 years to start damaging the blades. While employing the "realistic" condensation calculation approach with the RSM model for the T-junction and the 0D model for the EGR cooler, a period of 4.8 years is estimated for visible erosion to begin. Once the condensation at the junction is calculate from the 0D PM model but minimize with a constant efficiency of 50 %, 8.5 years is estimated to start eroding. There is a big difference between the estimation damage threshold with a 50 % constant efficiency and the difference RSM case, which it was not in-line with the Fig. 5.5 and the MAE values.

Table 5.1: *Impeller damaging threshold for each condensation approach considering one cold warm-up WLTC cycle a day with an ambient temp. of -7 °C*

Condensation approaches	Damaging threshold [years]
0D model (Tjunction + cooler)	4.3
RSM 3D Tjunction (difference)+ 0D cooler	4.8
RSM 3D Tjunction 50 % constant efficiency + 0D cooler	8.5

Following the discussion of the big difference between cases at the estimation damage threshold, Figure 5.11 presents a comparative between the water condensation at the junction obtained by a MF model of the difference, the

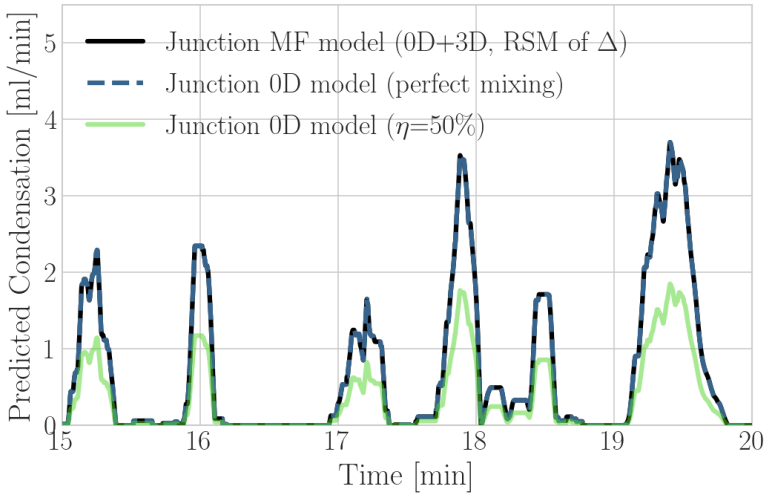

Figure 5.11: WLTC condensation evolution at the junction comparing different approaches

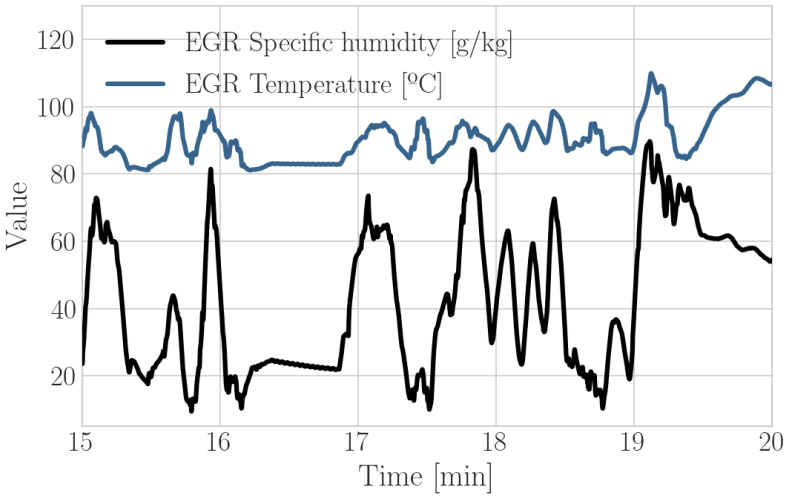

Figure 5.12: WLTC EGR temperature and specific humidity evolution during a period of time

junction 0D model and the junction 0D model employing a constant efficiency of 50 % during the WLTC cycle between the 15 to 20 minutes. As can be seen, the discrepancies between employing a MF model of the difference for predicting the water condensation at the junction or employing a 0D PM model were

non-existents, while some differences appear when a constant efficiency is employed, going in line with the results of the Table 5.1. Figure 5.12 presents the EGR temperature and specific humidity evolution during the WLTC cycle between the 15 to 20 minutes. As can be seen, the EGR temperature and the EGR specific humidity were outside of the range in which the RSM was trained (as can be seen in Table 4.3). The EGR temperature range was between 40 to 60 ºC and during this 15 to 20 minutes, the EGR temperature is above 80 ºC. Once the EGR specific humidity range was 30 to 70 g/kg and in some peaks at the Fig. 5.12 exceeds the level of 70 g/kg.

and could be the reason for obtaining an unpredictable behavior at the MF model of the difference.

5.4 Sensitivity analysis on condensation for ambiental parameters

A sensitivity analysis of water condensation in the Three-way junction mixture was performed using the RSM approach developed and with the 0D condensation model of the EGR cooler presented in Sect. 5.2.2, varying the ambient temperature of the heating WLTC cycle using LP-EGR for the entire cycle.

As can be seen in Fig. 5.13, the reduction in ambient temperature results in more water condensation during the cycle, but in a higher proportion after 5 min when the condensation mixture at the T-junction takes on a significant role. At this time, the EGR temperature is above the dew point, which prevents condensation in the EGR cooler. This assumption can be confirmed by looking at Table 5.2, as can be seen the percentage of accumulated water generated by the T-junction is much higher when the ambient temperature decreases, with almost zero condensation produced by the Three-way junction in the case of ambient temperature 20 °C.

A reduction of the damage threshold occurs as the total condensation of accumulated water increases with the reduction of the ambient temperature in the warm-up cycle. At the higher ambient temperature, the damage threshold could be considered almost impossible to reach considering one cycle per day.

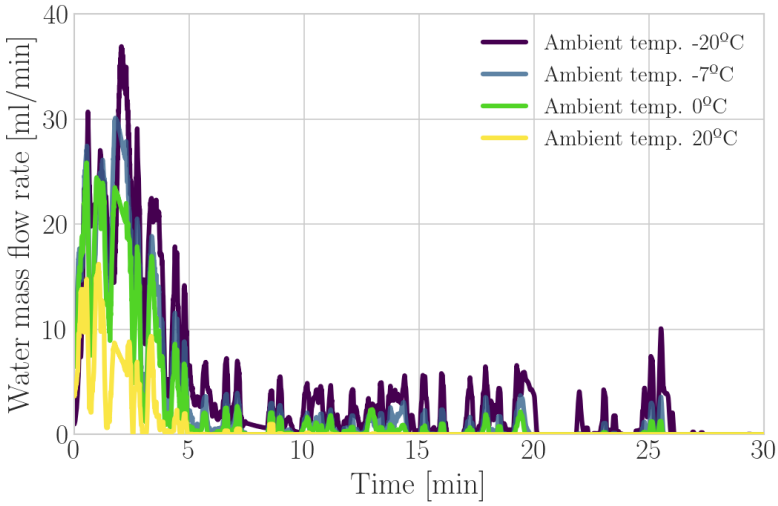

Figure 5.13: Predicted water condensation evolution on a WLTC cycle with different ambient temperatures

Table 5.2: Accumulative values of different parameters regarding condensation during WLTC warm-up cycles employing only LP-EGR

Ambiental cases	$m_{cond-total}$ [ml]	$m_{cond-cooler}$ [ml]	$m_{cond-Tjunction}$ [ml]	Damag. threshold [years]
Ambient temp. -20°C	130.9	79.4	51.5 (28 %)	2.5
Ambient temp. -7°C	88.8	69.0	19.8 (18 %)	4.8
Ambient temp. 0°C	69.0	58.4	10.6 (13 %)	7.2
Ambient temp. 20°C	26.1	24.7	1.4 (5 %)	24.1

Water condensation from the EGR cooler reduces as the ambient temperature increases, since the ambient temperature is the EGR temperature at the start of the cycle.

Regarding the emissions produced by the variation of the ambient temperature during the warm-up of the WLTC engine, the table 5.3 shows the average of the whole cycle in the different pollutants. As can be seen, the average fuel consumption (BSFC) increases significantly with decreasing ambient temperature. This trend appears in the average of CO, Soot and THC while for the different cases, the average of EGR rate and NOx are quite close. Special mention should be made of the Soot emissions, which are very important when the ambient temperature is reduced, increasing by 90 % between 20°C to -20°C.

Table 5.3: Average of different parameters during WLTC strategies of LP-EGR and HP-EGR

Ambiental cases	$\widetilde{EGR_{rate}}$ [%]	$\widetilde{NOx}$ [ppm]	$\widetilde{BSFC}$ [g/kW]	$\widetilde{CO}$ [ppm]	$\widetilde{Soot}$ [ppm]	$\widetilde{THC}$ [ppm]
Ambient temp. -20°C	33.36	131.26	305.3	177.7	1.25	29.20
Ambient temp. -7°C	33.52	128.02	297.05	172.76	0.81	24.88
Ambient temp. 0°C	33.51	128.04	292.95	163.16	0.76	23.64
Ambient temp. 20°C	33.29	130.21	284.34	136.5	0.66	22.97

5.5 Strategies for employing LP-EGR and HP-EGR at warm-up conditions

Different strategies are presented that vary the activation of LP-EGR and HP-EGR for a warm-up WLTC in cold conditions (ambient temperature set at -7°C), starting with HP-EGR until the coolant temperature reaches a certain value and then, sweeping the HP-EGR to an LP-EGR. These strategies are studied in terms of the EGR rate, the water condensation produced in the LP-EGR system and the emissions generated during the cycle for the different strategies.

Regarding the EGR rate and the use of HP-EGR and LP-EGR, Figure 5.14 shows the activation of each EGR system for the different strategies. As can be seen, when HP-EGR is activated the EGR rate is lower than the cases with LP-EGR at the same time. This trend can be seen in Table 5.4, where the average EGR rate grows when LP-EGR is activated earlier.

In terms of water condensation due to the different strategies in the LP-EGR system (T-junction and cooler) using the methods presented in this chapter such as the RSM to predict mixing condensation in the Three-way junction and the 0D condensation model for the EGR cooler, Figure 5.15 shows the evolution of condensation generation during the WLTC cycle obtaining higher water mass flow rates when the LP-EGR is activated earlier. This phenomenon produces a higher water accumulation at the end of the cycle. As can be seen in Fig. 5.16, it grows rapidly during the first 5 minutes as the LP-EGR cooler manages condensation. Looking at the table 5.5, the percentage of water produced at the junction with respect to the total condensation grows with increasing activation temperature of the LP-EGR. The damage threshold decreases with earlier LP-EGR activation due to higher water condensation.

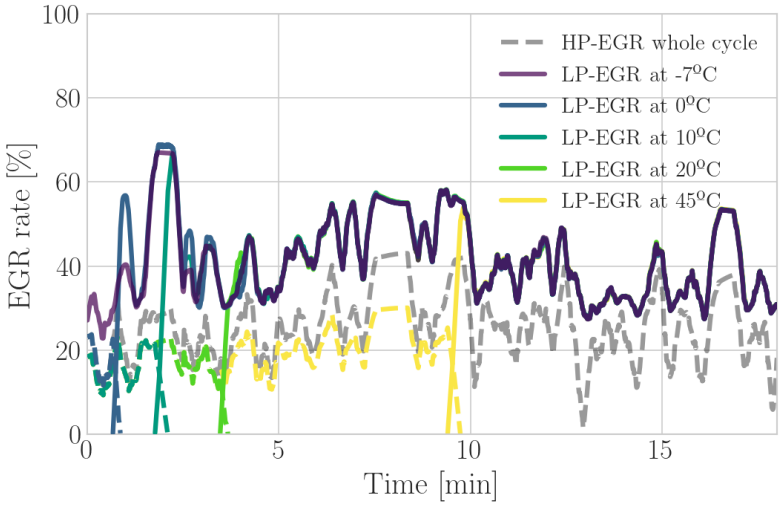

Figure 5.14: EGR evolution comparing HP-EGR and LP-EGR with different strategies on a warm-up WLTC cycle at cold conditions

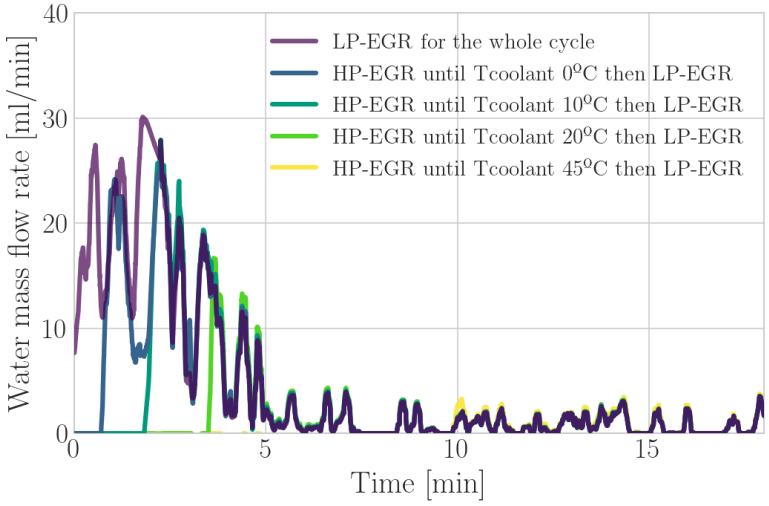

Figure 5.15: Predicted water condensation evolution on a warm-up WLTC cycle at cold conditions with difference LP-EGR and HP-EGR alternatives

Regarding NOx emissions during the different LP-EGR and HP-EGR strategies, Figure 5.17 shows the influence of employing HP-EGR in the early times until the coolant temperature reaches the target in terms of NOx emissions. As can be seen, emissions depend on the EGR system employed. The maximum EGR rates

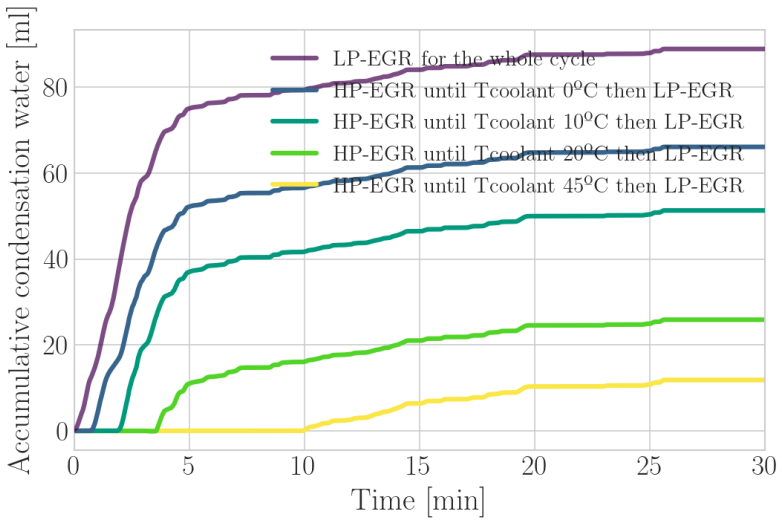

Figure 5.16: *Predicted accumulative water condensation on a warm-up WLTC cycle at cold conditions with difference LP-EGR and HP-EGR alternatives*

Table 5.4: *Accumulative and average of different parameters during WLTC strategies of LP-EGR and HP-EGR*

Strategies	$\widetilde{EGR_{rate}}$ [%]	$\widetilde{NOx}$ [ppm]	$\widetilde{BSFC}$ [g/kW]	$\widetilde{CO}$ [ppm]	$\widetilde{Soot}$ [ppm]	$\widetilde{THC}$ [ppm]
HP-EGR for the whole cycle	14.5	279.6	290.6	273.8	1.25	16.1
LP-EGR for the whole cycle	33.5	128.0	297.1	172.8	0.8	24.9
HP-EGR until Tcoolant 0°C	33.3	132.2	296.8	161.2	0.95	25.1
HP-EGR until Tcoolant 10°C	32.9	137.9	296.8	161.6	0.97	25.9
HP-EGR until Tcoolant 20°C	32.2	145.7	296.3	163.8	0.99	25.7
HP-EGR until Tcoolant 45°C	29.6	152.8	294.9	166.9	0.97	22.0

that can be achieved with HP-EGR and LP-EGR are different. With HP-EGR activated, high NOx emission values appear as opposed to the LP-EGR system which lower values appears.

Particular interest are the cumulative NOx emissions in Fig. 5.18, where the strong influence of the first few minutes on the different strategies and, therefore, the importance of activating LP-EGR as early as possible instead of HP-EGR can be seen. This trend can be seen in the average NOx emissions in the table 5.4.

An important parameter to study is the formation of soot emissions. At this case, Figure 5.19 shows how affects the different strategies of LP-EGR and HP-EGR into the soot formation. As can be seen, an early activation of the LP-EGR a lower soot formation on the WLTC cycle during the first minutes and thus, on

Table 5.5: Accumulative and average of different parameters during WLTC strategies of LP-EGR and HP-EGR

Strategies	$m_{cond-total}$ [ml]	$m_{cond-cooler}$ [ml]	$m_{cond-Tjunction}$ [ml]	Damag. threshold [years]
HP-EGR for the whole cycle	-	-	- (- %)	-
LP-EGR for the whole cycle	88.8	69.0	19.8 (19 %)	4.8
HP-EGR until Tcoolant 0°C	66.1	46.2	19.9 (23 %)	6.2
HP-EGR until Tcoolant 10°C	51.2	32.0	19.2 (27 %)	7.2
HP-EGR until Tcoolant 20°C	25.8	9.3	16.5 (39 %)	9.3
HP-EGR until Tcoolant 45°C	7.0	0.8	6.2 (47 %)	14.8

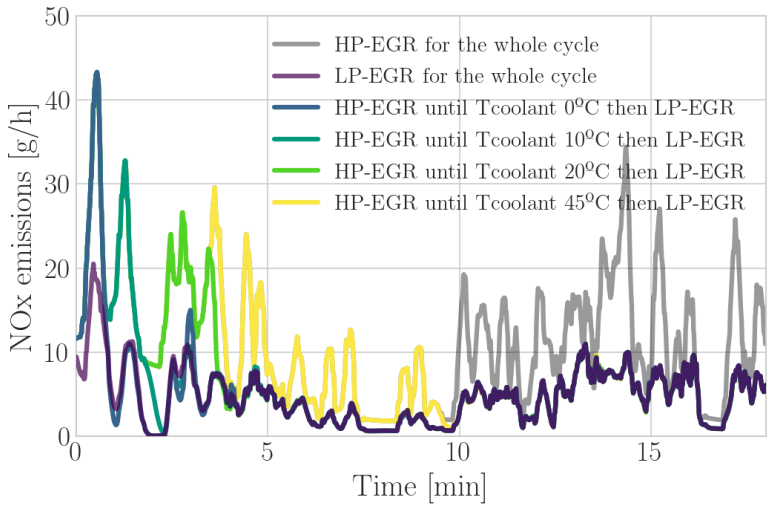

Figure 5.17: NO_X evolution on a WLTC cycle with difference LP-EGR and HP-EGR alternatives

the average soot emissions (Table 5.4).

Finally, some parameters such as mean BSFC, CO and THC are studied in Table 5.4. As can be seen, all three increase slightly with earlier activation of the LP-EGR.

5.6 Conclusions

In this chapter, a new methodology is presented to obtain realistic condensation in the LP-EGR loop with a novel 0D PM condensation model that includes the effects of the nozzle and evaporation process. This methodology is able to study

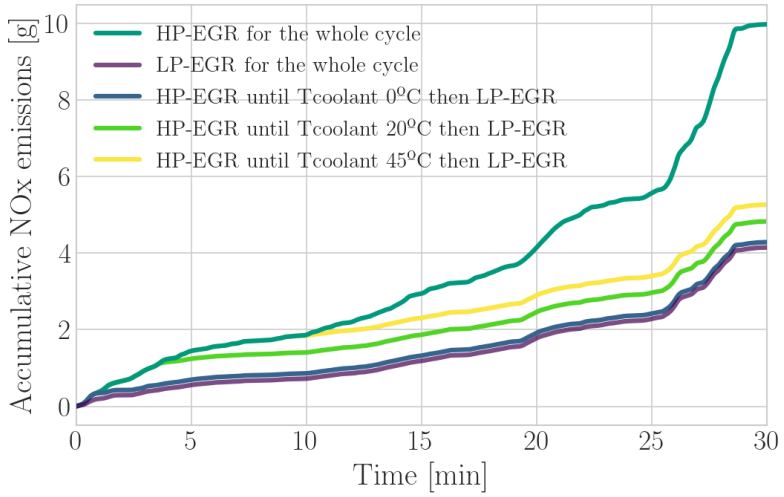

Figure 5.18: Accumulative NO_X emissions on a WLTC cycle with difference LP-EGR and HP-EGR alternatives

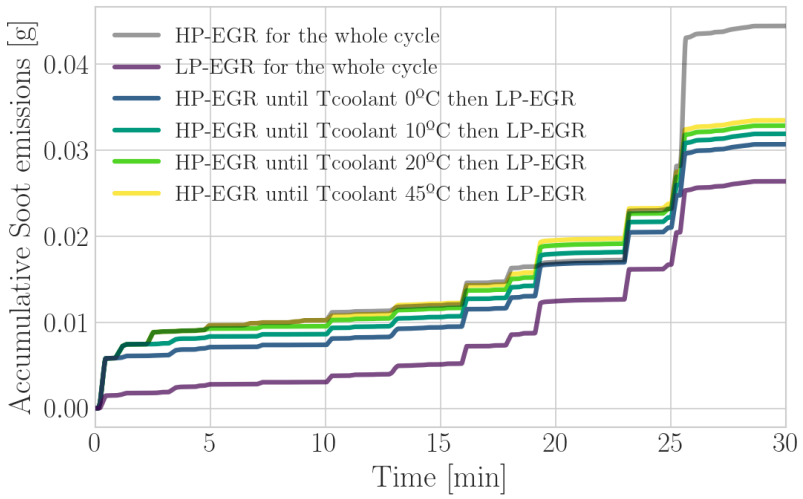

Figure 5.19: Predicted accumulative soot emissions on a WLTC cycle with difference LP-EGR and HP-EGR alternatives

different LP-EGR and HP-EGR strategies while studying how it affects emissions and condensation with the impact on compressor durability.

Regarding the methodology presented for modeling the condensation at the LP-EGR Three-way junction using a Polynomial Response Surface Model,

good agreement has been obtained by comparing the observed and predicted 3D condensation at the junction and much better to employ a RSM than directly employing the 0D PM model or imposing a constant efficiency. Stationary condensation maps have been presented for the LP-EGR Three-way junction and the LP-EGR cooler using the new RSM methodology in the junction modeling, obtaining a maximum water condensation of 64 ml/min in the line and 7 ml/min generated only in the Three-way junction. Likewise, condensation has been studied in the WLTC warm-up cycles with cold conditions in a particular case of -7°C obtaining a maximum condensation of 30 ml/min in the first minutes.

A quantification of compressor damage has been performed based on the stable experimental tests performed by Galindo et al. [74]. An estimation of a condensation threshold to notice a compressor impeller damage has been considered by performing a WLTC warm-up cycle per day at -7°C obtaining a time period of 6.2 years.

As for a sensitivity analysis to ambient temperature using the LP-EGR from the beginning of the test, a low temperature and high condensation produces in the whole LP-EGR line a higher percentage of condensation caused by the T-junction, and therefore a small damage threshold. Considering the emissions performed with variations in ambient temperature, noticeable pollutant differences appear in the mean BSFC, a low ambient temperature a high consumption.

A study of different LP-EGR and HP-EGR strategies in terms of condensation and emissions was performed. A WLTC warm-up cycle at -7°C was the basis for modifying LP-EGR activation as a function of refrigerant temperature and employing HP-EGR when LP-EGR was deactivated. A high variation of NO_x emissions depending on LP-EGR activation appears, an early activation a low NO_x emission realized. An increase of soot emissions appear when a late activation of the LP-EGR, but on the contrary, a reduction of THC emissions. A constant value of CO emissions was realized with respect to the different strategies, except when the LP-EGR was activated at the beginning. As for condensation, a late activation of the LP-EGR resulted in a small amount of condensation and a high threshold of impeller damage.

Therefore, the presented chapter highlights the importance of LP-EGR and HP-EGR strategies in relation to emissions and condensation in LP-EGR. In addition, an important role appears in the trade-off between compressor impeller durability and emission reduction, making a necessary task to model the condensation in homologation cycles with the proposed methodology. If the engine were a gasoline type with a relative air-fuel ratio of 1 and the specific humidity close to 100g/kg (much higher than the diesel engine as can be seen in Fig. 5.12). The condensation would be greater in general and would probably increase the weight of the condensation junction. As can be seen in Figs. 5.11,5.12, even at high EGR temperature (much higher than T_{dew}) there is condensation at the junction once the specific humidity gets high values. Thus, once a gasoline engine is simulated in terms of junction condensation with high specific humidity values, condensation will appear at the junction with a higher value.

Chapter 5 References

[19] M. Lapuerta, A. Ramos, D. Fernandez-Rodriguez, and I. Gonzalez-Garcia. "High-pressure versus low-pressure exhaust gas recirculation in a Euro 6 diesel engine with lean-NOx trap: Effectiveness to reduce NOx emission". *International Journal of Engine Research*, -, (Nov. 14, 2018), pp. 0–9. DOI: 10.1177/1468087418817447 (cit. on pp. 5, 7, 24, 151).

[20] J. M. Luján, C. Guardiola, B. Pla, and A. Reig. "Switching strategy between HP (high pressure)-and LPEGR (low pressure exhaust gas recirculation) systems for reduced fuel consumption and emissions". *Energy*, 90, (2015), pp. 1790–1798. DOI: 10.1016/j.energy.2015.06.138 (cit. on pp. 6, 7, 25, 140, 151).

[36] J. R. Serrano, P. Piqueras, E. Angiolini, C. Meano, and J. De La Morena. "On Cooler and Mixing Condensation Phenomena in the Long-Route Exhaust Gas Recirculation Line". In: *SAE Technical Paper*. 2015. DOI: 10.4271/2015-24-2521 (cit. on pp. 7, 31, 105, 108, 157, 185).

[57] H. Song and S. Song. "Numerical investigation on a dual loop EGR optimization of a light duty diesel engine based on water condensation analysis". *Applied Thermal Engineering*, 182, (2021), pp. 1–12. DOI: 10.1016/j.applthermaleng.2020.116064 (cit. on pp. 10, 25, 151).

[73] J. Serrano, P. Piqueras, R. Navarro, D. Tarí, and C. Meano. "Development and verification of an in-flow water condensation model for 3D-CFD simulations of humid air streams mixing". *Computers & Fluids*, 167, (2018), pp. 158 –165. ISSN: 0045-7930. DOI: 10.1016/j.compfluid.2018.02.032 (cit. on pp. 11, 13, 25, 51, 53, 66, 95, 105, 107, 153, 183, 184).

[74] J. Galindo, P. Piqueras, R. Navarro, D. Tarí, and C. Meano. "Validation and sensitivity analysis of an in-flow water condensation model for 3D-CFD simulations of humid air streams mixing". *International Journal of Thermal Sciences*, 136, (2019), pp. 410 –419. ISSN: 1290-0729. DOI: 10.1016/j.ijthermalsci.2018.10.043 (cit. on pp. 11, 25, 51, 68, 69, 73, 74, 107, 135, 153, 161, 175, 184).

[176] P. Arnau, J. Martín, B. Pla, and A. Aunón. "Diesel engine optimization and exhaust thermal management by means of variable valve train strategies". *International Journal of Engine Research*, 22 (4), (2021), pp. 1527 –1537. DOI: 10.1177/1468087419894804 (cit. on p. 151).

[177] A. Ramos, J. Munoz, F. Andres, and O. Armas. "NOx emissions from diesel light duty vehicle tested under NEDC and real-word driving conditions". *Transportation Research Part D: Transport and Environment*, 63 (0), (Aug. 1, 2018), pp. 37–48. DOI: 10.1016/j.trd.2018.04.018 (cit. on p. 151).

[178] J. Serrano, P.Piqueras, E. Sanchís, and B. Diesel. "Optimization of dual-loop exhaust gas recirculation splitting for a light-duty diesel engine with model-based control". *Applied Energies*, 181, (2021), pp. 268–277. DOI: 10.1016/j.apenergy.2016.07.128 (cit. on p. 151).

[179] J. M. Luján, H. Climent, S. Ruiz, and A. Moratal. "Influence of ambient temperature on diesel engine raw pollutants and fuel consumption in different driving cycles". *International Journal of Engine Research*, 20 (8), (2018), pp. 1527 –1537. DOI: 10.1177/1468087418792353 (cit. on p. 152).

[180] J. Serrano, P.Piqueras, E. Sanchís, and B. Diesel. "Analysis of the Driving Altitude and Ambient Temperature Impact on the Conversion Efficiency of Oxidation Catalysts". *Applied Energies*, 11 (3), (2021), pp. 1–10. DOI: 10.3390/app11031283 (cit. on p. 152).

[181] J. Martín, P. Arnau, P. Piqueras, and A. Aunón. "Development of an Integrated Virtual Engine Model to Simulate New Standard Testing Cycles". In: *WCX World Congress Experience*. SAE International, 2018. DOI: 10.4271/2018-01-1413 (cit. on p. 153).

[182] G. Guennebaud, B. Jacob, et al. *Eigen v3*. Last visited on 2021/04/19. 2010. URL: http://eigen.tuxfamily.org/ (cit. on p. 153).

[183] B. van Leer. "Towards the Ultimate Conservation Difference Scheme. II. Monotonicity and Conservation Combined in a Second-Order Scheme". *Journal of Computational Physics*, 14, (Mar. 1974), p. 361. DOI: 10.1016/0021-9991(74)90019-9 (cit. on p. 153).

[184] E. Toro, M. Spruce, and W. Speares. "Restoration of the contact surface in the HLL Riemann solver". *Shock Waves*, 4 (1), (1994), pp. 25–34. DOI: 10.1007/BF01414629 (cit. on p. 153).

[185] B. Van Leer. "Towards the ultimate conservative difference scheme III. Upstream-centered finite-difference schemes for ideal compressible flow". *Journal of Computational Physics*, 23 (3), (1977), pp. 263–275. ISSN: 0021-9991. DOI: 10.1016/0021-9991(77)90094-8 (cit. on p. 154).

[186] A. Broatch, P. Olmeda, J. Martin, and J. Salvador-Iborra. "Development and Validation of a Submodel for Thermal Exchanges in the Hydraulic Circuits of a Global Engine Model". In: *WCX World Congress Experience*. SAE International, 2018. DOI: 10.4271/2018-01-0160 (cit. on p. 154).

[187] J. Galindo, R. Navarro, L. M. García-Cuevas, D. Tarí, H. Tartoussi, and S. Guilain. "A zonal approach for estimating pressure ratio at compressor extreme off-design conditions". *International Journal of Engine Research*, (2018). DOI: 10.1177/1468087418754899 (cit. on p. 154).

[188] J. R. Serrano, F. J. Arnau, L. M. García-Cuevas, A. Dombrovsky, and H. Tartoussi. "Development and validation of a radial turbine efficiency and mass flow model at design and off-design conditions". *Energy Conversion and Management*, 128, (2016), pp. 281–293. ISSN: 0196-8904. DOI: 10.1016/j.enconman.2016.09.032 (cit. on p. 154).

[189] J. R. Serrano, P. Olmeda, A. Tiseira, L. M. García-Cuevas, and A. Lefebvre. "Theoretical and experimental study of mechanical losses in automotive turbochargers". *Energy*, 55, (2013), pp. 888–898. DOI: 10.1016/j.energy.2013.04.042 (cit. on p. 154).

[190] J. R. Serrano, P. Olmeda, F. J. Arnau, A. Dombrovsky, and L. Smith. "Turbocharger heat transfer and mechanical losses influence in predicting engines performance by using one-dimensional simulation codes". *Energy*, 86, (2015), pp. 204–218. ISSN: 0360-5442. DOI: 10.1016/j.energy.2015.03.130 (cit. on p. 154).

[191] J. R. Serrano, P. Olmeda, F. J. Arnau, and V. Samala. "A holistic methodology to correct heat transfer and bearing friction losses from hot turbocharger maps in order to obtain adiabatic efficiency of the turbomachinery". *International Journal of Engine Research*, 21 (8), (2020), pp. 1314–1335. DOI: 10.1177/1468087419834194 (cit. on p. 154).

Chapter 6

Concluding remarks

Contents

6.1 Introduction

This chapter summarizes the achievements and main contributions of the thesis. The summary of the results and contributions are presented in Section 6.2 divided into main contributions and methodological contributions. Next, Section 6.3 is devoted to list the limitations of the experimental techniques and on the modeling of condensation. Finally, Section 6.4 presents suggestions and future research studies and applications that can be explored to improve the knowledge and employ the investigations of this thesis.

6.2 Summary of findings and contributions

This thesis has contributed to the understanding and prediction of condensation in the LP-EGR system, focusing on the LP-EGR cooler and LP-EGR Three-way junction for automotive applications. The new experimental procedures to obtain the condensation in the LP-EGR cooler and in the Three-way junction have been deeply presented during the chapters. These new techniques have focused on measuring condensation in different conditions and locations in the LP-EGR line, being a completely novelty in the Three-way junction. These experimental results have allowed to validate the condensation models developed in this thesis for both phenomena.

In the contributions of the thesis, interesting findings on new methodologies for approaching real engineering problems in terms of dimension reduction and computational time reduction have been presented. It has deepened the knowledge of condensation phenomena and the modeling behavior with a study on the durability of the compressor impeller. Interesting contributions have appeared on the study of different EGR strategies, in relation to condensation and emission generation.

6.2.1 Main contributions

The main contributions of this thesis are based on three different groups. Firstly, the calculation and the measurement of condensation in heat exchangers (LP-EGR coolers), which is presented in chapter 2. Secondly, condensation in junctions has been studied starting from a 3D-CFD condensation submodel presented by Serrano et al. [73] but validating the model in this thesis with the experimental campaign and new techniques in chapter 3. Finally, work has been done on the modeling of the engine by adapting the water condensation models generated in the previous chapters for rapid calculation in engine cycles.

6.2.1.1 Condensation on Heat exchangers

The contribution of this thesis covers the development and validation of the model to predict water condensation in LP-EGR coolers or heat exchangers based on the outlet gas temperature.

The test rig used for the experimental work was a modified hot continuous flow test rig at CMT-Motores Térmicos. This gas stand laboratory was designed and modified to establish EGR conditions in terms of temperature, mass flow and wet air, with different changes and upgrades depending on the LP-EGR part studied. The challenge of designing the facility was to measure the hot mass flow with significant specific humidity and to measure condensation at the LP-EGR cooler outlet without affecting the condensation process.

Regarding the experimental measurements of condensation in the LP-EGR cooler, different conclusions have been obtained such as the important role of the coolant temperature in the condensation generation, obtaining with the lowest initial coolant temperature, the highest condensation rate and the highest accumulated water at the end of the homologation warm-up cycle. While the inlet gas temperature and the MFR gas have a notable but minor influence on condensation due to the modification of the efficiency of the cooler. In addition, a relevant trend appears in the cases with a refrigerant temperature of -10 °C. Ice forms inside the cooler at the beginning of the test and subsequently

melts rapidly and is expelled through the outlet increasing the condensation rate.

The results obtained demonstrate the robustness of the model, specially when experimental condensation begins, predicting with high fidelity the experimental results. Regarding the time until the condensation stops, a strong dependence on the refrigerant temperature has been found. High mass flow rates decrease the efficiency of the LP-EGR cooler, while increasing the condensation in a non-linear way and reducing the time to stop condensing. Finally, small discrepancies appear by not considering local effects. The development of this model allows to predict condensates in a simulated way and thus to perform calibration strategies knowing the condensation generated.

6.2.1.2 Condensation on Junctions

Regarding the contributions to the LP-EGR junction in the experimental part, a novel wet gas stand has been developed to reproduce the EGR and fresh ambient air, aided with a climatic chamber to provide the cold air mass flow and to test Three-way junctions. The proposed configuration allows the study of the junction outlet with different novel techniques to study the cross section through secondary flows, condensation patterns and the amount of condensed water. Techniques such as planar laser visualization, which had never been used to measure the condensation luminosity, obtained the condensation pattern with good fidelity. Another novel technique developed entirely in this thesis, and that has been a great challenge, has been the indirect measurement of condensation that experimentally characterizes the condensation mass flow rate in the flow, measuring the condensation rate by comparing temperatures and applying an enthalpy balance.

The CFD condensation submodel was presented by Serrano et al. [73] with no experimental verification regarding condensation patterns or condensation mass flow rate, the model was compared with erosion in the compressor impeller with durability tests in the work of Galindo et al. [74]. As a main contribution of this thesis, the model has been deeply validated with different techniques such as PIV to study in-plane velocities and secondary flows with good corre-

lation between simulations and experiments. Also the condensation pattern in experiments has been compared with the pattern in simulations with a good agreement between cases. Finally, the 3D-CFD condensation submodel was compared in some cases with the condensation mass flow rates from the experiments, obtaining a good correlation between the methods with an average difference of 11%.

The development carried out with the study of condensation at the junction of EGR with fresh air is really useful due to the large number of experimental tools developed and the validation of the condensation CFD model. It has been possible to measure a complex phenomenon and thus to have a basis for simplifying models and optimizing emission strategies. It has been demonstrated that when the mixture is reduced, condensation decreases. By having the 3D-CFD tool validated for condensation calculation, it is possible to optimize geometries for condensation attenuation.

6.2.1.3 Engine modeling

The condensation models presented in this thesis, such as the 0D condensation model for LP-EGR coolers, the 3D-CFD condensation submodel and the 0D perfect mixing condensation model for condensation in an LP-EGR junction, have been adapted to model realistic condensation in cold warm-up homologation cycles and, with this, perform different studies on the condensation threshold for compressor impeller damage or the consequences of employing LP-EGR or HP-EGR at different temperatures.

The 0D perfect mixing condensation model for LP-EGR junctions has been based on the work done by Serrano et al. [36]. In this model, perfect mixing between branches is used and the condensation obtained is the maximum amount of water that is able to be produced with these particular input conditions. In this thesis, effects such as water evaporation or section reduction due to a nozzle effect reducing the gas temperature are considered. The special interest of this model lies in the speed of the calculation results compared to 3D-CFD simulations, acquiring an important relevance for modeling engine cycles in chapter 5, with a good agreement with CFD simulations employing different

techniques to correct the results and approximate the 3D-CFD.

Regarding the methodology presented to model the condensation at the LP-EGR junction, different surrogate models with different study variables have been considered in combination between the 0D Perfect Mixing condensation model and the 3D-CFD condensation submodel. In particular, in this work, the Polynomial Response Surface Model with the difference variable has been selected to proceed to the condensation approximation, obtaining good agreement by comparing the observed and predicted condensation at the Three-way junction. Employing this methodology, stationary condensation maps have been presented at the LP-EGR Three-way junction and at the LP-EGR cooler, obtaining 8 times more condensation in the EGR line than on the three-way junction. Focusing on the WLTC warm-up cycles under cold conditions (-7 °C), a compressor damage threshold of 4.8 yr were obtained. As for an ambient temperature sensitivity analysis it has been obtained that at low temperature a high condensation occurs in the whole LP-EGR line with a higher percentage of condensation caused by the Three-way junction. The emissions performed by the analysis have been calculated with a remarkable difference of pollutants in the mean BSFC, a low ambient temperature a high consumption. Finally, an in-depth study of different LP-EGR and HP-EGR strategies was performed focusing on condensation and emissions by activating at different temperatures the LP-EGR or HP-EGR. An early activation of LP-EGR, a low NO_x emission realized by the engine and in terms of condensation, a late activation of LP-EGR a small amount of condensation and a high impeller damage threshold. Advancing condensation activation from $T_{gas.out} = T_{dew}$ reduces NO_x emissions by 54.5 % but increases condensation by 4 ml/cycle and reduces compressor durability damaging threshold to 14.8 years.

Particularly useful is the adaptation of complete models to the rapid calculation of condensation in regulation cycles. Condensation is no longer an almost unquantifiable phenomenon, but can be estimated over long periods of time with variations of the operating points.

6.3 Limitations

The objectives presented in chapter 1 have been fulfilled during the thesis. However, it should be noted that some of the conclusions obtained depend on the case and on the limitations of the experimental measurements and the constraints of the numerical model.

- The experimental setup has some limitations in terms of the maximum gas MFR and the achievable water injection rate. However, the requirements for simulating a C-segment passenger car diesel engine are covered. In this particular test bench, a maximum MFR of 60 kg/h and a maximum specific humidity of 60 g/kg can be achieved. To simulate the conditions of a heavy-duty engine, an improvement should be applied to the test rig by including more water injectors.
  - The scope in which the MF models have been tested are characteristic for a diesel engine. Once the models would applied to a gasoline engine with high values of EGR specific humidity the ranges should increase and also, the experimental setup.
- Experimental tests performed with the LP-EGR cooler to collect condensation water present uncertainties, since the absorption capacity of the LP-EGR cooler and evaporation phenomena when the temperature is above the dew point are not considered.
- The optical techniques used and developed for the study of condensation and secondary flows at the LP-EGR junction present some uncertainties promoted by the resolution of the techniques and time averaging, but when comparing between techniques it is not necessary to apply further corrections. Another discrepancy could appear due to differences between experiments and CFD simulations as the simulations employ a free discharge configuration to measure at the outlet of the LP-EGR junction, but some simulations have been performed to obtain the maximum discrepancy and a value of 3 % appears in the condensation when a free discharge configuration was selected in the CFD simulations instead of an extruded outlet.

- The 0D condensation model for predicting condensation in a LP-EGR cooler has some simplifications and assumptions since it considers instantaneous condensation and does not include a time delay due to the absorption capacity of the cooler or ice formation inside the refrigerator. In addition, the walls are assumed to have the same temperature as the outlet gas and constant at the walls and local temperatures are not considered. An advanced model could include some of these simplifications.

- In the 0D perfect mixing condensation model only simple ducts with three branches are considered, with the possibility of including a reduction of the nozzle section at the outlet of the Three-way junction. As it calculates the condensation when the two flows are fully mixed and the simplification of the Three-way junctions could calculate with a wide range of junction designs.

- The calculation of the condensation threshold for compressor damage is particularized for a given compressor impeller tested on the gas bench with durability tests with some simplifications and assumptions. To extrapolate to another compressor, it is necessary to perform a specific test to obtain the threshold at which erosion appears on the blades, as it could change the hardness and the impeller coating material.

- During the calculation of water condensation in the warm-up cycles some simplifications were made. The main simplification was not to apply the release heat produced in the condensation behavior, this heat release increases the gas temperature reducing the water condensation in the next step. An advanced model should cover this heat release energy to correct the water generation.

6.4 Suggestions for future works

All the scientific contributions of this thesis are suitable for further research into new studies and improvements, including the application of modeling and experimental techniques in novel areas that are growing with green and sustainable energy trends.

As for future studies proposed to improve the modeling of condensation in a junction and heat exchangers, it is proposed to improve the resolution of the novel technique developed entirely in this thesis of indirect condensation measurement, by increasing the samples obtaining a more realistic condensation mass flow rate measurement. Future work on this topic is aimed at developing an advanced condensation model with higher accuracy for heat exchangers, including local wall temperature distribution and partial evaporation. Also, an advanced condensation model or the 0D condensation model developed in this thesis could be applied to the study of water condensation in the charge-air-cooler. New strategies could be studied in terms of coolant temperature in the LP-EGR cooler to heat independently of engine conditions or even establish coolant bypass valves to decouple the influence of coolant temperature on water formation in the heat exchanger.

Following the trends of keeping diesel engines in heavy-duty vehicles and employing LP-EGR more often, some new strategies to collect condensed water in the LP-EGR cooler could be studied and thus reintroduced into the cylinders to reduce in-cylinder and exhaust temperature, mitigate combustion knock, improve combustion phasing, and decrease NOx emissions. An optimal LP-EGR junction design could be developed by focusing on mitigating condensation due to mixing phenomena and thereby reducing erosion in the compressor impeller. An in-depth study of the optimum LP-EGR and HP-EGR could be approached by focusing on transient operations of water condensation and emissions.

New related research topics that could be addressed in the near future include green and sustainable energies. In these new areas that the contributions of this thesis can be applied are hydrogen engines and fuel cell vehicles. In particular, hydrogen engines need a massive amount of EGR in the combustion process with a huge amount of H_2O as gas, producing in the EGR coolers (HP and LP) unwanted water condensation [192]. Focusing on fuel cell vehicles, a humidification is performed before the fuel cell membrane and a turbine is placed after the membrane to supply power in the compressor, this process of gas expansion with highly humid air inside the turbine produces condensation that could be studied with the contributions and models of this thesis [193, 39].

Chapter 5 References

[19] M. Lapuerta, A. Ramos, D. Fernandez-Rodriguez, and I. Gonzalez-Garcia. "High-pressure versus low-pressure exhaust gas recirculation in a Euro 6 diesel engine with lean-NOx trap: Effectiveness to reduce NOx emission". *International Journal of Engine Research*, -, (Nov. 14, 2018), pp. 0–9. DOI: 10.1177/1468087418817447 (cit. on pp. 5, 7, 24, 151).

[20] J. M. Luján, C. Guardiola, B. Pla, and A. Reig. "Switching strategy between HP (high pressure)-and LPEGR (low pressure exhaust gas recirculation) systems for reduced fuel consumption and emissions". *Energy*, 90, (2015), pp. 1790–1798. DOI: 10.1016/j.energy.2015.06.138 (cit. on pp. 6, 7, 25, 140, 151).

[36] J. R. Serrano, P. Piqueras, E. Angiolini, C. Meano, and J. De La Morena. "On Cooler and Mixing Condensation Phenomena in the Long-Route Exhaust Gas Recirculation Line". In: *SAE Technical Paper*. 2015. DOI: 10.4271/2015-24-2521 (cit. on pp. 7, 31, 105, 108, 157, 185).

[57] H. Song and S. Song. "Numerical investigation on a dual loop EGR optimization of a light duty diesel engine based on water condensation analysis". *Applied Thermal Engineering*, 182, (2021), pp. 1–12. DOI: 10.1016/j.applthermaleng.2020.116064 (cit. on pp. 10, 25, 151).

[73] J. Serrano, P. Piqueras, R. Navarro, D. Tarí, and C. Meano. "Development and verification of an in-flow water condensation model for 3D-CFD simulations of humid air streams mixing". *Computers & Fluids*, 167, (2018), pp. 158 –165. ISSN: 0045-7930. DOI: 10.1016/j.compfluid.2018.02.032 (cit. on pp. 11, 13, 25, 51, 53, 66, 95, 105, 107, 153, 183, 184).

[74] J. Galindo, P. Piqueras, R. Navarro, D. Tarí, and C. Meano. "Validation and sensitivity analysis of an in-flow water condensation model for 3D-CFD simulations of humid air streams mixing". *International Journal of Thermal Sciences*, 136, (2019), pp. 410 –419. ISSN: 1290-0729. DOI: 10.1016/j.ijthermalsci.2018.10.043 (cit. on pp. 11, 25, 51, 68, 69, 73, 74, 107, 135, 153, 161, 175, 184).

[176] P. Arnau, J. Martín, B. Pla, and A. Aunón. "Diesel engine optimization and exhaust thermal management by means of variable valve train strategies". *International Journal of Engine Research*, 22 (4), (2021), pp. 1527 –1537. DOI: 10.1177/1468087419894804 (cit. on p. 151).

[177] A. Ramos, J. Munoz, F. Andres, and O. Armas. "NOx emissions from diesel light duty vehicle tested under NEDC and real-word driving conditions". *Transportation Research Part D: Transport and Environment*, 63 (0), (Aug. 1, 2018), pp. 37–48. DOI: 10.1016/j.trd.2018.04.018 (cit. on p. 151).

[178] J. Serrano, P.Piqueras, E. Sanchís, and B. Diesel. "Optimization of dual-loop exhaust gas recirculation splitting for a light-duty diesel engine with model-based control". *Applied Energies*, 181, (2021), pp. 268–277. DOI: 10.1016/j.apenergy.2016.07.128 (cit. on p. 151).

[179] J. M. Luján, H. Climent, S. Ruiz, and A. Moratal. "Influence of ambient temperature on diesel engine raw pollutants and fuel consumption in different driving cycles". *International Journal of Engine Research*, 20 (8), (2018), pp. 1527 –1537. DOI: 10.1177/1468087418792353 (cit. on p. 152).

[180] J. Serrano, P.Piqueras, E. Sanchís, and B. Diesel. "Analysis of the Driving Altitude and Ambient Temperature Impact on the Conversion Efficiency of Oxidation Catalysts". *Applied Energies*, 11 (3), (2021), pp. 1–10. DOI: 10.3390/app11031283 (cit. on p. 152).

[181] J. Martín, P. Arnau, P. Piqueras, and A. Aunón. "Development of an Integrated Virtual Engine Model to Simulate New Standard Testing Cycles". In: *WCX World Congress Experience*. SAE International, 2018. DOI: 10.4271/2018-01-1413 (cit. on p. 153).

[182] G. Guennebaud, B. Jacob, et al. *Eigen v3*. Last visited on 2021/04/19. 2010. URL: http://eigen.tuxfamily.org/ (cit. on p. 153).

[183] B. van Leer. "Towards the Ultimate Conservation Difference Scheme. II. Monotonicity and Conservation Combined in a Second-Order Scheme". *Journal of Computational Physics*, 14, (Mar. 1974), p. 361. DOI: 10.1016/0021-9991(74)90019-9 (cit. on p. 153).

[184] E. Toro, M. Spruce, and W. Speares. "Restoration of the contact surface in the HLL Riemann solver". *Shock Waves*, 4 (1), (1994), pp. 25–34. DOI: 10.1007/BF01414629 (cit. on p. 153).

[185] B. Van Leer. "Towards the ultimate conservative difference scheme III. Upstream-centered finite-difference schemes for ideal compressible flow". *Journal of Computational Physics*, 23 (3), (1977), pp. 263–275. ISSN: 0021-9991. DOI: 10.1016/0021-9991(77)90094-8 (cit. on p. 154).

[186] A. Broatch, P. Olmeda, J. Martin, and J. Salvador-Iborra. "Development and Validation of a Submodel for Thermal Exchanges in the Hydraulic Circuits of a Global Engine Model". In: *WCX World Congress Experience*. SAE International, 2018. DOI: 10.4271/2018-01-0160 (cit. on p. 154).

[187] J. Galindo, R. Navarro, L. M. García-Cuevas, D. Tarí, H. Tartoussi, and S. Guilain. "A zonal approach for estimating pressure ratio at compressor extreme off-design conditions". *International Journal of Engine Research*, (2018). DOI: 10.1177/1468087418754899 (cit. on p. 154).

[188] J. R. Serrano, F. J. Arnau, L. M. García-Cuevas, A. Dombrovsky, and H. Tartoussi. "Development and validation of a radial turbine efficiency and mass flow model at design and off-design conditions". *Energy Conversion and Management*, 128, (2016), pp. 281–293. ISSN: 0196-8904. DOI: 10.1016/j.enconman.2016.09.032 (cit. on p. 154).

[189] J. R. Serrano, P. Olmeda, A. Tiseira, L. M. García-Cuevas, and A. Lefebvre. "Theoretical and experimental study of mechanical losses in automotive turbochargers". *Energy*, 55, (2013), pp. 888–898. DOI: 10.1016/j.energy.2013.04.042 (cit. on p. 154).

[190] J. R. Serrano, P. Olmeda, F. J. Arnau, A. Dombrovsky, and L. Smith. "Turbocharger heat transfer and mechanical losses influence in predicting engines performance by using one-dimensional simulation codes". *Energy*, 86, (2015), pp. 204–218. ISSN: 0360-5442. DOI: 10.1016/j.energy.2015.03.130 (cit. on p. 154).

[191] J. R. Serrano, P. Olmeda, F. J. Arnau, and V. Samala. "A holistic methodology to correct heat transfer and bearing friction losses from hot turbocharger maps in order to obtain adiabatic efficiency of the turbomachinery". *International Journal of Engine Research*, 21 (8), (2020), pp. 1314–1335. DOI: 10.1177/1468087419834194 (cit. on p. 154).

Bibliography

[1] S. Guilain, R. Boubennec, M. Doublet, C. Clement, R. Navarro, D. Tarí, and F. Moya. "Condensation before compressor: a key issue of Low Pressure EGR in Eu7 context". In: *24th Supercharging Conference 2019, Aufladetechnische Konferenz, Dresden*. Sept. 26, 2019 (cit. on pp. xi, 51, 128).

[2] J. Galindo, R. Navarro, D. Tari, and F. Moya. "Development of an experimental test bench and a psychrometric model for assessing condensation on a Low Pressure EGR cooler". *International Journal of Engine Research*, (2020). DOI: 10.1177/1468087420909735 (cit. on pp. xi, 7, 27, 51).

[3] J. Galindo, R. Navarro, D. Tari, and F. Moya. "Analysis of condensation and secondary flows at T-junctions using optical visualization techniques and Computational Fluid Dynamics". *International Journal of Multiphase Flow*, (2021). DOI: 10.1016/j.ijmultiphaseflow.2021.103674 (cit. on p. xi).

[4] J. Galindo, R. Navarro, D. Tari, and F. Moya. "Quantitative validation of an in-flow water condensation model for 3D-CFD simulations of three-way junctions using indirect condensation measurements". *International Journal of Thermal Sciences*, 172, (2022), pp. 1–11. DOI: 10.1016/j.ijthermalsci.2021.107303 (cit. on p. xi).

[5] J. Galindo, R. Navarro, F. Moya, and A. Conchado. "Comprehensive method for obtaining multi-fidelity surrogate models for design space approximation: application to multi-dimensional simulations of condensation due to mixing streams". *submitted to Applied Mathematics and Computation*, (2022) (cit. on p. xi).

[6] J. Galindo, R. Navarro, L. M. García-Cuevas, and F. Moya. "Engine modeling of heat-exchanger and mixing-streams condensation mechanisms: impact of Exhaust Gas Recirculation strategy on trade-off between emissions and compressor durability during engine cold start". *submitted to Applied Energy*, (2022) (cit. on p. xi).

[7] W. in data. URL: https://ourworldindata.org/ (cit. on pp. 2, 3).

[8] *European Automobile Manufacturers' Association's (ACEA). Brussels. The Automobile industry Pocket Guide*. 2018-2019. URL: https://www.acea.be/uploads/publications/ACEA_Pocket_Guide_2018-2019.pdf (cit. on pp. 3, 24).

[9] Volkswagen. URL: https://www.volkswagenag.com/presence/konzern/group-fleet/dokumente/wltp/GFI_WTLP_Broschuere_EN_WLTP_and_RDE_Insights_WEB.pdf (cit. on p. 4).

[10] *European Automobile Manufacturers Association Position Paper. Views on proposals for Euro 7 emission standard*. 2020. URL: https://www.acea.be/uploads/publications/ACEA_Position_Paper-Views_on_proposals_for_Euro_7_emission_standard.pdf (cit. on p. 4).

[11] M. Weilenmann, J.-Y. Faves, and R. Alvarez. "Cold-start emissions of modern passenger cars at different low ambient temperatures and their evolution over vehicle legislation categories". *Atmospheric Environment*, 43, (15 May 5, 2009), pp. 2419–2429. DOI: 10.1016/j.atmosenv.2009.02.005 (cit. on pp. 4, 7, 25).

[12] T. V. Johnson. "Review of Vehicular Emissions Trends". *SAE Int. J. Engines*, 8, (Apr. 2015), pp. 1152–1167. DOI: 10.4271/2015-01-0993 (cit. on p. 4).

[13] H. Chen and J. Yin. "Turbocharger compressor development for diesel passenger car applications". In: 8^{th} *International Conference on Turbochargers and Turbocharging*. IMechE. 2006 (cit. on p. 5).

[14] Y. B. Zeldovich. *The oxidation of nitrogen in combustion explosions*. 21. URSS: Acta Physicochimica, 1946, pp. 577–628 (cit. on p. 5).

[15] Y. B. Zeldovich. "The Oxidation of Nitrogen in Combustion andExplosions". *Selected Works of Yakov Borisovich Zeldovich, Volume I. Princeton University Press*, (2015). DOI: 10.1515/9781400862979.364 (cit. on p. 5).

[16] Petersen Publishing Company and E. Rosen. *The Petersen Automotive Troubleshooting & Repair Manual*. Grosset & Dunlap, 1975. ISBN: 9780448119465 (cit. on p. 5).

[17] C. Giorgio. Zamboni. Massimo. "Experimental study on the effects of HP and LP EGR in an automotive turbocharged diesel engine". *Applied Energy*, 94, (2012). DOI: 10.1016/j.apenergy.2012.01.046 (cit. on p. 5).

[18] J. M. Luján, H. Climent, R. Novella, and M. E. Rivas-Perea. "Influence of a low pressure EGR loop on a gasoline turbocharged direct injection engine". *Applied Thermal Engineering*, 89, (2015), pp. 432–443. DOI: 10.1016/j.applthermaleng.2015.06.039 (cit. on p. 5).

[19] M. Lapuerta, A. Ramos, D. Fernandez-Rodriguez, and I. Gonzalez-Garcia. "High-pressure versus low-pressure exhaust gas recirculation in a Euro 6 diesel engine with lean-NOx trap: Effectiveness to reduce NOx emission". *International Journal of Engine Research*, -, (Nov. 14, 2018), pp. 0–9. DOI: 10.1177/1468087418817447 (cit. on pp. 5, 7, 24, 151).

[20] J. M. Luján, C. Guardiola, B. Pla, and A. Reig. "Switching strategy between HP (high pressure)-and LPEGR (low pressure exhaust gas recirculation) systems for reduced fuel consumption and emissions". *Energy*, 90, (2015), pp. 1790–1798. DOI: 10.1016/j.energy.2015.06.138 (cit. on pp. 6, 7, 25, 140, 151).

[21] S. Moroz, G. Bourgoin, J. M. Luján, and B. Pla. "Acidic condensation in low pressure EGR systems using diesel and biodiesel fuels". *SAE Int. J. Fuels Lubr*, 2009-01-2805, (2009). DOI: 10.4271/2009-01-2805 (cit. on pp. 6, 7, 25).

[22] D. T. Hountalas, G. C. Mavropoulos, and K. B. Binder. "Effect of exhaust gas recirculation (EGR) temperature for various EGR rates on heavy duty DI diesel engine performance and emissions". *Energy*, 33 (2), (2008), pp. 272–283. DOI: 10.1016/j.energy.2007.07.002 (cit. on pp. 6, 7, 25).

[23] D. Roth, I. G. Tabares, and A. S. Álvarez. "Condensing LPL EGR Mixer with Mid-Pressure Loop". *SAE International Journal of Engines*, 8 (2015-01-1257), (2015), pp. 1544–1552 (cit. on pp. 6, 11).

[24] J. M. Desantes, J. M. Luján, B. Pla, and J. A. Soler. "On the combination of high-pressure and low-pressure exhaust gas recirculation loops for improved fuel economy and reduced emissions in high-speed direct-injection engines". *International Journal of Engine Research*, 14 (1), (2013), pp. 3–11. DOI: 10.1177/1468087412437623 (cit. on p. 6).

[25] L. Cornolti, A. Onorati, T. Cerri, G. Montenegro, and F. Piscaglia. "1D simulation of a turbocharged Diesel engine with comparison of short and long EGR route solutions". *Applied Energy*, 111, (2013), pp. 1–15. DOI: 10.1016/j.apenergy.2013.04.016 (cit. on pp. 7, 140).

[26] P. Michel, A. Charlet, G. Colin, Y. Chamaillard, G. Bloch, and C. Nouillant. "Optimizing fuel consumption and pollutant emissions of gasoline-HEV with catalytic converter". *Control Engineering Practice*, 61, (2017), pp. 198 –205. ISSN: 0967-0661. DOI: 10.1016/j.conengprac.2015.12.010 (cit. on pp. 7, 51).

[27] A. Maiboom, X. Tauzia, and J.-F. Hetet. "Influence of high rates of supplemental cooled EGR on NOx and PM emissions of an automotive HSDI diesel engine using an LP EGR loop". *International Journal of Energy Research*, 32 (15), (2008), pp. 1383–1398. DOI: 10.1002/er.1455 (cit. on p. 7).

[28] Galindo, J. and Serrano, J.R. and Navarro, R. and García Olivas, G. "Numerical modeling of centrifugal compressors with heterogeneous incoming flow due to low pressure exhaust gas recirculation". In: *Proceedings of ASME Turbo Expo 2020: Turbomachinery Technical Conference and Exposition*. GT2020-16030. American Society of Mechanical Engineers. 2020 (cit. on pp. 7, 73).

[29] A. Maiboom, X. Tauzia, and J.-F. Hétet. "Influence of EGR unequal distribution from cylinder to cylinder on NOx-PM trade-off of a HSDI automotive Diesel engine". *Applied Thermal Engineering*, 29 (10), (2009), pp. 2043 – 2050. ISSN: 1359-4311. DOI: 10.1016/j.applthermaleng.2008.10.017 (cit. on p. 7).

[30] A. Sakowitz, M. Mihaescu, and L. Fuchs. "Flow decomposition methods applied to the flow in an IC engine manifold". *Applied Thermal Engineering*, 65 (1–2), (2014), pp. 57–65. ISSN: 1359-4311. DOI: 10.1016/j.applthermaleng.2013.12.082 (cit. on p. 7).

[31] J. Galindo, H. Climent, R. Navarro, G. García-Olivas, S. Guilain, and R. Boubennec. *Effect of Numerical Configuration on Predicted EGR Cylinder-to-Cylinder Dispersion*. Tech. rep. SAE Technical Paper, 2020. DOI: 10.4271/2020-01-1113 (cit. on p. 7).

[32] J. Bishop, M. Stettler, N. Molden, and A. Boies. "Engine maps of fuel use and emissions from transient driving cycles". *Applied Energy*, 183, (Dec. 1, 2016), pp. 202–217. DOI: 10.1016/j.apenergy.2016.08.175 (cit. on pp. 7, 25).

[33] Z. Wei, X. Jinliang, and L. Guohua. "Multi-channel effect of condensation flow in a micro triple-channel condenser". *International Journal of Multiphase Flow*, 34, (12 Dec. 1, 2008), pp. 1175–1184. DOI: 10.1016/j.ijmultiphaseflow.2008.05.004 (cit. on pp. 7, 25).

[34] A. Castorrini, A. Corsini, F. Rispoli, P. Venturini, K. Takizawa, and T. E. Tezduyar. "Computational analysis of wind-turbine blade rain erosion". *Computers & Fluids*, 141 (Supplement C), (2016), pp. 175 –183. ISSN: 0045-7930. DOI: 10.1016/j.compfluid.2016.08.013 (cit. on pp. 7, 51).

[35] P. Z. John, T. Koka, and S. Dayalan. "Water droplet erosion simulation of a turbocharger compressor wheel". In: *ASME Turbo Expo 2014: Turbine Technical Conference and Exposition*. GT2014-26974. American Society of Mechanical Engineers. 2014 (cit. on pp. 7, 51).

[36] J. R. Serrano, P. Piqueras, E. Angiolini, C. Meano, and J. De La Morena. "On Cooler and Mixing Condensation Phenomena in the Long-Route Exhaust Gas Recirculation Line". In: *SAE Technical Paper*. 2015. DOI: 10.4271/2015-24-2521 (cit. on pp. 7, 31, 105, 108, 157, 185).

[37] Y. Zhang, S. Xu, and C. Lin. "Performance improvement of fuel cell systems based on turbine design and supercharging system matching". *Applied Thermal Engineering*, 180, (2020), pp. 1–11. DOI: 10.1016/j.applthermaleng.2020.115806 (cit. on p. 8).

[38] P. Chuang, M. Rahman, F. Mojica, D. Hussey, D. Jacobson, and J. LaManna. "The interactive effect of heat and mass transport on water condensation in the gas diffusion layer of a proton exchange membrane fuel cell". *Journal of Power Sources*, 480, (2020), pp. 1–10. DOI: 10.1016/j.jpowsour.2020.229121 (cit. on p. 8).

[39] T. Wittmann, S. Luck, C. Bode, and J. Friedrichs. "Modelling the Condensation Phenomena within the Radial Turbine of a Fuel Cell Turbocharger". *International Journal of Turbomachinery Propulsion and Power*, (2021). DOI: 10.3390/ijtpp6030023 (cit. on pp. 8, 189).

[40] X. Yu, Z. Guo, L. He, W. Dong, and P. Sun. "Experimental study on lean-burn characteristics of an SI engine with hydrogen/gasoline combined injection and EGR". *International Journal of Hydrogen Energy*, 44, (2019), pp. 1–10. DOI: 10.1016/j.ijhydene.2019.03.236 (cit. on p. 8).

[41] S. S. Hoseini, G. Najafi, and B. Ghobadia. "Experimental and numerical investigation of heat transfer and turbulent characteristics of a novel EGR cooler in diesel engine". *Applied Thermal Engineering*, 108, (2016), pp. 1344–1356. DOI: 10.1016/j.applthermaleng.2016.08.018 (cit. on pp. 9, 26).

[42] C. Cuevas, D. Makaire, and P. Ngendakumana. "Thermo-hydraulic characterization of an automotive intercooler for a low pressure EGR application". *Applied Thermal Engineering*, 31, (14-15 Apr. 19, 2011), pp. 2474–2484. DOI: 10.1016/j.applthermaleng.2011.04.013 (cit. on pp. 9, 25).

[43] M. Abarham, T. Chafekar, J. Hoard, D. Styles, and D. Assanis. "A visualization test setup for investigation of water-deposit interaction in a surrogate rectangular cooler exposed to diesel exhaust flow". *SAE Technical Paper*, 2012-01-0364, (2012). DOI: 10.4271/2012-01-0364 (cit. on pp. 9, 26).

[44] C. Guo, Q. Liu, B. Zheng, Y. You, and Y. Li. "Development of model based on condensation area ratio and effect on heat transfer capacity of indirect evaporative cooling". *Applied Thermal Engineering*, 164, (Jan. 5, 2020). DOI: 10.1016/j.applthermaleng.2019.114557 (cit. on pp. 9, 25).

[45] A. Razmavar, M. Malayeri, and M. Abd-Elhady. "Influence of secondary flow on the thermal performance of exhaust gas recirculation (EGR) coolers". *International Journal of Thermal Sciences*, (2021). DOI: 10.1016/j.ijthermalsci.2020.106720 (cit. on pp. 9, 26).

[46] A. R. Razmavar and M. R. Malayeri. "Thermal performance of a rectangular exhaust gas recirculation cooler subject to hydrocarbon and water vapor condensation". *International Journal of Thermal Sciences*, 143, (Sept. 1, 2019), pp. 1–13. DOI: 10.1016/j.ijthermalsci.2019.05.006 (cit. on pp. 9, 26).

[47] A. Warey, D. Long, S. Balestrino, and P. Szymkowcz. "Visualization and Analysis of Condensation in Exhaust Gas Recirculation Coolers". In: *SAE International Paper*. Aug. 4, 2013. DOI: 10.4271/2013-01-0540 (cit. on pp. 9, 25).

[48] C. Paz, E. Suarez, J. Vence, and A. Cabarcos. "Numerical modelling of fouling process in EGR system: A review". *Environmental Issues and Sustainable Development*, (2020). DOI: 10.5772/intechopen.93062 (cit. on pp. 9, 26).

[49] C. Paz, E. Suarez, J. Vence, and J. Hoard. "Evolution of EGR cooler deposits under hydrocarbon condensation: Analysis of local thickness, roughness, and fouling layer density". *International Journal of Thermal Sciences*, (2021). DOI: 10.1016/j.ijthermalsci.2020.106744 (cit. on pp. 9, 26).

[50] A. Pandal, J. M. Garcia-Oliver, and J. M. Pastor. "Eulerian CFD modeling of nozzle geometry effects on ECN Sprays A and D: Assessment and analysis". *IJER*, 21, (2019), pp. 73–88. DOI: 10.1177/1468087419882500 (cit. on p. 10).

[51] R. Payri, G. Bracho, P. Marti-Aldaravi, and J. Marco-Gimeno. "Analysis of spray/wall impingement using an ECN single-hole injector and a controlled-temperature wall under realistic engine conditions". *Applied Thermal Engineering*, 208, (2022), pp. 118–167. DOI: 10.1016/j.applthermaleng.2022.118167 (cit. on p. 10).

[52] G. Montenegro and A. Onorati. "1D Thermo-Fluid Dynamic Modeling of Reacting Flows inside Three-Way Catalytic Converters". In: 2009, pp. 1444–1459 (cit. on p. 10).

[53] R. J. Clarkson and S. F. Benjamin. "Modelling the Effect of Moisture on Catalyst Warm-up". In: 1995, pp. 555–562 (cit. on p. 10).

[54] R. Payri, G. Bracho, P. Marti-Aldaravi, and J. Marco-Gimeno. "Numerical Analysis of Urea to Ammonia Conversion in Automotive Selective Catalytic Reduction Realistic Conditions". *Ind. Eng. Chem. Res.*, 60, (2021), pp. 14329–14340. DOI: 10.1021/acs.iecr.1c02627 (cit. on p. 10).

[55] J. Galindo, V. Dolz, J. Monsalve-Serrano, M. Maldonado, and L. Odillard. "Advantages of using a cooler bypass in the low-pressurre exhaust gas recirculation line of a compression ignition diesel engine operating at cold conditions". *Internal Journal of Engine Research*, (Apr. 29, 2020). DOI: 10.1177/1468087420914725 (cit. on pp. 10, 25, 51, 140).

[56] N. Ghassembaglou and L. Torkaman. "Efficient design of exhaust gas cooler in cold EGR equipped diesel engine". *Alexandria Engineering Journal*, 55, (2016), pp. 769–778. DOI: 10.1016/j.aej.2016.01.023 (cit. on pp. 10, 25).

[57] H. Song and S. Song. "Numerical investigation on a dual loop EGR optimization of a light duty diesel engine based on water condensation analysis". *Applied Thermal Engineering*, 182, (2021), pp. 1–12. DOI: 10.1016/j.applthermaleng.2020.116064 (cit. on pp. 10, 25, 151).

[58] B. Yang, W. Su, S. Deng, and L. Zhao. "State-of-art of branching T-junction: Experiments, modeling, developing prospects and applications". *Experimental Thermal and Fluid Sciences*, 109, (2019). DOI: 10.1016/j.expthermflusci.2019.109895 (cit. on pp. 10, 51).

[59] H. Li, G. Wei, Y. Wang, D. Yang, B. Sun, and W. Hong. "Investigation on the phase split characteristics of slug and annular flow in a metal foam-filled T-junction". *Experimental Thermal and Fluid Science*, 109 (109878), (Dec. 1, 2019). DOI: 10.1016/j.expthermflusci.2019.109878 (cit. on p. 10).

[60] P. Lu, S. Deng, L. Zhao, Y. Zhao, W. Xu, and Y. Zhang. "Analysis of pressure drop in T-junction and its effect on thermodynamic cycle efficiency". *Applied Energy*, 231, (2018), pp. 1–13. DOI: 10.1016/j.apenergy.2018.09.134 (cit. on p. 10).

[61] M. Zhou, R. Kulenovic, and E. Laurien. "Advanced flow pattern for describing tangential flow oscillation in thermal-mixing pipe flow at a horizontal T-Junction". *International Journal of Thermal Sciences*, 136, (Feb. 1, 2019), pp. 328–336. DOI: 10.1016/j.ijthermalsci.2018.10.045 (cit. on pp. 10, 51).

[62] M. Zhou, R. Kulenovic, and E. Laurien. "T-junction experiments to investigate thermal-mixing pipe flow with combined measurement techniques". *Applied Thermal Engineering*, 150, (Mar. 5, 2019), pp. 237–249. DOI: 10.1016/j.applthermaleng.2018.12.161 (cit. on pp. 10, 51).

[63] C. Evrim, X. Chu, and E. Laurien. "Analysis of thermal mixing characteristics in different T-junction configurations". *International Journal of Heat and Mass Transfer*, 158, (2020), pp. 1–10. DOI: 10.1016/j.ijheatmasstransfer.2020.120019 (cit. on pp. 10, 51).

[64] C. Evrim and E. Laurien. "Numerical study of thermal mixing mechanisms in T-junctions". *Applied Thermal Engineering*, 138, (2021), pp. 1–13. DOI: 10.1016/j.applthermaleng.2020.116155 (cit. on pp. 10, 51).

[65] M. Georgiou and M. V. Papalexandris. "Turbulent mixing in T-junctions: The role of the temperature as an active scalar". *International Journal of Heat and Mass Transfer*, 115, (2017), pp. 793–809. DOI: 10.1016/j.ijheatmasstransfer.2017.08.081 (cit. on pp. 10, 52).

[66] A. Sakowitz, M. Mihaescu, and L. Fuchs. "Turbulent flow mechanisms in mixing T-junctions by Large Eddy Simulations". *International Journal of Heat and Fluid Flow*, 45, (2014), pp. 135–146. DOI: 10.1016/j.ijheatfluidflow.2013.06.014 (cit. on pp. 10, 52, 78, 80).

[67] A. Sakowitz, S. Reifarth, M. Mihaescu, and L. Fuchs. "Modeling of EGR Mixing in an engine intake manifold using LES". *Oil & Gas Science and Technology*, 69 (1), (2014), pp. 167–176. DOI: 10.2516/ogst/2013118 (cit. on p. 10).

[68] A. Sakowitz, M. Mihaescu, and L. Fuchs. "Effects of velocity ratio and inflow pulsations on the flow in a T-junction by Large Eddy Simulation". *Computers & Fluids*, 88, (2013), pp. 374–385. ISSN: 0045-7930. DOI: 10.1016/j.compfluid.2013.10.001 (cit. on p. 10).

[69] A. Reihani, J. Hoard, S. Klinkert, C.-K. Kuan, and D. Styles. "Numerical Evaluation of the Effects of Low Pressure EGR Mixer Configuration on Turbocharger Compressor Performance". In: *ASME 2018 Internal Combustion Engine Division Fall Technical Conference*. American Society of Mechanical Engineers Digital Collection. 2018 (cit. on p. 10).

[70] A. Reihani, J. Hoard, S. Klinkert, C.-K. Kuan, D. Styles, and G. McConville. "Experimental response surface study of the effects of low-pressure exhaust gas recirculation mixing on turbocharger compressor performance". *Applied Energy*, 261, (2020), p. 114349. DOI: 10.1016/j.apenergy.2019.114349 (cit. on pp. 10, 104).

[71] J. Galindo, R. Navarro, D. Tarí, and G. García-Olivas. "Centrifugal compressor influence on condensation due to Long Route-Exhaust Gas Recirculation mixing". *Applied Thermal Engineering*, 144, (2018), pp. 901 –909. ISSN: 1359-4311. DOI: 10.1016/j.applthermaleng.2018.09.005 (cit. on pp. 11, 51, 52, 69, 70, 77, 82, 107).

[72] J. Galindo, A. Gil, R. Navarro, and G. García-Olivas. "Numerical assessment of humid air streams in three-way junctions and impact on volume condensation". *Applied Thermal Engineering*, (2022). DOI: 10.1016/j.applthermaleng.2021.117676 (cit. on pp. 11, 115).

[73] J. Serrano, P. Piqueras, R. Navarro, D. Tarí, and C. Meano. "Development and verification of an in-flow water condensation model for 3D-CFD simulations of humid air streams mixing". *Computers & Fluids*, 167, (2018), pp. 158 –165. ISSN: 0045-7930. DOI: 10.1016/j.compfluid.2018.02.032 (cit. on pp. 11, 13, 25, 51, 53, 66, 95, 105, 107, 153, 183, 184).

[74] J. Galindo, P. Piqueras, R. Navarro, D. Tarí, and C. Meano. "Validation and sensitivity analysis of an in-flow water condensation model for 3D-CFD simulations of humid air streams mixing". *International Journal of Thermal Sciences*, 136, (2019), pp. 410 –419. ISSN: 1290-0729. DOI: 10.1016/j.

ijthermalsci.2018.10.043 (cit. on pp. 11, 25, 51, 68, 69, 73, 74, 107, 135, 153, 161, 175, 184).

[75] N. Zheng, L. Zhao, and J. Wei. "Experimental research on liquid-vapor two-phase flow separation of zeotropic mixtures at an impacting T-junction". *Experimental Thermal and Fluid Science*, 89, (2017), pp. 140–152. DOI: 10.1016/j.expthermflusci.2017.08.012 (cit. on p. 11).

[76] C Walker, M Simiano, R. Zboray, and H.-M. Prasser. "Investigations on mixing phenomena in single-phase flow in a T-junction geometry". *Nuclear Engineering and Design*, 239 (1), (2009), pp. 116–126. DOI: 10.1016/j.nucengdes.2008.09.003 (cit. on p. 11).

[77] Z. Wang, S. Sanders, J. A. Backhaus, A. Munnannur, and N. M. Schmidt. "H2O absorption tomography in a diesel aftertreatment system using a polymer film for optical access". *Applied Physic B*, 127, (286 2017). DOI: 10.1007/s00340-017-6867-8 (cit. on pp. 11, 52).

[78] J. V. Pastor, J. J. Lopez, J. E. Julia, and J. V. Benajes. "Planar Laser-Induced Fluorescence fuel concentration measurements in isothermal Diesel sparys". *Optical Society of America*, 10, (7 2002). DOI: 10.1364/OE.10.000309 (cit. on pp. 11, 60).

[79] T. Xue and S. Zhang. "Investigation on heat transfer characteristics of falling liquid film by planar laser-induced fluorescence". *International Journal of Heat and Mass Transfer*, 126, (2018), pp. 715–724. DOI: 10.1016/j.ijheatmasstransfer.2018.05.039 (cit. on pp. 11, 52).

[80] A.J.Torregrosa, A.Broatch, J.V.Pastor, and J.García-Tíscar. "Measuring turbocharger compressor inlet backflow through particle image velocimetry". *Experimental Thermal and Fluid Science*, 99, (2018), pp. 420–432. DOI: 10.1016/j.expthermflusci.2018.08.015 (cit. on pp. 11, 55, 56).

[81] C. Brucker. "Study of the three-dimensional flow in a T-junction using a dual-scanning method for three-dimensional scanning-particle-image velocimetry (3-D SPIV)". *Experimental Thermal and Fluid Science*, 14 (1), (1997), pp. 35–44. DOI: 10.1016/S0894-1777(96)00110-0 (cit. on pp. 11, 52).

[82] C. Espinoza, M. Simmons, F. Alberini, O. Mihailova, D. Rothman, and A. Kowalski. "Flow studies in an in-line Silverson 150/250 high shear mixer using PIV". *Chemical Engineering Research and Design*, (2018). ISSN: 0263-8762. DOI: 10.1016/j.cherd.2018.01.028 (cit. on pp. 11, 52).

[83] R. D. Reitz, H. Ogawa, R. Payri, T. Fansler, and S. Kokjohn. "IJER editorial: The future of the internal combustion engine". *International Journal of engine Research*, 21, (1 2020), pp. 0–8. DOI: 10.1177/1468087419877990 (cit. on p. 24).

[84] M. Dalla Chiara B. Pellicelli. "Sustainable road transport from the energy and modern society points of view: Perspectives for the automotive industry and production". *Journal of cleaner production*, 133, (2016), pp. 1283–1301. DOI: 10.1016/j.jclepro.2016.06.015 (cit. on p. 24).

[85] P. Prevedouros and L. Mitropoulos. "Life Cycle Emissions and Cost Study of Light Duty Vehicles". *Transportation Research Procedia*, 15, (2016), pp. 749–760. DOI: 10.1016/j.trpro.2016.06.062 (cit. on p. 24).

[86] M. Andre. "The ARTEMIS European driving cycles for measuring car pollutant emissions". *Science of The Total Environment*, 334-335, (Dec. 1, 2004), pp. 73–84. DOI: 10.1016/j.scitotenv.2004.04.070 (cit. on p. 24).

[87] P. Olmeda, J. Martín, F. Arnau, and S. Artham. "Analysis of the energy balance during World harmonized Light vehicles Test Cycle in warmed and cold conditions using a Virtual Engine". *International Journal of Engine Research*, -, (Oct. 3, 2019), pp. 0–18. DOI: 10.1177/1468087419878593 (cit. on p. 24).

[88] J. M. Luján, H. Climent, L. M. García-Cuevas, and A. Moratal. "Pollutant emissions and diesel oxidation catalyst performance at low ambient temperatures in transient load conditions". *Applied Thermal Engineering*, 129, (2018), pp. 1527 –1537. ISSN: 1359-4311. DOI: 10.1016/j.applthermaleng.2017.10.138 (cit. on p. 24).

[89] K. Jinyoung, S. Jeonghun, M. Cha-Lee, and P. Simsoo. "Comparative study on low ambient temperature regulated/unregulated emissions characteristics of idling light-duty diesel vehicles at cold start and hot restart". *Fuel.*, 233, (2018), pp. 620–631. DOI: 10.1016/j.fuel.2018.05.144 (cit. on p. 24).

[90] K. Fotis, S. Kim, S. Shobhana, and C. Thomas. "Modeling and optimization of integrated exhaust gas recirculation and multi-stage waste heat recovery in marine engines". *Energy Conversion and Management*, 151, (Nov. 1, 2017), pp. 286–295. DOI: 10.1016/j.enconman.2017.09.004 (cit. on p. 24).

[91] X. Yang, J. Liu, P. Fu, N. Chen, and J. Wei. "Experimental and theoretical study of pressure oscillation of unstable steam-air jet condensation in water in a rectangular channel". *International Journal of Multiphase Flow*, 119, (Oct. 1, 2019), pp. 14–27. DOI: 10.1016/j.ijmultiphaseflow.2019.07.009 (cit. on p. 25).

[92] L. Seungho, C. Jinho, L. Haneol, K. Taejoon, and S. Weon. "Understanding the condensation process of turbulent steam jet using the PDPA system". *International Journal of Multiphase Flow*, 98, (Jan. 1, 2018), pp. 168–181. DOI: 10.1016/j.ijmultiphaseflow.2017.09.007 (cit. on p. 25).

[93] D. Hongbing, W. Chao, and C. Chao. "Experimental and numerical studies on self-excited periodic oscillation of vapor condensation in a sonic nozzle". *Experimental Thermal and Fluid Science*, 68, (November 2015), pp. 288–299. DOI: 10.1016/j.expthermflusci.2015.05.002 (cit. on p. 25).

[94] N. Rahim, W. Davies, P. Hrnjakbc, and J. Meyera. "Numerical study of steam condensation inside a long inclined flattened channel". *International Journal of Heat and Mass Transfer*, 134, (May 1, 2019), pp. 450–467. DOI: 10.1016/j.ijheatmasstransfer.2019.01.063 (cit. on p. 25).

[95] D. Murphy, M. Macdonald, A. Mahvi, and S. Garimella. "Condensation of propane in vertical minichannels". *International Journal of Heat and Mass Transfer*, 137, (July 1, 2019), pp. 1154–1166. DOI: 10.1016/j.ijheatmasstransfer.2019.04.023 (cit. on p. 25).

[96] Y. Vasyliv, D. Lee, R. Tower Ted. Ng, V. Polashock, and A. Alexeed. "Modeling condensation on structured surfaces using lattice Boltzmann method". *International Journal of Heat and Mass Transfer*, 136, (June 1, 2019), pp. 196–212. DOI: 10.1016/j.ijheatmasstransfer.2019.02.090 (cit. on p. 25).

[97] J. M. Luján, V. Dolz, J. Monsalve-Serrano, and M. A. Bernal. "High-pressure exhaust gas recirculation line condensation model of an internal combustion diesel engine operating at cold conditions". *International Journal of Engine Research*, -, (July 4, 2019), pp. 0–10. DOI: 10.1177/1468087419868026 (cit. on p. 26).

[98] Z. Akram Ali. Zachary. "Open Source Building Science Sensors (OSBSS): A low-cost Arduino-based platform for long-term indoor environmental data collection". *Building and Environmental*, 100, (May 1, 2016), pp. 114–126. DOI: 10.1016/j.buildenv.2016.02.010 (cit. on p. 29).

[99] K. L. Wang, D. Li, N. Husnain, and S. Fareed. "Numerical and experimental investigation on water vapor condensation in turbulent flue gas". *Applied Thermal Engineering*, 160, (Sept. 1, 2019). DOI: 10.1016/j.applthermaleng.2019.114009 (cit. on p. 51).

[100] K.-H. Brune, H.-P. Schiffer, R Christmann, and M Gnewikow. "Experimental investigations of the disturbed inlet-flow structure caused by mixing geometries and its influence on the performance of a turbocharger centrifugal compressor". In: *ASME Turbo Expo 2009: Power for Land, Sea, and Air*. American Society of Mechanical Engineers Digital Collection. 2009, pp. 1295–1304 (cit. on p. 51).

[101] J. Choi, S. Satpathy, J. Hoard, D. Styles, and C. Kuan. "An Experimental and Computational Analysis of Water Condensation Separator Within a Charge Air Cooler". *International Combustion Engine Division Fall Technical Conference*, (2017), pp. 1–11. DOI: 10.1115/ICEF2017-3609 (cit. on pp. 52, 140).

[102] E. Randolph, F. Bocher, S. Kroll, and N. Wright. "Visual, Thermodynamic, and Electrochemical Analysis of Condensate in a Stoichiometric Spark-Ignited EGR Engine". *SAE Technical Paper*, (2017), pp. 1–12. DOI: 10.4271/2018-01-1406 (cit. on p. 52).

[103] L. Chen, X. Zhang, C. Wang, and C. Yang. "Analysis on High-Pressure Water Separator". *Procedia Engineering*, 121, (Aug. 10, 2015), pp. 558–566. DOI: 10.1016/j.proeng.2015.08.1034 (cit. on p. 52).

[104] E. Randolph, F. Bocher, S. Kroll, and N. Wright. "Research and development of Self-contained Water Injection Systems". *International Journal of Environmental Research and Public Health*, 18, (2017), pp. 1–10. DOI: 10.3390/ijerph18105392 (cit. on p. 52).

[105] *STAR-CCM+*. Release version 12.06.010. CD-adapco. 2018. URL: http://ww.cd-adapco.com (cit. on pp. 52, 74).

[106] J. Galindo, A. Gil, R. Navarro, and D. Tarí. "Analysis of the impact of the geometry on the performance of an automotive centrifugal compressor using CFD simulations". *Applied Thermal Engineering*, 148, (2019), pp. 1324–1333. ISSN: 1359-4311. DOI: 10.1016/j.applthermaleng.2018.12.018 (cit. on p. 53).

[107] J. V. Pastor, J. M. García-Oliver, A. García, and M. Pinotti. "Effect of laser induced plasma ignition timing and location on Diesel spray combustion". *Energy Conversion and Management*, 133, (2017), pp. 41–55. DOI: 10.1016/j.enconman.2016.11.054 (cit. on p. 55).

[108] A. Sciacchitano and B. Wieneke. "PIV uncertainty propagation". *Measurement Science and Technology*, 27, (2016), pp. 1–16. DOI: 10.1088/0957-0233/27/8/084006 (cit. on p. 57).

[109] L. Pickett, C. Genzale, J. Manin, and L.-M. Malbec. "Measurement Uncertainty of Liquid Penetration in Evaporating Diesel Sprays". In: 23^{rd} *Annual Conference on Liquid Atomization and Spray Systems*. ILASS Americas. 2011 (cit. on p. 58).

[110] A. Charogiannis, J. Sik, V. Voulgaropoulos, and C. Markides. "Structured planar laser-induced fluorescence (S-PLIF) for the accurate identification of interfaces in multiphase flows". *International Journal of Multiphase Flow*, 118, (2019), pp. 193–204. DOI: 10.1016/j.ijmultiphaseflow.2019.06.002 (cit. on p. 60).

[111] S. Schuster, D. Brillert, and F. Benra. "Condensation in Radial Turbines-Part I: Mathematical Modeling". *Journal of Turbomachinery*, 140, (2018), pp. 1–9. DOI: 10.1115/1.4040934 (cit. on p. 68).

[112] S. Schuster, D. Brillert, and F. Benra. "Condensation in Radial Turbines-Part II: Application of the Mathematical Model to a Radial Turbine Series". *Journal of Turbomachinary*, 140, (2018), pp. 1–7. DOI: 10.1115/1.4040935 (cit. on p. 68).

[113] T. Wittmann, C. Bode, and J. Friedrichs. "The Feasibility of an Euler-Lagrange Approach for the Modeling of Wet Steam". *Journal of Engineering for gas turbines and power*, 143, (2021), pp. 1–8. DOI: 10.1115/1.4049859 (cit. on p. 68).

[114] T. Wittman, S. Luck, C. Bode, and J. Friedrichs. "Numerical Simulation of Nucleation and Condensation and Radial Turbines". In: *CAD-FEM ANSYS Simulation Conference, Dusseldorf, Germany*. 2019 (cit. on p. 68).

[115] D. C. Wilcox. "Reassessment of the scale-determining equation for advanced turbulence models". *AIAA journal*, 26 (11), (1988), pp. 1299–1310. DOI: 10.2514/3.10041 (cit. on p. 74).

[116] D. Tarí. "Effect of inlet configuration on the performance and durability of an automotive turbocharger compressor". PhD thesis. Universitat Politècnica de València. Departamento de Máquinas y Motores Térmicos, 2018. DOI: 10.4995/Thesis/10251/104410. URL: http://hdl.handle.net/10251/104410 (cit. on pp. 75, 106).

[117] R. Tunstall, D. Laurence, R. Prosser, and A. Skillen. "Large eddy simulation of a T-Junction with upstream elbow: The role of Dean vortices in thermal fatigue". *Applied Thermal Engineering*, 107, (Aug. 25, 2017), pp. 672–680. DOI: 10.1016/j.applthermaleng.2016.07.011 (cit. on pp. 78, 80).

[118] E. Idelchik and E. Fried. *Handbook of hydraulic resistance*. Jaico Publishing House, 1986. ISBN: 9788179921180 (cit. on p. 78).

[119] Y. Xue, R. Hhellmuth, and D. Shin. "Formation of Vortices in Idealised Branching Vessels: A CFD Benchmark Study". *Cardiovascular Engineering and Technology*, 11, (2020), pp. 544–559. DOI: 10.1007/s13239-020-00477-9 (cit. on p. 78).

[120] T. Lu, D. Attinger, and S. M. Liu. "Large-eddy simulations of velocity and temperature fluctuations in hot and cold fluids mixing in a tee junction with an upstream straicht or elbow main pipe". *Nuclear Engineering and Design*, 263, (Apr. 2, 2013), pp. 32–41. DOI: 10.1016/j.nucengdes.2013.04.002 (cit. on p. 80).

[121] W. H. Lyne. "Unsteady viscous flow in a curved pipe". *Journal of Fluid Mechanics*, 45 (1), (1971), pp. 13–31. DOI: 10.1017/S0022112071002970 (cit. on p. 80).

[122] P. Jiang, Q. Zhou, and X. Shao. *Surrogate Model-Based Engineering Design and Optimization*. Springer Tracts in Mechanical Engineering, 2020. ISBN: 978-981-15-0730-4. DOI: 10.1007/978-981-15-0731-1 (cit. on pp. 103, 122, 128).

[123] B. Rodic. "Industry 4.0 and the New Simulation Modelling Paradigm". *Organizacija*, 50, (2017), pp. 193–207. DOI: 10.1515/orga-2017-0017 (cit. on p. 103).

[124] A. Barkanyi, T. Chovan, S. Nemeth, and J. Abonyi. "Modelling for Digital Twins-Potential Role of Surrogate Models". *Processes*, 9, (2021), p. 476. DOI: 10.3390/pr9030476 (cit. on p. 103).

[125] L. Wright and S. Davidson. "How to tell the difference between a model and a digital twin". *Advanced Modeling and Simulation in Engineering Sciences*, 7, (2020), pp. 1–10. DOI: 10.1186/s40323-020-00147-4 (cit. on p. 103).

[126] K. Cheng and C. Ling. "Surrogate-assisted global sensitivity analysis: an overview". *Structural and Multidisciplinary Optimization*, 61, (2020), pp. 1187–1213. DOI: 10.1007/s00158-019-02413-5 (cit. on p. 103).

[127] J. Galindo, H. Climent, R. Navarro, and G. Garcia-Olivas. "Assessment of the numerical and experimental methodology to predict EGR cylinder-to-cylinder dispersion and pollutant emissions". *International Journal of Engine Research*, 1, (2020), pp. 1–10. DOI: 10.1177/1468087420972544 (cit. on p. 103).

[128] P. Piqueras, M. J. Ruiz, J. Martin, and A. Tsolakis. "Sensitivity of pollutants abatement in oxidation catalysts to the use of alternative fuels". *Fuel*, 297, (2021), pp. 1–10. DOI: 10.1016/j.fuel.2021.120686 (cit. on p. 103).

[129] Z. Li and X. Zheng. "Review of design optimization methods for turbomachinery aerodynamics". *Progress in aerospace science*, 93, (2017), pp. 1–23. DOI: 10.1016/j.paerosci.2017.05.003 (cit. on p. 103).

[130] A. Forrester, A. Sobester, and A. Keane. "Engineering Design via Surrogate Modelling". *Proceedings of the royal society A*, 463, (2007), pp. 3251–3269. DOI: 10.1098/rspa.2007.1900 (cit. on pp. 103, 104, 123).

[131] S. Shan and G. Wang. "Survey of modeling and optimization strategies to solve high-dimensional design problems with computationally-expensive black-box functions". *Structural and Multidisciplinary Optimization*, 41, (2010), pp. 219–241. DOI: 10.1007/s00158-009-0420-2 (cit. on p. 103).

[132] J. Galindo, R. Navarro, L. M. García-Cuevas, D. Tarí, H. Tartoussi, and S. Guilain. "A zonal approach for estimating pressure ratio at compressor extreme off-design conditions". *International Journal of Engine Research*, 20 (4), (2019), pp. 393–404. DOI: 10.1177/1468087418754899 (cit. on p. 103).

[133] J. Galindo, A. Tiseira, R. Navarro, D. Tarí, H. Tartoussi, and S. Guilain. "Compressor Efficiency Extrapolation for 0D-1D Engine Simulations". In: *SAE Technical Paper*. SAE International, Apr. 2016. DOI: 10.4271/2016-01-0554 (cit. on p. 103).

[134] R.Tirnovan, S.Giurgea, A.Miraoui, and M.Cirrincione. "Surrogate modelling of compressor characteristics for fuel-cell applications". *Applied Energy*, 85, (2008), pp. 394–403. DOI: 10.1016/j.apenergy.2007.07.003 (cit. on p. 103).

[135] Z. Leylek and A. J. Neely. "Global Three-Dimensional Surrogate Modeling of Gas Turbine Aerodynamic Performance". In: *Proceedings of ASME Turbo Expo 2017: Power for Land, Sea and Air*. ASME, 2017, pp. 1–12. DOI: 10.1115/GT2017-63920 (cit. on p. 103).

[136] Z. Qian, C. Seepersad, V. Roshan, and J. Allen. "Building Surrogate Models Based on Detailed and Approximate Simulations". *Journal of mechanical design*, 128, (2006), pp. 668–677. DOI: 10.1115/1.2179459 (cit. on p. 103).

[137] F. Sanchez, M. Budinger, and I. Hazyuk. "Dimensional analysis and surrogate models for the thermal modeling of Multiphysics systems". *Applied Thermal Engineering*, 110, (2017), pp. 758–771. DOI: 10.1016/j.applthermaleng.2016.08.117 (cit. on p. 103).

[138] C. Xin, L. Li, L. Teng, and Y. Zhenjiang. "A reduced order aerothermodynamic modeling framework for hypersonic vehicles based on surrogate and POD". *Chinese Journal of Aeronautics*, 28, (2015), pp. 1328–1342. DOI: 10.1016/j.cja.2015.06.024 (cit. on p. 103).

[139] J. M. Luján, H. Climent, L. M. García-Cuevas, and A. Moratal. "Volumetric efficiency modelling of internal combustion engines based on a novel adaptive learning algorithm of artificial neural networks". *Applied Thermal Engineering*, 123, (2017), pp. 625–634. DOI: 10.1016/j.applthermaleng.2017.05.087 (cit. on p. 104).

[140] R. Yondo, E. Andres, and E. Valero. "A review on design of experiments and surrogate models in aircraft real-time and many-query aerodynamic analyses". *Progress in Aerospace Sciences*, 96, (2018), pp. 23–61. DOI: 10.1016/j.paerosci.2017.11.003 (cit. on p. 104).

[141] G. Fernandez, C. Park, N. Kim, and R. Haftka. "Issues in Deciding Whether to Use Multifidelity Surrogates". *AIAA Journal*, 57, (2019), pp. 1–16. DOI: 10.2514/1.J057750 (cit. on p. 104).

[142] B. Williams and S. Cremaschi. "Selection of surrogate modeling techniques for surface approximation and surrogate-based optimization". *Chemical Engineering Research and Design*, 170, (2021), pp. 76–89. DOI: 10.1016/j.cherd.2021.03.028 (cit. on p. 104).

[143] T. Simpson, T. Mauery, J. Norte, and F. Mistree. "Kriging models for global approximation in simulation-based multidisciplinary design optimization". *AIAA Journal*, 39, (2001), pp. 2233–2241. DOI: 10.2514/3.15017 (cit. on p. 104).

[144] H. Fang and M. Horstemeyer. "Global response approximation with radial basis functions". *Engineering Optimization*, 38, (2006), pp. 407–424. DOI: 10.1080/03052150500422294 (cit. on p. 104).

[145] L. Jia, R. Alizadeh, J. Hao, G. Wang, J. Allen, and F. Mistree. "A rule-based method for automated surrogate model selection". *Advanced Engineering Informatics*, 45, (2020), pp. 1–16. DOI: 10.1016/j.aei.2020.101123 (cit. on p. 104).

[146] B. Peherstorfer, K. Willcox, and M. Gunzburger. "Survey of Multifidelity Methods in Uncertainty Propagation, Inference, and Optimization". *Society for Industrial and Applied Mathematics*, 60, (2018), pp. 1–42. DOI: 10.1137/16M1082469 (cit. on p. 104).

[147] N. Razaaly, G. Persico, and P. Congedo. "Multi-fidelity surrogate-based optimization of transonic and supersonic axial turbine profiles". In: *Proceedings of ASME Turbo Expo 2020*. 2020 (cit. on p. 104).

[148] K. Yoo, O. Bacarreza, and M. Ferri. "Multi-fidelity robust design optimisation for composite structures based on low-fidelity models using successive high-fidelity corrections". *Composite structures*, 259, (2021), pp. 1–12. DOI: 10.1016/j.compstruct.2020.113477 (cit. on p. 104).

[149] C. Bastidasa, M. DeFilippo, C. Chryssostomidis, and G. E. Karniadakis. "A Multifidelity Framework and Uncertainty Quantification for Sea Surface Temperature in the Massachusetts and Cape Cod Bays". *Earth and Space science*, 7, (2020), pp. 1–10. DOI: 10.1029/2019EA000954 (cit. on p. 104).

[150] K. Vishal and R. Ganguli. "Multi-fidelity analysis and uncertainty quantification of beam vibration using co-kriging interpolation method". *Applied Mathematics and Computation*, 398, (2021), pp. 1–10. DOI: 10.1016/j.amc.2021.125987 (cit. on p. 104).

[151] A. Hebbal, L. Brevault, M. Balesdent, E. Talbi, and N. Melab. "Multi-fidelity modeling with different input domain definitions using Deep Gaussian processes". *Structural and Multidisciplinary Optimization*, (2021). DOI: 10.1007/s00158-020-02802-1 (cit. on p. 104).

[152] M. Xiao, G. Zhang, P. Breitkopf, and P. Villon. "Extended Co-Kriging interpolation method based on multi-fidelity data". *Applied Mathematics and Computation*, 323, (2018), pp. 120–131. DOI: 10.1016/j.amc.2017.10.055 (cit. on p. 104).

[153] P. Vojkuvkova, O. Sikula, and J. Weyr. "Assessment of condensation of water vapor in the mixing chamber by CFD method". In: *EPJ Web of Conferences*. Vol. 92. 2015. DOI: 10.1051/epjconf/20159202112 (cit. on p. 105).

[154] N. Kimura, H. Ogawa, and H. Kamide. "Experimental study on fluid mixing phenomena in T-pipe junction with upstream elbow". *Nuclear Engineering and Design*, 240 (10), (2010), pp. 3055–3066. DOI: 10.1016/j.nucengdes.2010.05.019 (cit. on p. 115).

[155] S. Rezaeiravesh, R. Vinuesa, and P. Schlatter. "Towards multifidelity models with calibration for turbulent flows". In: *14th WCCM-ECCOMAS Congress*. 2020 (cit. on p. 115).

[156] G. Box and D. Benhken. "How to tell the difference between a model and a digital twin". *Technometrics*, 2, (1960), pp. 455–475. DOI: 10.1080/00401706.1960.10489912 (cit. on p. 119).

[157] S. Ferreira, R. Bruns, H. Ferreira, and G. Matos. "Box-Behnken design: An alternative for the optimization of analytical methods". *Analytica Chimica Acta*, 597 (2), (2007), pp. 179–186. DOI: 10.1016/j.aca.2007.07.011 (cit. on p. 120).

[158] W. Song and A. Keane. "Parameter screening using impact factors and surrogate-based ANOVA techniques". In: *11th AIAA/ISSMO Multidisciplinary Analysis and Optimization Conference*. AIAA, 2006, pp. 188–196 (cit. on p. 120).

[159] V. B. Silva and A. Rouboa. "Optimizing the DMFC operating conditions using a response surface method". *Applied Mathematics and Computation*, 218 (12), (2012), pp. 6733–6743. ISSN: 0096-3003. DOI: 10.1016/j.amc.2011.12.039 (cit. on p. 120).

[160] J. D. C. Díaz, P. G. Nieto, D. Castro-Fresno, and P. M. Rodríguez. "Steady state numerical simulation of the particle collection efficiency of a new urban sustainable gravity settler using design of experiments by FVM". *Applied Mathematics and Computation*, 217 (21), (2011), pp. 8166–8178. ISSN: 0096-3003. DOI: 10.1016/j.amc.2011.03.044 (cit. on p. 122).

[161] L. Chen, Y. Ma, Y. Guo, C. Zhang, Z. Liang, and X. Zhang. "Quantifying the effects of operational parameters on the counting efficiency of a condensation particle counter using responde surface Design of Experiments (DOE)". *Journal of Aerosol Science*, 106, (2017), pp. 11–23. DOI: 10.1016/j.jaerosci.2016.12.005 (cit. on p. 122).

[162] S. Subramani, R. Govindasamy, G. Lakshmi, and N. Rao. "Predictive correlations for NOx and smoke emission of DI CI engine fuelled with diesel-biodiesel-higher alcohol blends-response surface methodology approach". *Fuell*, 269, (Feb. 1, 2020). DOI: 10.1016/j.fuel.2020.117304 (cit. on p. 122).

[163] R. V. Lenth. "Response-Surface Methods in R, Using rsm". *Journal of Statistical Software*, 32 (7), (2009), pp. 1–17. DOI: 10.18637/jss.v032.i07 (cit. on p. 122).

[164] I. for the Design of Advanced Energy Systems. URL: https://idaes-pse.readthedocs.io/en/1.5.1/surrogate/pysmo/pysmo_radialbasisfunctions.html (cit. on p. 123).

[165] D. G. Krige. "A statistical approach to some mine valuation and allied problems on the Witwatersrand: By DG Krige". PhD thesis. University of the Witwatersrand, 1951 (cit. on p. 123).

[166] U. o. M. Department of Aerospace Engineering. URL: https://smt.readthedocs.io/en/latest/_src_docs/surrogate_models/krg.html (cit. on p. 123).

[167] M. A. Bouhlel, J. T. Hwang, N. Bartoli, R. Lafage, J. Morlier, and J. R. R. A. Martins. "A Python surrogate modeling framework with derivatives". *Advances in Engineering Software*, (2019), p. 102662. ISSN: 0965-9978. DOI: https://doi.org/10.1016/j.advengsoft.2019.03.005 (cit. on p. 123).

[168] M. Xiao, P. Breitkopf, R. Filomeno, and C. Knopf-Lenoir. "Model reduction by CPOD and Kriging-application to the shape optimization of an intake port". *Structural and Multidisciplinary Optimization*, 41, (2010), pp. 555–574. DOI: 10.1007/s00158-009-0434-9 (cit. on p. 124).

[169] S. Bagheri, W. Konen, and T. Bäck. "Comparing kriging and radial basis function surrogates". In: *Proc. 27. Workshop Computational Intelligence*. Universitätsverlag Karlsruhe. 2017, pp. 243–259 (cit. on p. 124).

[170] P. Chandrashekarappa and R. Duvigneau. "Radial basis functions and kriging metamodels for aerodynamic optimization". *INRIA Document*, (2007), p. 44 (cit. on p. 124).

[171] D. Legates and G. Mccabe. "Evaluating the Use Of Goodness-of-Fit Measures in Hydrologic and Hydroclimatic Model Validation". *Water Resources Research*, 35, (1999), pp. 233–241. DOI: 10.1029/1998WR900018 (cit. on p. 124).

[172] A. Davydenko and R. Fildes. "Measuring Forecasting Accuracy: Problems and Recommendations (by the example of SKU-level judgmental adjustments)". *Intelligent Fashion Forecasting Systems: Models and Applications*, 43, (2013), pp. 43–70. DOI: 10.1007/978-3-642-39869-8_4 (cit. on p. 124).

[173] K. Roy, R. Nayaran, P. Ambure, and R. Aher. "Be aware of error measures. Further studies on validation of predictive QSAR models". *Chemometrics and Intelligent Laboratory Systems*, 152, (2016), pp. 18–33. DOI: 10.1016/j.chemolab.2016.01.008 (cit. on pp. 125, 133).

[174] Galindo, José and Climent, Héctor and Navarro, Roberto. "Modeling of EGR Systems". In: *1D and Multi-D Modeling Techniques for IC Engine Simulation*. Ed. by A. Onorati and G. Montenegro. SAE International, 2020. Chap. 7, pp. 257–278. DOI: 10.4271/9780768099522 (cit. on p. 128).

[175] M. Fernandez, S. Dubreuil, N. Bartoli, and C. Gogu. "Linear regression-based multifidelity surrogate for disturbance amplification in multiphase explosion". *Structural and Multidisciplinary Optimization*, 60, (2019), pp. 2205–2220. DOI: 10.1007/s00158-019-02387-4 (cit. on pp. 133, 136).

[176] P. Arnau, J. Martín, B. Pla, and A. Aunón. "Diesel engine optimization and exhaust thermal management by means of variable valve train strategies". *International Journal of Engine Research*, 22 (4), (2021), pp. 1527–1537. DOI: 10.1177/1468087419894804 (cit. on p. 151).

[177] A. Ramos, J. Munoz, F. Andres, and O. Armas. "NOx emissions from diesel light duty vehicle tested under NEDC and real-word driving conditions". *Transportation Research Part D: Transport and Environment*, 63 (0), (Aug. 1, 2018), pp. 37–48. DOI: 10.1016/j.trd.2018.04.018 (cit. on p. 151).

[178] J. Serrano, P.Piqueras, E. Sanchís, and B. Diesel. "Optimization of dual-loop exhaust gas recirculation splitting for a light-duty diesel engine with model-based control". *Applied Energies*, 181, (2021), pp. 268–277. DOI: 10.1016/j.apenergy.2016.07.128 (cit. on p. 151).

[179] J. M. Luján, H. Climent, S. Ruiz, and A. Moratal. "Influence of ambient temperature on diesel engine raw pollutants and fuel consumption in different driving cycles". *International Journal of Engine Research*, 20 (8), (2018), pp. 1527 –1537. DOI: 10.1177/1468087418792353 (cit. on p. 152).

[180] J. Serrano, P.Piqueras, E. Sanchís, and B. Diesel. "Analysis of the Driving Altitude and Ambient Temperature Impact on the Conversion Efficiency of Oxidation Catalysts". *Applied Energies*, 11 (3), (2021), pp. 1–10. DOI: 10.3390/app11031283 (cit. on p. 152).

[181] J. Martín, P. Arnau, P. Piqueras, and A. Aunón. "Development of an Integrated Virtual Engine Model to Simulate New Standard Testing Cycles". In: *WCX World Congress Experience*. SAE International, 2018. DOI: 10.4271/2018-01-1413 (cit. on p. 153).

[182] G. Guennebaud, B. Jacob, et al. *Eigen v3*. Last visited on 2021/04/19. 2010. URL: http://eigen.tuxfamily.org/ (cit. on p. 153).

[183] B. van Leer. "Towards the Ultimate Conservation Difference Scheme. II. Monotonicity and Conservation Combined in a Second-Order Scheme". *Journal of Computational Physics*, 14, (Mar. 1974), p. 361. DOI: 10.1016/0021-9991(74)90019-9 (cit. on p. 153).

[184] E. Toro, M. Spruce, and W. Speares. "Restoration of the contact surface in the HLL Riemann solver". *Shock Waves*, 4 (1), (1994), pp. 25–34. DOI: 10.1007/BF01414629 (cit. on p. 153).

[185] B. Van Leer. "Towards the ultimate conservative difference scheme III. Upstream-centered finite-difference schemes for ideal compressible flow". *Journal of Computational Physics*, 23 (3), (1977), pp. 263–275. ISSN: 0021-9991. DOI: 10.1016/0021-9991(77)90094-8 (cit. on p. 154).

[186] A. Broatch, P. Olmeda, J. Martin, and J. Salvador-Iborra. "Development and Validation of a Submodel for Thermal Exchanges in the Hydraulic Circuits of a Global Engine Model". In: *WCX World Congress Experience*. SAE International, 2018. DOI: 10.4271/2018-01-0160 (cit. on p. 154).

[187] J. Galindo, R. Navarro, L. M. García-Cuevas, D. Tarí, H. Tartoussi, and S. Guilain. "A zonal approach for estimating pressure ratio at compressor extreme off-design conditions". *International Journal of Engine Research*, (2018). DOI: 10.1177/1468087418754899 (cit. on p. 154).

[188] J. R. Serrano, F. J. Arnau, L. M. García-Cuevas, A. Dombrovsky, and H. Tartoussi. "Development and validation of a radial turbine efficiency and mass flow model at design and off-design conditions". *Energy Conversion and Management*, 128, (2016), pp. 281–293. ISSN: 0196-8904. DOI: 10.1016/j.enconman.2016.09.032 (cit. on p. 154).

[189] J. R. Serrano, P. Olmeda, A. Tiseira, L. M. García-Cuevas, and A. Lefebvre. "Theoretical and experimental study of mechanical losses in automotive turbochargers". *Energy*, 55, (2013), pp. 888–898. DOI: 10.1016/j.energy.2013.04.042 (cit. on p. 154).

[190] J. R. Serrano, P. Olmeda, F. J. Arnau, A. Dombrovsky, and L. Smith. "Turbocharger heat transfer and mechanical losses influence in predicting engines performance by using one-dimensional simulation codes". *Energy*, 86, (2015), pp. 204–218. ISSN: 0360-5442. DOI: 10.1016/j.energy.2015.03.130 (cit. on p. 154).

[191] J. R. Serrano, P. Olmeda, F. J. Arnau, and V. Samala. "A holistic methodology to correct heat transfer and bearing friction losses from hot turbocharger maps in order to obtain adiabatic efficiency of the turbomachinery". *International Journal of Engine Research*, 21 (8), (2020), pp. 1314–1335. DOI: 10.1177/1468087419834194 (cit. on p. 154).

[192] A. Nande, S. Szwaja, and J. Naber. "Impact of EGR on Combustion Processes in a Hydrogen Fuelled SI Engine". *SAE paper*, (2008). DOI: 10.4271/2008-01-1039 (cit. on p. 189).

[193] S. Luck, T. Wittmann, J. G. C. Bode, and J. Friedrichs. "Impact of Condensation on the System Performance of a Fuel Cell Turbocharger ". *Machines*, (2022). DOI: 10.3390/machines10010059 (cit. on p. 189).

"When Henry Ford made cheap reliable cars, peaple said 'nah, what is wrong with a horse?' that was a huge bet he made and it worked"

— Elon Musk